

NASA CR-143695

N74-25957  
CR-139014

"DEVELOPMENT AND PERFORMANCE OF IR DETECTORS IN THE  
1.5 TO 2.4 MICROMETER REGION THAT OPERATE AT 240 K"

A. F. Chiang and N. C. Aldrich  
Honeywell Radiation Center  
2 Forbes Road  
Lexington, Mass. 02173

November 1973  
Final Report  
NAS5-21646

Prepared for  
Goddard Space Flight Center  
Greenbelt, Maryland 20771



1. Report No.	2. Government Accession No.	3. Recipient's Catalog No.	
4. Title and Subtitle "DEVELOPMENT AND PERFORMANCE OF IR DETECTORS IN THE 1.5 TO 2.4 MICROMETER REGION THAT OPERATE AT 240 K"		5. Report Date	6. Performing Organization Code
7. Author(s) Alice F. Chiang and Nancy C. Aldrich		8. Performing Organization Report No.	
9. Performing Organization Name and Address Honeywell Radiation Center 2 Forbes Road Lexington, Mass. 02173		10. Work Unit No.	11. Contract or Grant No. NAS5-21646
		13. Type of Report and Period Covered Final Technical Report	
12. Sponsoring Agency Name and Address Goddard Space Flight Center Greenbelt, Maryland 20771		14. Sponsoring Agency Code	
		15. Supplementary Notes	
16. Abstract  <p>The work effort under this study resulted in the production of high performance 1.5 to 2.4 micrometers (Hg,Cd)Te photodetectors for operating at 240 °K or above. The detailed characterization of the detector with respect to detector temperature and background flux led to a development of an empirical model for minority carrier trapping. The concept of detective time constant is presented and successfully demonstrated by the four detectors delivered on this contract. An alternative approach is presented with the use of photovoltaic (Hg,Cd)Te detectors.</p>			
17. Key Words (Hg,Cd)Te Near Infrared Detectors		18. Distribution Statement	
19. Security Classif. (of this report)	20. Security Classif. (of this page)	21. No. of Pages	22. Price

## PREFACE

This is the final Technical Report under NASA-Goddard Contract NAS5-21646. The specific design objectives for the mercury, cadmium telluride (Hg,Cd)Te-detectors were as follows:

- 1) Specific detectivity,  $D^*_{\lambda p}$ , greater than  $4 \times 10^{11}$  cm Hz<sup>1/2</sup>/watt.
- 2) Operating temperature greater than 240 °K.
3. Detective time constant less than 10 μs.

The required 1.5 to 2.4 μm region is divided into two bands, Band 1 for detectors which respond to radiation in the 1.55 to 1.75 μm interval, Band 2 for detectors which respond in the 2.08 to 2.35 μm interval. Of the four final detectors shipped, W1 and W2 are in Band 1 and W3 and W4 are in Band 2. W2 has the highest specific detectivity at 240 °K, with

$$D^*_{\lambda p} (\lambda p = 1.7 \mu\text{m}, 10^3, 6) = 6.5 \times 10^{11} \text{ cm Hz}^{1/2}/\text{watt}$$

The detectivity for all the detectors increased rapidly with decrease in temperature to 200 °K. The work effort under this study resulted in the production of high performance 1.5 to 2.4 micrometer mercury cadmium telluride infrared photodetectors for operating at 240 °K or above.

Each of the four shipped detectors has a detective time constant less than 5 μs, which well surpassed the specification.

Near infrared photoconductive (Hg,Cd)Te detectors have been shown to have very high performance due to minority carrier trapping. An empirical model for trapping in (Hg,Cd)Te is presented. This shows an understanding of the effects of photoconductive trapping in (Hg,Cd)Te. Further effort is required to understand the mechanism behind this effect and to control it an alternative approach is presented with the use of photovoltaic (Hg,Cd)Te.

## TABLE OF CONTENTS

SECTION	TITLE	PAGE
1	INTRODUCTION.....	1-1
2	TECHNICAL DISCUSSION.....	2-1
2.1	MATERIAL PROPERTY OF (Hg,Cd)Te.....	2-1
2.2	THEORETICAL STUDY.....	2-6
2.2.1	Radiative Limits.....	2-6
2.2.2	D* <sub>BB</sub> Derivation.....	2-13
2.2.3	Trapping Model.....	2-16
2.2.4	PV-PC Detector Trade-Off.....	2-42
2.3	MEASUREMENT TECHNIQUES.....	2-58
2.3.1	Variable Temperature Dewar.....	2-58
2.3.2	Blackbody Measurements.....	2-58
2.3.3	Light Emitting Diode Measurement.....	2-70
2.3.4	Testing Schedule.....	2-75
2.4	DETECTOR CHARACTERISTICS.....	2-79
2.4.1	Temperature and Background Dependence of Response Time.....	2-79
2.4.2	The Temperature and Background Dependence of Responsivity.....	2-79
2.4.3	Comparison of the Trapping Model and Experimental Data.....	2-87
2.4.4	Final Detectors.....	2-91
3	NEW TECHNOLOGY.....	3-1
APPENDIX A	TEST REPORTS.....	A-1
APPENDIX B	NEAR INFRARED (Hg,Cd)Te PHOTODETECTORS....	B-1
APPENDIX C	LIST OF SYMBOLS.....	C-1

SECTION 1  
INTRODUCTION

This is the final Technical Report under NASA/Goddard Contract NAS5-21646. The work effort under this resulted in the production of high performance 1.5 to 2.4  $\mu\text{m}$  (Hg,Cd)Te photodetectors for operating at 240  $^{\circ}\text{K}$  or above.

The specific design objectives and data requirements for the (Hg,Cd)Te detectors were as follows:

1. Specific detectivity,  $D^*_{\lambda}$  greater than  $4 \times 10^{11}$   $\text{cm Hz}^{1/2}/\text{watt}$ .
2. Operating temperature greater than 240  $^{\circ}\text{K}$
3. Detective time constant less than 10 microseconds.

In addition, measurements were made of:

1.  $D^*_{\lambda}$  vs wavelength at 240  $^{\circ}\text{K}$ .
2.  $D^*_{\lambda p}$  vs detector temperature.
3.  $R_{\lambda p}$  vs detector temperature.
4.  $D^*_{\lambda p}$  vs chopping frequency at optimum bias at 240  $^{\circ}\text{K}$ .
5.  $R^*_{\lambda p}$  vs chopping frequency at optimum bias at 240  $^{\circ}\text{K}$ .
6. Noise spectrum at optimum bias at 240  $^{\circ}\text{K}$ .

In order to reach the design goals for the 1.5 to 2.4  $\mu\text{m}$  (Hg,Cd)Te photodetectors, we have concentrated on relatively large bandgap material, i.e.  $E_g$  greater than 0.53 eV, in which the signal and response time constant exhibit a temperature and background radiation dependence, which are generally attributed to minority carrier trapping. We have demonstrated that the classical single-level trapping model is not adequate to explain the details of the temperature and background dependent results observed in (Hg,Cd)Te. A trapping model was developed during the course of this program which postulates a continuum of levels with an exponential distribution of occupied sites in the bandgap. The results calculated from this model provide reasonably good agreement with our experimental data. An alternative approach using pv (Hg,Cd)Te is considered in comparison with the trapping mode photoconductive

detectors. All this is presented in Section 2 of this report.

The program was divided into the following procedures:

- 1) A theoretical calculation of device performance was made and the bulk parameter (n value) were optimized for operation at 240 °K.
- 2) An (Hg,Cd)Te ingot with the desired properties was grown and characterized.
- 3) Detectors were fabricated and tested at 232 °K.
- 4) If the measured detectivity falls within a specified range of design goal, then the spectral response is determined.
- 5) The best detectors were tested at different temperature for temperatures bracketing 240 °K.
- 6) Those detectors which have passed the critical spectral and temperature requirements were tested to give data on noise spectra, response time,  $\tau_{pc}$ , and the detective time constant  $\tau_{det}$ .
- 7) The four best detectors, two in each band, were selected, retested and packaged. These were shipped with a data package for each.

## SECTION 2

### TECHNICAL DISCUSSION

The technical discussion is divided into four major sections: material properties of (Hg,Cd)Te, theoretical study, measurement techniques and detector characteristics.

(Hg,Cd)Te is a variable bandgap semiconductor material which can be grown to meet a specific cutoff wavelength at the operating temperature desired. The first part of this chapter discusses the major material consideration in designing detectors which meet the program goals.

During the course of this program, emphasis was placed on obtaining the theoretical limit for predicting high performance near infrared (Hg,Cd)Te photodetectors in an elevated temperature region and the understanding of the controlling mechanism for the behavior of near infrared (NIR) photodetectors as a function of temperature, background, photon flux, and wavelength. These subjects will be discussed in Section 2.2. The present approach is empirical, based on extensive and detailed data. Thus, measurement techniques, which played an important role, will be discussed in Section 2.3. A thorough description of the characteristics of the final detectors shipped will be found in Section 2.4.

#### 2.1 MATERIAL PROPERTY OF (Hg,Cd)Te

Materials in the alloy system  $\text{Hg}_{1-x}\text{Cd}_x\text{Te}$  have energy gaps which are continuously variable from 0 to 1.6 eV. The temperature and compositional dependence of the energy gap have been determined by measuring the cutoff wavelengths of detectors of different compositions at a number of different temperatures.

The cutoff wavelength was defined as the wavelength at which response was one-half peak value.

from

$$E_g = \frac{1.24}{\lambda_{co}} \quad (2.1)$$

where  $E_g$  is in electron volts when  $\lambda$  is in micrometers.

Figure 2.1 is a plot of  $E_g$  versus  $T$  obtained from data on eight detectors of different  $x$ -values. Note that the energy gap appears to be an almost linear function of temperature. The following empirical expression was derived to describe the temperature and composition dependence of the energy gap.

$$E_g = 1.59 x - 0.25 + 5.23 \times 10^{-4} T (1 - 2.08 x) + 0.327 x^3 \quad (2.2)$$

The data of Figure 2.1 are presented in Figure 2.2 and compared with values calculated from equation 2.2. The values of  $x$  were adjusted by a small amount as indicated to provide a better fit.

Figure 2.3 is a plot of equation 2.2 suitable for quick interpolation. For example, a  $2.35 \mu\text{m}$  detector requires an energy gap of  $0.528 \text{ eV}$ , which can be obtained at  $240 \text{ }^\circ\text{K}$  from material with an  $x$ -value of approximately  $0.45$ .

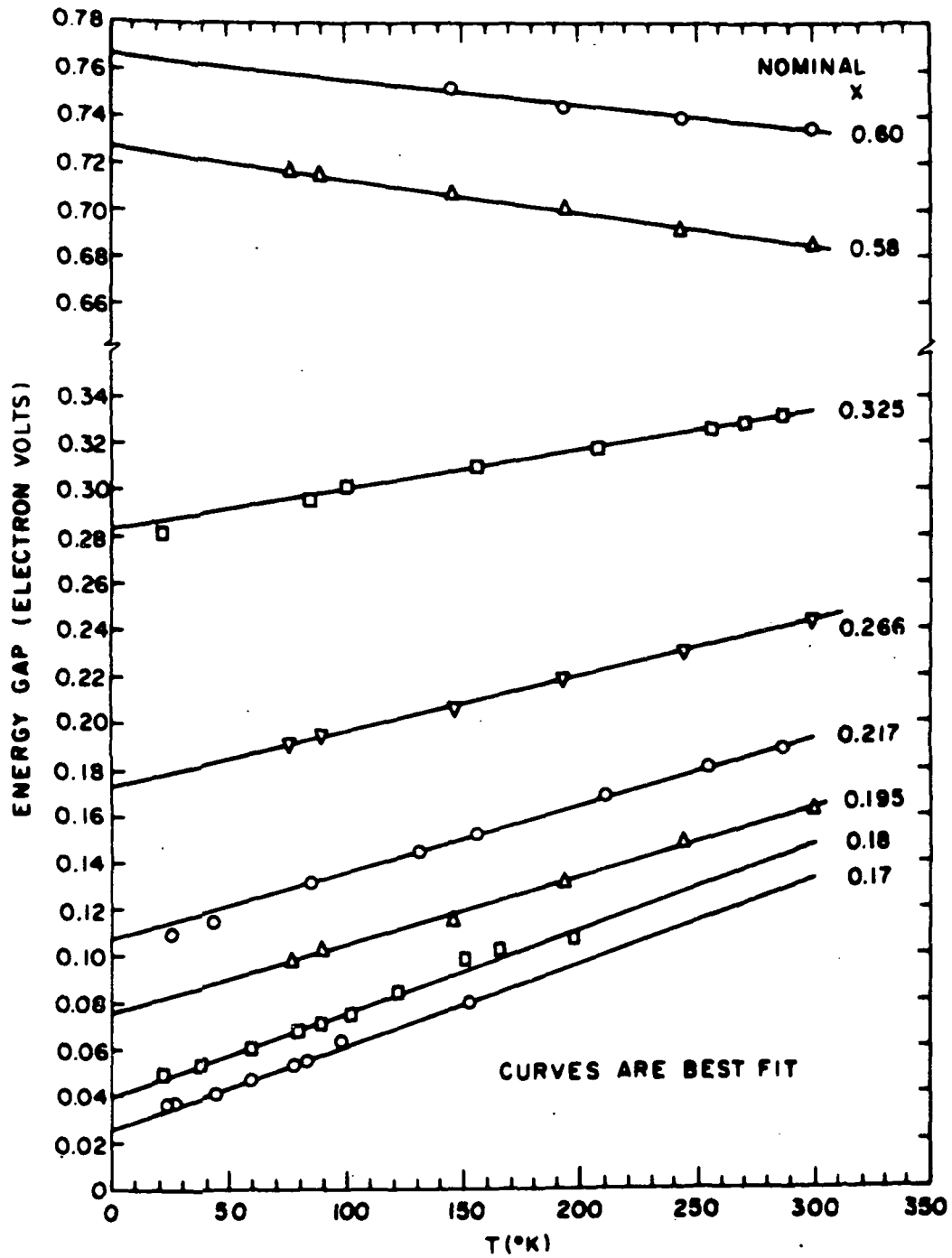


Figure 2.1 ENERGY GAP VS TEMPERATURE FOR EIGHT DETECTORS WITH BEST FIT STRAIGHT LINES THROUGH THE DATA

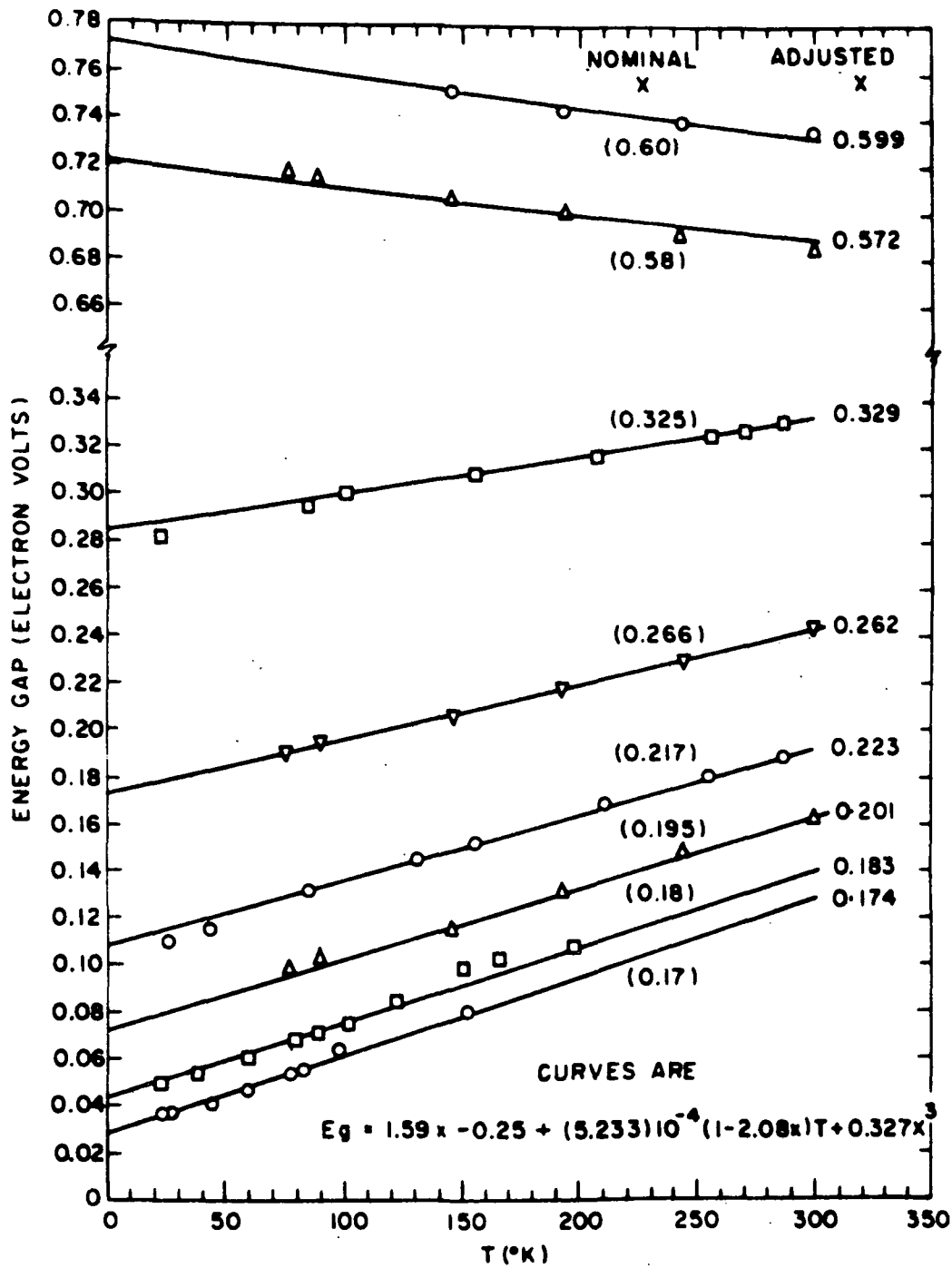


Figure 2.2 ENERGY GAP VS TEMPERATURE WITH CURVES GENERATED FROM THE EMPIRICAL EXPRESSION USING ADJUSTED X VALUES

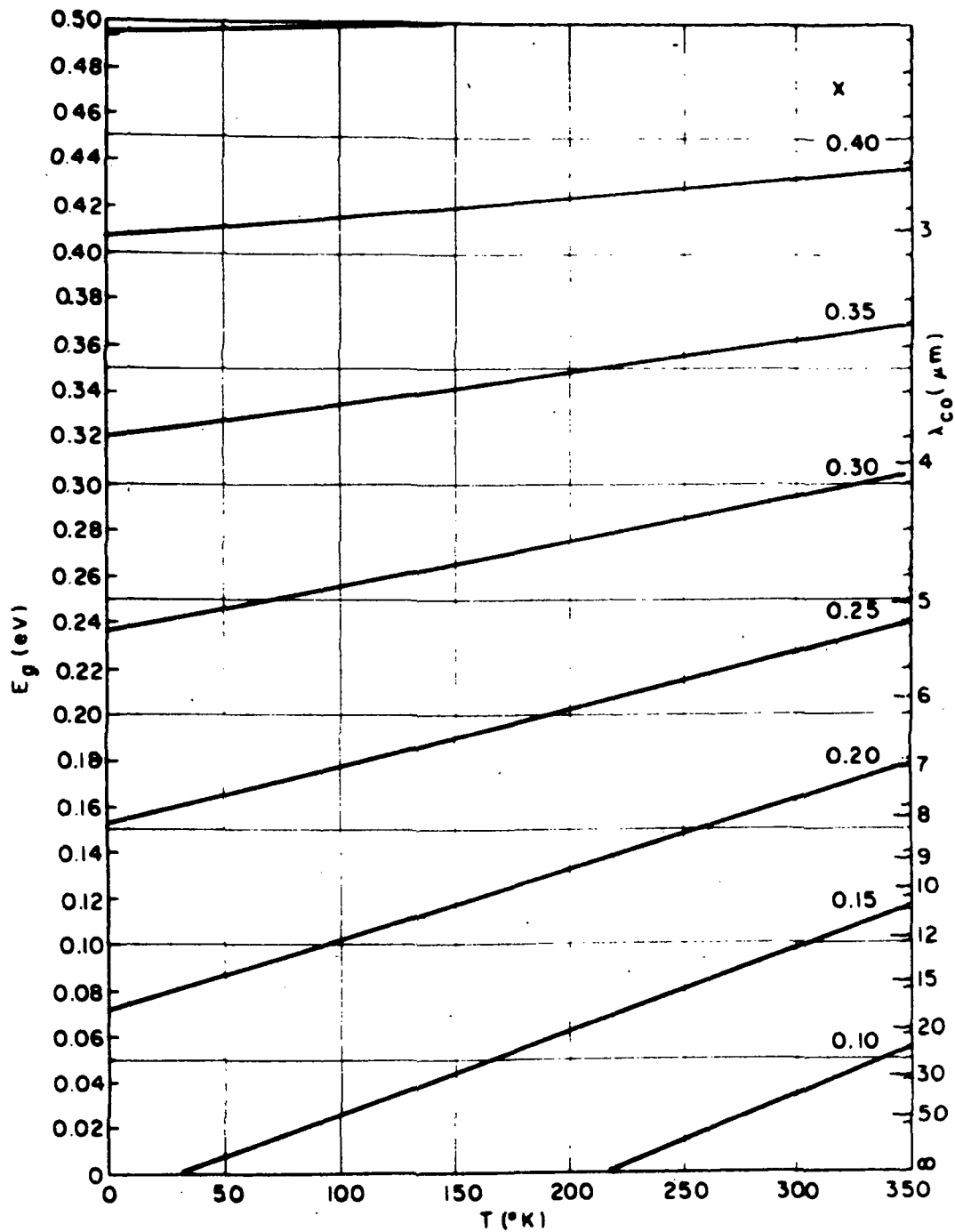


Figure 2.3 FAMILY OF ENERGY GAP VS TEMPERATURE CURVES  
GENERATED FROM THE EMPIRICAL EXPRESSION

## 2.2 THEORETICAL STUDY

### 2.2.1 Radiative Limits

Under the conditions where the detector noise is not dominated by Johnson noise, detectivities limited by fluctuations in the generation recombination mechanism can be obtained. Such fluctuations are due primarily to either photons from the background (BLIP condition) or, in the case of thermal equilibrium, due to the lattice generated carriers. We can derive the various theoretical generation recombination limits for (Hg,Cd)Te photoconductors by considering the general case of dynamic equilibrium.

To simplify the analysis, we will consider only that the case where the dominant recombination mechanism is radiative. Under these conditions, the g-r noise voltage may be written as

$$\left[ V_{g-r}^2 \right]^{1/2} = \frac{2 \bar{V}_o \tau^{1/2} \Delta f^{1/2}}{n(\ell w d)^{1/2}} \left( \frac{np}{n+p} \right)^{1/2} \quad (2.3)$$

and the detectivity

$$D_{\lambda}^* = \frac{\eta_{\lambda} \tau^{1/2}}{2 hc d^{1/2}} \left( \frac{np}{n+p} \right)^{1/2} \quad (2.4)$$

where  $V_o$  is the applied dc bias, and  $d$  is the device thickness.

The condition of dynamic equilibrium states:

$$\Sigma \text{ generation rates} = \Sigma \text{ recombination rates}$$

Therefore,

$$\eta_S Q_B + \eta_{\ell} Q_{\ell} = \left( \frac{np}{n+p} \right) \frac{d}{\tau} \quad (2.5)$$

where  $Q_{\ell}$  is the effective generation term and  $\eta_{\ell}$  is the effective quantum efficiency for this process. Let us now analyze equation 2.5 for the conditions where

$$\eta_S Q_B \gg \eta_{\ell} Q_{\ell} \quad \text{and} \quad \eta_{\ell} Q_{\ell} \gg \eta_S Q_B$$

### 2.2.1.1 $D_{\lambda}^{*}$ BLIP

In the background limit case,  $\eta_S Q_B \gg \eta_l Q_l$ . Then  $n = n_o + \Delta n$  and  $p = p_o + \Delta n$  implies that  $\Delta n = 2 Q_B \tau \eta/d$  and

$$\lim D_{\lambda}^{*} = D_{\lambda}^{*} \text{BLIP} = \frac{\eta^{1/2} \lambda}{2 hc \sqrt{Q_B}} \quad Q_B \gg Q_l \quad (2.6)$$

Equation 2.6 describes the upper detectivity limit for a photoconductor for any given background temperature and device cutoff wavelength.

### 2.2.1.2 $D_{\lambda}^{+}$

In the internal limited case,  $\eta_l Q_l \gg \eta_S Q_B$ . Since we have assumed that the lifetime is radiative.

$$\lim D_{\lambda}^{+} = \frac{\eta \lambda \tau_{\text{rad}}}{2 hc d^{1/2} \left( \frac{n_o p_o}{n_o + p_o} \right)^{1/2}} \quad (2.7)$$

$$Q_l \gg Q_B$$

$$\tau \rightarrow \tau_{\text{rad}}$$

But the radiative lifetime may be written as

$$\tau_{\text{rad}} = \frac{n_o p_o}{(n_o + p_o) G_r} \quad (2.8)$$

where  $n_i^2 = n_o p_o$  is the intrinsic free-carrier concentration and  $G_r$  is the rate of spontaneous recombination in the material.

Substituting equation 2.8 into 2.7 yields,

$$D_{\lambda}^{+} = \frac{\eta \lambda_p}{2 hc d^{1/2} G_r^{1/2}} \quad (2.9)$$

$D_{\lambda}^{+}$  is a most useful concept because it establishes the highest practically achievable detectivity in a photoconductor as a function of very fundamental material constants. In particular,

$$G_r = 2.52 \times 10^{11} r_i^2 T_{det}^3 \int_{\epsilon_0}^{\infty} \epsilon^2 \alpha(\epsilon) \exp(-\epsilon) d\epsilon \quad (2.10)$$

where  $\epsilon_0 = E_{gap}/k T_{det}$ ,  $r_i$  is the material index of refraction,  $\alpha$  is the absorption coefficient, and  $E_{gap}$  the band gap and  $\epsilon = E/k T$  the variable of integration.

Figure 2.4 describes  $D^*_{BLIP}$ ,  $D^*_\lambda$  in (Hg,Cd)Te for the condition where  $T_{det} = T_{BKG} = 295^\circ K$ .

### 2.2.1.3 $D^*_{BLIP} f^*$ vs $D^*_\lambda f^*$

The development and optimization of near infrared (Hg,Cd)Te photodetector for this program requires very high detectivities and wide electrical bandwidth capabilities. For this reason, it is convenient to define a parameter which will quickly describe the detective bandwidth capability for a given detector. This parameter is defined as the detectivity  $f^*$  bandwidth product, or in short,  $D^*f^*$  product. In the following, we are going to show that the relation  $D^*_{BLIP} f^* = D^*_\lambda f^*$  holds.

The time dependent detectivity is

$$D^*_\lambda = \frac{R_o \sqrt{A_{det}} \cdot \Delta f}{(1+\omega^2 \tau_{pc}^2)^{1/2} \left[ V_j^2 + \frac{V_{gr_o}^2}{1+\omega^2 \tau_{pc}^2} + V_a^2 + V_{1/f}^2 \right]^{1/2}} \quad (2.11)$$

A constant low frequency value  $D^*_{\lambda_0}$  can be written as

$$D^*_{\lambda_0} = \frac{R_o \sqrt{A_{det}} \Delta f}{[V_j^2 + V_{gr_o}^2 + V_a^2 + V_{1/f}^2]^{1/2}} \quad (2.12)$$

Looking for the frequency where  $D^*_\lambda$  is  $1/\sqrt{2}$  times  $D^*_{\lambda_0}$ , it leads to

$$\omega^2 \tau_{pc}^2 (V_j^2 + V_a^2 + V_{1/f}^2) = V_j^2 + V_{gr_o}^2 + V_a^2 + V_{1/f}^2 \quad (2.13)$$

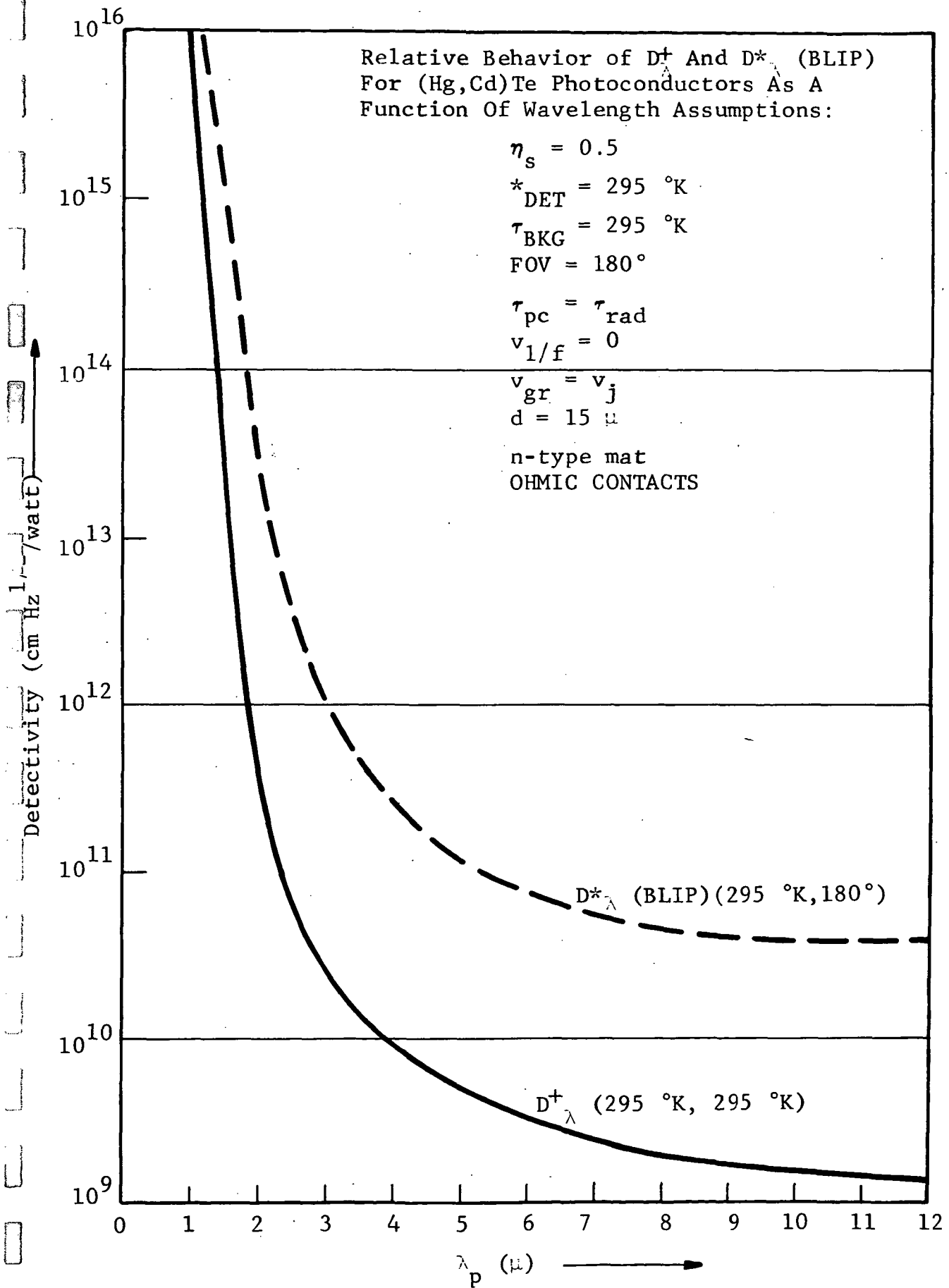


Figure 2.4 QUADRATIC THEORY

The frequency at which this occurs is defined as  $f^*$ . Thus, a detective time constant can be defined

$$\tau_{\text{det}} = 1/\omega^* = 1/2 \pi f^* \quad (2.14)$$

Examining 2.13 and using 2.14 yields

$$\tau_{\text{det}}^2 = \frac{1}{\omega^{*2}} = \tau_{\text{pc}}^2 \frac{(V_j^2 + V_a^2 + V_{1/f}^2)}{(V_{g-r_o}^2 + V_j^2 + V_a^2 + V_{1/f}^2)} \quad (2.15)$$

If  $V_{g-r_o}^2 \gg V_{1/f}^2 + V_a^2 + V_j^2$  and

$V_j^2 \gg V_a^2 + V_{1/f}^2$ , then 2.15 becomes

$$\tau_{\text{det}}^2 = \tau_{\text{pc}}^2 \frac{V_j^2}{V_{g-r_o}^2} \quad (2.16)$$

Now to express  $\tau_{\text{det}}$  in material parameters,

$$V_j^2 = 4 k T r_d \Delta f \quad (2.17a)$$

$$V_{g-r_o}^2 = \frac{4 V_o^2 \tau_{\text{pc}} \Delta f}{n^2 (\ell w d)} \left( \frac{np}{n+p} \right) \quad (2.17b)$$

$$P_{\text{diss}} = E^2 \ell^2 / r_d \quad (2.17c)$$

For background limited case, combining equations 2.15, 2.16 and 2.17

$$\tau_{\text{det}} = nd \left( \frac{k T \ell w}{\eta Q_B P_{\text{diss}}} \right)^{1/2} \quad (2.18)$$

Solving for  $f^*$

$$f^* = \frac{1}{2 \pi \tau_{\text{det}}} = \frac{1}{2 \pi n d} \left( \frac{\eta Q_B P_{\text{diss}}}{k T \ell w} \right)^{1/2} \quad (2.19)$$

Thus,

$$D^*_{\text{BLIP}} f^* = \frac{\eta \lambda P_{\text{diss}}^{1/2}}{4 \pi h c n d (k T \ell w)^{1/2}} \quad (2.20)$$

For internal noise limited case, we assume the radiative life time. Combining equations 2.15, 2.16, 2.17 and radiative life time equation 2.18,

$$\tau_{\text{det}}^2 = \frac{k T n^2 \ell w d}{P_{\text{diss}} G_r} \quad (2.21)$$

Solving for  $f^*$ ,

$$f^* = \frac{1}{2 \pi \tau_{\text{det}}} = \frac{1}{2 \pi n} \left( \frac{P_{\text{diss}} G_r}{k T \ell w d} \right)^{1/2} \quad (2.22)$$

For internal limited case, the  $D^+_{\lambda} f^*$  product would be

$$D^+_{\lambda} f^* = \frac{\eta \lambda P_{\text{diss}}^{1/2}}{4 \pi h c n d (k T \ell w)^{1/2}} \quad (2.23)$$

Comparing with equation 2.20, we found that

$$D^*_{\text{BLIP}} f^* = D^+_{\lambda} f^*$$

#### 2.2.1.4 Theoretical Limit of Detectivity of an NIR (Hg,Cd)Te Detector at Elevated Operating Temperature

A calculation of theoretical limits  $D^+_{\lambda}$  and  $D^*_{\text{BLIP}}$  of an NIR (Hg,Cd)Te photoconductors at 240 °K with 300 °K background is shown in Figure 2.5. We found that the background limited detec-

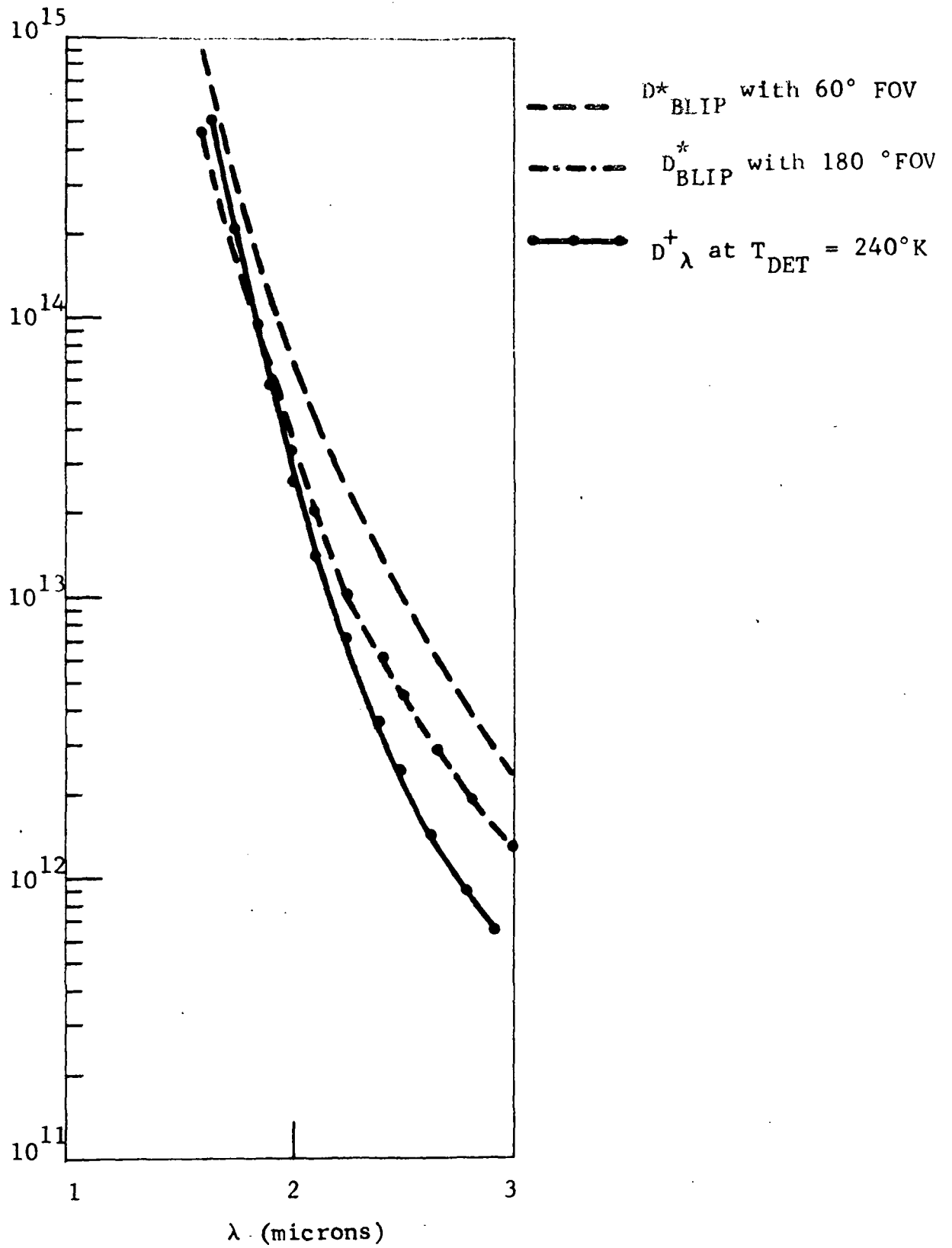


Figure .25 THEORETICAL  $D^*_\lambda$  AND  $D^*_{BLIP}$  LIMITS VERSUS WAVELENGTH

tivity  $D^*_{BLIP}$  is nearly equal to the internal noise limited detectivity  $D^*_\lambda$ . Decreasing the background will only shift  $D^*_{BLIP}$  up and  $D^*_\lambda$  limit will prevail with little improvement. In another words, the detector performance will not improve by a reduced field of view. On the other hand, increasing background level by externally applied radiation will lower  $D^*_{BLIP}$  and reduce the detector performance. These assertions were experimentally verified. The detectivity is measured as a function of background photon flux furnished by a 0.9  $\mu\text{m}$  light emitting diode. The detectivity decreases with externally applied background. However, as the background is reduced, the detectivity seems to approach a limit as expected, as shown in Figure 2.6.

### 2.2.2 $D^*_{BB}$ Derivation

The detectivity can be defined as:

$$D^* = \frac{A^{1/2} \Delta f^{1/2} S/N}{P}$$

Where: A = Sensitive area of the detector, in square centimeters.

$\Delta f$  = Frequency bandwidth of the noise measuring circuit in Hertz

S/N = Signal to noise ratio of the detector

P = Input signal power

The input power is:

$$f = \frac{\phi \cdot A_{BB} \cdot A}{d^2}$$

Where :  $A_{BB}$  = Area of blackbody aperture in square centimeters

$\phi$  = Flux density of the emitted irradiance in volts per square centimeter of blackbody aperture area

d = Distance between blackbody & incident plans of detector

Calculation of flux density,  $\phi$ , is as follows:

$$\phi = \frac{\sigma (\epsilon_{BB} T_{BB}^4 - \epsilon_c T_c^4)}{(\pi c_1)}$$

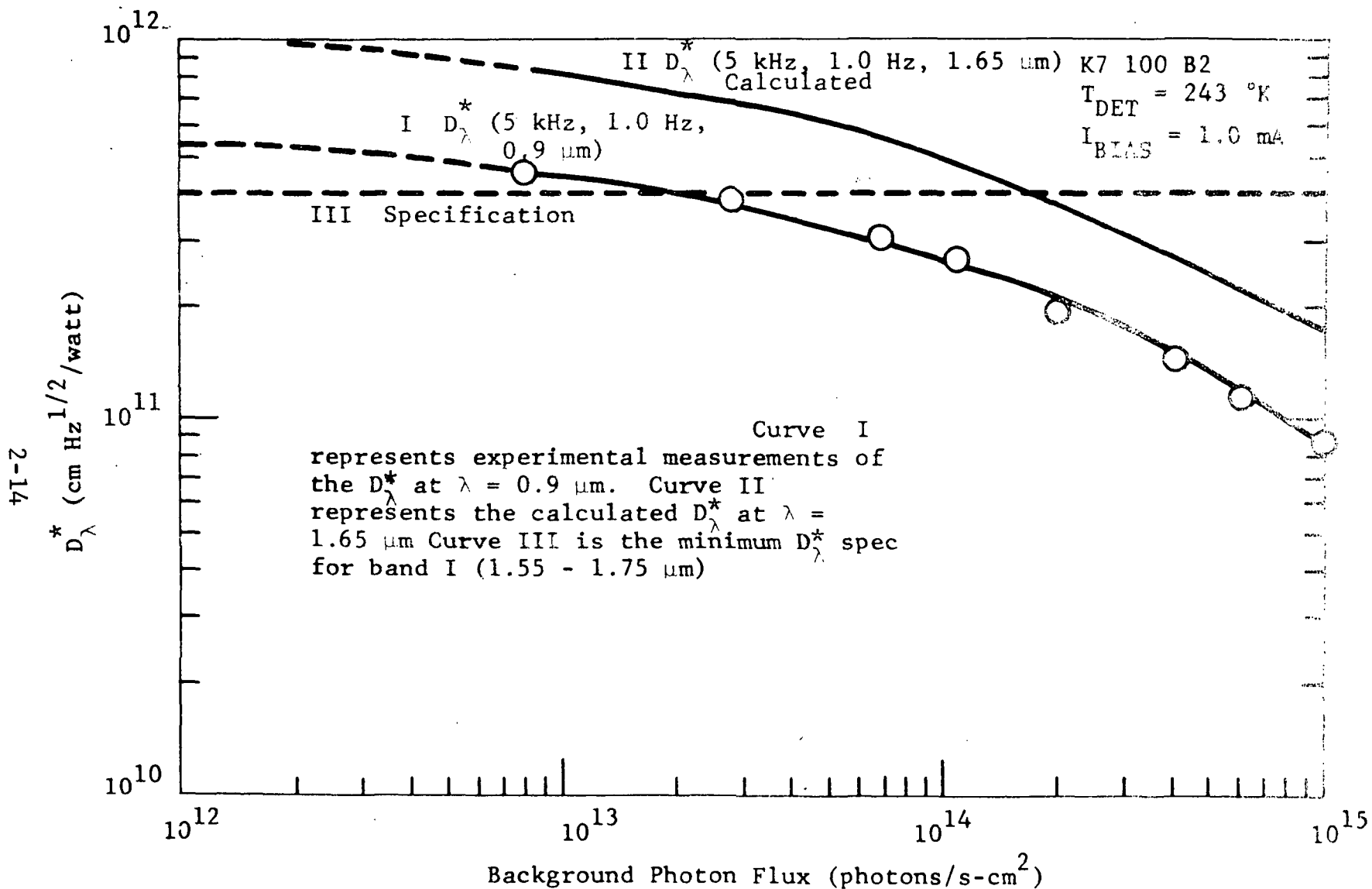


Figure 2.6 DETECTIVITY AS A FUNCTION BACKGROUND PHOTON RADIATION

Where:  $\sigma$  = Stefan Boltzman constant =  $5.6686 \times 10^{-12}$  Watts  
 $\text{cm}^{-2} \text{ } ^\circ\text{K}^{-4}$

$\epsilon_{\text{BB}}$  = Blackbody emissivity

$T_{\text{BB}}$  = Blackbody temperature

$\epsilon_{\text{c}}$  = Chopper blade emissivity

$T_{\text{c}}$  = Chopper blade temperature

$c_1$  = rms factor for chopper and blackbody aperture

$\pi$  = 3.1416

The input power is:

$$P_{\text{BB}} = \frac{\sigma (\epsilon_{\text{BB}} T_{\text{BB}}^4 - \epsilon_{\text{c}} T_{\text{c}}^4) A_{\text{BB}} A}{d^2 (\pi c_1)}$$

$D^*_{\text{BB}}$  is:

$$D^*_{\text{BB}} = \frac{(\Delta f)^{1/2} d^2 (\pi c_1) S/(kN)}{\sigma (\epsilon_{\text{BB}} T_{\text{BB}}^4 - \epsilon_{\text{c}} T_{\text{c}}^4) A^{1/2} A_{\text{BB}}}$$

Where:  $k$  = Experimentally determined correction factor for  
Hewlet Packard wave analyzer noise readings = 1.12

The rms chopping factor for an 80-blade chopper and 0.0125 inch diameter operation is 2.24. Thus combining constants and neglecting the  $(\epsilon_{\text{c}} T_{\text{c}}^4)$  terms.

$$D^*_{\text{BB}} = \frac{1.10 \times 10^{12} (\Delta f)^{1/2} S/N d^2}{\epsilon_{\text{BB}} T_{\text{BB}}^4 A^{1/2} A_{\text{BB}}}$$

### 2.2.3 Trapping Model

During the course of this program, from the classical single level trap model presented by Fan in 1954, a new continuum model of trapping photoconductivity was developed, which yields results in essential agreement with experimentally observed effects of temperature and background flux on responsivity and response time of a near infrared (Hg,Cd)Te photodetector. A steady state, as well as time dependent, solutions for this model are discussed below.

#### 2.2.3.1 Background

Semiconductors are known to possess localized sites which are capable of capturing and emitting carriers. These electronic states, which occur at imperfections in the crystal, are commonly referred to as "traps". It has been recognized for some time that there are two mechanisms by which traps influence photoconductive gain. Either they provide the mechanism for recombination of electrons and holes or they act directly as capture sites for carriers.

The effect of traps on carrier recombination was derived by Shockley and Read (Phys. Rev. 87, 835 (1952)). In the "Shockley-Read" mode, electrons (holes) which are captured by traps, rapidly combine with holes (electrons) in the valence (conduction) band. Since recombination occurs in two steps, transition probabilities are much greater. At lower temperatures, recombination via traps becomes important, and Shockley-Read recombination becomes the controlling factor in determining lifetimes and therefore photoconductive gain.

On the other hand, recombination times can become longer than times required for interchanges between trapped carriers and the nearest allowed band. Then a different mechanism for photoconductive gain arises because carriers are prohibited from moving freely through the material. Modern terminology generally reserves the name "trap" and "trapping" when this mechanism predominates, and uses the terms "recombination center" to refer to the Shockley-Read mechanism. In this section we are concerned mainly with the action of traps as sites for carrier immobilization. Subsequently the terminology "Trap and Trapping" will refer only to this mode of operation.

The effect of traps on intrinsic photoconductivity in semiconductors was published by Fan in 1954 in a classic paper (H. Y. Fan, Phys. Rev. 92, 1424 (1954)) which determined the basic approach to the analysis of trap behavior. Traps were considered to be simply

states which can either capture or emit electrons (and, of course, holes), and equations were derived for contributions of trapped carriers to both steady state and transient photoconductivity.

Fan's theory, and the many similar analyses that have subsequently appeared, have had much success in explaining observed temperature dependences. However, theories based on such models always predict that traps saturate rather abruptly. In contrast to the experimental results, photoconductivity is predicted to decrease sharply with increasing background and decreasing temperature. Nevertheless, traps must be considered. It is difficult to explain many features of low temperature, low background photoconductivity without invoking some type of trapping mechanism. The large photoconductive gains, as well as observed background, temperature, and time dependent effects, all points in this direction.

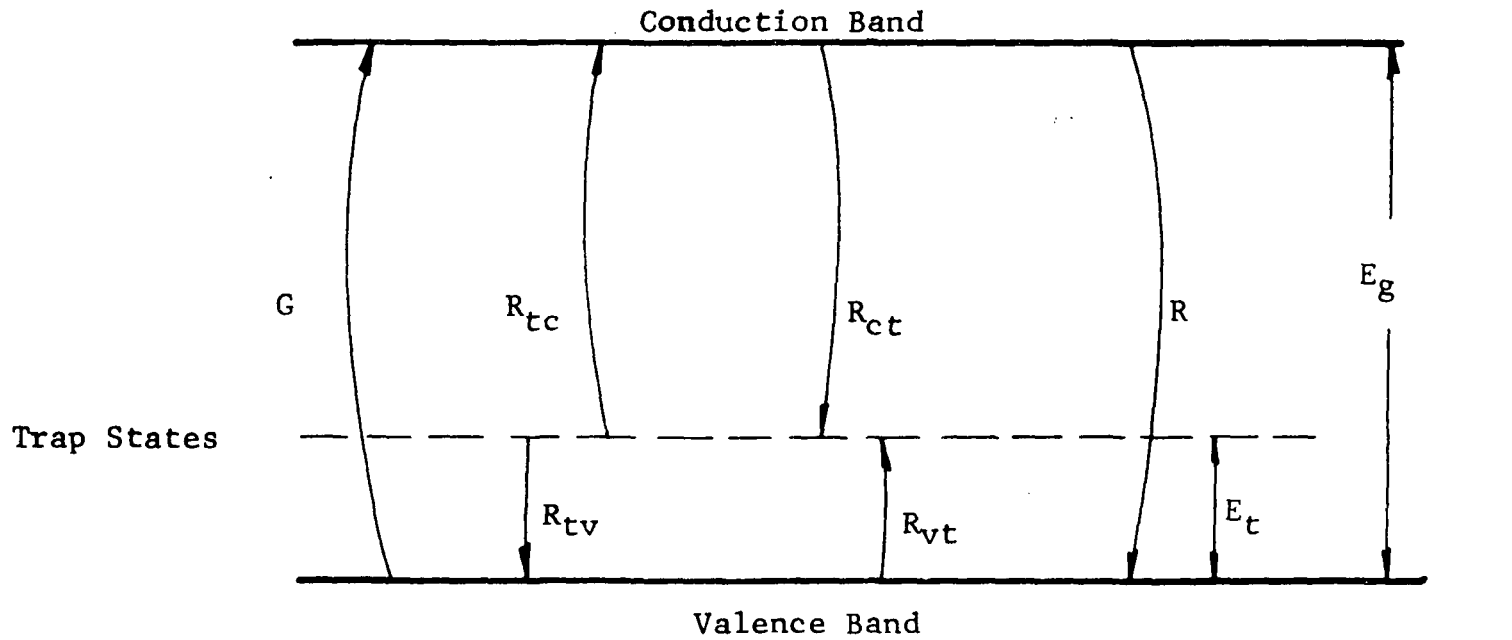
Since the simple trapping model pioneered by Fan proves to be inadequate, there are two approaches that can be taken in order to understand observed material behavior. For example, one might consider more complex models of traps, for which trap occupation could depend on illumination intensity in some new unexplained fashion. On the other hand, the simplicity and physical reasonableness of Fan's model can lead one to look for extensions and/or improvement. We take the latter approach here.

In this section we begin with the simple theory, relate it to trap behavior in general, and then show how the new model evolves naturally therefrom.

### 2.2.3.2 Simple Trap Model-Fan's Theory

#### a) The Basic Model - Traps at Energy $E_t$

The basic model, which includes all manifestations of trap behavior in semiconductors, is illustrated in Figure 2.7. Electrons combine with and are excited from trap states with density  $N$  located at an energy  $E_t$  above the valence band. Excitation rates are proportional to the product of carrier density and available sites multiplied by rate constants.  $R_{tc}$  and  $R_{tv}$  are excitation rates (per unit volume) of electrons from trap to conduction band and from trap to valence band.  $R_{ct}$  and  $R_{vt}$  represent excitation rates per unit volume of electrons from conduction band and from valence band to the trap level. Excitation constants to conduction and valence band are given by  $r_c$  and  $r_v$ , respectively.  $G$  is the generation rate (per unit volume) of conduction band electrons



$$R_{tv} = r_v n_t p$$

$$R_{vt} = r_v p_1 (N - n_t)$$

$$p_1 = N_v e^{-E_t/kT}$$

$$R = \frac{p}{\tau}$$

$$R_{ct} = r_c n (N - n_t)$$

$$R_{tc} = r_c n_1 n_t e^{-(E_g - E_t)/kT}$$

$$n_1 = N_c e^{-E_t/kT}$$

Figure 2.7 SEMICONDUCTOR WITH TRAPS AT ENERGY  $E_t$

with valence band holes, and  $\tau$  is the recombination time constant. The density of occupied (with electrons) traps is given by  $n_t$ . The quantities  $p_1$  and  $n_1$  are essentially rate probabilities for excitation over energy barriers  $E_t$  and  $E_g - E_t$ , where  $N_c$  and  $N_v$  are the densities of states in conduction and valence band, respectively. The net effect of illumination, as illustrated in Table 2.1 is to generate excess carriers of three types. Since trapping lifetimes can be long,  $\Delta p_t$  can be much larger than  $\Delta p$ . Since charge neutrality requires one electron for each trapped hole as well as for each free hole, large photoconductive gain enhancement can be obtained by trapping of holes.

Because here we are interested in intrinsic photoconductors, Figures 2.7 and Table 2.1 have been chosen to consider optical excitation only from valence to conduction band. It is interesting to note the generality of the model since extrinsic photoconduction can be included merely by adding generation terms from trap levels to conduction bands.

In general,  $\tau$  depends on  $n$  and  $p$  in a rather complex but well known fashion. If recombination proceeds via recombination trap states, Shockley-Read statistics will apply.

The equations which determine the excitations of carriers referred to in Figure 2.7 are:

$$dp/dt = G - R = G - p/\tau + dn_t/dt \quad (2.24)$$

$$dn_t/dt = R_{vt} - R_{tv} + R_{ct} - R_{tc} \quad (2.25)$$

Now, let  $n = \Delta n + n_o$ , and  $p = \Delta p + p_o$ , where  $n_o$  and  $p_o$  are the electron and hole concentrations with no illumination present. Then for n-type extrinsic material at sufficiently low temperatures,

$$\Delta n \ll n_o \text{ and } \Delta p \gg p_o \quad (2.26)$$

The rate equation for trapped holes with  $N_t$  trapping sites becomes:

$$\frac{dn_t}{dt} = r_v \left\{ \left[ p_1 + \frac{r_c}{r_v} n_o \right] [N_t - n_t] - \left[ \Delta p + \frac{r_c}{r_v} n_1 \right] n_t \right\} \quad (2.27)$$

We now concentrate on hole traps which have transition probabilities to conduction band much smaller than those to valence bands, as postulated by Fan. Thus  $r_c/r_v \ll 1$ , and equation 2.27 becomes:

$$-\frac{dp_t}{dt} = \frac{dn_t}{dt} = r_v p_1 (N_t - n_t) - r_v \Delta p n_t \quad (2.28)$$

where  $p_t (= N_t - n_t)$  is the concentration of trapped holes.

The elimination of terms in  $r_c$  states simply that one considers traps which interact only with the valence band. Since there is no excitation to the conduction band, and since  $p_0 \ll \Delta p$ , the traps will be filled with electrons (empty of holes) in the absence of illumination. Therefore, we can identify  $\Delta p_t$  with  $p_t$ .

#### b) The Steady State Solution

In the steady state, all time rates can be set to zero, and one obtains from equations 2.24 and 2.28:

$$\Delta p = G\tau = (\eta\tau/d) Q, \quad (2.29)$$

$$\Delta p_t = \frac{N_t \Delta p}{p_1 + \Delta p} \quad (2.30)$$

Equation 2.30 shows that for small excitation intensities (small  $Q$  gives small  $\Delta p$  from 2.29)  $\Delta p_t$  is proportional to  $Q$ . As  $Q$  (and  $\Delta p$ ) increases beyond  $p_1$ , the trapped holes saturate to the value  $N_t$ , and  $\Delta p_t$  becomes independent of excitation. Using the expressions for  $\Delta n$ ,  $p_1$ , and  $\Delta p$ , from Figure 2.7, Table 2.1 and equation 2.29, the excess electrons can be written as follows:

$$\Delta n = \Delta p + \Delta p_t = \frac{\eta \tau Q}{d} \left[ 1 + N_t (N_{ve}^{-E_t/kT} + \frac{\eta\tau}{d} Q^{-1}) \right] \quad (2.31)$$

The small signal solution can be readily obtained from equation 2.31 by taking  $\partial\Delta n/\partial Q$  when  $\Delta Q \ll Q_B$ , the background photon flux. The small signal solution is illustrated in Figure 2.8 and Figure 2.9, which show  $\partial\Delta n/\partial\Delta p$  (the trapping photoconductive gain) as a function of temperature and background, for long wavelength (small  $E_a$ ) and short wavelength (large  $E_a$ ) material. The parameters shown in Figures 2.8 and 2.9 were chosen to provide maximum responsivity near observed values.

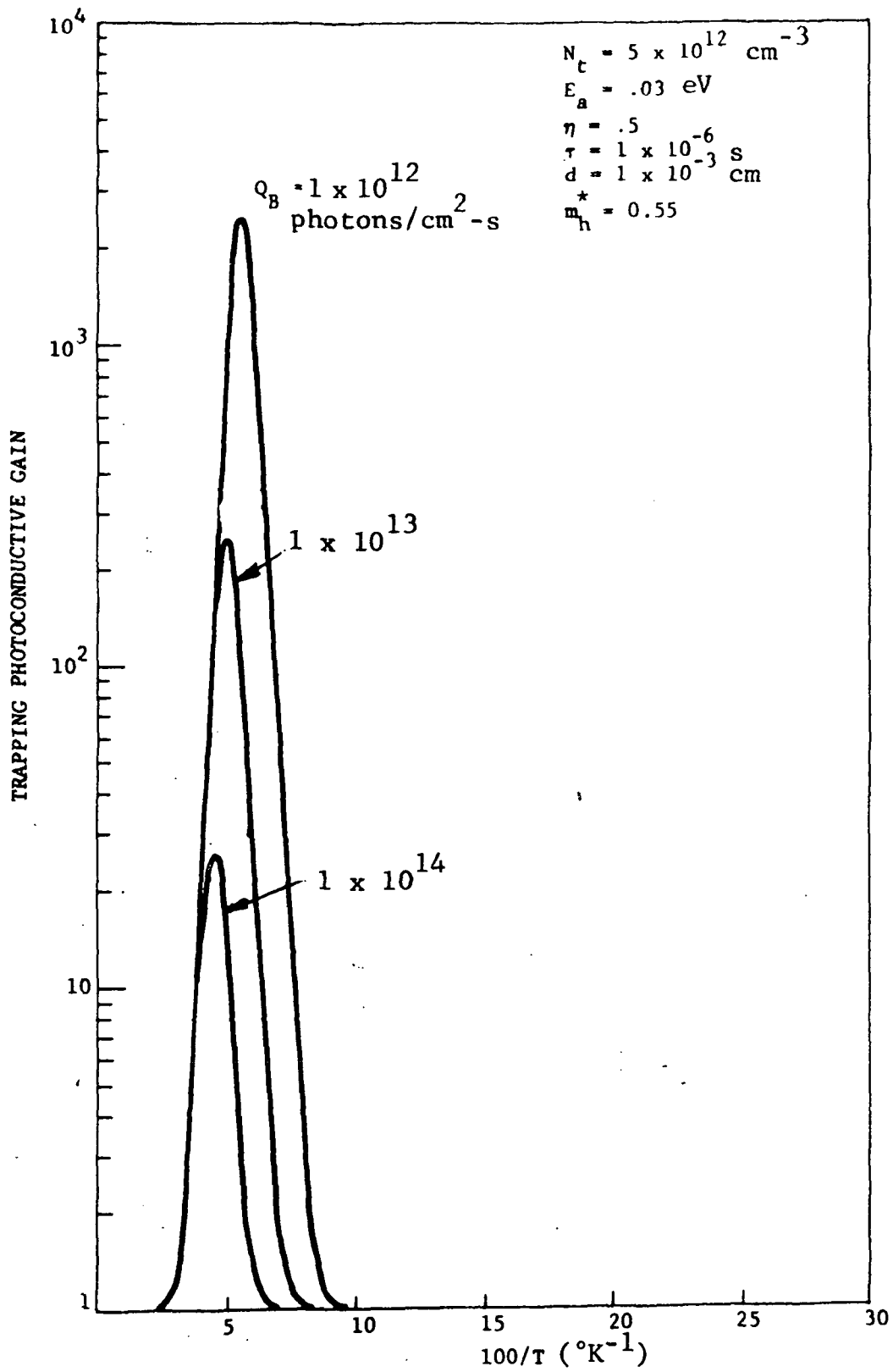


Figure 2.8 SINGLE TRAP

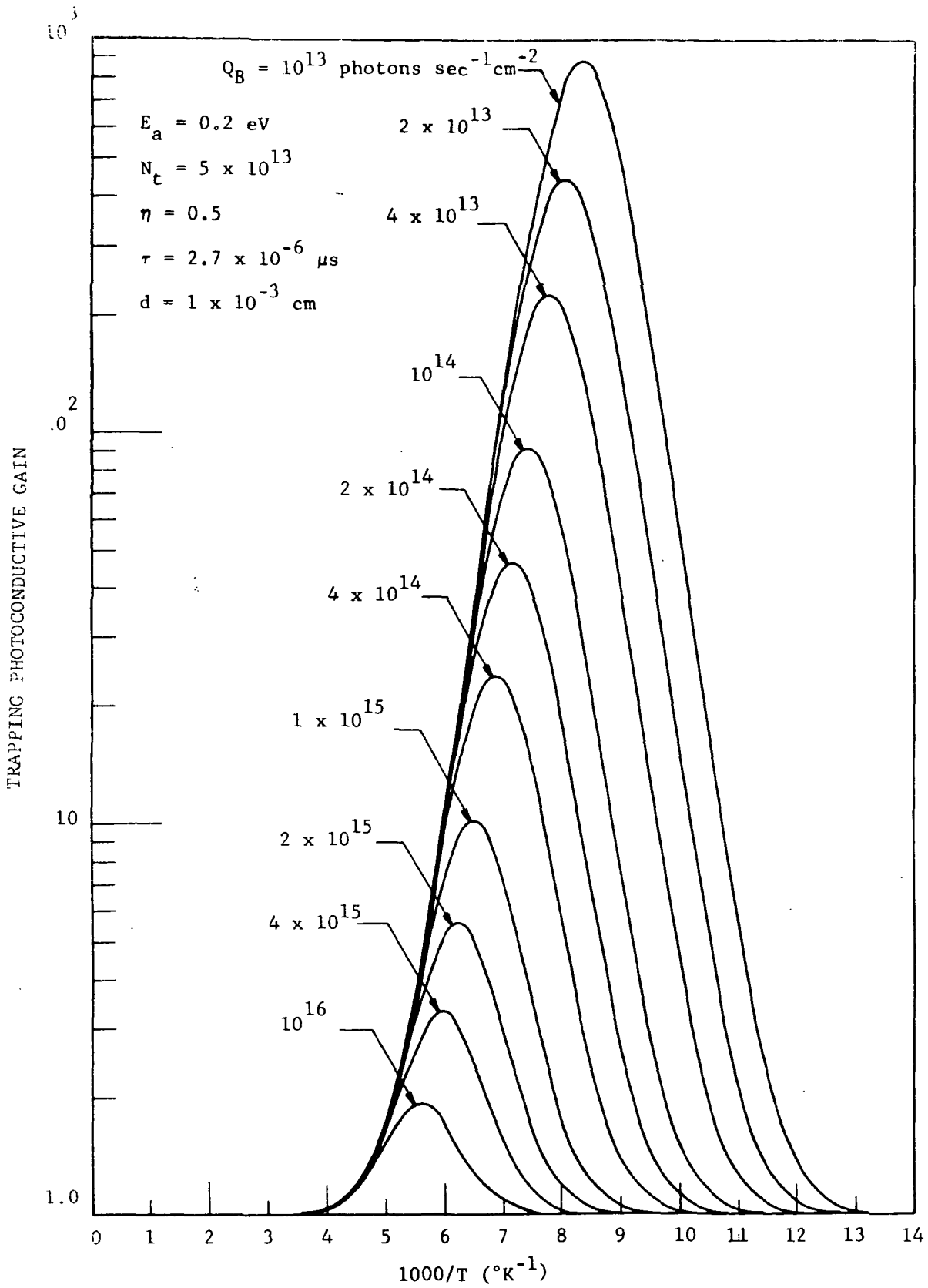


Figure 2.9 SINGLE TRAP MODEL

Table 2.1

Three species develop with illumination

Excess Holes	$\Delta p$
Excess Electrons	$\Delta n$
Excess Trapped Holes	$\Delta p_t$

Charge Conservation

$$\Delta n = \Delta p + \Delta p_t$$

Trap Photoconductive Gain

$$G_{pc} = \frac{\Delta n}{\Delta p} = 1 + \frac{\Delta p_t}{\Delta p}$$

The areas of agreement and disagreement of Fan's simple trap theory are illustrated by comparison with experimental responsivities such as those shown in Figure 2.10. As temperature decreases, until trap saturation becomes appreciable, the observed exponential temperature dependence is predicted by the theory. But experimental responsivities reach a plateau at lower temperatures, whereas theoretical signals decrease rapidly as the traps become saturated. Thus, a different theory is required.

The approach we take to explain the experimental results is suggested by the simplicity and physical reasonableness of Fan's theory, as well as by the agreement with experiment at higher temperatures. Let us consider equation 2.30. It states that  $\Delta p_t$  is linear in  $\Delta p$  when  $\Delta p \ll p_1$ , and when  $\Delta p > p_1$ , trap saturation occurs. Only in the narrow range where  $\Delta p \sim p_1$ , is there appreciable nonlinearity. Careful comparison with experimental results strongly suggests that in improving the theory, the objective should be to extend the range of non-linearity. We do this by postulating the existence of traps at many energies, each of which contribute to the total photoconductivity. The effect will be to extend trap saturation with both background and temperature.

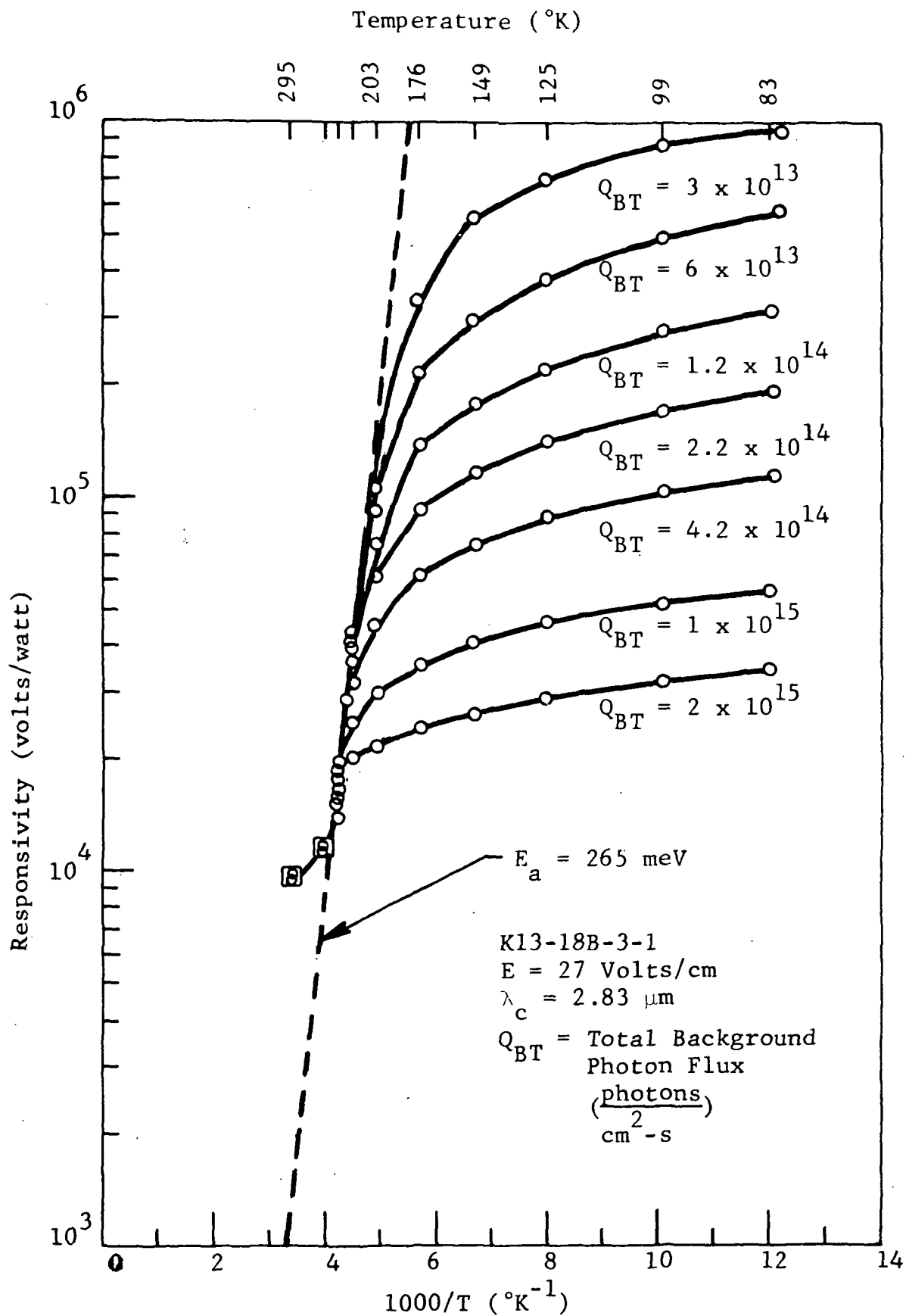


Figure 2.10 EXPERIMENTAL RESPONSIVITIES

### 2.2.3.3 The Continuum Trap Model

#### a) Uniform Continuum, General Solution

A multiplicity of trapping levels is assumed to extend throughout the energy gap. All traps are considered to behave independently, i.e., they interact only with the valence band and trap-to-trap transitions are small.

The initial calculation, for convenience, assumes a uniform, constant density continuum of levels extending from the valence band edge up to a maximum energy,  $E_m$ , which will be near  $E_g/2$ . It should be mentioned that we do not necessarily imply that no levels exist above  $E_m$ , but merely that the operant levels for this preliminary theoretical approach occur below  $E_m$ . Using equation 2.30 we obtain:

$$\begin{aligned} \Delta p_t &= \int_0^{E_m} N(E) \Delta p_t(E) dE = N \int_0^{E_m} \frac{\Delta p}{p_1 + \Delta p} dE \\ &= N \int_0^{E_m} \frac{\Delta p dE}{N_v \exp(-E/kT) + \Delta p} \end{aligned} \quad (2.32)$$

where  $N$  is the density of trap levels between  $E$  and  $E + dE$ , and  $\Delta p_t$  is the density of trapped holes due to traps at all energies. This gives:

$$\Delta p_t = NE_m + NkT \log \frac{N_v e^{-E_m/kT} + \Delta p}{N_v + \Delta p} \quad (2.33)$$

Using the fact that  $N_v \gg \Delta p$  this becomes

$$\Delta p_t = NkT \log \left[ 1 + \frac{\Delta p}{N_v e^{-E_m/kT}} \right], \quad (2.34)$$

where from equation 2.29

$$\Delta p = G \tau = (\eta Q/d) \tau. \quad (2.35)$$

$Q$  is the radiation flux,  $\eta$  the quantum efficiency,  $d$  the detector thickness and  $\tau$  the recombination lifetime (Note that  $\tau$  can also be a function of temperature).

Finally, from equations 2.34, 2.35 and Table 2.1 we obtain for the total photoconductivity (due to recombination and trapping effects):

$$\Delta n = \frac{\eta \tau Q}{d} + N k T \log \left[ 1 + \frac{\eta \tau Q / d}{N_v \exp(-E_m / k T)} \right] \quad (2.36)$$

b) Uniform Continuum, Small Signal Case

For signals much less than the background ( $Q \ll Q_B$ ) we use the small signal solution of equation 2.36.

$$\frac{d \Delta n}{d Q} = \frac{\eta \tau}{d} \left[ 1 + N k T \frac{1}{N_v \exp(-E_m / k T) + (\eta \tau / d) Q_B} \right] \quad (2.37)$$

It can be seen at once, that equation 2.37 has the qualitative features of the experimental results. At high background and low temperatures, the second term in the denominator predominates, and the photoconductivity goes as  $Q_B^{-1}$ . At low background and high temperatures, the background dependence disappears and the trapping contribution to photoconductivity decreases with temperature and the activation energy  $E_m$ . The corner temperature is approximately determined when the two terms in the denominator are equal:

$$N_v \exp(-E_m / k T) = (\eta \tau / d) Q_B \quad (2.38)$$

Thus, for the uniform density model in essential agreement with experiment the corner temperature is proportional to the activation energy.

$$T_c = E_m / k \log \left[ (d / \eta \tau) (N_v / Q_B) \right] \quad (2.39)$$

The physical behavior of this model can be understood by considering the energy  $E_s$ , which is called "saturation level". Traps with energies above  $E_s$  are filled (with holes, i.e., emptied of

electrons); those below are empty.  $E_s$  is estimated by equating the two terms in the denominator of the integrand in 9.

$$N_v \exp(-E_s/kT) = (\eta\tau/d) Q \quad (2.40)$$

For an energy range of  $kT$  about  $E_s$ , the traps are partly filled (or "partly saturated").

The position of the saturating level,  $E_s$  is determined both by temperature and flux. When the temperature decreases and/or  $Q$  increases,  $E_s$  will decrease. These effects are illustrated in Figure 2.11 which shows the various states in the energy gap.

In this model, it is just the shifting up and down of  $E_s$  with temperature and flux which causes the observed effects. Trapping photoconductivity originates in changes in hole population and depopulation at  $E_s$ . In fact, it can be shown that in this case:

$$\tau_t \propto \exp(+E_s/kT) \quad (2.41)$$

where  $\tau_t$  is the small signal time constant. This means that levels closer to the valence band are faster. Thus, as  $E_s$  decreases due to higher background and/or lower temperature,  $\tau_t$  will decrease. The large signal case is more complex because large changes in  $Q$  will cause considerable movement of  $E_s$ , and no simple time constant will be observed.

Important features of the small signal dependences of responsivity ( $R$ ) and time constant ( $\tau$ ) on temperature and background are readily seen from this viewpoint.  $E_s$  goes as  $T \log(Q-1)$ , i.e.,

$$E_s = kT \log \left( \frac{N_v d}{\eta\tau Q_B} \right) \quad (2.42)$$

When  $E_s > E_m$ , the maximum trap energy, then no traps are completely saturated and  $R$  increases exponentially with  $T^{-1}$ . When  $E_s < E_m$ , a plateau region occurs and  $R$  decreases with  $Q$ , thereby lowering  $E_s$  to faster trap levels, thus decreasing  $\tau_t$ . The improved agreement with experiment is illustrated in Figures 2.12 and 2.13 which plot  $\partial\Delta n/\partial\Delta p$  from equation 2.37 for the same parameters used to illustrate the single energy trap model in Figures 2.8 and 2.9.

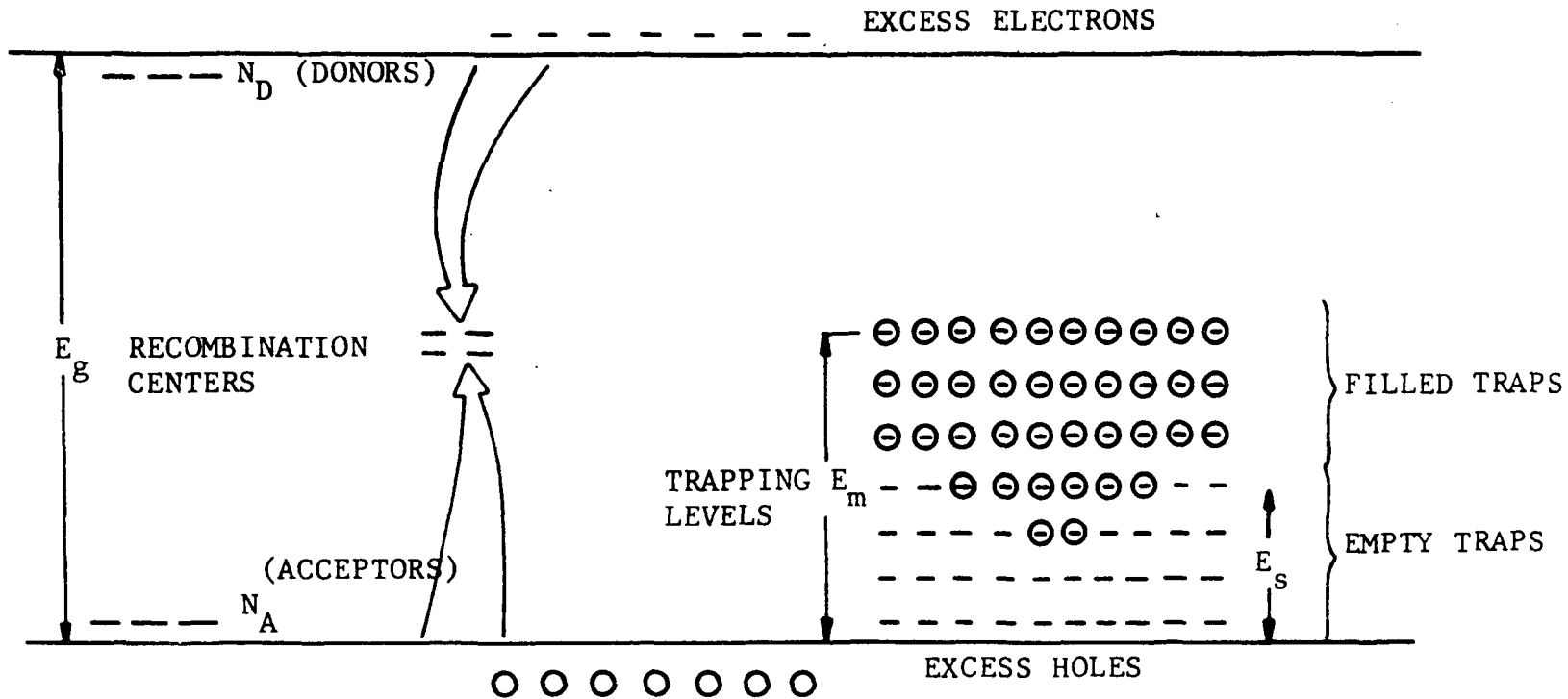


Figure 2.11 PHOTOC ONDUCTIVITY WITH TRAP CONTINUUM

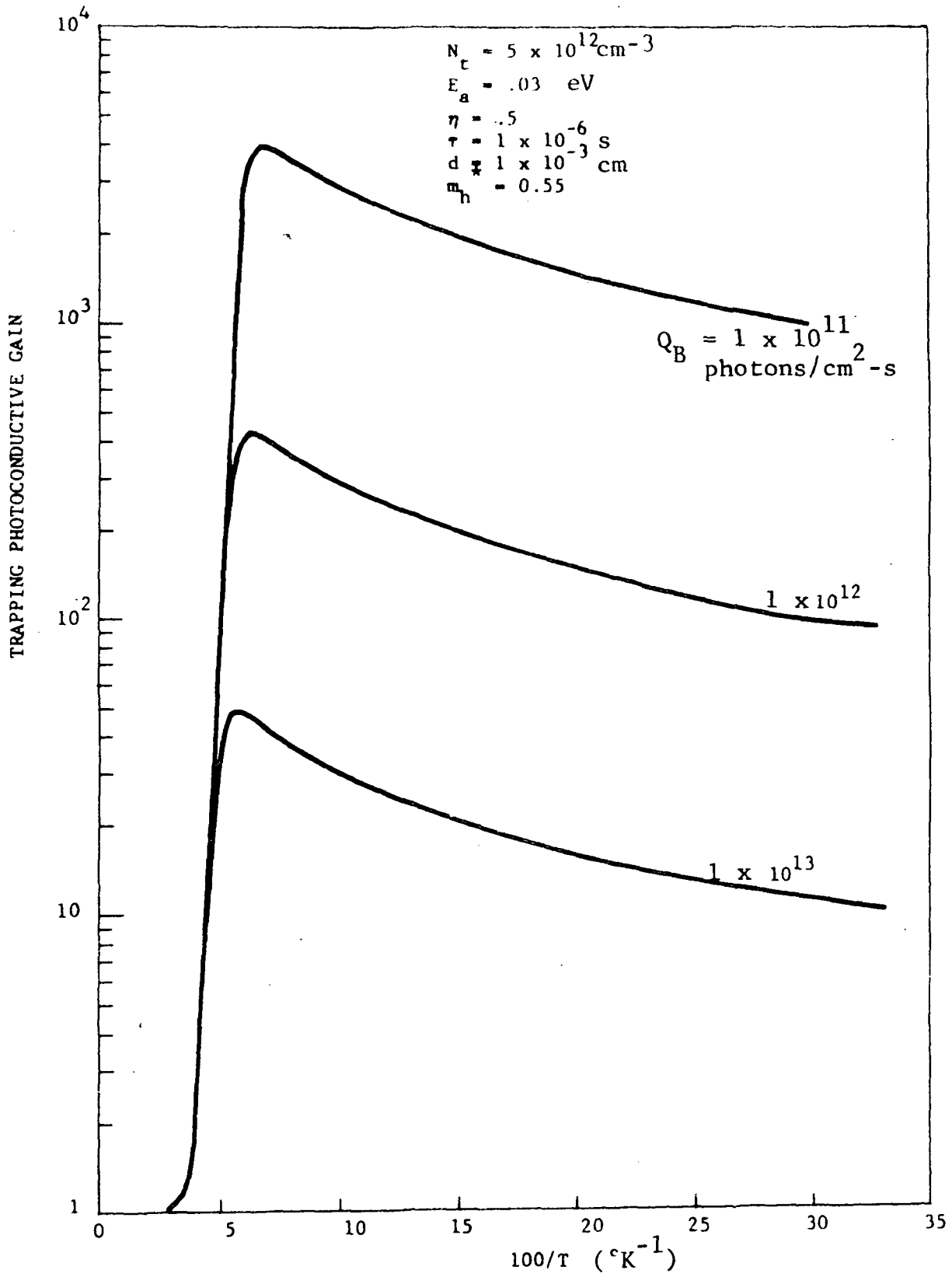


Figure 2.12 TRAP CONTINUUM

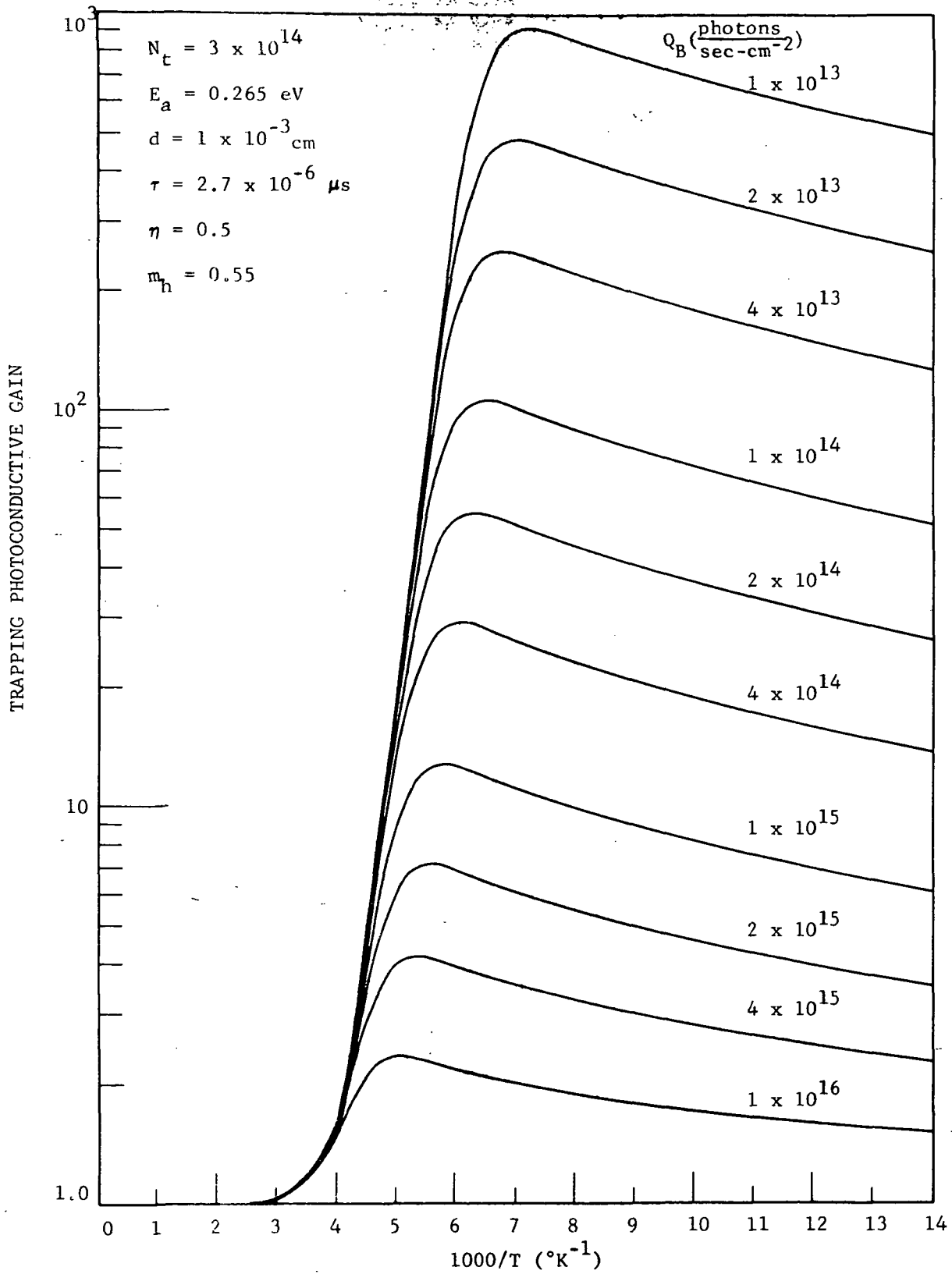


Figure 2.13 TRAP CONTINUUM  
2-30

c) The Non-uniform Continuum

Comparison of Figures 2.8 and 2.9 with 2.12 and 2.13 shows that a quasi-continuum trap model is in essential agreement with the important features of experimental data. We now turn our attention to bringing details of the model in closer agreement. Note that equation 2.37 contains a linear term in  $kT$  in low temperature region, which predicts a gradual decrease in responsivity with temperature, (as shown in Figures 2.12 and 2.13) whereas observed responsivities are either constant (as shown in Figure 2.10) or slightly increase with decreasing temperature. Moreover, in the low temperature region, responsivities usually decrease somewhat less rapidly with background than  $Q_B^{-1}$  as predicted for a uniform continuum. Consideration of the Figures and equations 2.37 to 2.40 suggests that a distribution of traps more highly concentrated near the valence band will bring the experiment and theory in closer agreement.

Thus, for the next step in improving the modeling, an exponential density of traps has been selected:

$$N(E) = N_0 \exp(-E/E_x) \quad (2.43)$$

Where:  $N(E)$  = density of trap states at energy  $E$  above the valence band edge, and  $N_0$  = trap density at  $E = 0$ , the valence band energy. Thus,

$$\Delta p_t = N_0 \int_0^{E_m} \frac{e^{-E/E_x} \Delta p \, dE}{p_1 (E) + \Delta p} \quad (2.44)$$

d) Determination of  $E_m$

The maximum energy of integration,  $E_m$ , can be estimated when we recognize that, as trap energy levels approach the conduction band, the interaction rates increase exponentially with energy between trap and conduction band. Thus, for sufficiently large  $E_t$ , traps can be emptied of electrons (filled with holes) by excitation to the upper band, and thus are no longer available for occupation due to optical excitation.

We now estimate the energy at which conduction band trap excitation becomes large, and identify this energy as  $E_m$ . Consider equation

2.27 which contains all terms of single energy trap occupation. Solving for  $p_t$  we find

$$p_t = N_t - n_t = N_t \frac{\Delta p + (r_c/r_v) n_1}{\Delta p + (r_c/r_v) n_1 + p_1 + (r_c/r_v) n_0} \quad (2.45)$$

The term  $(r_c/r_v) n_1$  in the denominator is the excitation rate of electrons from trap to conduction band. Now, the influence of  $E_m$  is significant only at higher temperatures, where  $p_1 \gg \Delta p$ . Thus, when  $E_t = E_m$ , the upward excitation rate equals the downward rate, and

$$(r_c/r_v) n_1 (E_m) = p_1 (E_m) \quad (2.46)$$

where, as shown in Figure 2.8

$$n_1 = N_c e^{-(E_g - E_t)/kT}, \quad p_1 = N_v e^{(-E_t/kT)} \quad (2.47)$$

This gives for  $E_m$ :

$$E_m = \frac{E_g}{2} + kT \log \left( \frac{N_v}{N_c} \frac{r_v}{r_c} \right)^{1/2} \quad (2.48)$$

Thus,  $E_m = 1/2$  the energy gap plus a term of the order of several  $kT$ . Although the term on the right hand side of 2.47 contains the unknown material parameter  $r_c/r_v$ , the logarithmic dependence shows that  $E_m$  will not depend strongly on the parameters, and one may estimate, roughly

$$E_m \approx \frac{E_g}{2} + 4kT \quad (2.49)$$

Equation 2.49 agrees with the experimental findings that generally activation energies are found to be slightly above  $E_g/2$ , as can be seen, e.g., in Figure 2.10.

If warranted, the exact solution for  $\Delta p_t$  is available from equation

2.45 which contains all terms. The solution to the complete equation will, of course be more difficult, but in principle there is no limitation to finding it, other than time and complexity. As suggested by the excellent agreement between theory and experiment, most systems of physical interest will be accessible to approximate methods.

#### 2.2.3.4 Time-Dependent Behavior

##### a) The General Approach

Essentially the same procedure is followed as in the steady state solution, but the additional complexity of temporal variation is included. That is, we begin with the basic equations for single energy traps and obtain solutions under assumptions which have proven applicable to the steady state. Then the solutions are integrated over a continuum trap distribution.

For ease of treatment, and because good results were found for the steady state, we begin with the uniform continuum.

##### b) Time Dependent Equation for Traps at $E_t$

Time dependent occupation for traps at energy  $E_t$  is given from equations 2.24 and 2.28:

$$\frac{dp}{dt} = G - \frac{\Delta p}{\tau} + \frac{dn_t}{dt}, \quad (2.50)$$

$$\frac{dn_t}{dt} = r_v p_1 N_t - r_v (\Delta p + p_1) n_t \quad (2.51)$$

Thus, photocarriers are determined by two coupled differential equations. The general solution is possible in principle but can be quite complex. Moreover, there is the added complication that, since a distribution of traps requires integration over  $n_t$ , the equations will take integro-differential form, because the last term on the right hand side of 2.50 includes effects of all trap levels. However, when trapping rates are much slower than recombination rates, which usually occurs, much simpler and more tractable forms of these equations can be obtained. Then the last term on the right hand side of 2.50 can be neglected and we can approximate:

$$\Delta p \approx G(t) \tau, \quad (2.52)$$

where  $G(t)$  includes the time dependence of the illumination. Equation 2.52 is the mathematical statement that, because of rapid recombination, the excess hole concentration adiabatically follows the time variation of illumination. It is applicable when  $dG/dt \ll \tau^{-1}$ , which includes the magnitude of time variation of interest here. Furthermore, the range or validity for using equation 2.52 for  $\Delta p$  to determine  $\Delta p_t$ , can be determined by placing the expression in 2.51 and iterating back to 2.50 with  $dn_t/dt$  small. When this is done, this approach is valid.

$$r_v N_t \tau \ll 1 \quad (a) \quad (2.53)$$

$$r_v N_t \tau p_1 / \Delta p \ll 1 \quad (b)$$

Consistent with the initial assumption, 2.53a states that recombination rates are much faster than trapping rates. Equation 2.53b provides the further requirement that  $\Delta p$  be not very much smaller than  $p_1$ --at very low backgrounds, the approximation cannot be used. Thus, except in this case, we can write for equation 2.51:

$$\frac{dn_t}{dt} + r_v n_t (\Delta p(t) + p_1) = r_v p_1 N_t \quad (2.54)$$

The form of this equation, with  $y = n_t$ , is:

$$\frac{dy}{dt} + F(t) y = K, \quad (2.55)$$

where

$$F(t) = r_v (\Delta p(t) + p_1) = \frac{r_v \eta \tau}{d} [Q(t) + Q_B] + r_v p_1 \quad (2.56)$$

$$K = r_v p_1 N_t; \quad p_1 = N_v e^{-E_t/kT} \quad (2.57)$$

Equation 2.55 has the well-known form of a linear differential

equation with variable coefficient. The value of  $y$  is determined at any time for any given input  $F(t)$ . The illumination is included in  $F(t)$ , where, as shown in equation 2.56, the photon flux is separated into a dc background term and a time dependent term. Now, although some difficulties may be involved, the solution can be obtained for any input (remembering that it must be consistent with the requirement that  $dQ/dt \ll \tau^{-1}$ ). At present, we have obtained solutions for two simple but useful forms of input:

c) Transient Response

The general solution for the linear differential equation is:

$$y = K \exp(-u(t)) \int dt' \exp(u(t')) + c \exp(-u(t)) \quad (2.58)$$

where  $c$  is a constant to be determined by boundary conditions and where

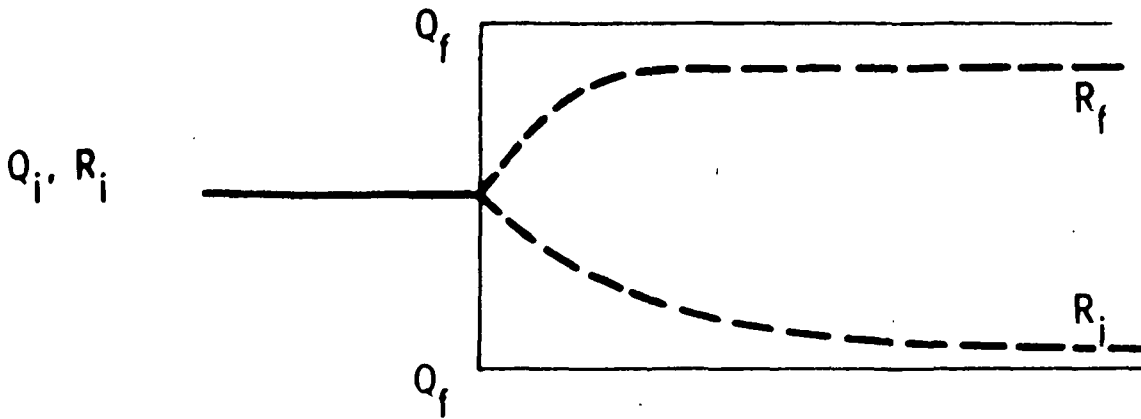
$$u(t) = \int dt' F(t').$$

For the transient solution, we assume that a steady state has been reached, with  $\Delta p = \Delta p_i$ . Then at  $t = 0$ , the illumination intensity is suddenly changed (either increased or decreased) from  $\Delta p_i$  to  $\Delta p_f$ , as illustrated in Figure 2.14. Using equations 2.54 to 2.57, the solution is:

$$n_t = p_1 N_t \left\{ \frac{1}{\Delta p_f + p_1} + \left[ \frac{1}{\Delta p_i + p_1} - \frac{1}{\Delta p_f + p_1} \right] \exp \left[ -r_v t (\Delta p_f + p_1) \right] \right\} \quad (2.59)$$

Once more beginning with the uniform continuum, we let  $N_t(E)dE = \nu dE$ , where  $\nu$  is a constant, and obtain:

$$\frac{n_{tot}}{\nu k T} = \int_{\nu_m}^1 \frac{\gamma d\nu e^{-\rho(\beta + \nu)}}{\nu(\gamma + \nu)} + \int_{\nu_m}^1 \frac{\beta d\nu}{\nu(\beta + \nu)} - \int_{\nu_m}^1 \frac{\beta d\nu e^{-\rho(\beta + \nu)}}{\nu(\beta + \nu)} \quad (2.60)$$



$$R_f = R_i + F(Q_i, Q_f, t / \tau_t, E_m \approx E_g/2)$$

Figure 2.14 TRANSIENT RESPONSE

$$\beta = \Delta p_f / N_v, \quad \gamma = \Delta p_i / N_v, \quad \rho = r_v N_v t \quad (2.61)$$

$$v = \exp(-E/kT), \quad f_m = \exp(-E_m/kT)$$

After some manipulation, the solution for  $\Delta p_{tot} = N_t - n_{tot}$  is given by:

$$\Delta p_{tot} = vkT \left\{ \log \left( 1 + \frac{\beta}{v_m} \right) + E_1 \left( \rho [\beta + v_m] \right) - \exp(-\rho [\beta - \gamma]) E_1 \left( \rho [\gamma + v_m] \right) \right\} \quad (2.62)$$

where  $E_1(z)$  is the exponential integral

$$E_1(z) = \int_z^{\infty} \frac{e^{-t}}{t} dt \quad (2.63)$$

which is tabulated, e.g., in "Handbook of Mathematical Functions" by Abramowitz and Stegun, National Bureau of Standards Applied Mathematics Series 1964. Thus, using equation 2.62 transient responsivity is determined as a function of  $Q_i$ ,  $Q_f$  and time.

At present, we are investigating the functional behavior of equation 2.61 in relation to experiment, and are developing convenient analytical expressions. Preliminary results appear to fit the experimental behavior.

#### d) Response to ac Input

We wish to obtain the solution of equation 2.55 with  $F(t)$  given by  $F + F_1 \sin \omega t$ . This can be done by using the general form, 2.58. It is perhaps more illustrative to obtain the small signal solution by making a Fourier series expansion in equation. The input now has a dc component and a periodic component.

$$\Delta p = \Delta p_B + \Delta p_o e^{i\omega t} \quad (2.64)$$

therefore

$$F(t) = \Delta p + p_1 = \Delta p_B + p_1 + \Delta p_o e^{i\omega t} \quad (2.65)$$

where  $\Delta p_B$  is the hole concentration due to the background. Then we expand

$$n_t = \sum_{-\infty}^{+\infty} a_n e^{in\omega t} \quad (2.66)$$

Placing 2.64 and 2.66 in 2.54 we find that the following Fourier expansion must be satisfied:

$$\sum_{-\infty}^{\infty} e^{in\omega t} \left\{ a_n \left[ in\omega + r_v (\Delta p_B + p_1) \right] + r_v \Delta p_o a_{n-1} \right\} - r_v p_1 N_t = 0 \quad (2.67)$$

Equating each term in the expansion to zero, we find

$$a_0 = \frac{p_1 N_t}{\Delta p_B + p_1} - \frac{\Delta p_o a_{-1}}{\Delta p_B + p_1} \quad (a)$$

$$a_n = \frac{-r_v \Delta p_o a_{n-1}}{in\omega + r_v (\Delta p_B + p_1)} \quad (b) \quad (2.68)$$

$$a_{-n} = \frac{-r_v \Delta p_o a_{-n-1}}{-in\omega + r_v (\Delta p_B + p_1)} \quad (c)$$

If the Fourier expansion approach is valid, then the higher order terms will decrease in amplitude (except in the large signal case, to which this method is inapplicable). Thus, the second term on the right hand side of 2.68a can be neglected, both because  $\Delta p_o$  may be small and because  $a_{-1}$  will be moderately small. Moreover, note that the positive order coefficients are determined in relation to lower orders, whereas the opposite occurs for the negative coefficients. Thus, again for small or medium signals, the dc solution is given by  $a_0$ , and we can neglect the negative order coefficients. Then,

$$a_0 \approx \frac{p_1 N_t}{\Delta p_B + p_1} \quad (a)$$

$$a_1 \approx \frac{-r_v \Delta p_o a_0}{i\omega + r_v (\Delta p_B + p_1)} \quad (b) \quad (2.69)$$

The amplitude of the fundamental frequency solution is given by  $a_1$ . Higher harmonics can be obtained from 2.68 if desired.

The amplitude of the fundamental is obtained by integrating  $a_1$  over all traps. For the uniform continuum, using  $\Delta p_t = N - n_t$

$$\Delta p_{\text{tot}} \propto A_1 = \nu \int_0^{E_m} \frac{N_v e^{-E/kT} dE}{\left[ \frac{\eta\tau Q}{d} + N_{ve}^{-E/kT} + i\omega/r_v \right] \left[ \frac{\eta\tau Q}{d} + N_{ve}^{-E/kT} \right]} \quad (2.70)$$

After some manipulation, this becomes:

$$A_1 = \frac{\Delta p_0 \nu kT}{i\omega/r_v} \log \left[ 1 + i\omega\tau_s \right], \quad (2.71)$$

where

$$\tau_s = [r_v]^{-1} \left[ \frac{\eta\tau Q}{d} + N_v e^{-E_m/kT} \right]^{-1} \quad (2.72)$$

Eliminating the phase factor, we obtain the frequency dependence of the amplitude of the fundamental component of the responsivity,  $R(\omega)$ :

$$\left| \frac{R(\omega)}{R(0)} \right| = \left\{ \left[ \frac{\tan^{-1}(\omega\tau_s)}{\omega\tau_s} \right]^{-2} + \frac{1}{4} \left[ \frac{\log(1 + (\omega\tau_s)^2)}{(\omega\tau_s)^2} \right]^2 \right\}^{1/2} \quad (2.73)$$

Equation 2.73 predicts a slow decrease in  $R(\omega)/R(0)$  with  $\omega$ , it can be seen by the ratio  $R(1/\tau) / R(0) = 0.867$ . There is no simple time constant, and the falloff is much less abrupt than the 6 dB per octave expected for a single time constant. The quantity  $\tau_s$  given in equation 2.72, determines the rate behavior.

### 2.2.3.5 Derivation of the Small Signal, Low Frequency Responsivity from the Single Trap Model

From Section 2.2.3.2 the fundamental results of applicability to the derivation to follow are summarized below. We found the following relationships to hold for minority carrier trapping at a single level in an n-type semiconductor. Under steady state conditions. Shockley-Read combination is the assumed mechanism by which holes and electrons eventually recombine.

$$\Delta n = \Delta p + \Delta p_t \quad (2.74)$$

$$\Delta p_t = \frac{N_t \Delta p}{\Delta p + p_1(E_a)} \quad (2.75)$$

$$\Delta n = \Delta p \left[ 1 + \frac{N_t}{\Delta p + p_1(E_a)} \right] \quad (2.76)$$

$$\Delta p = \frac{n \tau_{SR} Q}{d} \quad (2.77)$$

$$p_1(E_a) = N_v \exp(-E_a/kT) \quad (2.78)$$

In order to derive the responsivity we start with the general definition which does not assume anything about the magnitude of the signal voltage  $V_{sig}$  that results from an optical signal power  $H A_S$  incident on the sample.

$$R = \frac{V_{sig}}{A_S H} \quad (2.79)$$

For the small signal responsivity, we recognize that it is the limit of the above expression as  $V_{sig}$  and  $H$  go to zero. This is just the derivative. Hence for the small signal responsivity:

$$R = \frac{1}{A_S} \frac{\partial V_{sig}}{\partial Q} \frac{\partial Q}{\partial H} \quad (2.80)$$

The formula for the signal voltage was:

$$V_{sig} = E \ell \frac{\Delta n}{n_o} \quad (2.81)$$

Substituting Equation 2.81 into Equation 2.80 and carrying out the differentiation of Q with respect to H from the well known relationship we obtain:

$$R_{\lambda} = \frac{\lambda E \ell}{hc A_S n_o} \frac{\partial \Delta n}{\partial Q} \quad (2.82)$$

Differentiation of  $\Delta n$  with respect to Q gives Equation 2.83 which when substituted into Equation 2.84 gives the desired expression for the responsivity.

$$\frac{\partial \Delta n}{\partial Q} = \frac{\eta \tau_{SR}}{d} \left[ 1 + \frac{N_t p_1 (E_a)}{p_1 (E_a) + \Delta p} \right] \quad (2.83)$$

$$R_{\lambda} (Q_B, T) = \frac{e \lambda \eta r_s}{hc} \left( \frac{E \mu_e \tau_{SR}}{\ell} \right) \left[ 1 + \frac{N_t p_1 (E_a)}{(p_1 (E_a) + \Delta p)^2} \right] \quad (2.84)$$

where:

$$r_s = \frac{\ell}{e n_o w d \mu_e} \quad (2.85)$$

The factor in parentheses is the photoconductive gain in the absence of trapping. The factor in brackets embodies the effects of trapping and contains the temperature and background dependence of interest. This factor is referred to as the trapping gain enhancement factor  $G_t(Q_B, T)$  because it results in an effective gain enhancement when trapping is operative.

$$G_t (Q_B, T) = \left[ 1 + \frac{N_t p_1 (E_a)}{[p_1 (E_a) + \Delta p]^2} \right] \quad (2.86)$$

Hereafter, the "trapping gain enhancement factor" will be referred to as the "trapping gain." Also when trapping is operative, the responsivity will often be expressed by  $R_{\lambda} (Q_B, T)$  to emphasize the dependence on  $Q_B$  and T and denote trapping responsivity. When trapping is not operative, the symbol  $R_{\lambda}$  will be used.

With these notational conventions  $G_t(Q_B, T)$  is

$$G_t(Q_B, T) = \frac{R_{\lambda'}(Q_B, T)}{R_{\lambda}} \quad (2.87)$$

Therefore, if the responsivity can be measured under a set of conditions such that trapping is inoperative, then the trapping gain can be determined by taking the ratio  $R_{\lambda'}(Q_B, T)/R_{\lambda}$ . This will be valid if the responsivity is measured under constant E field conditions. Also  $\tau_{SR}$ ,  $\eta$ , and  $n_o$  must not vary with temperature. The extrinsic condition insures us that  $n_o$  and  $\tau_{SR}$  do not vary appreciably with temperature. The assumption of a constant quantum efficiency  $\eta$  is less substantiated. However, it is believed that  $\eta$  does not strongly depend on temperature for lack of evidence that it does. Furthermore, surface recombination effects have not been considered.

Under these assumptions the responsivity will have the same relative functional dependence on temperature and background as the trapping gain  $G_t(Q_B, T)$ . Therefore, theoretical and experimental comparisons of the functional dependence are possible even if the experimentation of the absolute value of  $G_t(Q_B, T)$  is impossible.

It must be emphasized that this derivation is valid in the limit of zero modulation frequency. Practically speaking, this requires that the modulation be sufficiently slow in time such that equilibrium conditions are reached at a rate much faster than the rate of signal fluctuation.

#### 2.2.4 PV-PC Detector Trade-Off

(Hg,Cd)Te can be operated in either the photoconductive or photovoltaic mode. Historically the simpler photoconductive mode has been developed first to give excellent performance in both single elements and array applications. (Hg,Cd)Te can be tailored to respond anywhere from 1 to 30 micrometers giving it a broad spectral range of applications. Recent work in photovoltaic (Hg,Cd)Te has shown promising results especially where high speed is important. Appendix B describes a two-color photovoltaic detector fabricated for the 1.55-1.75 micrometer and 2.08-2.35 micrometer bands. This section will consider the differences between the photoconductive detectors developed for this program and the photovoltaic two-color detectors discussed in Appendix B. Earth Resources applications will be used to establish desired operating conditions.

#### 2.2.4.1 Quantum Efficiency

The three factors in the PV mode which theoretically determine the quantum efficiency are the loss of radiation through surface reflections, absorption of radiation in the bulk more than a diffusion length away from the junction and loss due to surface recombination.

$$\eta = \frac{1 - r}{\text{cash } (d/L_k) + (S\tau_h/L_h) \text{ sink } (d/L_h)} \text{ PV mode} \quad (2.88)$$

where

r = reflection  
d = depth of junction  
s = surface recombination velocity  
 $L_h$  = hole diffusion length  
 $\tau_h$  = hole lifetime

In the pc mode quantum efficiency is determined theoretically by the reflection losses at the surface and the optical thickness of the detector (absorption coefficient  $[\alpha]$  times thickness of detector [d])

$$\eta = \frac{[1-r](1-e^{-\alpha d})}{(1-re^{-\alpha d})} \text{ PC mode} \quad (2.89)$$

In both cases the reflection loss may be minimized by antireflection coatings. For the photodiode the junction can be made less than a diffusion length away from the surface so that all of the energy near the bandgap will be absorbed.

#### 2.2.4.2 Responsivity

In the PV mode quantum efficiency is the only variable in the current responsivity

$$R_\lambda (i) = \frac{\eta q \lambda}{hc} \text{ (amps/watt)} \quad (2.90)$$

where

q = electronic charge  
 $\lambda$  = wavelength  
h = Plank's constant  
c = speed of light

Thus a measurement of responsivity gives a direct indication of quantum efficiency. In the PC mode the responsivity depends on both the photoconductive gain (G) and the quantum efficiency. It is difficult to separate these experimentally.

$$R_{\lambda} (V) = \frac{\eta q \lambda G R_d}{hc} \quad (\text{volts/watt}) \quad (2.91)$$

where

G = photoconductive gain

R<sub>d</sub> = resistance of device

The pc responsivity is normally measured in volts/watt. The generalized responsivity can be written as

$$R_{\lambda} (i) = \frac{\eta q \lambda G}{hc} \quad (\text{amps/watt}) \quad (2.92)$$

The gain (G) for photovoltaic detectors is unity whereas the pc mode has photoconductive (trapping or non-trapping) gain which is proportional to the dc applied field. The importance of the photoconductive gain is seen when the detector is matched with a preamplifier. In comparison with a photovoltaic detector: 1) the responsivity is larger requiring less gain in the preamplifier, 2) the gain in the detector may be changed by changing the electric field adding an extra degree of freedom in the design of the detector preamplifier combination 3) the noise is larger and thus the amplifier noise may be larger without degradation to the performance of the detector. Therefore, because of the photoconductive gain, the PC mode is more easily matched to the preamplifier without degradation of the D\*. For each application the basic question becomes how do photovoltaic and photoconductive detectors compare after matching with a preamplifier.

#### 2.2.4.3 Noise

The important aspect of noise is to determine whether the detector noise will be dominated by amplifier noise and thus degrade the sensitivity of the detector. In the PC mode, for earth resources applications the g-r noise will dominate over the Johnson noise. The g-r noise assuming radiative lifetime has the same gain factor as in the PC responsivity and thus gives the same opportunity to increase the gain by an increase in E-field.

$$\langle v_{g-r}^2 \rangle^{1/2} = 2 q \sqrt{\eta G_r} R_d \sqrt{A} G \quad (2.93)$$

where A = area of detector

G<sub>r</sub> = thermal generation rate of carriers

The noise sources for the PV mode are shown in Figure 2.15. The dominant noise at elevated temperature should be Johnson noise.

$$\langle i_J^2 \rangle^{1/2} = \frac{4 kT \Delta f}{R_D} \quad (2.94)$$

where

k = Boltzmann's constant  
 T = temperature of detector  
 $\Delta f$  = Noise bandwidth

Photodiodes are typically used with operational amplifiers operating in the current mode.

Assuming the detector to be Johnson noise limited and that the various noise sources are independent, then the total rms noise current is

$$i_t^2 = \frac{4kT}{R_d} + \frac{4kT}{10 R_d} + v_A^2 \left( \frac{1}{R_d^2} + \omega^2 c^2 \right) + i_A^2 \quad (2.95)$$

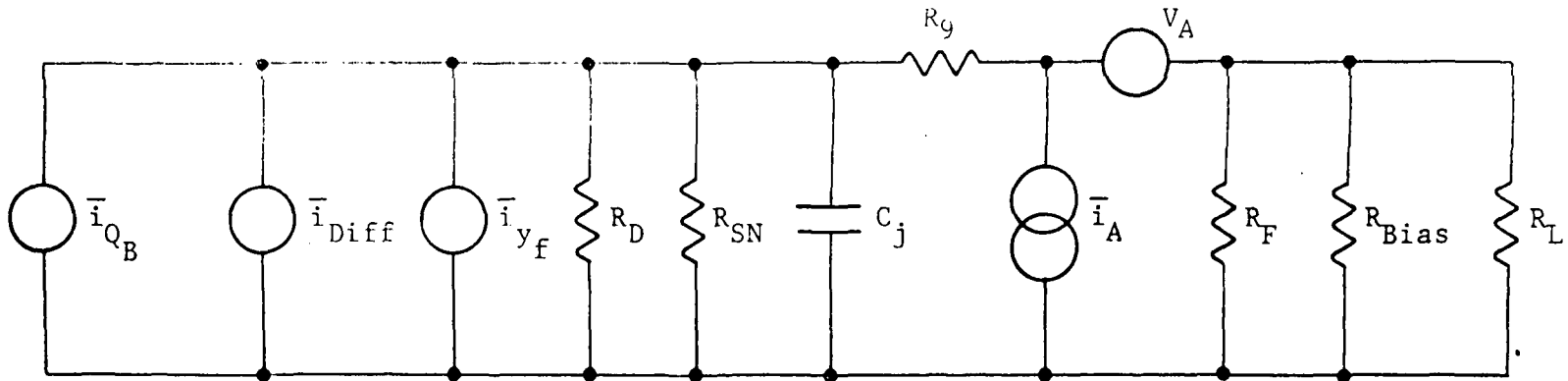
This assumes that the feedback resistor is ten times the detector resistance, and the detector is thermal noise limited. For the detector noise to be dominant the following three conditions must exist:

$$R_d \leq \frac{4kT}{i_A^2} \quad (2.96)$$

$$R_d \geq \frac{v_A^2}{4kt} \quad (2.97)$$

$$R_d \leq \frac{4kt}{v_A^2 \omega^2 c^2} \quad (2.98)$$

Table 1 gives the current responsivity, noise and capacitance for the two PV detectors discussed in Appendix B. For the detectors shown in Table 2.2 this amplifier would be adequate for both bands at elevated temperatures. Further amplifier design would have to be initiated in order to optimize the 77 °K detectors with a 200 kHz bandwidth. Thus the possibilities of amplifier degradation of PV performance are seen with lower temperatures but do not seriously effect the near room temperature conditions being studied in this contract.



$$R_D = \frac{\partial V}{\partial I} = R_D e^{-qV/kT}$$

NOISE SOURCES

1. Short circuit shot noise from background  $\bar{i}^2 = 2\eta q^2 A(Q_S + Q_B)$
2. Shot noise and thermal noise from  $R_D$   $\bar{i}_D^2 = \frac{2kT}{R_o} (e^{qV/kT} + 1)$
3. Thermal noise of Shunt  $R_{sh}$   $i_{sh}^2 = \frac{4kT}{R_{sh}}$
4. 1/f noise  $\bar{i}_{1/f}^2 = \frac{1}{f} [k_1 \left(\frac{V^2}{R_{sh}}\right) + k_2 \left(I - \frac{V}{sh}\right)^2 + k_3 I^2]$
5. Thermal noise of series resistance  $i_s^2 = 4kTR_s / \left(R_s + \frac{R_{sh}R_D}{R_{sh} + R_D}\right)^2$
6. Amplifier noise  $i_{na}^2$

Figure 2.15 NOISE EQUIVALENT CIRCUIT

#### 2.2.4.4 Response Time

In photovoltaic detectors the response time is controlled either by the bulk carrier lifetime or by the RC time constant of the detector circuit combination. A 200 kHz bandwidth detector requires a 800 ns response time. Although the minority carrier lifetime has not been directly measured Honeywell has fabricated 1-3 micrometer (Hg,Cd)Te photodiodes with 20 to 40 ns response times at 300 °K (contract DAAB05-71-C-2610) at room temperature. This indicates that the bulk lifetime should not be a limiting factor for a 800 ns requirement near room temperature. The RC time constant can be approximated by the series resistance times the sum of the detector and circuit capacitance. Assuming a 6 pfd JFET the RC time constant will be less than 100 ns for each case. Thus, as expected, the photodiode is a very fast detector which can easily meet the 800 ns earth resources applications requirements.

One of the obvious advantages of PV mode when used in the unbiased mode is the freedom from 1/f noise at low frequency which has been observed in diodes made from some materials. (Hg,Cd)Te diodes were made at HRC for the 1-3 micrometers region and specifically designed for high speed operation with the result that data extends only down to 100 Hz. Down to that point however no 1/f noise, under zero bias conditions, was observed.

Table 2.2

	300 °K	77 °K
1.8	$R_i = 0.07 \text{ A/watt}$	$R_i = 0.6 \text{ A/watt}$
	$i_n = 3 \times 10^{-13} \text{ A/Hz}^{1/2}$	$i_n = 8 \times 10^{-14} \text{ A/Hz}^{1/2}$
	$c = 1.85 \text{ pfd}$	$c = 1.55 \text{ pfd}$
2.5	$R_i = 0.65 \text{ A/watt}$	$R_i = 1 \text{ A/watt}$
	$i_n = 2.4 \times 10^{-12} \text{ A/Hz}^{1/2}$	$i_n = 3.6 \times 10^{-14} \text{ A/Hz}^{1/2}$
	$c = 28 \text{ pfd}$	$c = 16.2 \text{ pfd}$

In the PC mode the concept of detective time constant is very important as has been demonstrated in this contract. The trapping response times are relatively long (~100  $\mu$ s) but can be frequency boosted with the amplifier to have a flat response for the whole 200 kHz bandwidth.

#### 2.2.4.5 Detectivity

The detectivity limits are the same for PC and for zero biased PV modes.

$$D_{BLIP}^* = \frac{\eta^{1/2} \lambda}{2 hc Q_B} \quad \text{PC or zero-biased PV} \quad (2.99)$$

For the reverse biased PV mode the blip limit is:

$$D_{BLIP}^* = \frac{\eta^{1/2} \lambda}{hc Q_B} \quad \text{reverse biased PV} \quad (2.100)$$

Using reverse bias and very high quantum efficiency photodiodes it is possible for the PV mode to outperform the PC mode.

(Hg,Cd)Te material considerations are very important in reaching optimum detector performance. For the PC mode very high purity n-type material is required. Considerable effort has been spent to produce the necessary material. For the PV mode, p-type material with a higher carrier concentration is required. P-type (Hg,Cd)Te is easier to grow than n-type and the higher carrier concentration requirement utilizes doping rather than the more difficult task of extreme purity control. Less work has been done on p-type (Hg,Cd)Te and thus material parameters are not as well known. However, considering all these factors, p-type (Hg,Cd)Te for PV mode appears to offer an easier material system to work in than n-type (Hg,Cd)Te for the PC mode.

#### 2.2.4.6 Linearity

Trapping photoconductivity as described above shows how the responsivity and response time change with background levels for the photoconductive (Hg,Cd)Te detector in the trapping mode. Based on this analysis specific earth resources applications parameters may be used to derive the time dependent pulse response and the linearity of the responsivity of the detector for bands 1 and 2.

Figure 2.16 shows the model used for the pulse response. The detectors view the scene with  $Q$  ph/cm<sup>2</sup>-s for a long enough time that the variations in signal are considered small. Since the detectors operate at elevated temperatures where single trap, uniform continuum and exponential distribution models give the correct functional dependence for the trapping gain (or responsivity) as a function of temperature and photon flux, we will use the simplest model (the single trap) to study the changes in responsivity. The trap level is  $E_m$  which is shown in Figure 2.17.

$$E_m = \frac{E_g}{2} + kT \quad (2.101)$$

At 200 °K.

$$E_m (2.35 \mu\text{m}) = .334 \text{ eV} \quad (2.102)$$

$$E_m (1.75 \mu\text{m}) = .423 \text{ eV}$$

The time dependence of the number of electrons occupying traps is given in equation 2.59 of Section 2.2.3.4 with its derivation preceding it.

$$n_t = p_1 N_t \frac{1}{\Delta p_f + p_1} + \frac{1}{\Delta p_2 + p_1} - \frac{1}{\Delta p_f + p_1} \exp [-r_v t (\Delta p_f + p_1)] \quad (2.103)$$

Definition of terms is given in Appendix C. Looking at each term for our specific case,

$$p_1 = N_v e^{-E_t/kT} \simeq 10^{15} (T)^{3/2} e^{-E_m/kT}$$

$$\Delta p_f = \frac{\eta \tau_{SR} Q}{d} \quad (2.104)$$

$$\Delta p_i = \frac{\eta \tau_{SR} Q_B}{d}$$

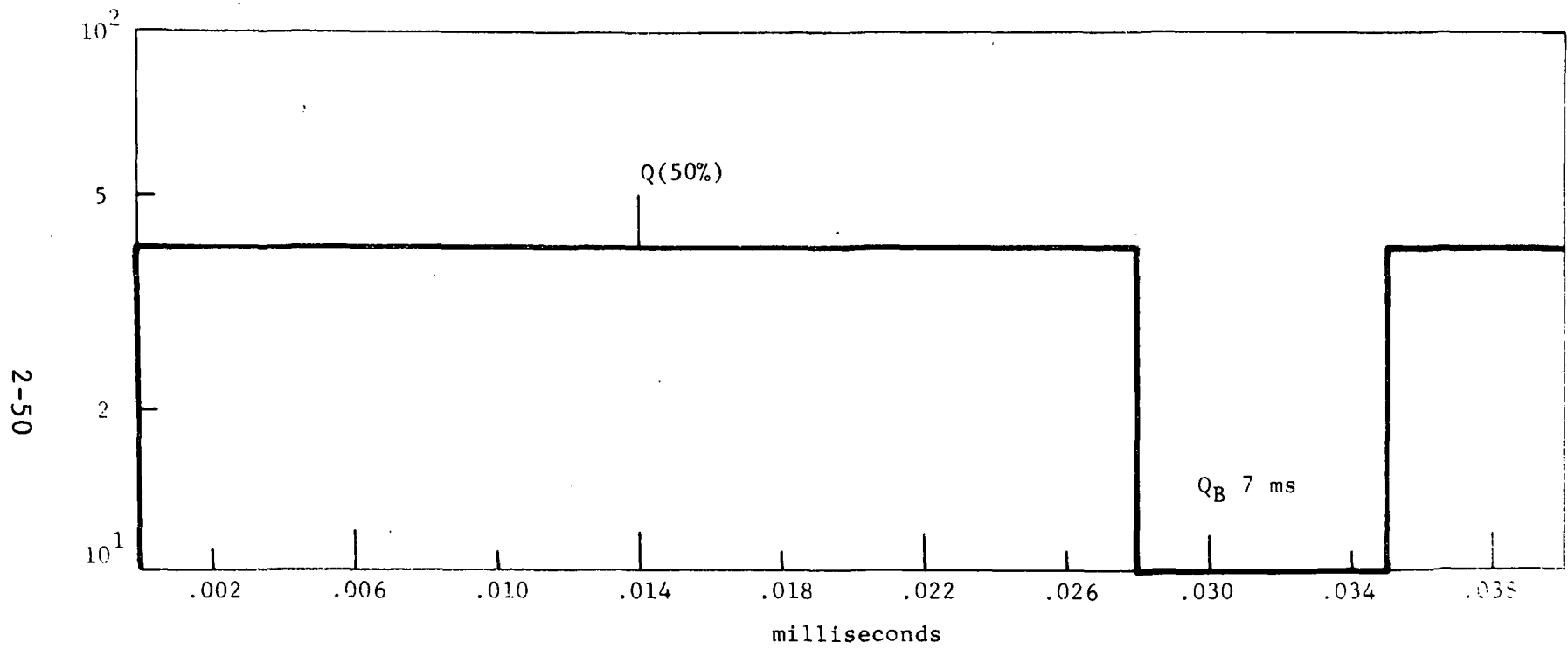


Figure 2.16 ASSUMED MODEL

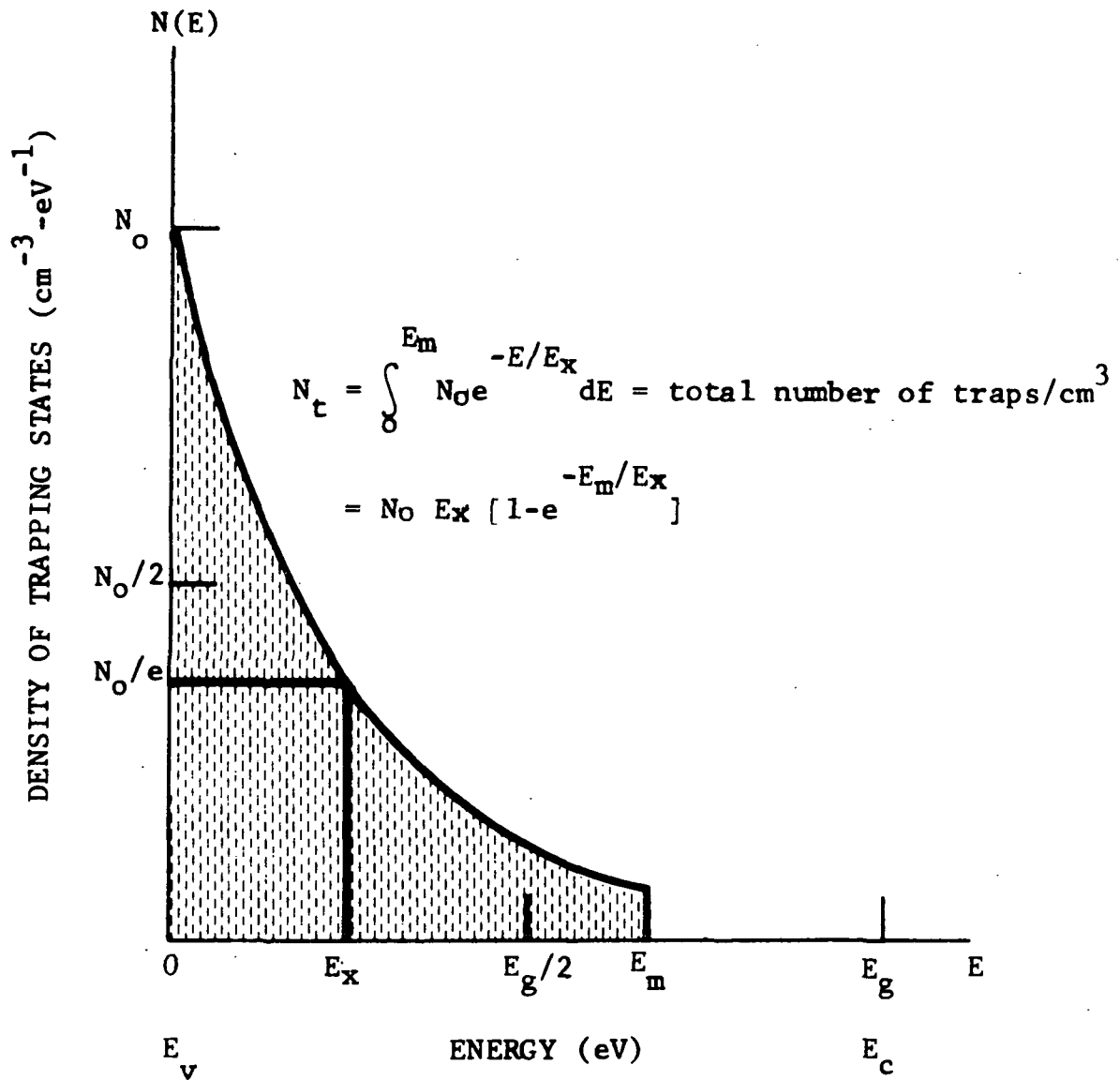


Figure 2.17 EXPONENTIAL DISTRIBUTION OF TRAPS

Equations 2.102 and 2.103 assume that we wish to examine the time dependence of trap density caused by a step function from  $Q_B$  to  $Q$ .  $\Delta p_i$  can be interchanged with  $\Delta p_f$  to examine the time dependent behavior at the trapping gain on the step function; we use the following derivation:

$$G = \frac{\Delta n}{\Delta p} = 1 + \frac{p_t}{\Delta p_f} \quad (2.105)$$

$$p_t = N_t - n_t \quad (2.106)$$

With the following assumed parameters, the time dependence of the photoconductive gain is calculated and shown in Figures 2.18 and 2.19 assuming a 50%  $Q$  level.

$$N_t = 10^{14} \text{ cm}^{-3} \quad d = 10^{-3} \text{ cm}$$

$$\tau = 5 \times 10^{-6} \text{ s} \quad r_v = 10^{-8}$$

The small signal responsivity as derived in equation (2.82) is proportional to:

$$\frac{\partial \Delta n}{\partial Q} = \frac{\eta \tau_{SR}}{d} \left[ 1 + \frac{N_t p_1}{p_1 + \Delta p} \right] \quad (2.107)$$

This function is plotted versus  $Q$  for both bands 1 and 2 in Figures 2.20 and 2.21.

The activation energy which is the slope of the responsivity versus  $1/kT$  graph has been observed to vary between different detectors with the same cutoff wavelength where the detectors are fabricated from different ingots, thus indicating that the trap level may vary somewhat from the assumed  $E_m$  energy level. This would probably make the largest difference in performance of these detectors. In addition, the assumed parameters also introduce a possible variation between predicted performance. However, Figures 2.18 through 2.21 give a good estimate of the predicted behavior of bands 1 and 2.

Photovoltaic detectors do not have trapping gain and thus do not show the same effects. The responsivity, as discussed in Section 2.2.3.2 depends only on the quantum efficiency (Section 2.2.4.1) of the detector. It is expected that the responsivity will not change appreciably until there is sufficient power to do physical damage to the detector. The earth resources applications with  $Q_B$  between  $10^{11}$  to  $10^{14}$  photons/cm<sup>2</sup> s have very low power inputs to the detector and all experiments have shown the responsivity to be completely linear.

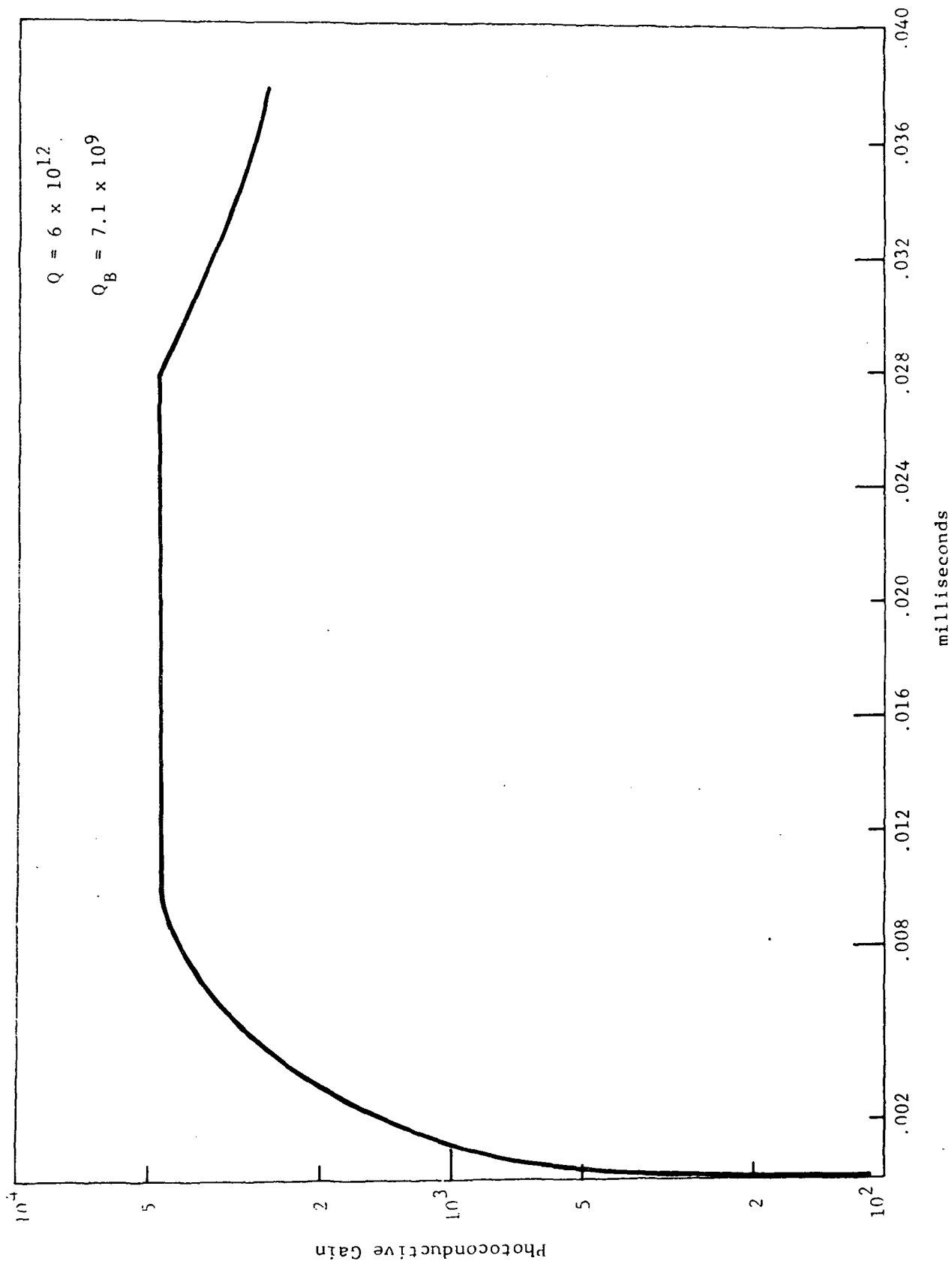


Figure 2.18 BAND 1

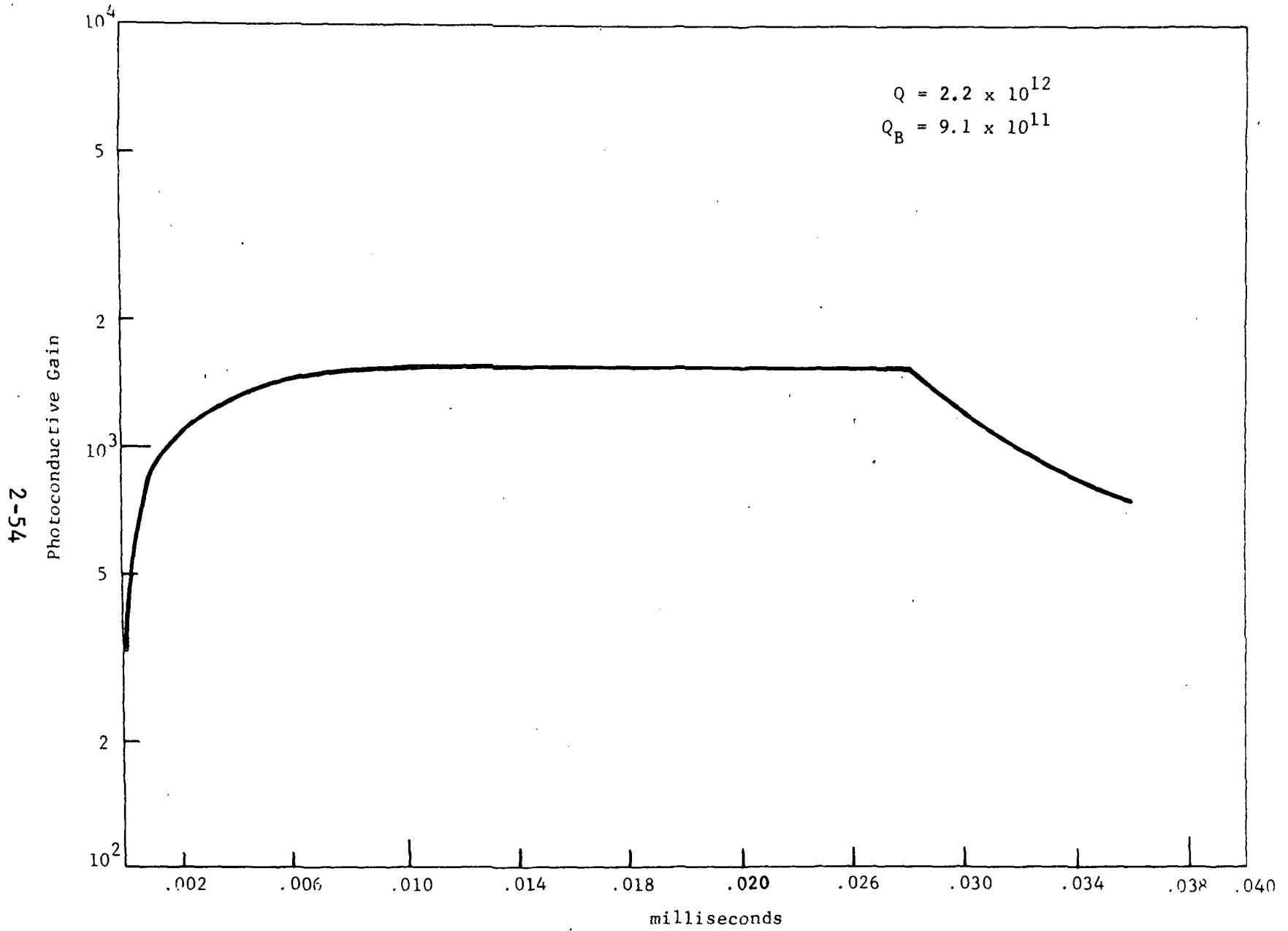


Figure 2.19 BAND 2

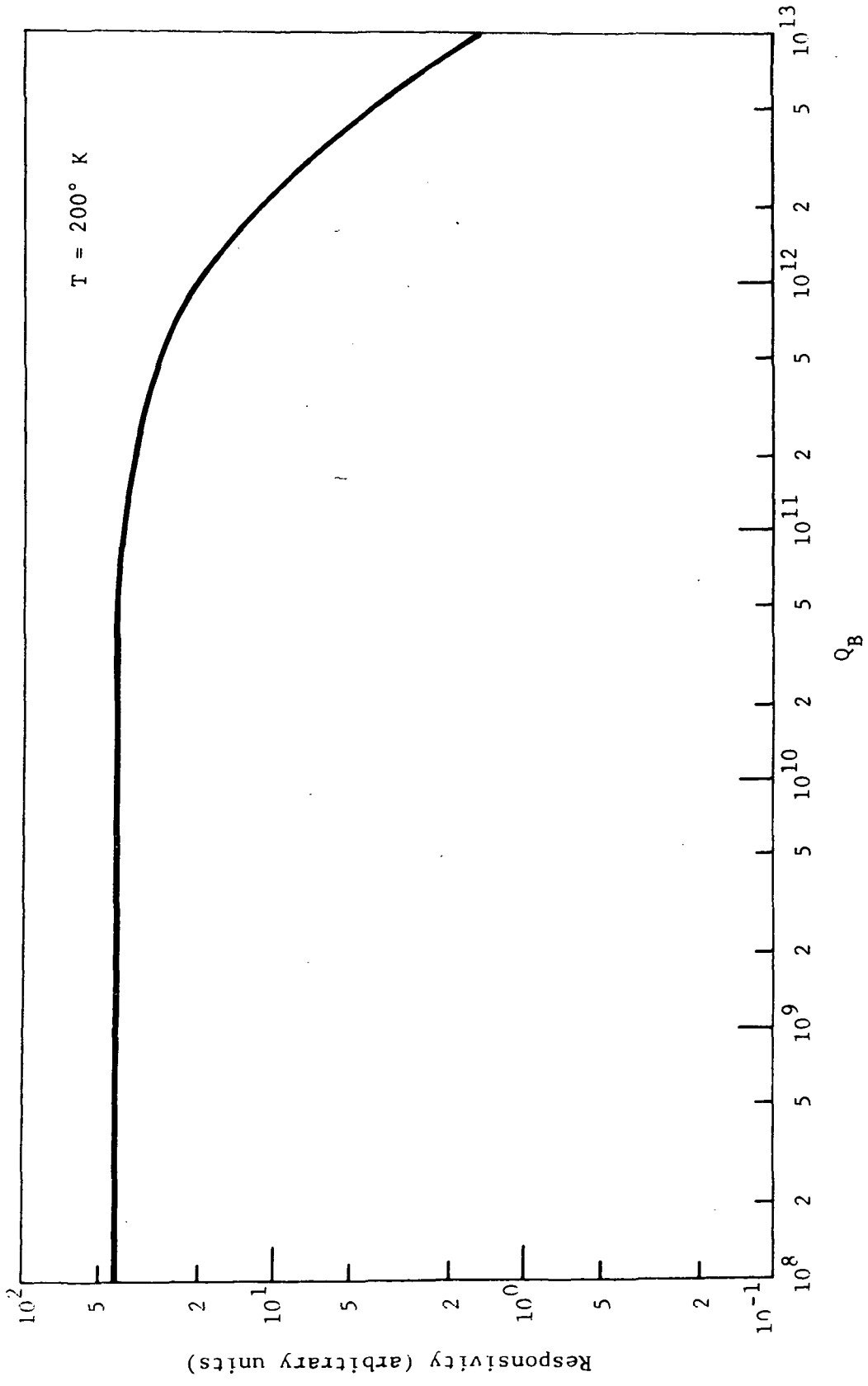


Figure 2.20 BAND 1

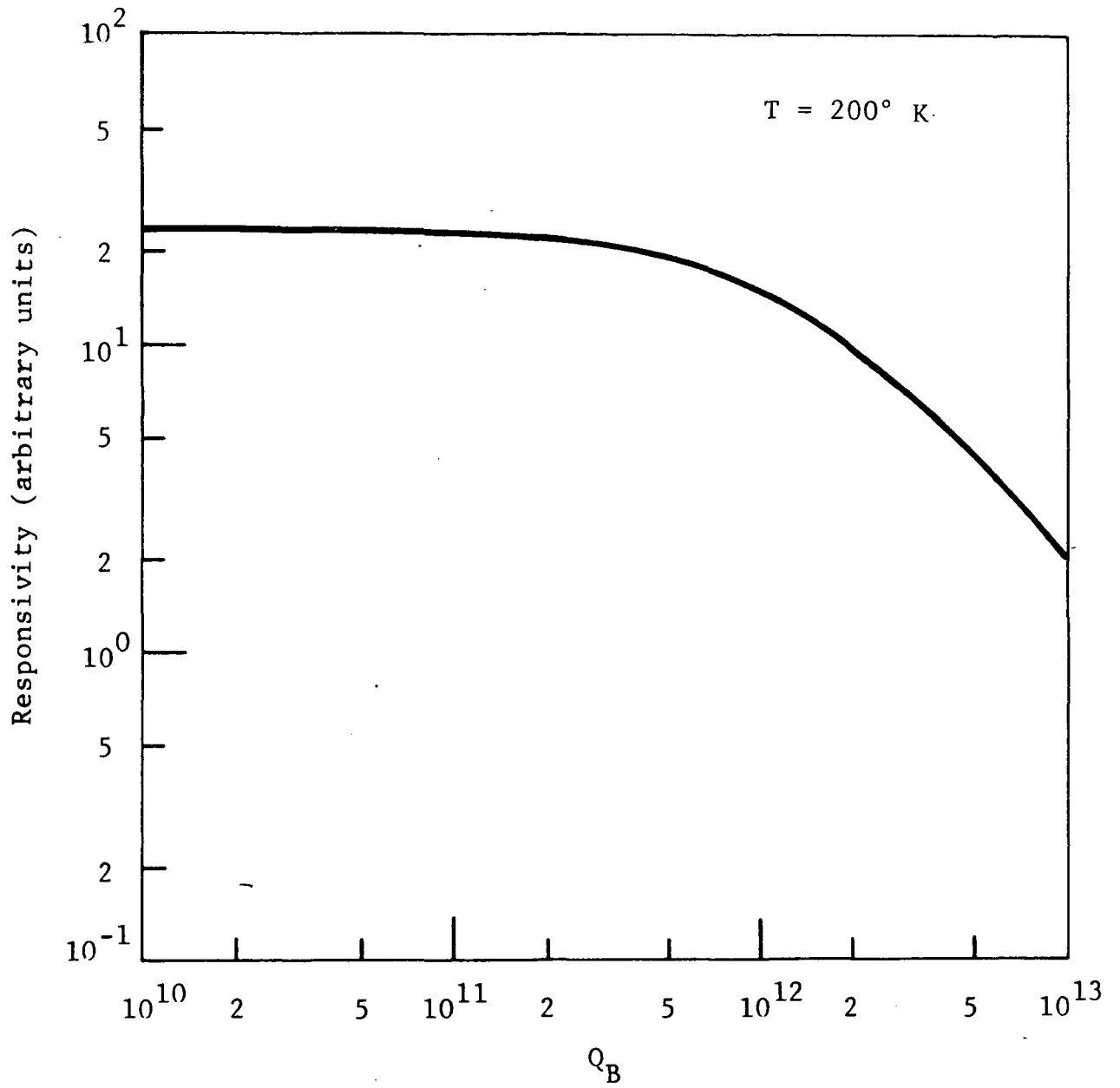


Figure 2.21 BAND 2

#### 2.2.4.7 Fabrication

Photoconductive (Hg,Cd)Te has reached a high degree of sophistication in array fabrication. Photovoltaic (Hg,Cd)Te technology is not as advanced. However, the technique of ion implantation is being used very successfully at HRC in producing very high performance PV (Hg,Cd)Te detectors.

Ion implantation is quite conducive to planar technology. To date we have fabricated arrays with 0.010 inch x 0.010 inch elements and 0.001 inch, 0.002 inch, 0.003 inch, 0.004 inch spacings very successfully. With increased experience in the PV area fabrication problems should not be a restriction.

## 2.3 MEASUREMENT TECHNIQUES

One of the goals of this program was to characterize the behaviors of near infrared (Hg,Cd)Te photodetectors as a function of temperature, background flux and wavelength. Certain measurement techniques and tools had to be developed and/or analyzed in order to perform this task. A variable temperature dewar (VTD) was evaluated and used for the variable temperature measurements. The errors involved using a 1000 °K blackbody were analyzed and concluded that under proper operating conditions there was less error than the normal experimental error. A light emitting diode (LED) was built and utilized for measuring signal and noise as a function of background and frequency. In addition, the effect of minority carrier trapping was considered in each test set up and proper adjustment was made. Finally, techniques were developed for the rapid screening of many detectors in order to select those closest to the program specification without extensive testing.

### 2.3.1 Variable Temperature Dewar

A variable temperature dewar was used to obtain measurement from approximating 82 °K to room temperature. With liquid nitrogen (LN<sub>2</sub>) the dewar reached a minimum of 82 °K. With 20 watts applied to the heaters, the temperature stabilized at 210 °K and the boil-off time was 45 minutes. A temperature range from 190 °K to 273 °K was easily accomplished with dry-ice and methanol.

Figures 2.22 and 2.23 illustrate the temperature versus power curves for the two temperature ranges. Because of the long boil-off time at 210 °K, and because the maximum operating power capability is 40 watts, even higher temperature with liquid nitrogen are possible.

Several different coolants including Argon (89 °K), Freon 14 (140 °K), Freon 13 (193 °K), Freon 22 (230 °K) and Freon 12 (243 °K) were used at different times with this variable temperature dewar.

### 2.3.2 Blackbody Measurements

Detectors for this program were fabricated to operate over two spectral regions from 1.55 to 1.75 μm in one band and from 2.08 to 2.35 μm in the other. A 1000 °K blackbody is the standard source for  $D^*_{bb}$  and  $R_{bb}$  measurements from which spectral detectiv-

2-59

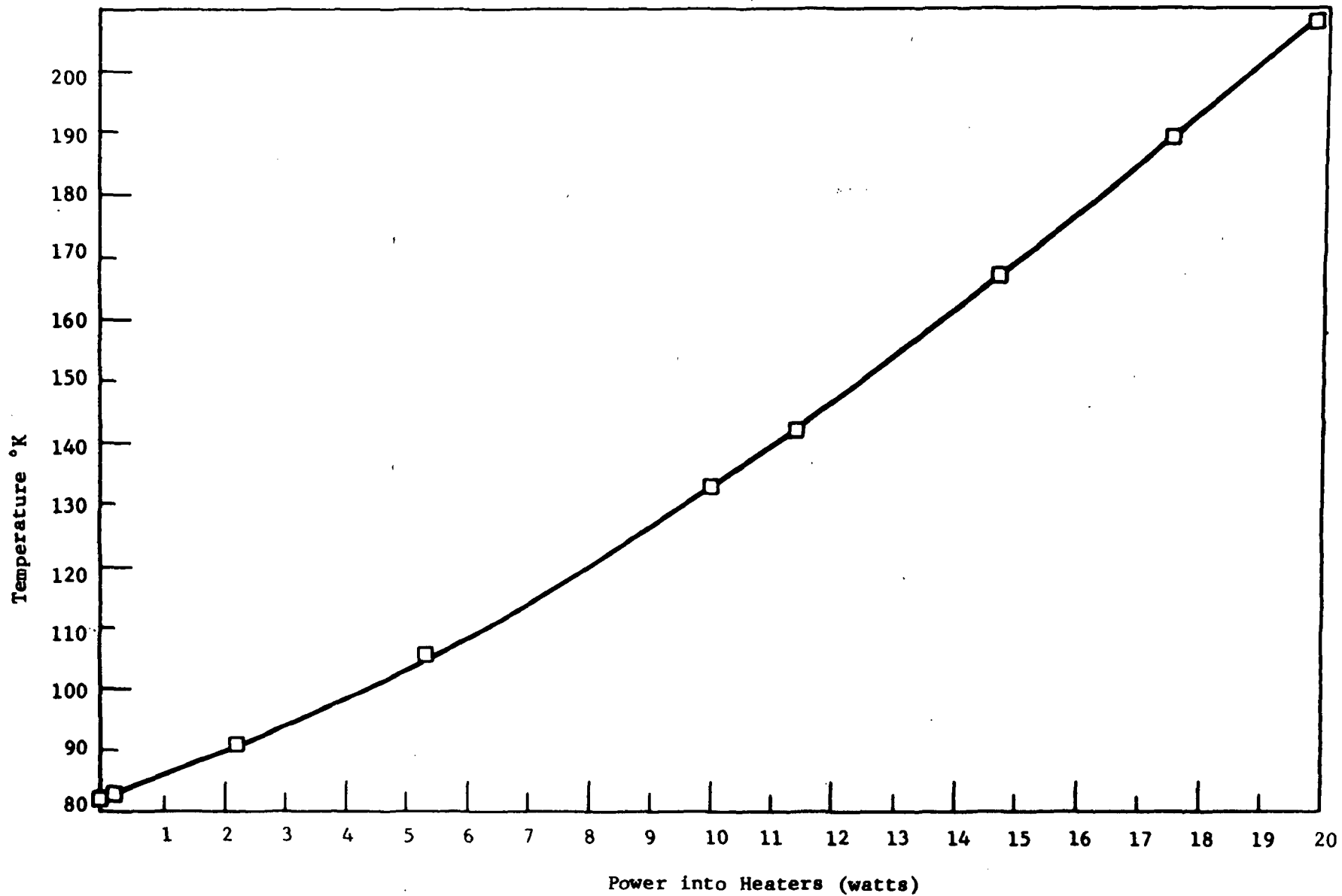


Figure 2.22 VARIABLE TEMPERATURE DEWAR (VTD-1) TEMPERATURE VS POWER INTO HEATERS LN<sub>2</sub> COOLANT

2-60

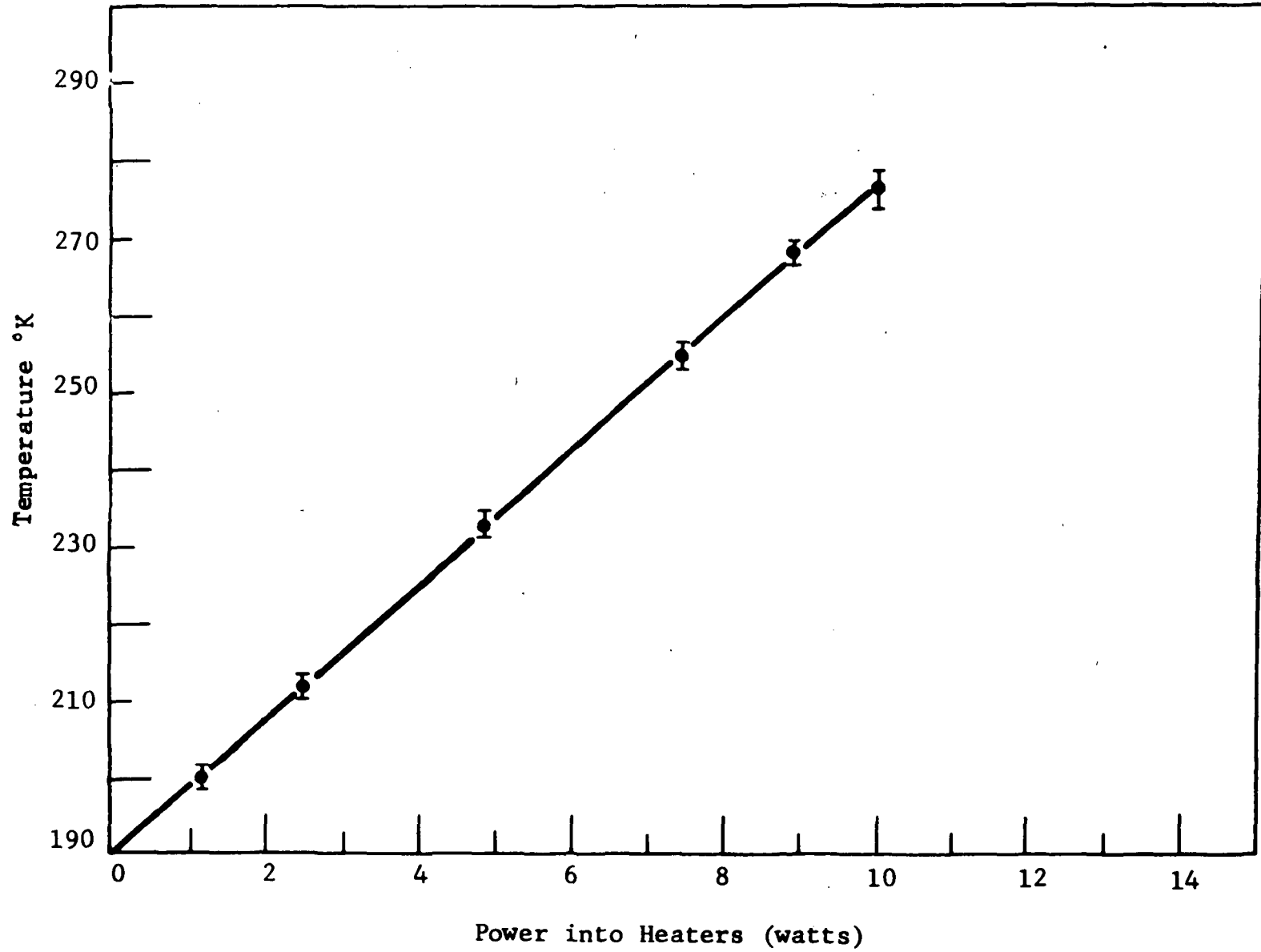


Figure 2.23 VARIABLE TEMPERATURE DEWAR (VTD-1) TEMPERATURE VS POWER INTO HEATER-DRY ICE AND METHANOL

ity  $D^*_\lambda$  and spectral responsivity  $R_\lambda$  are derived from the conversion factor,  $G$ , which is a function of the blackbody temperature and the detector cutoff wavelength,  $\lambda_c$ .

The wavelength,  $\lambda_p$ , corresponding to the peak spectral radiant energy density from a 1000 °K blackbody is 2.9  $\mu\text{m}$ . Thus, the spectral region of interest is on the side of the blackbody radiation curve which is highly sensitive to temperature and wavelength. Consequently,  $G$  becomes more sensitive to  $\lambda_c$  and  $T_{\text{BB}}$  as  $\lambda_c$  becomes shorter. The question was, therefore, what conversion factor error can be expected for a given temperature excursion from 1000 °K and for a given uncertainty in  $\lambda_c$ ? How accurately must this temperature be maintained and how accurately must  $\lambda_c$  be determined to keep the error to within acceptable limits?

The answers to these questions depend upon knowledge of the functional dependence of  $G$  on the blackbody temperature and the cutoff wavelength of the detector. The fundamentals of the blackbody responsivity measurement were reviewed and from the expression for the blackbody responsivity  $R_{\text{BB}}$  the conversion factor  $G$  was derived. Once an expression for  $G$  is obtained, the sensitivity of  $G$  to blackbody temperature excursions and cutoff wavelength determination errors can be calculated.

Figure 2.24 illustrated the relative spectral radiant energy density curve for a 1000 °K blackbody and the location of the wavelength bands of interest to this contract. This blackbody curve of course was obtained from Planck's famous equation for blackbody radiation:

$$u(\lambda) = \frac{8 \pi c h}{\lambda^5 \left( \exp \left( \frac{hc}{k T \lambda} \right) - 1 \right)} \quad (2.107)$$

where  $u(\lambda)$  is the spectral radiant energy density in  $\text{ergs}/\text{cm}^4$ . For mathematical simplicity Equation 2.107 is re-expressed in terms of the constants  $C_1$  and  $C_2$ .

$$u(\lambda) = C_1 \lambda^{-5} \left( e^{C_2/\lambda T} - 1 \right)^{-1} \quad (2.108)$$

To derive the photoconductive response of a detector with area  $A_d$  ( $\text{cm}^2$ ) we assume that the detector is ideal. By "ideal" we mean that the detector exhibits a constant quantum efficiency for

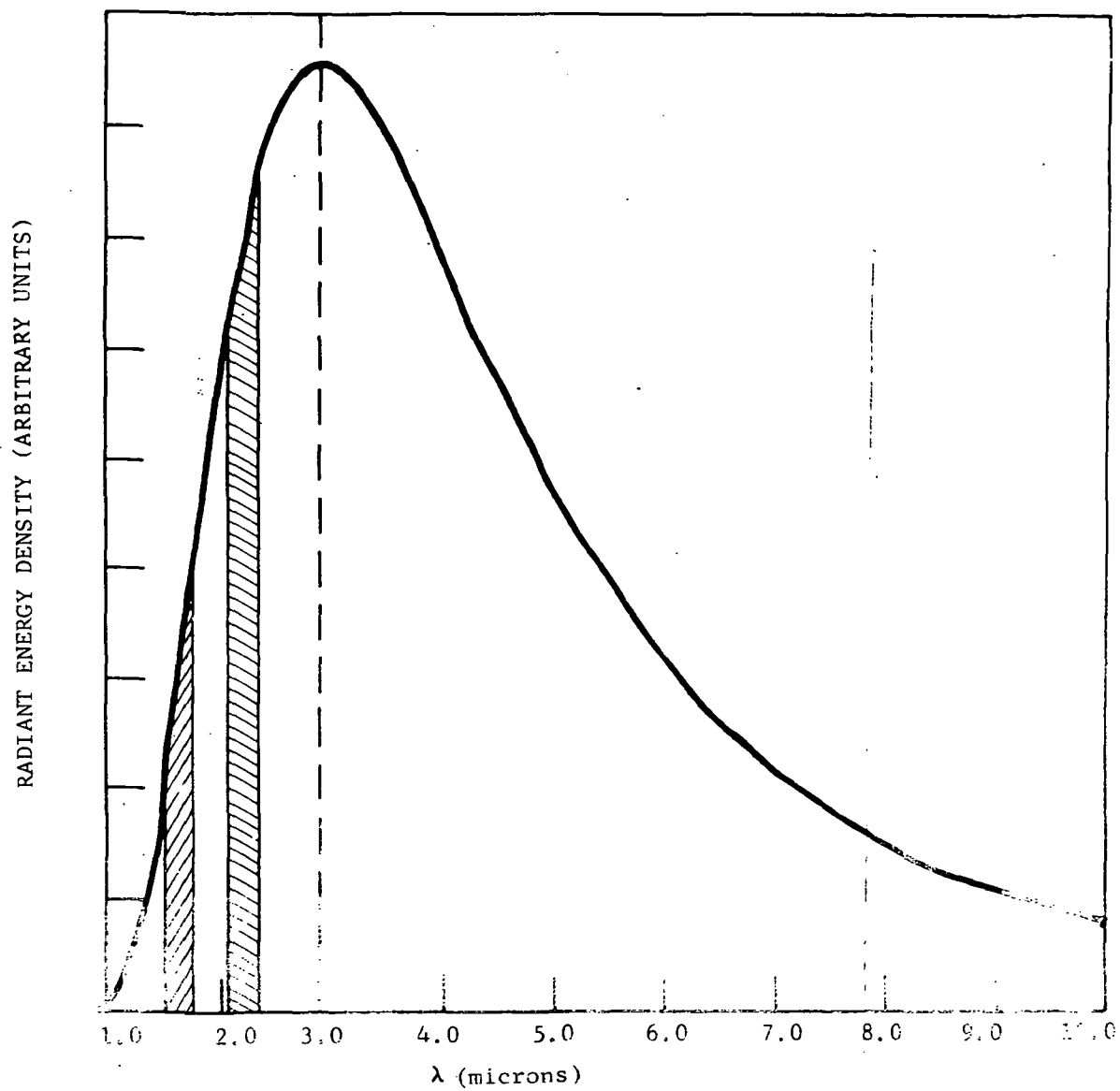


Figure 2.24 BLACKBODY SPECTRAL RADIANT ENERGY DENSITY FOR A 1000 °K BLACKBODY

wavelengths less than or equal to the cutoff wavelength  $\lambda_c$ . For wavelengths greater than  $\lambda_c$  the responsivity abruptly goes to zero. In this model the wavelength of peak responsivity " $\lambda_p$ " is equal to  $\lambda_c$ . The responsivity as a function of wavelength which is graphically shown in Figure 2.25 is mathematically described as follows:

$$R_{\lambda}(\lambda) = \begin{cases} R_{\lambda_p} \frac{\lambda}{\lambda_p} & \text{for } \lambda \leq \lambda_p = \lambda_c \\ 0 & \text{for } \lambda > \lambda_p = \lambda_c \end{cases} \quad (2.109)$$

where:  $R_{\lambda}$  is the spectral responsivity in volts/watt.  
 $R_{\lambda_p}$  is the peak responsivity.

Consider the signal voltage that would result from exciting such a photodetector with a chopped blackbody source. The rms spectral irradiance from the blackbody at temperature  $T_{BB}$  is denoted by  $H(T_{BB}, \lambda)$  where, except for a change in the constant  $C_1$ ,  $H(T_{BB}, \lambda)$  has the same functional form with respect to temperature and wavelength as  $u(\lambda)$ , Equation 2.108. The signal voltage is just the integral of the product of the spectral energy incident on the detector and the spectral responsivity of the detector integrated over all wavelengths.

$$V_{sig} = \int_0^{\infty} A_d H(T_{BB}, \lambda) R(\lambda) d\lambda \quad (2.110)$$

For the ideal case as defined by Equation 2.109 the expression for the signal voltage becomes more specific.

$$V_{sig} = \frac{A_d R_{\lambda_p}}{\lambda_p} \int_0^{\lambda_c} \lambda H(T_{BB}, \lambda) d\lambda \quad (2.111)$$

The blackbody responsivity " $R_{BB}$ " is defined as the ratio of the signal voltage over the total power incident on the detector, equation 2.112.

$$R_{BB} = \frac{V_{sig}}{P_T} = \frac{R_{\lambda_p}}{\lambda_p} \frac{\int_0^{\lambda_c} \lambda H(T_{BB}, \lambda) d\lambda}{\int_0^{\infty} H(T_{BB}, \lambda) d\lambda} \quad (2.112)$$

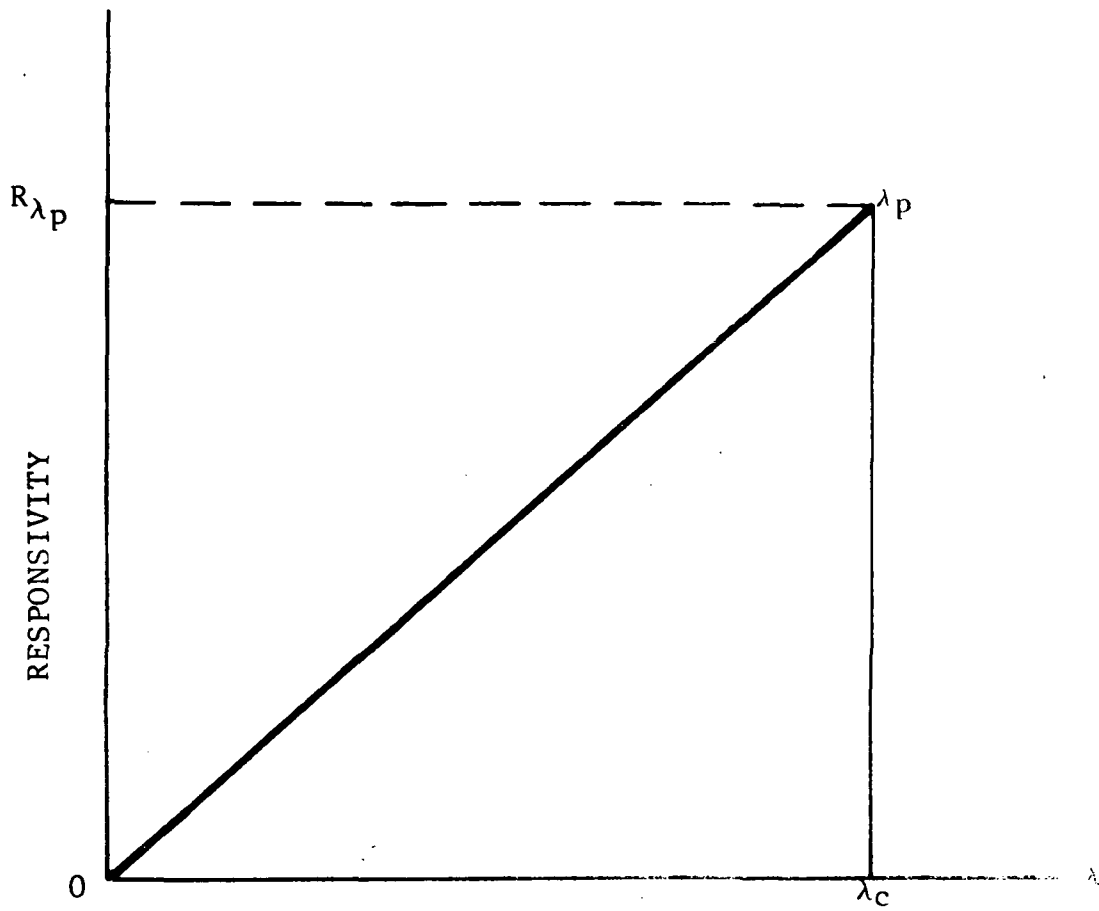


Figure 2.25 IDEAL RESPONSIVITY ASSUMPTION

The conversion factor " $G(T_{BB}, \lambda_c)$ " is a pure number which when multiplied by the blackbody responsivity gives the spectral responsivity of the detector at its peak response wavelength,  $\lambda_p$  which in this case is also  $\lambda_c$ . Thus,  $G$  is the ratio of  $R_{\lambda_p}$  to  $R_{BB}$ . Let the conversion factor be denoted by  $G(T_{BB}, \lambda_c)$  which emphasizes its dependence upon the blackbody temperature and the cutoff wavelength of the detector. From equation 2.112 an expression for  $G$  is obtained by solving for the ratio of  $R_{\lambda_p}$  to  $R_{BB}$ :

$$G(T_{BB}, \lambda_c) = \frac{R_{\lambda_p}}{R_{BB}} = \frac{\lambda_p \int_0^{\infty} H(T_{BB}, \lambda) d\lambda}{\lambda_c \int_0^{\lambda_c} \lambda H(T_{BB}, \lambda) d\lambda} \quad (2.113)$$

The integral in the numerator is an exact definite integral which when evaluated simplifies equation 2.113 to equation 2.114 below.

$$G(T_{BB}, \lambda_c) = \frac{\lambda_p}{15} \left(\frac{kT}{2ch}\right)^4 \left[ \int_0^{\lambda_c} \lambda^{-4} (e^{C2/T\lambda} - 1)^{-1} d\lambda \right]^{-1} \quad (2.114)$$

Using this expression for  $G$ , we can obtain error arising from temperature deviations about  $T_{BB} = 1000$  °K

Consider the fractional change in  $G$  for a given temperature excursion  $\Delta T$  from  $T_{BB}$ :

$$\epsilon = \frac{G(T_{BB} + \Delta T, \lambda_c) - G(T_{BB}, \lambda_c)}{G(T_{BB}, \lambda_c)} \quad (2.115)$$

To a first approximation the fractional change in  $G$  for  $\Delta T$  about  $T_{BB}$  is given by the following equation:

$$\epsilon \approx \frac{\Delta T}{G(T_{BB}, \lambda_c)} \left( \frac{\partial G(T_{BB}, \lambda_c)}{\partial T} \right)_{T_{BB}} \quad (2.116)$$

When equation 2.114 is substituted into 2.115 we obtain:

$$\epsilon = \left[ \frac{\int_0^{\lambda_c} \lambda^{-4} (e^{C_2/\lambda T} - 1)^{-1} d\lambda - C_2/T^2 \int_0^{\lambda_c} \lambda^{-5} (e^{C_2/\lambda T} - 1)^{-2} d\lambda}{\int_0^{\lambda_c} \lambda^{-4} (e^{C_2/\lambda T} - 1)^{-1} d\lambda} \Delta T \right] \quad (2.117)$$

The factor in brackets was quite small (less than  $\sim .004/^\circ\text{K}$ ) for the cutoff wavelength range from 1.5 to 3.0  $\mu\text{m}$  and the nominal blackbody temperature at 1000  $^\circ\text{K}$ . This means that G is relative insensitive to temperature deviations about 1000  $^\circ\text{K}$ . This result can be explained by the observation that both integrals in equation 2. go the same way with temperature and thus compensate for each other leaving G relatively invariant.

However,  $V_{\text{sig}}$  is quite sensitive to temperature. Since the value of the signal voltage measured is used directly to calculate  $R_{\text{BB}}$  and  $D^*_{\text{BB}}$ , it is important that the temperature of the blackbody is kept close to the value assumed for it in the calculation. In our case it is necessary to know how accurately the temperature must be maintained at 1000  $^\circ\text{K}$  to stay within a certain acceptable error tolerance. This temperature was also found to depend on the cutoff wavelength of the detector.

The procedure we follow here for  $V_{\text{sig}}$  similar to that previously applied to G. Again defining a fractional change for  $V_{\text{sig}}$  we arrive at a analogous expression to that for G.

$$\epsilon (V_{\text{sig}}) \approx \frac{\Delta T}{V_{\text{sig}T_{\text{BB}}}} \left( \frac{\partial V_{\text{sig}}}{\partial T} \right)_{T_{\text{BB}}} \quad (2.118)$$

Substituting the expression for the signal voltage, equation 2.111 into equation 2.118 we obtain for the fractional change the following:

$$\epsilon_{V_{\text{sig}}}(T_{\text{BB}}, \lambda_c) = \frac{\int_0^{\lambda_c} \lambda \left( \frac{\partial H}{\partial T} \right) d\lambda}{\int_0^{\lambda_c} \lambda H d\lambda} \Delta T \quad (2.119a)$$

$$= \frac{C^2}{T^2} \frac{\int_0^{\lambda_c} \lambda^{-5} e^{C_2/\lambda T} - 1^{-2} d\lambda}{\int_0^{\lambda_c} \lambda^{-4} e^{C_2/\lambda T} - 1^{-1} d\lambda} \Delta T \quad (2.119b)$$

Equation 2.119b evaluated by numerical computer techniques and the results are plotted in Figure 2.26 for several values of  $\Delta T$  over the wavelength range from 1.4 to 3.6  $\mu\text{m}$ .

Figure 2.19 tells us how tightly  $T_{\text{BB}}$  must be maintained about 1000  $^\circ\text{K}$  in order that the calculations of  $D^*_{\text{BB}}$  may still assume  $T_{\text{BB}} = 1000$   $^\circ\text{K}$  and stay within an acceptance error tolerance range. For example, the graph shows that to keep the error to within 5% for detectors in this wavelength range, the blackbody temperature should be kept to within five degrees of 1000  $^\circ\text{K}$ .

### 2.3.2.1 Error Arising from Uncertainties in the Accurate Measurement of $\lambda_c$

Since the conversion factor directly depends on the cutoff wavelength  $\lambda_c$ , we calculated the fractional change in  $G$  for a given uncertainty  $\Delta \lambda_c$ . This fractional change is directly related to the error in our  $D^*_\lambda$  and  $R_\lambda$  calculations.

Proceeding as before we approximate the fractional change by evaluating the expression:

$$\epsilon_G (T_{\text{BB}}, \lambda_c) = \frac{\Delta \lambda_c}{G} \left( \frac{\partial G}{\partial \lambda_c} \right)_{\lambda_c} \quad (2.120a)$$

$$= \frac{1}{\lambda_c} - \frac{\lambda_c^{-4} e^{C_2/\lambda_c T} - 1^{-1}}{\int_0^{\lambda_c} \lambda^{-4} e^{C_2/\lambda T} - 1^{-1} d\lambda} \Delta \lambda \quad (2.120b)$$

Equation 2.120b was evaluated numerically and the results are plotted in Figure 2.27 which graphs the error in the  $D^*_\lambda$  or  $R_\lambda$  calculation over the cutoff wavelength range from 1.5 to 3.5  $\mu\text{m}$  for several different values of  $\Delta \lambda_c$  where  $\Delta \lambda_c$  is the measure-

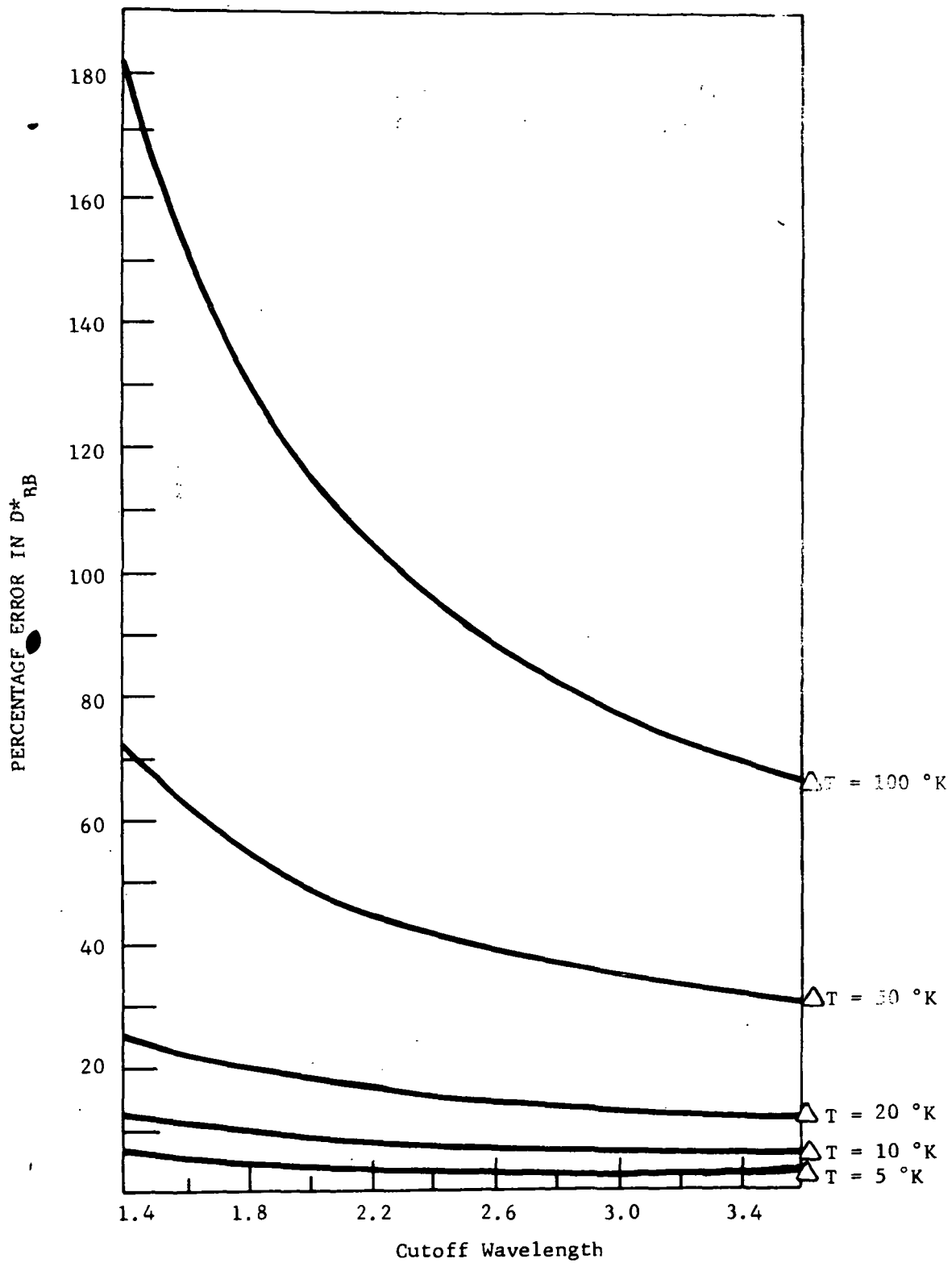


Figure 2.26 PERCENTAGE ERROR IN  $D^*_{BB}$  ASSUMING  $T_{BB} = 1000 \text{ }^\circ\text{K}$  FOR DEVIATIONS  $\Delta T$  FROM  $T_{BB}$

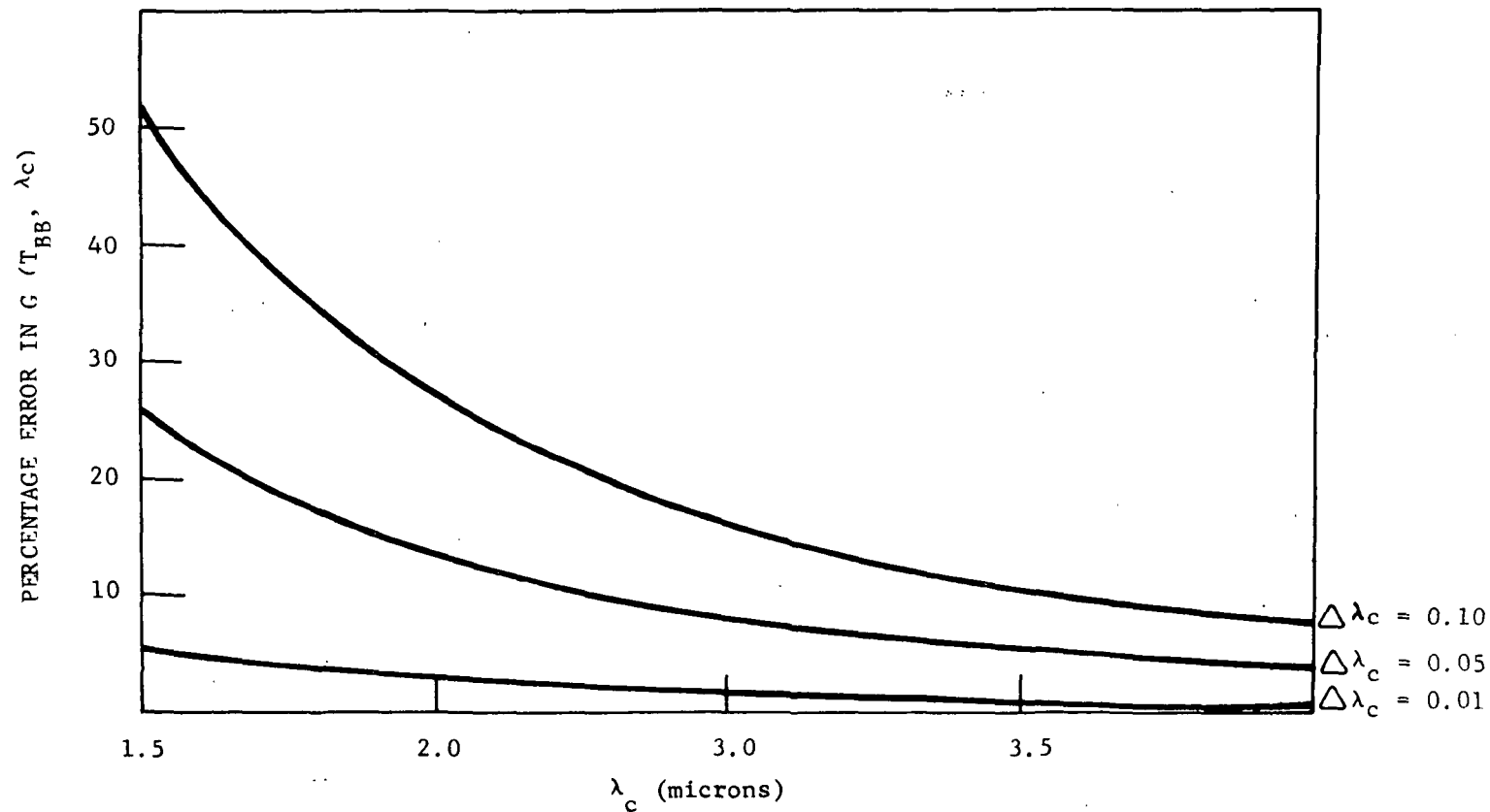


Figure 2.27 PERCENTAGE ERROR IN  $G(T, \gamma)$  AS A FUNCTION OF  $\gamma_c$  FOR A GIVEN UNCERTAINTY IN  $\Delta \gamma_c$  IN  $\gamma_c$  WITH BLACKBODY AT 1000 °K (ASSUMES AN ABRUPT CUTOFF)

ment error uncertainty. As expected, the calculated error increases as the wavelength gets shorter.

### 2.3.2.1 Conclusions

The questions concerning the accuracy of 1000 °K blackbody measurements on near IR detectors have been answered quantitatively. The results indicate that acceptable detectivity measurements are feasible in the near IR spectral regions applicable to this contract, since the temperature and the cutoff wavelength tolerances ( $\Delta T$ ,  $\Delta \lambda_c$ ) for a 20% accuracy are within our ability to meet. Presently we maintain our blackbody temperatures to within 5 °K of 1000 °K. The cutoff wavelength determination is accurate to within several hundredths of a micrometer and this inaccuracy is probably overridden by the fact that the actual detector spectral responsivities are non-ideal.

In the course of actual testing with a blackbody, three factors were quite important and different from 8 - 14  $\mu\text{m}$  testing. First, the detector has to be shielded from all visible light because it is very sensitive to the visible light as well as the near infrared. Secondly, the signal must be considered as a source of background radiation. This has two effects: the noise should be measured with the same background radiation as was presented for the signal measurement and the detectivity will vary with changing in blackbody radiation in the Blip limit since the background flux is changing. Thirdly, there are several important water absorption bands in the near infrared and thus the humidity in the test area must be controlled in order not to have part of the signal absorbed before reaching the detector.

### 2.3.3 Light Emitting Diode Measurement

A GaAs light emitting diode (LED) test station was used extensively to obtain pertinent data for this program. The station (shown in Figure 2.28) is similar to the more traditional blackbody test station except that the blackbody is replaced by a LED which is a Gallium Arsenide emitter having a spectral output at 0.9  $\mu\text{m}$ . The LED has the advantage of being compatible with direct electronic modulation of the optical output. The configuration shown in Figure 2.29 is a closed-loop, self-tracking frequency response system. The beat frequency oscillator inside the wave analyzer applies a sinusoidal modulation signal to the LED. The response of the detector to this signal is continuously tracked by the wave analyzer as the frequency is swept over the range of interest.

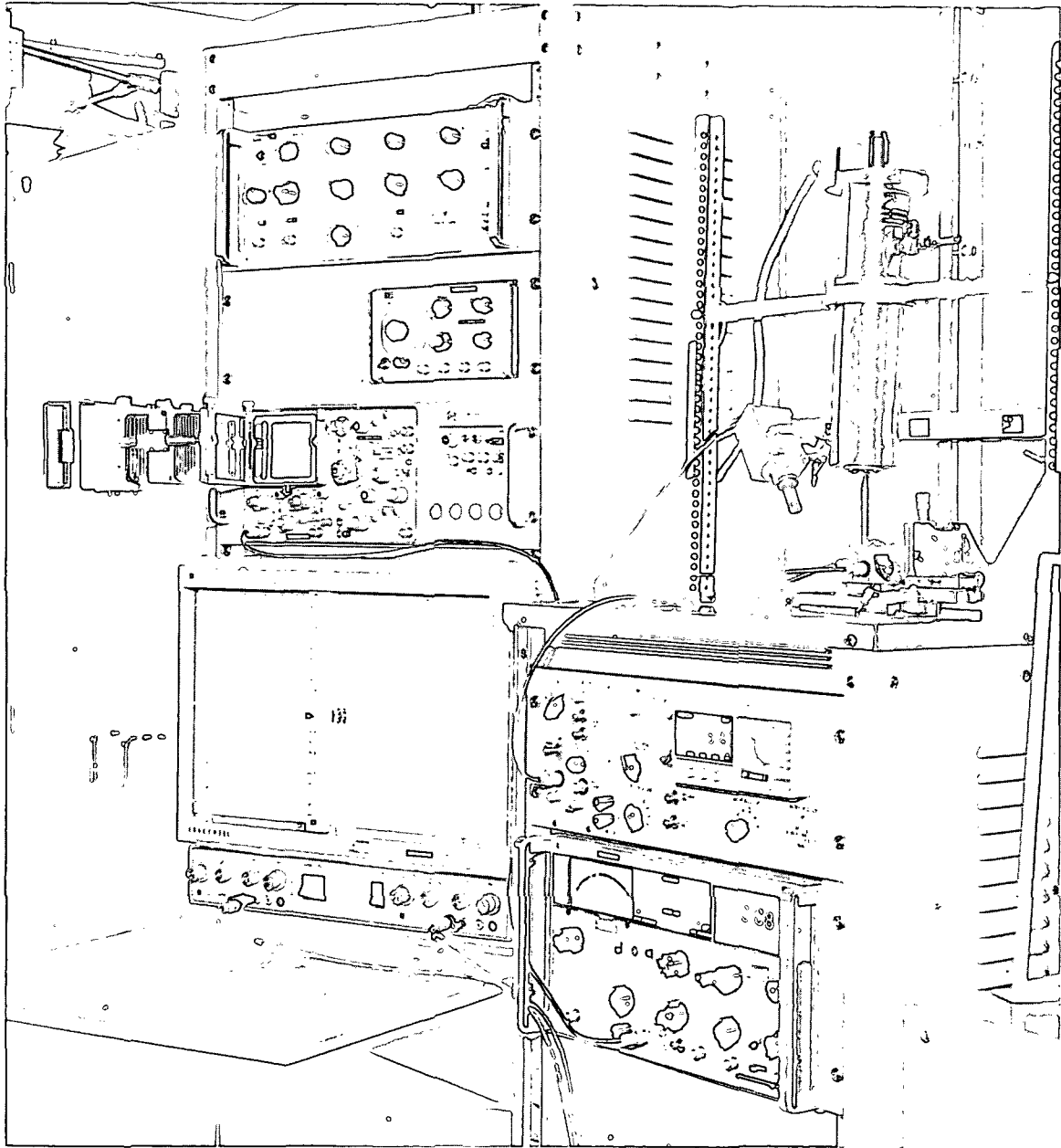
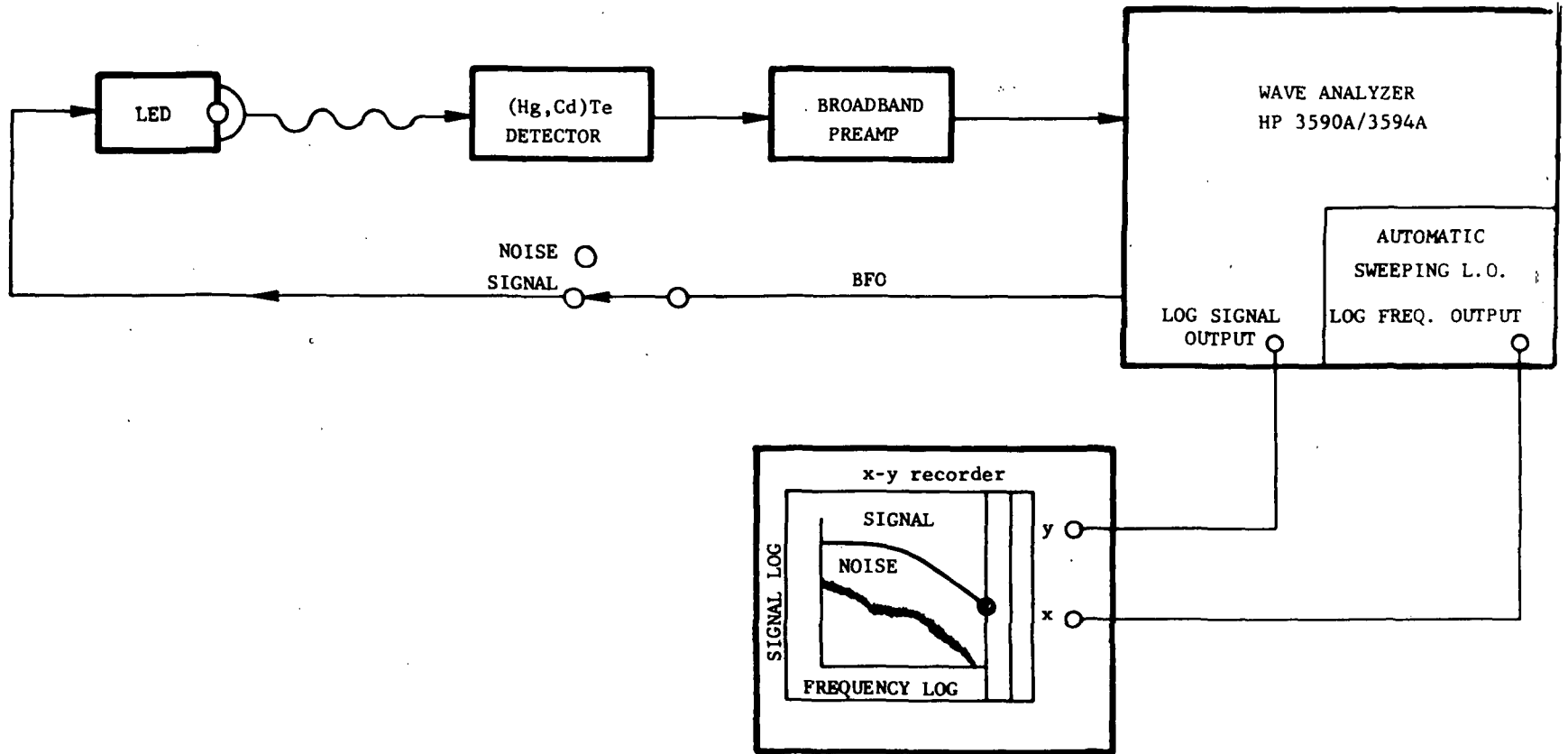


Figure 2.28 LIGHT-EMITTING DIODE TEST STATION



2-72

Figure 2.29 REAL TIME SIGNAL AND NOISE SPECTRUM PLOTTER

With the X-Y recorder bode plots of the frequency response can be obtained by using the log X and log Y outputs where log X is proportional to the log of the modulation frequency and log Y is proportional to the log of the corresponding signal. This system was also used to plot detector noise spectrum by turning off the modulation and sweeping over the frequency range.

The station has LEDs which may be used simultaneously. One provides the dc background photon flux while the other is used as an ac signal source. With  $Q_{sig}$  held constant in frequency and amplitude the dc value of  $Q_B$  is gradually increased by the ramp voltage applied to the background photon flux LED. A calibrated silicon photodiode was used to measure the intensity of radiation from the LED. In this manner, the responsivity and frequency were measured as a function of background radiation. This is shown in Figure 2.30.

In addition, this station was used for direct measurement of  $D^*_{\lambda}$ . A square wave from a signal generator was used to reduce the effective background from the signal. A signal flux of  $2.02 \times 10^{12}$  photons/cm<sup>2</sup>-s as measured by the calibrated silicon photodiode was used to obtain the signal to noise ratios as a function of electrical bias. This data could be directly converted to  $D^*$  at 0.9 micrometer.

$$D^*_{.9 \mu m} = \frac{R (A \Delta f)^{1/2}}{V_r}$$

where

$$R = V_s / P, \quad P = Q \frac{hc}{\lambda} A.$$

thus,

$$D^*_{.9 \mu m} = \frac{9}{1.98} \left( \frac{V_{sig}}{VN} \right) \left( \frac{\Delta f}{A'} \right)^{1/2} \left( \frac{10^{19}}{Q} \right)$$

Assuming, as in the case of ideal photoconductors, that the responsivity increases linearly with the wavelength up to the peak spectral responsivity and that the noise is independent of the wavelength, the following relation should hold

$$D^*_{.9 \mu m} = \frac{0.9}{\lambda} D^*_{\lambda}, \quad \text{if } \lambda < \lambda_p.$$

Thus, using the middle band point 1.65  $\mu m$  and 2.215  $\mu m$  for the band 1 and band 2 respectively, the required  $D^*_{.9}$  should be

2-74

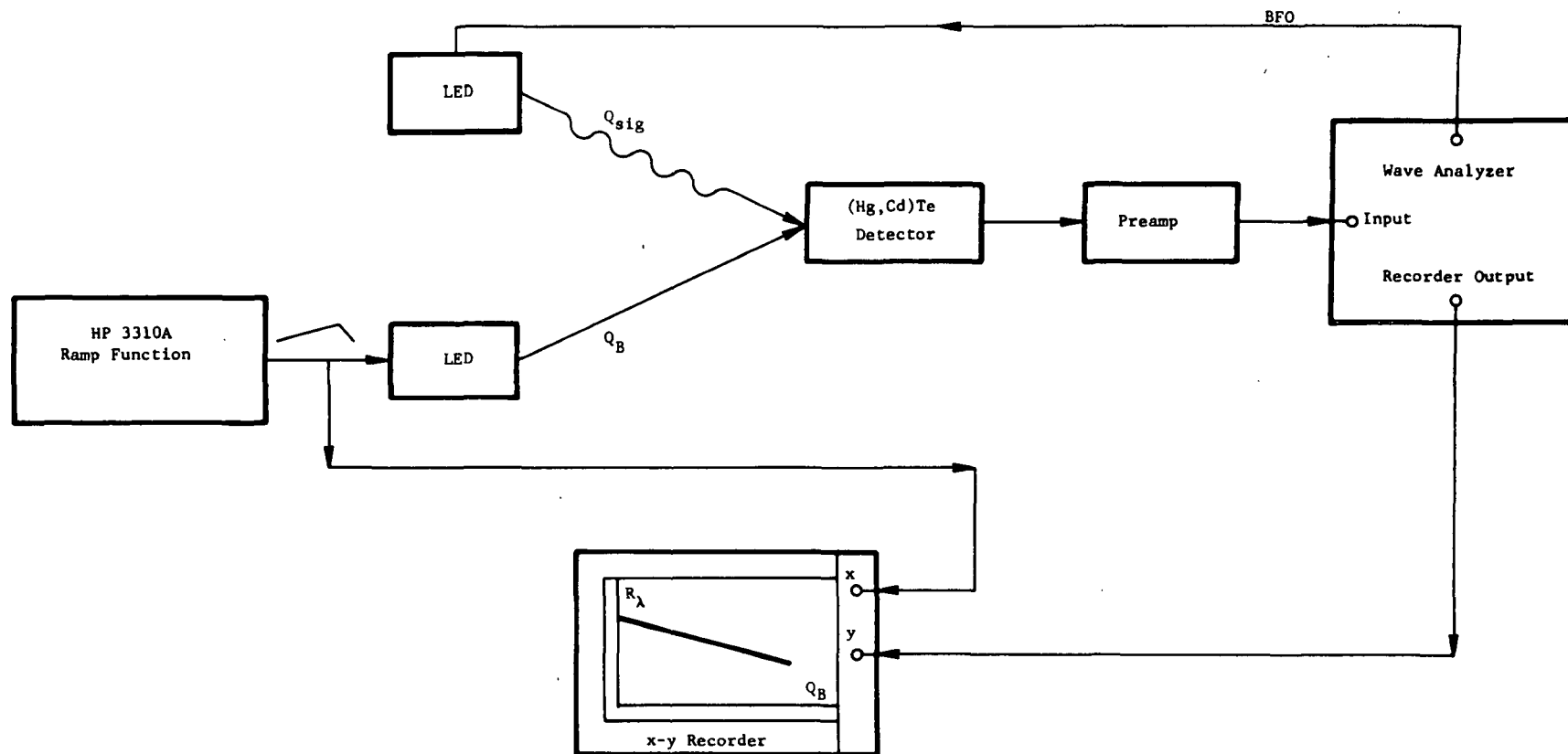


Figure 2.30 RESPONSIVITY VS BACKGROUND PHOTON FLUX EXPERIMENT  
( $V_{SIG}$  VS  $Q_B$ , WITH  $Q_{SIG}$  HELD CONSTANT)

## BAND 1

$$\begin{aligned}(D^*_{.9 \mu})_{\text{spec}} &= \frac{0.9}{1.65} (4 \times 10^{11} \text{ cm Hz}^{1/2}/\text{watt}) \\ &= 2.18 \times 10^{11} \text{ cm Hz}^{1/2}/\text{watt}\end{aligned}$$

## BAND 2

$$\begin{aligned}(D^*_{.9 \mu})_{\text{spec}} &= \frac{0.9}{2.215} (4 \times 10^{11} \text{ cm Hz}^{1/2}/\text{watt}) \\ &= 1.6 \times 10^{11} \text{ cm Hz}^{1/2}/\text{watt}\end{aligned}$$

### 2.3.4 Testing Schedule

In this program, we followed the testing schedule shown in Figure 2.31. The material from which sample detectors are fabricated is selected on the basis of two criteria: 1) the compositional parameter  $x$  is of the proper value to provide the required spectral characteristics; 2) the material is n-type. Samples fabricated from material meeting these requirements then undergo a preliminary detectivity at a operating temperature of 232 °K (Freon 22). The detectivity is measured using the calibrated signal from 0.9 micrometer LED and is compared to the design specifications for each band. The spectral detectivity measured at 0.9 micrometer is extrapolated back to median wavelength of each band (1.65 micrometers for Band 1 and 2.23 micrometers for Band 2) as outlined in Table 2.3. If the measured detectivity falls within a specified range of the design goal, then the spectral response is determined. From the spectral response the wavelength of peak response  $\lambda_p$  and the cutoff wavelength  $\lambda_c$  is found. If these wavelengths are compatible with either Band 1 or Band 2, the detectors become candidates for further testing. The next test entails measuring the detectivity as a function of temperature for temperatures bracketing 240 °K, the specified minimum operating temperature. The resulting data tells us two important things: 1) the  $D^*_{\lambda}$  at 240 °K; 2) the temperature at which the measured  $D^*_{\lambda}$  is equal to the  $D^*_{\lambda}$  specification for this program. Both pieces of information permit evaluation of the detector's performance relative to the design specification. The second piece of information provides the information that would be necessary for a detectivity versus temperature tradeoff.

FIGURE 1  
1-3μ PROGRAM  
TESTING AND DELIVERY PROGRAM

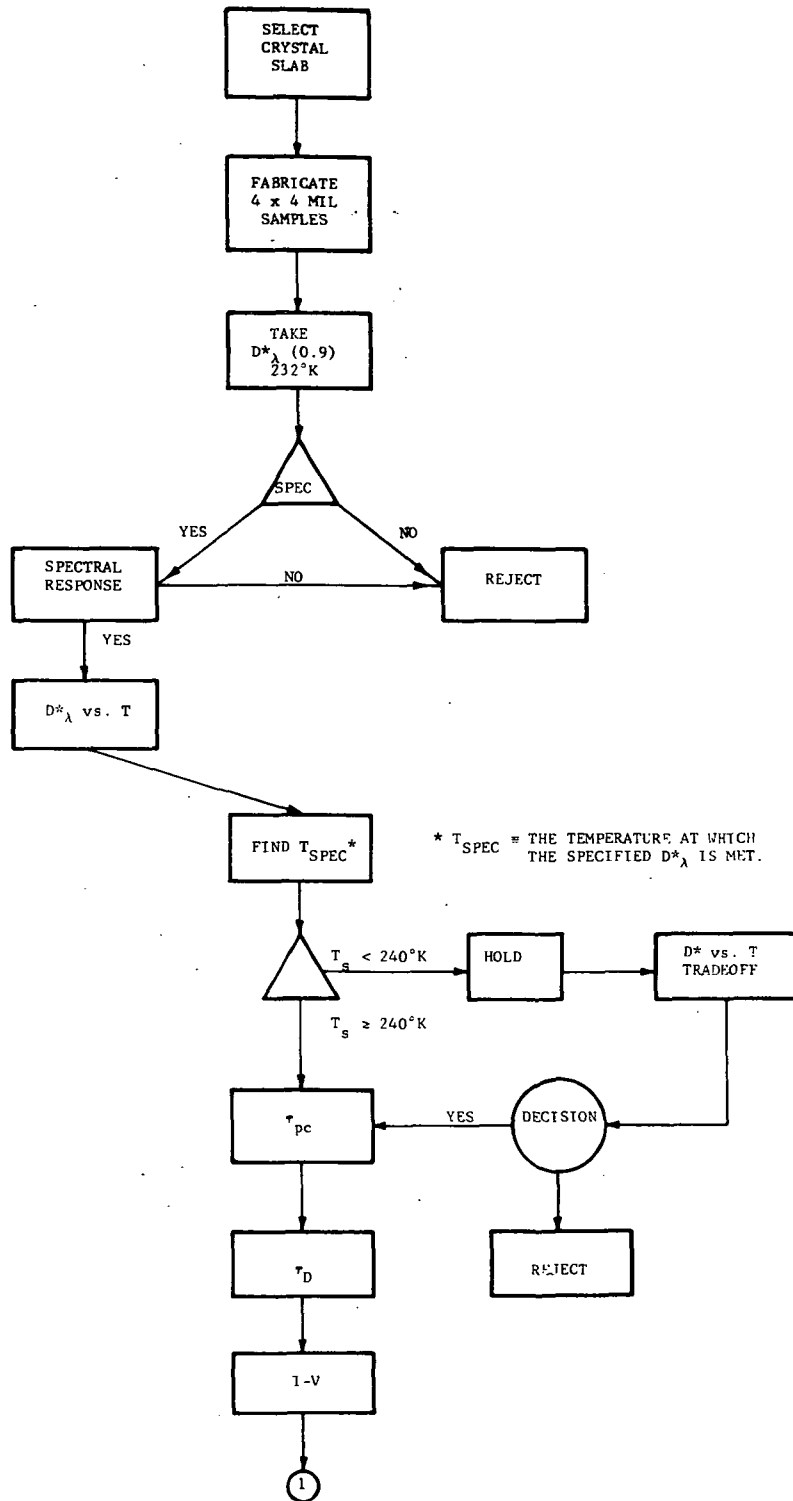


Figure 2.31 1 - 3μ PROGRAM TESTING AND DELIVERY PROGRAM

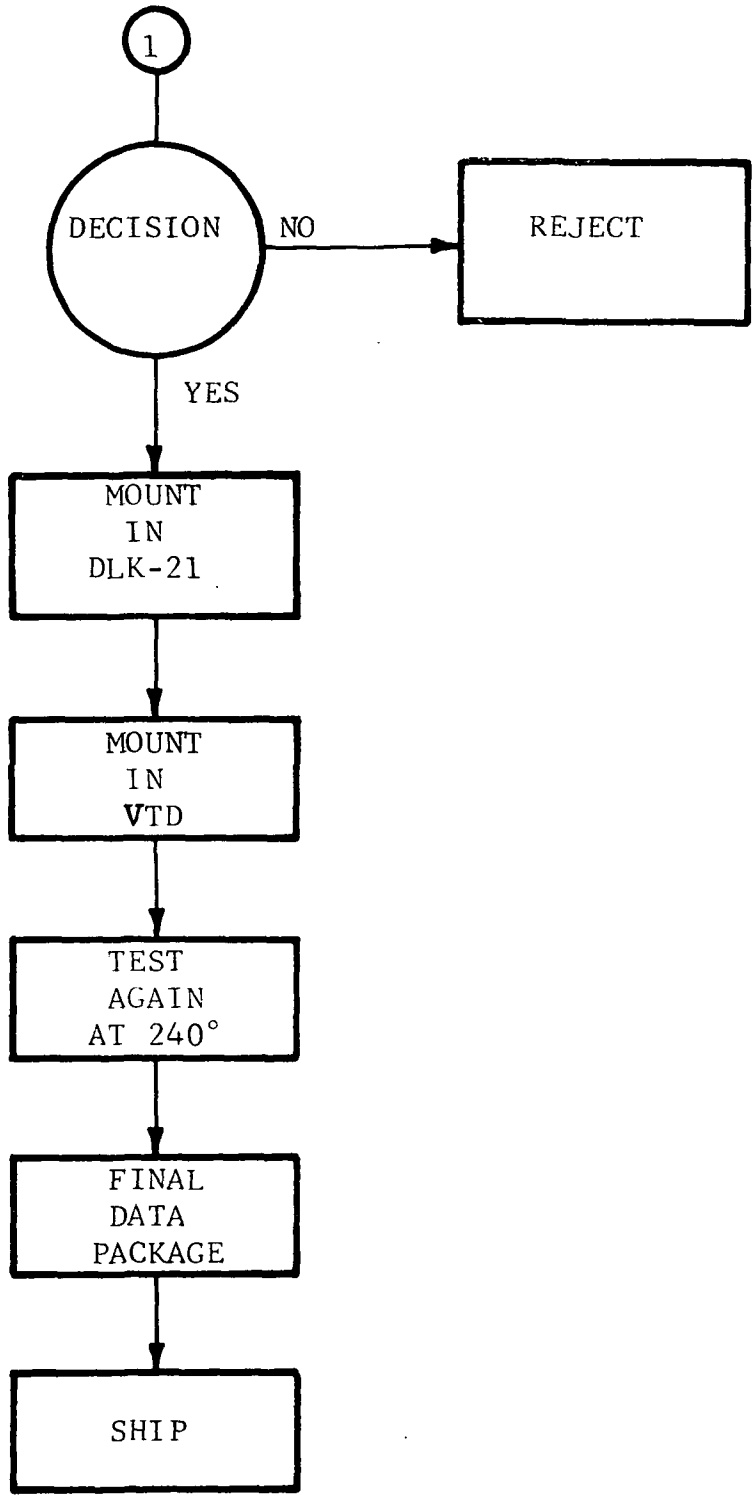


Figure 2.31 (CONTINUED)

Table 2.3

SPECTRAL DETECTIVITY MEASUREMENTS WITH THE 0.9  $\mu\text{m}$  GaAs LED.  
 EXTRAPOLATION FROM THE  $D^*_{\lambda}$  (0.9  $\mu\text{m}$ ) MEASURED TO THE SPECIFIED  
 DETECTIVITY  $D^*_{\lambda}$  FOR BAND 1 AND BAND 2.

BAND 1

$$D^*_{\lambda} (1.65 \mu\text{m})_{\text{spec}} = 4 \times 10^{11} \text{ cm-Hz}^{1/2}/\text{w}$$

$$D^*_{\lambda} (0.9 \mu\text{m})_{\text{spec}} = D^*_{\lambda} (1.65 \mu\text{m})_{\text{spec}} \times \frac{0.9 \mu\text{m}}{1.65 \mu\text{m}}$$

$$D^*_{\lambda} (0.9 \mu\text{m})_{\text{spec}} = 2.2 \times 10^{11} \text{ cm-Hz}^{1/2}/\text{w}$$

BAND 2

$$D^*_{\lambda} (2.23 \mu\text{m})_{\text{spec}} = 5 \times 10^{11} \text{ cm-Hz}^{1/2}/\text{w}$$

$$D^*_{\lambda} (0.9 \mu\text{m})_{\text{spec}} = D^*_{\lambda} (2.23 \mu\text{m})_{\text{spec}} \times \frac{0.9 \mu\text{m}}{2.23 \mu\text{m}}$$

$$D^*_{\lambda} (0.9 \mu\text{m})_{\text{spec}} = 2.0 \times 10^{11} \text{ cm-Hz}^{1/2}/\text{w}$$

The next steps in the testing process are performed on those detectors which have passed the critical spectral and temperature requirements. These tests include measurements of the photoconductive response time,  $\tau_{pc}$ , the detective time constant  $\tau_D$ , and the resistance from the  $I-V$  characteristic. Detectors which perform satisfactorily in these tests are then mounted in the modified DLK-21 vehicles for final testing and eventual delivery.

## 2.4 DETECTOR CHARACTERISTICS

### 2.4.1 Temperature and Background Dependence of Response Time

The dependence of response time of a near IR (Hg,Cd)Te photodetectors on the background and temperature are shown in Figures 2.32, 2.33, 2.34, and 2.35. The time constant exhibits the expected temperature dependence for a trapping detector as predicted by the small signal trapping photoconductivity discussed in Section 2.2.

### 2.4.2 The Temperature and Background Dependence of Responsivity

During the process of this program, we found that the temperature of the detector and the incident background photon flux are the two fundamental conditions which govern the behavior of (Hg,Cd)Te detectors operating in the trapping mode.

Experimental data which shows the dependence of responsivity on the background and temperature is shown in Figures 2.36 and 2.37. The temperature range investigated is from 83 °K to 295 °K while the background is varied from  $3 \times 10^{13}$  photons/cm<sup>2</sup>-s to  $2 \times 10^{15}$  photons/cm<sup>2</sup>-s. The responsivity behavior can be divided into three temperature region of operation illustrated in Figure 2.38.

#### Region 1: Low Temperature Region

A low temperature region which is characterized by a strong background dependence and a gradual temperature dependence. In this region, the responsivity varies as  $Q_B^{-\gamma}$  where  $\gamma$  is generally between 1/2 and 1. The responsivity gradually increases with decreasing temperature. At low background conditions a gain enhancement was observed due to minority carrier trapping which can be several orders of magnitude. In this experiment (at  $3 \times 10^{13}$  photons s<sup>-1</sup> cm<sup>-2</sup> and 80 °K) Detector 3-1 exhibited a gain enhancement of approximately 100.

#### Region 2: Intermediate Temperature Region

An intermediate temperature region exhibits a strong temperature dependence. For the lower backgrounds the temperature dependence is stronger and seems to approach an exponential dependence of the form  $\text{Exp}(-E_a/kT)$  where  $E_a$  is defined as the activation energy. In Region 2 the background dependence quickly diminishes with increasing temperature.

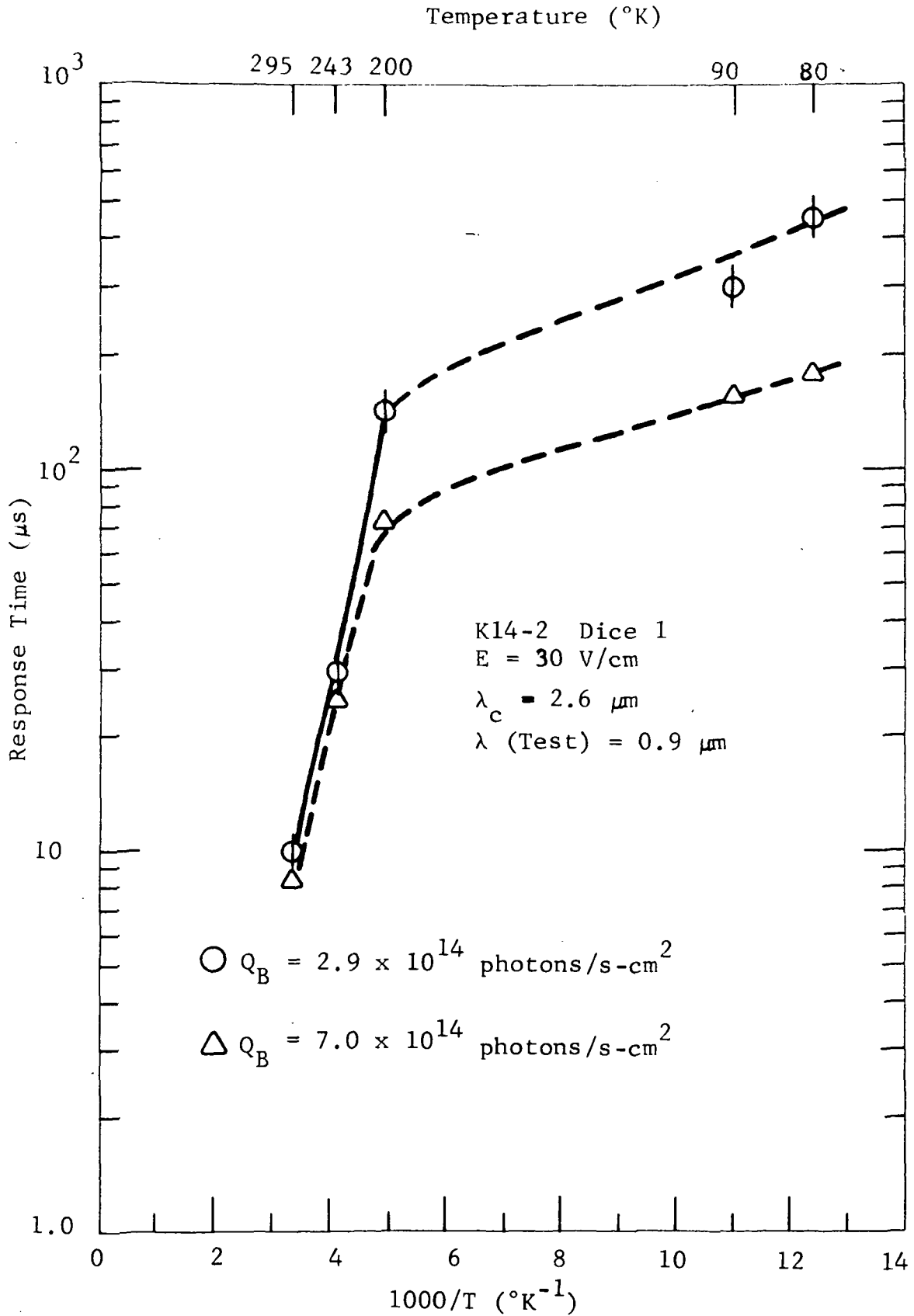


Figure 2.32 RESPONSE TIME VS TEMPERATURE

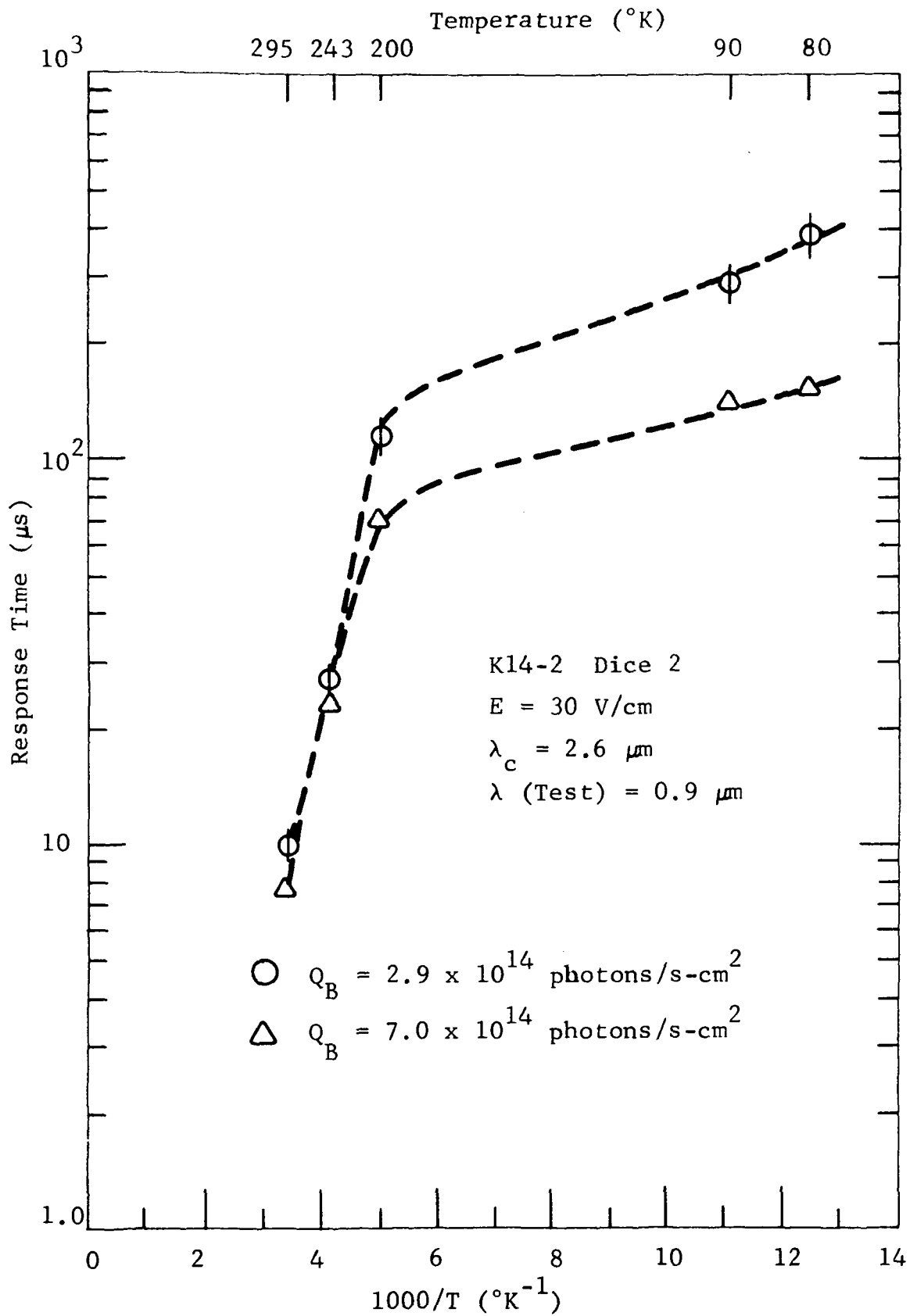


Figure 2.33 RESPONSE TIME VS TEMPERATURE



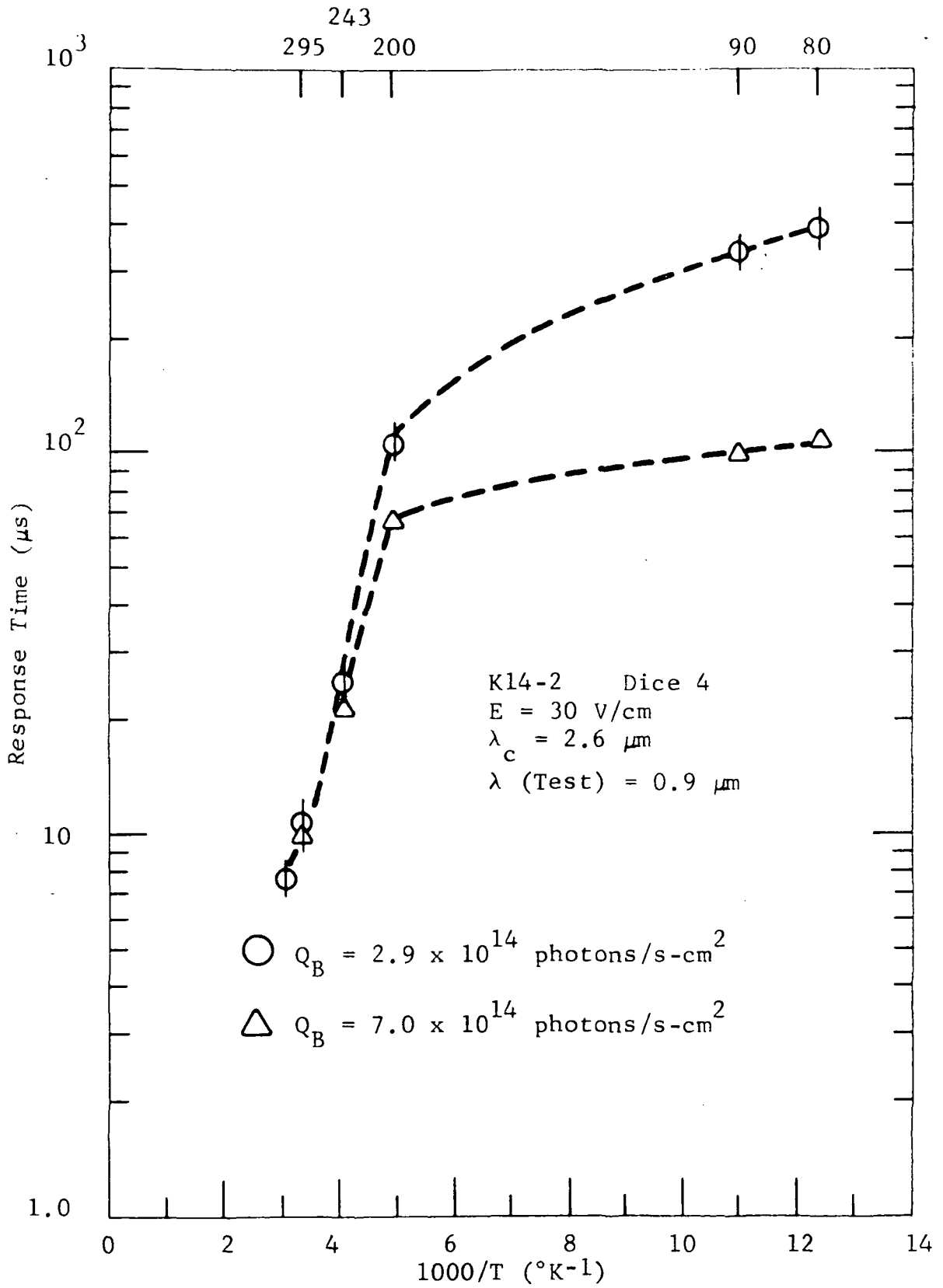


Figure 2.35 RESPONSE TIME VS TEMPERATURE

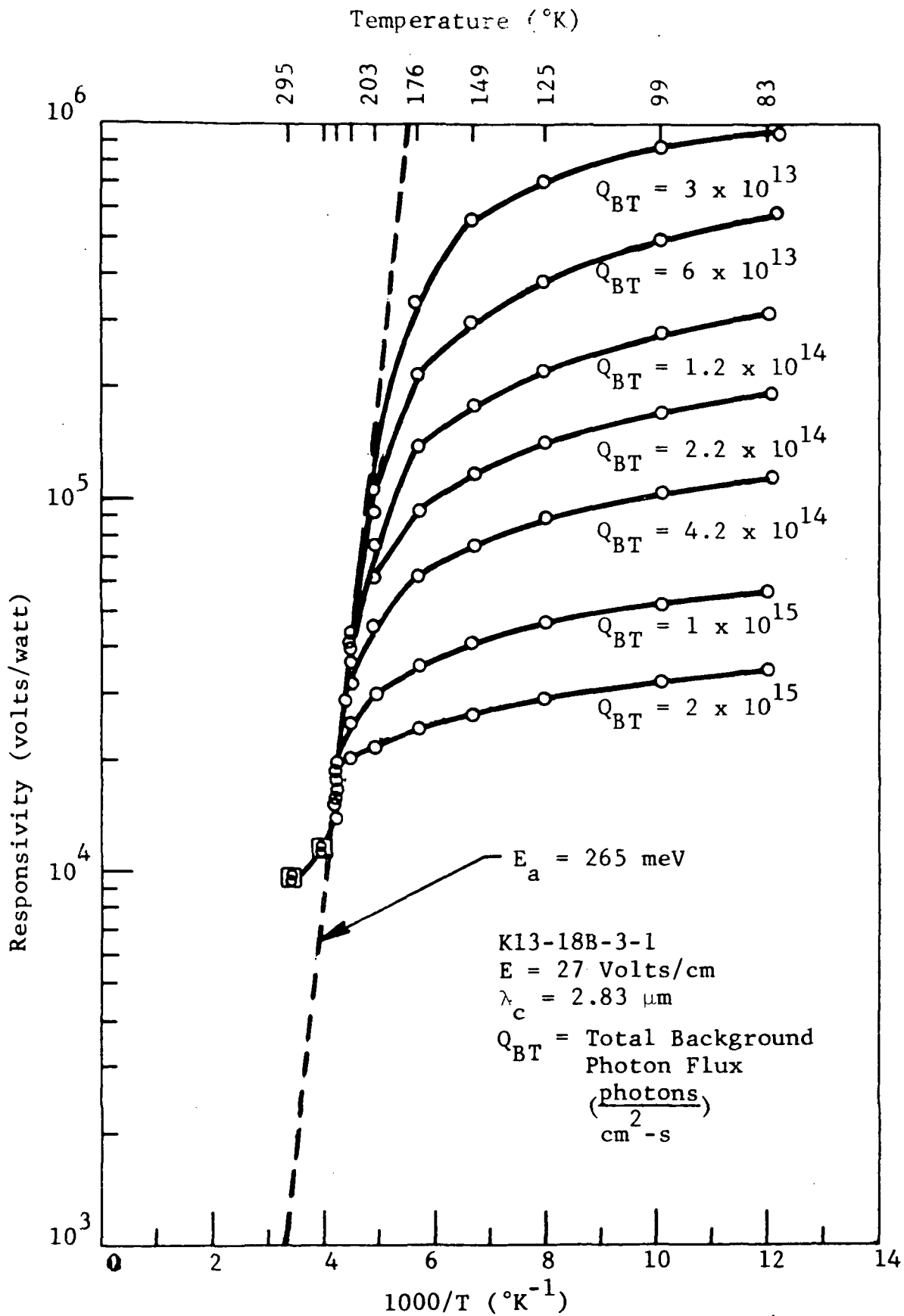


Figure 2.36 SMALL SIGNAL RESPONSIVITY VERSUS 1000/T AT DIFFERENT BACKGROUND LEVELS  $Q_{BT}$ . TEST FREQUENCY: 1000 Hz.

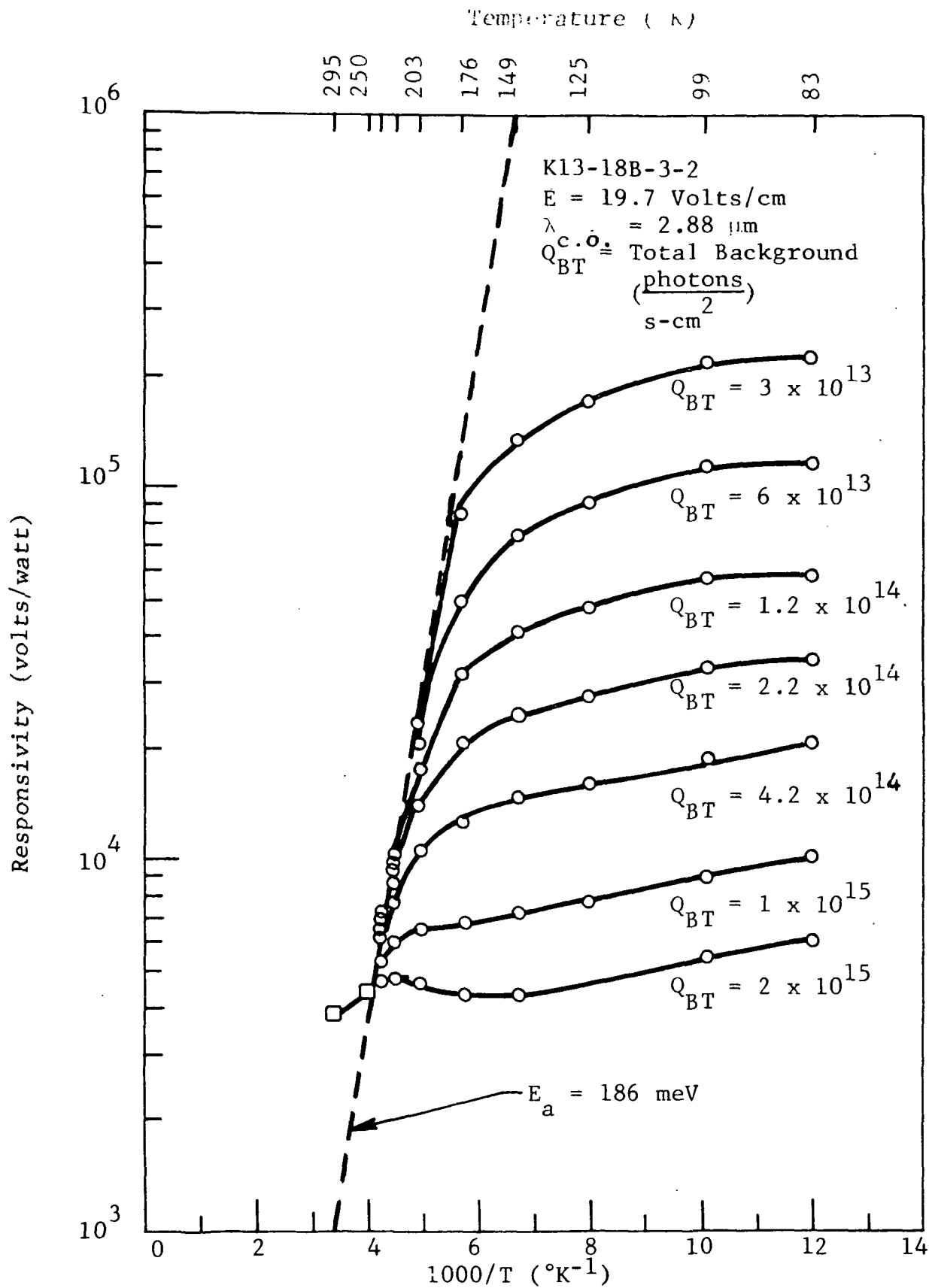
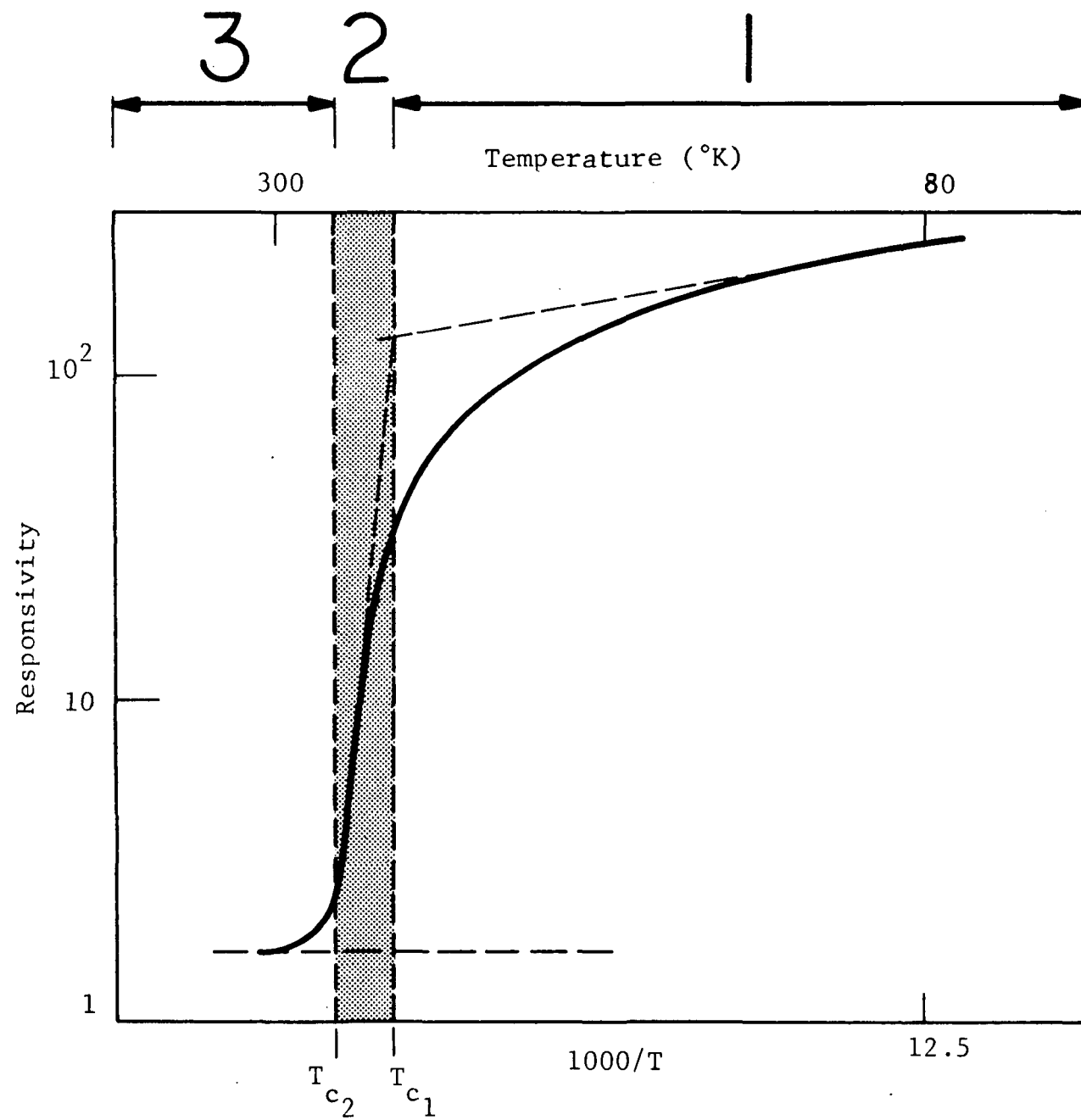


Figure 2.37 SMALL SIGNAL RESPONSIVITY VERSUS 1000/T AT DIFFERENT BACKGROUND LEVELS  $Q_{BT}$ . TEST FREQUENCY: 1000 Hz



REGIONS OF OPERATION FOR A NEAR IR (Hg,Cd)Te DETECTOR EXHIBITING MINORITY CARRIER TRAPPING. 1) STRONG BACKGROUND DEPENDENCE; 2) STRONG TEMPERATURE DEPENDENCE; 3) BACKGROUND INDEPENDENT, DISAPPEARANCE OF MINORITY CARRIER TRAPPING.  $T_{c1}$  AND  $T_{c2}$  ARE TEMPERATURES WHICH DEFINE THESE REGIONS.

### Region 3: High Temperature Region

This region is background independent. The background dependence, if any, was unobservable within experimental error. Furthermore, the strong temperature dependence observed in Region 2 quickly transforms into a gradual function which appears to be approaching a constant value as the temperature is increased. In Region 3 it is believed that minority carrier trapping is replaced by Shockley-Read recombination.

A comparison between Figure 2.37 and 2.38 indicates that Detector 3-2 (Figure 2.38) has a smaller density of effective trapping centers than Detector 3-1 (Figure 2.37). This conclusion is based two observations:

1. A background of  $2 \times 10^{15}$  photons-s<sup>-1</sup>-cm<sup>-2</sup> nearly saturates the traps in Detector 3-2 as indicated by smaller relative change in responsivity in going from Region 1 to Region 3.
2. The gain enhancement of Detector 3-1 is larger than that of Detector 3-2. By a comparison of the responsivity ratios at 83 °K and 300 °K, Detector 3-2 had a gain enhancement of 60, while Detector 3-1 showed an enhancement factor of 100 at a background of  $3 \times 10^{13}$  photons-s<sup>-1</sup>-cm<sup>-2</sup>.

In particular, the effect of the background radiation flux on the detector was studied by changing this flux over the  $8 \times 10^{12}$  to  $4 \times 10^{14}$  photons/s/cm<sup>2</sup>. Figure 2.39 shows the frequency response of a small ( $4 \times 10^{12}$  photons/cm<sup>2</sup> s) signal with the background flux varied. Curves such as those in Figure 2.39 show improved responsivity at the expense of bandwidth, the kind of performance change required to produce sensitive lower background detectors.

#### 2.4.3 Comparison of the Trapping Model and Experimental Data

The exponential density of traps model which was developed during the course of this program is compared here with the experimental data. Detector K13-18B-3-1 has been tested under three different backgrounds.  $Q_B$  varies from  $3.0 \times 10^{13}$  to  $1.0 \times 10^{15}$ . The trapping gain enhancement factor was fitted to the exponential trapping model. Figure 2.40, shows the agreement between the calculated and experimental data. Similar analysis has been applied to Detector K13-18B-3-2, the result is plotted in Figure 2.41.

2-88

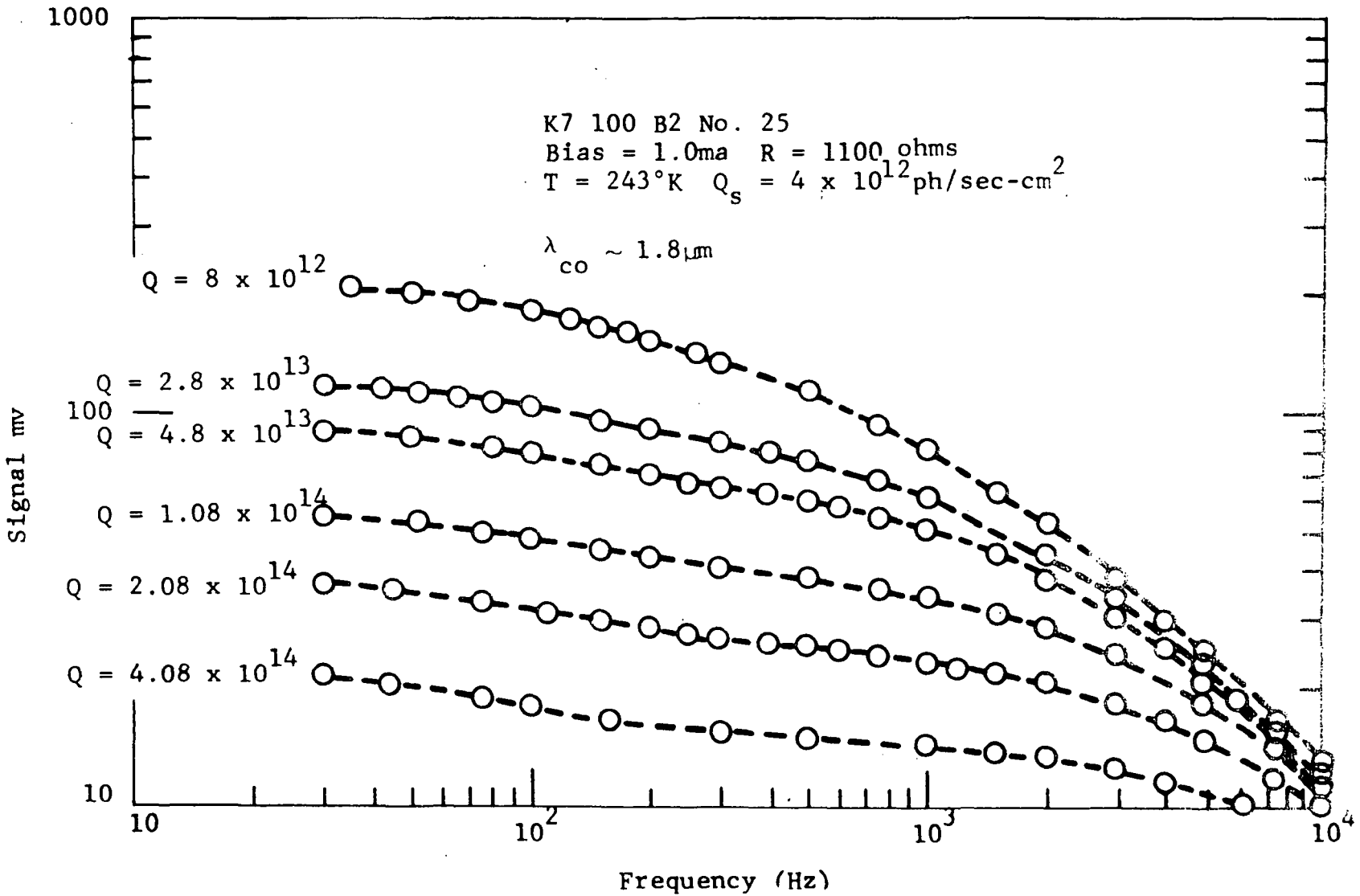


Figure 2.39 FREQUENCY RESPONSE OF A 1.8  $\mu\text{m}$  DETECTOR VERSUS  $Q_B$  AT 243 °K

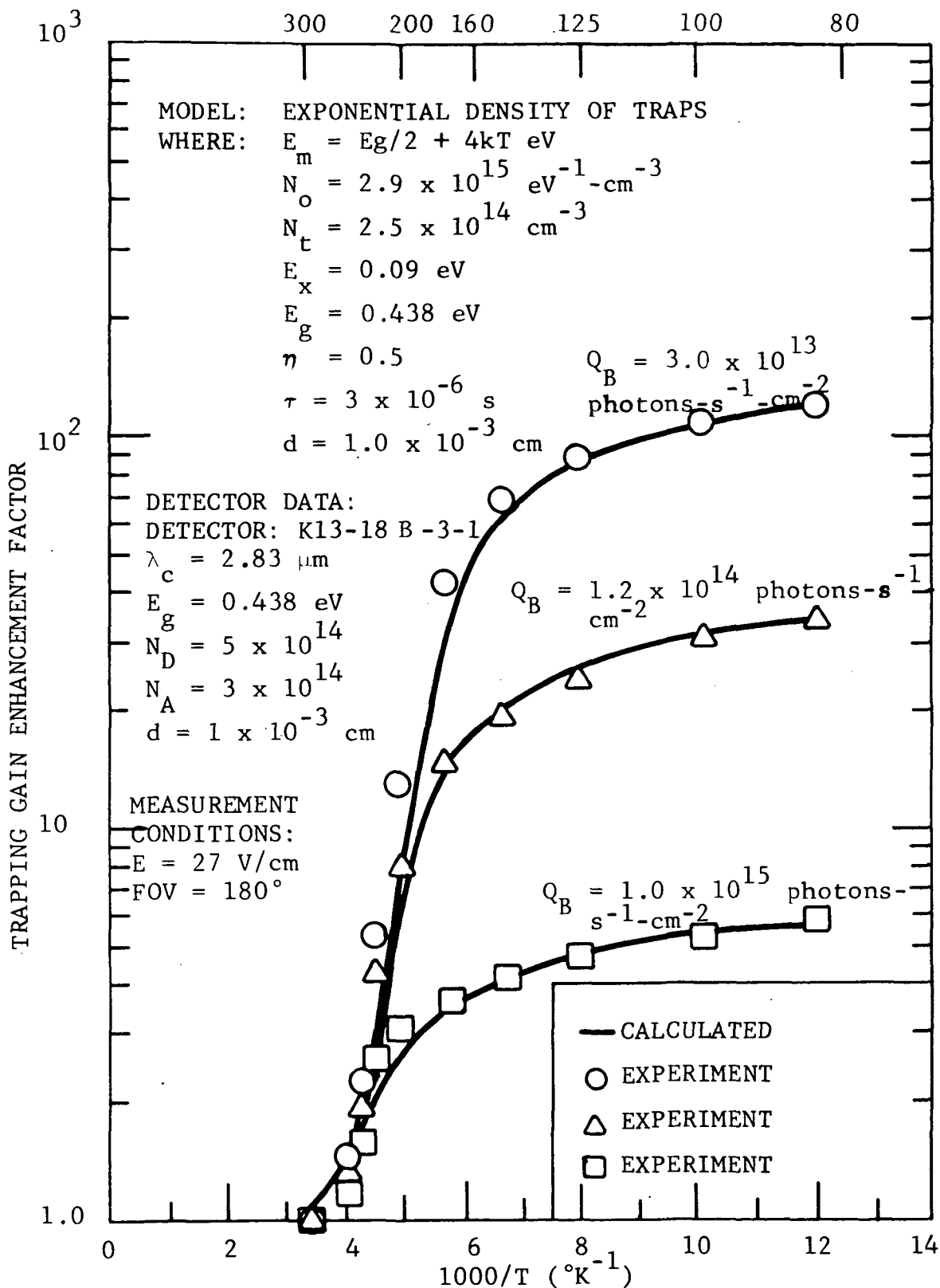


Figure 2.40 CALCULATED AND EXPERIMENTAL DEPENDENCE OF THE TRAPPING GAIN ON TEMPERATURE AND BACKGROUND

2-90

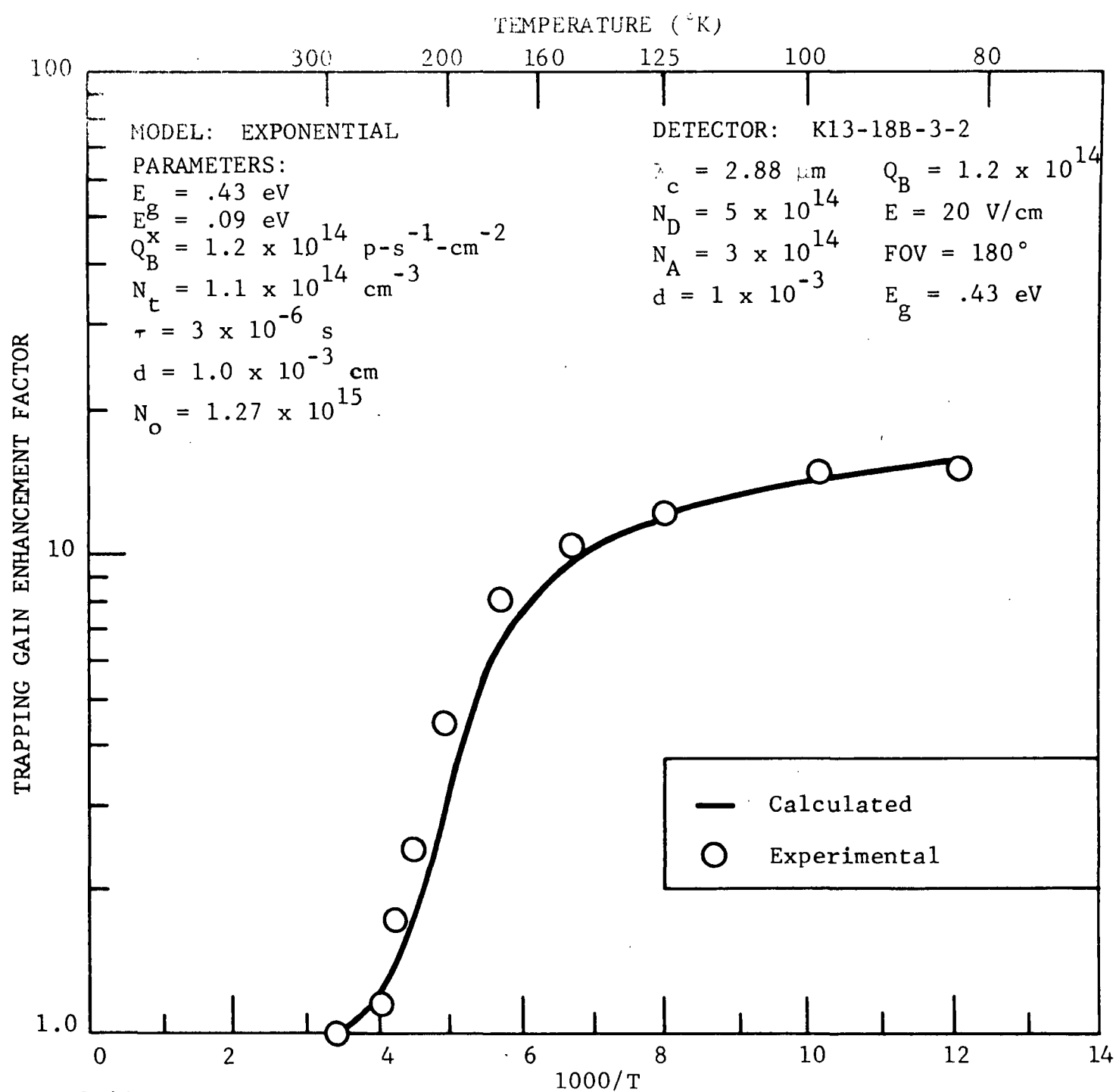


Figure 2.41 CALCULATED AND EXPERIMENTAL DEPENDENCE OF THE TRAPPING GAIN ON TEMPERATURE

#### 2.4.4 Final Detectors

Test reports on the four final detectors shipped to NASA are included in Appendix A. In Figure 2.42, the  $D^*_\lambda$  of the four detectors, W1, W2, W3 and W4, are plotted vs  $1000/T^\lambda$ . We obtained the following conclusions.

In the elevated temperature region, 200 °K and higher, the  $D^*_\lambda$  are strongly temperature dependent. A slight decrease in temperature would drastically increase the value of  $D^*_\lambda$ .

In the temperature region which we are interested, 240 °K and higher, the  $D^*_\lambda$  of W1 and W2 in band I, are much higher than that of W3 and W4 in band II. (almost difference by a factor of 9). This is due to the difference in cutoff wavelength of the two bands. The  $\lambda_{co}$  of band I is 1.75  $\mu\text{m}$  and  $\lambda_{co}$  of band II is 2.35  $\mu\text{m}$ . From the analysis which we presented in Section 2.2 of the Technical Discussion of this report, in the wavelength region 1.55 - 2.35  $\mu\text{m}$  the  $D^*_\lambda$  would increase sharply with shorter cutoff wavelength.

With minority carrier trapping very high photoconductive gains were realized without the previously expected sweep-out of carriers.

Figure 2.43 shows the responsivity of the four final devices plotted versus  $1000K$ . It should be noted that W4 has both a low responsivity and a very short response time (6 microseconds). Since responsivity is a function of response time this result is expected.

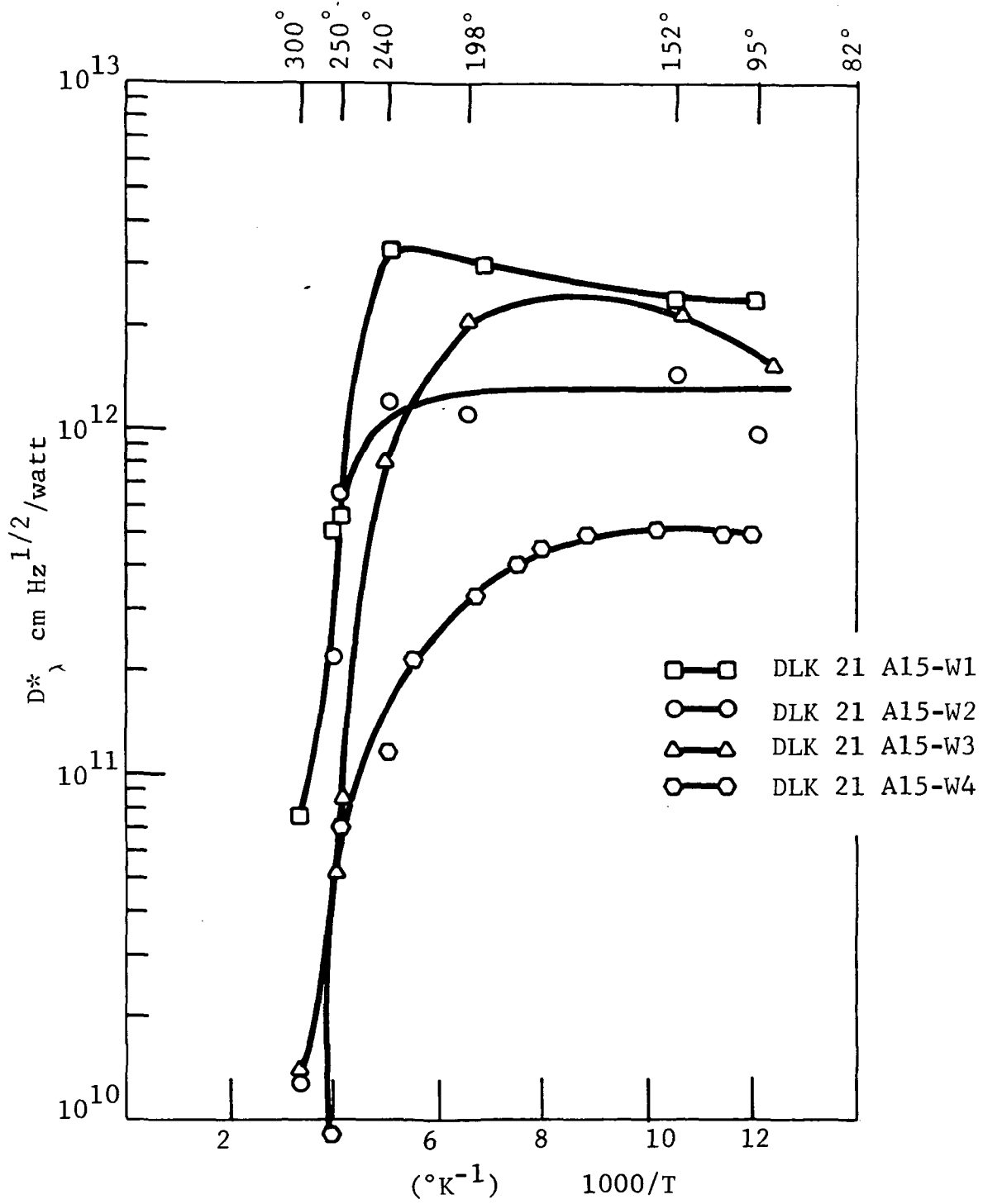


Figure 2.42

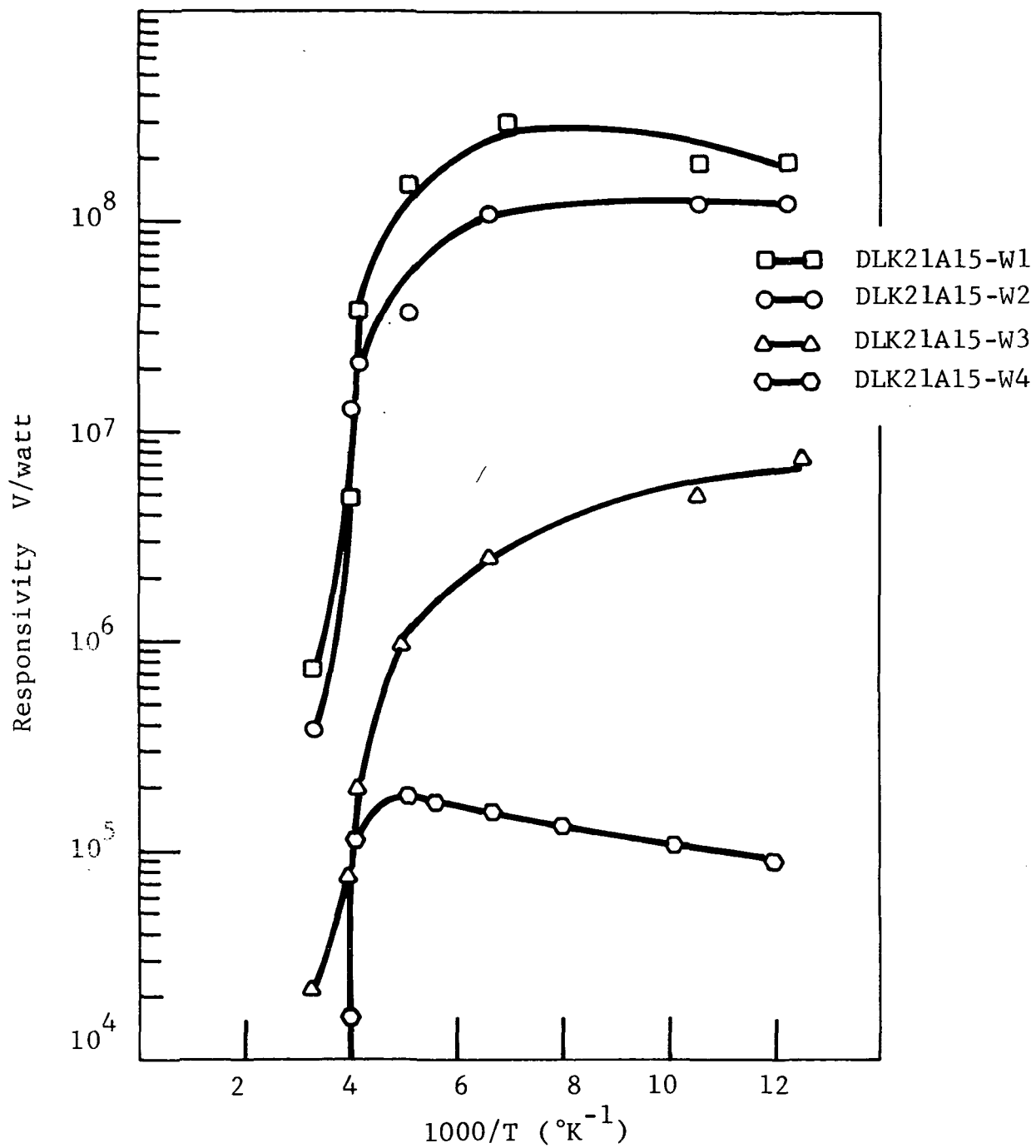


Figure 2.43

SECTION 3  
NEW TECHNOLOGY

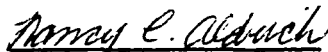
No new technology has been developed on this contract.

APPENDIX A  
TEST REPORTS

TEST REPORT 23971-1  
FOR  
DLK21A15-W1 INFRARED DETECTOR  
FOR  
NASA/GODDARD

CONTRACT NO.  
NAS 5-21646

  
PRODUCT ASSURANCE  
ENGINEER

  
PROJECT ENGINEER

  
PROGRAM MANAGER

Honeywell Inc.  
Radiation Center  
2 Forbes Road  
Lexington, Massachusetts 02173

ELEVATED OPERATING TEMPERATURE NEAR INFRARED PHOTODETECTOR

TEST REPORT

Manufacturer  
 HONEYWELL RADIATION CENTER  
 2 Forbes Road  
 Lexington, Massachusetts 02173

Detector Number - DLK21A15-W1

Date of Measurements - JAN, 1973

DETECTOR DESCRIPTION

Type	HgCdTe Photo-conductive
Dimensions	$9.14 \times 10^{-3}$ cm. X $9.14 \times 10^{-3}$ cm
Sensitive Area, A	$8.8 \times 10^{-6}$ cm <sup>2</sup>
Window Material	Sapphire
Field of View	72° 30' Degrees
Resistance	ohms @ 240°K 16,620
Optimum Bias Current	0.075 ma

CONDITIONS OF MEASUREMENT

Detector Temperature	240 °K
Chopping Frequency	1000 Hz
Noise Bandwidth $\Delta f$	6.2 Hz
Blackbody Temperature $T_{BB}$	1000 °K
Amplifier Gain	$10^3$ nominally
Distance - Source to Det. d	24. cm
Blackbody Aperture Shape & Size	Circular 0.0125 in Dia.
Spectral Wavelength Intervals	0.10 $\mu$ m

TEST RESULTS @ OPT. BIAS

Signal, S	164 mv
Noise, N	.95 ms
$D^*_{BB}$	$2.2 \times 10^{10}$ cm Hz <sup>1/2</sup> /watt
$R_{BB}$	$1.5 \times 10^6$ volts/watt
$P_n$ [NEP]	$4.26 \times 10^{-13}$ watts/Hz <sup>1/2</sup>
$\lambda_{peak}$	1.87 $\mu$ m
$D^*_{\lambda pk}$	$5.4 \times 10^{11}$ cm Hz <sup>1/2</sup> /watt
$R_{\lambda pk}$	$3.8 \times 10^7$ volts/watt
$\tau_{response}$	318 $\mu$ s
$\tau_{detective}$	3.1 $\mu$ s @ 0.06 ma

$T_c$  = chopper blade temp. = 300°K  
 $\epsilon_c$  = chopper blade emissivity  $\approx 1.0$   
 $\epsilon_{BB}$  = blackbody emissivity  $\approx 1.0$   
 $A_{BB}$  = area of blackbody aperture (cm<sup>2</sup>)

Radiant Signal Wave Shape and Amplitude

$$N(t) = \frac{\pi R^2}{2} I_0 \left\{ 1 - \frac{4R}{r} \sum_{K=1}^{\infty} \left( \frac{2r}{K\pi R} \right)^2 J_K \right.$$

$$\left. \cdot \left( \frac{K\pi R}{2r} \right) \sin \frac{K\pi}{2} \cos K\omega t \right\}$$

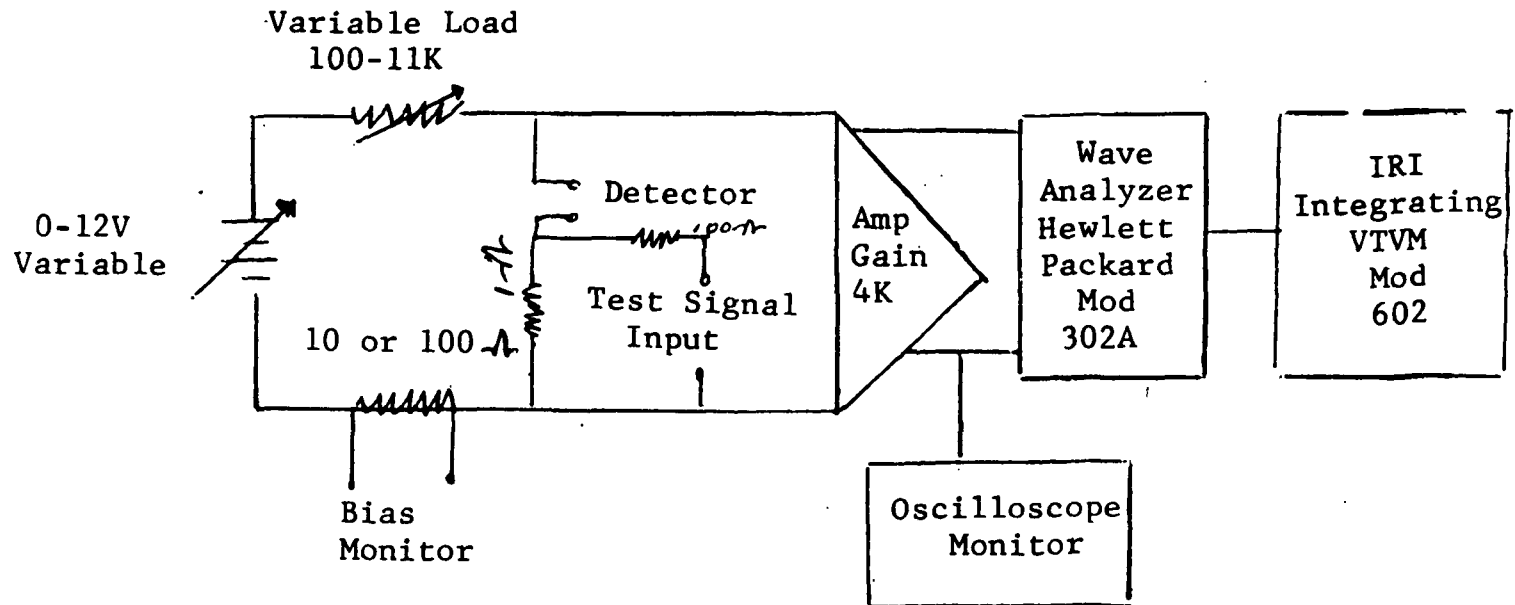
where:  $I_0$  = radiant emittance from source (watts-cm<sup>-2</sup>)  
 $2R$  = source aperture dia.  
 $2r$  = chopper tooth width (inches) = 0.1987  
 $J_1$  = 1st order Bessel function

ref: R.B. McQuistan, Journal of the Optical Society of America, 48, 1, 63, Jan. '58

$$D^*_{BB} = \frac{1.10 \times 10^{12} (\Delta f)^{1/2} d^2 S/N}{(\epsilon_{BB} T_{BB}^4 - \epsilon_c T_c^4) A_{BB}^{1/2}}$$

(see attached derivation)

## Detector Readout Circuitry



### 3.0 Graphs

$S, N$  vs Bias @ 1000 Hz, 240°K

$D_{\lambda}^*$  vs Bias @ 1000 Hz, 240°K

$D_{\lambda}^*$  vs T @ 1000 Hz

$r_d$  vs T

$D_{\lambda}^*$  vs f @ 240°K

$R_{\lambda}$  vs T @ 1000 Hz

$R_{\lambda}$  vs f @ 240°K

$V_n$  vs f @ 240°K

$D_{\lambda}^*$  vs  $\lambda$  @ 240°K

$D_{\lambda}^*$  vs  $\lambda$  @ 290°K

$R_{\lambda}$  vs  $\lambda$  @ 240°K

$R_{\lambda}$  vs  $\lambda$  @ 290°K

S,N  
1000.  
(mV)

S,N vs BIAS  
@ 1000 Hz  
240°K

DLR21A15-W1

100.

10.

1.

S/N  
V SIGNAL

V noise

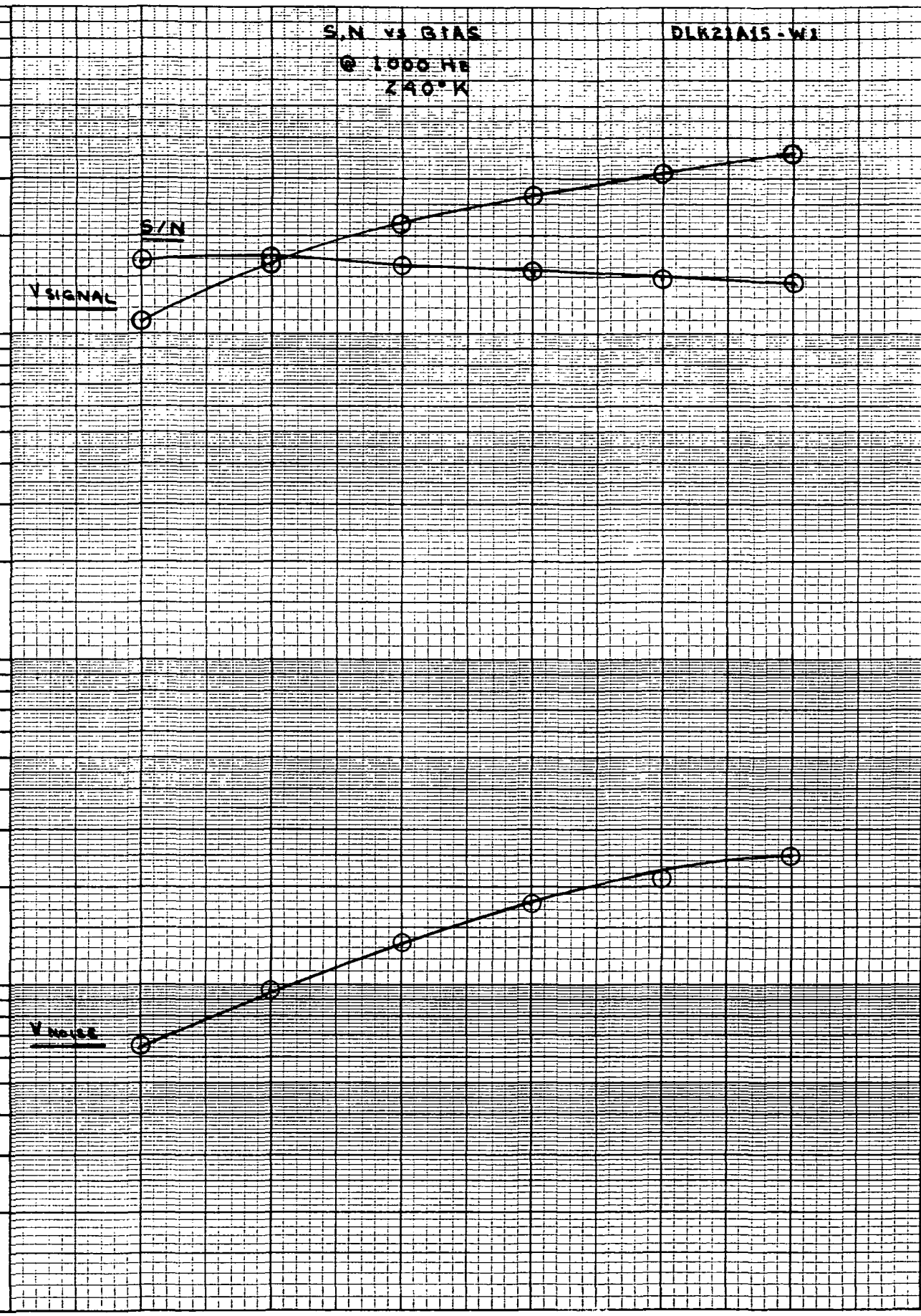
.05

.1

.15

.2

I BIAS (mA)



$D_{\lambda}^*$  vs BIAS

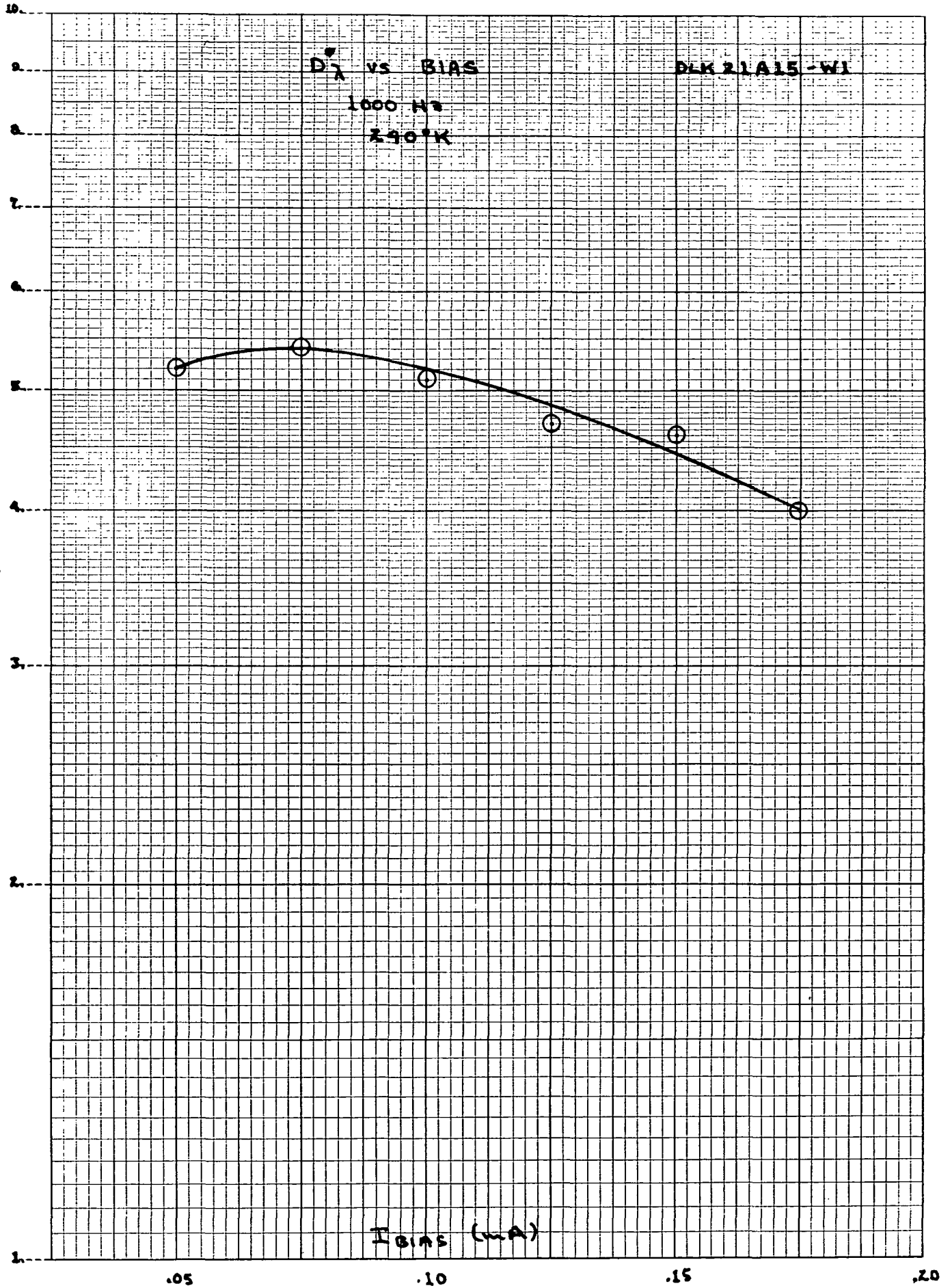
DLK 21A15-W1

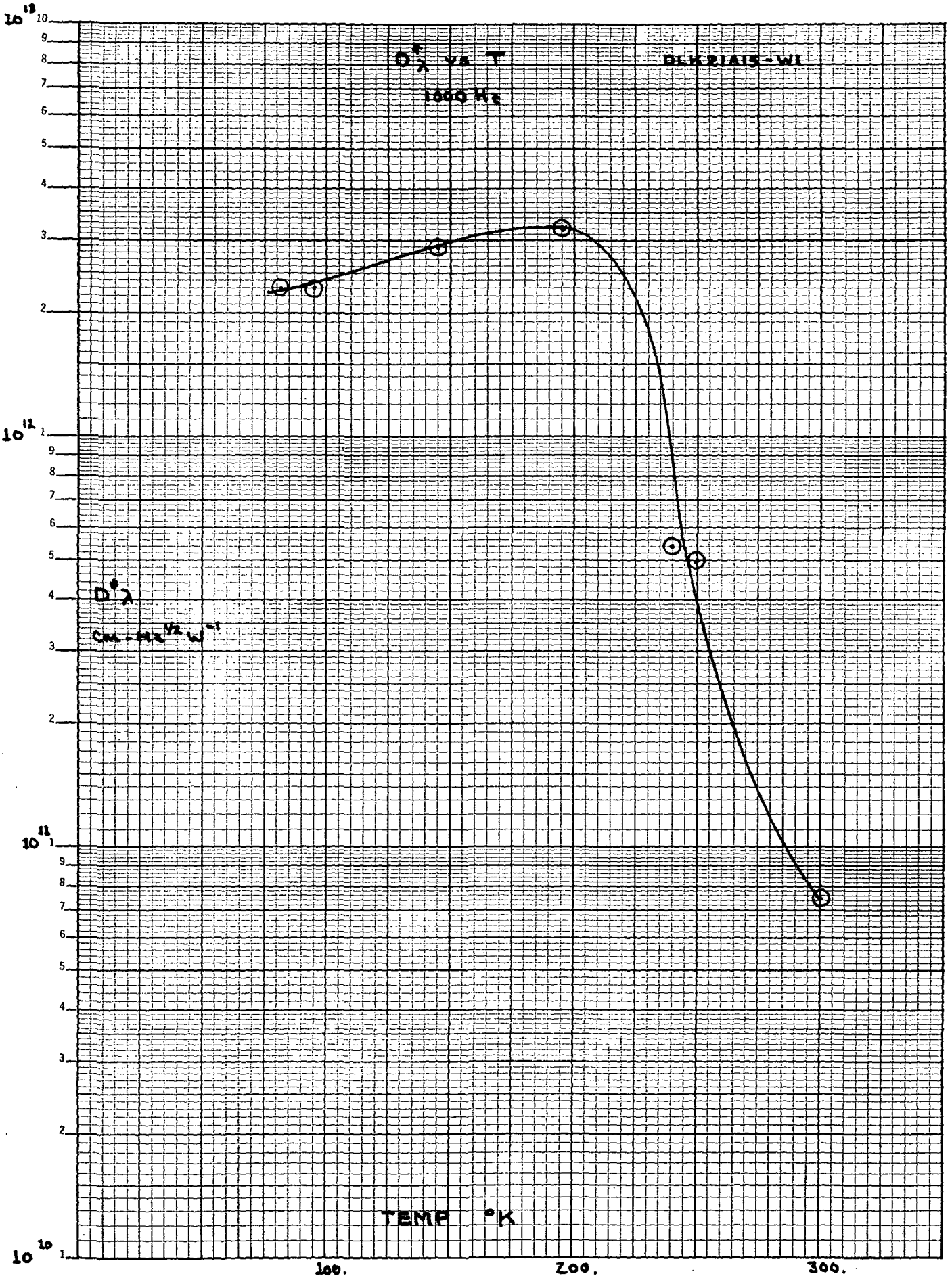
1000 Hz

290°K

$D_{\lambda}^* \times 10^{11} \text{ cm}^{-2} \text{ Hz}^{1/2} \text{ W}^{-1}$

$I_{\text{BIAS}} (\mu\text{A})$

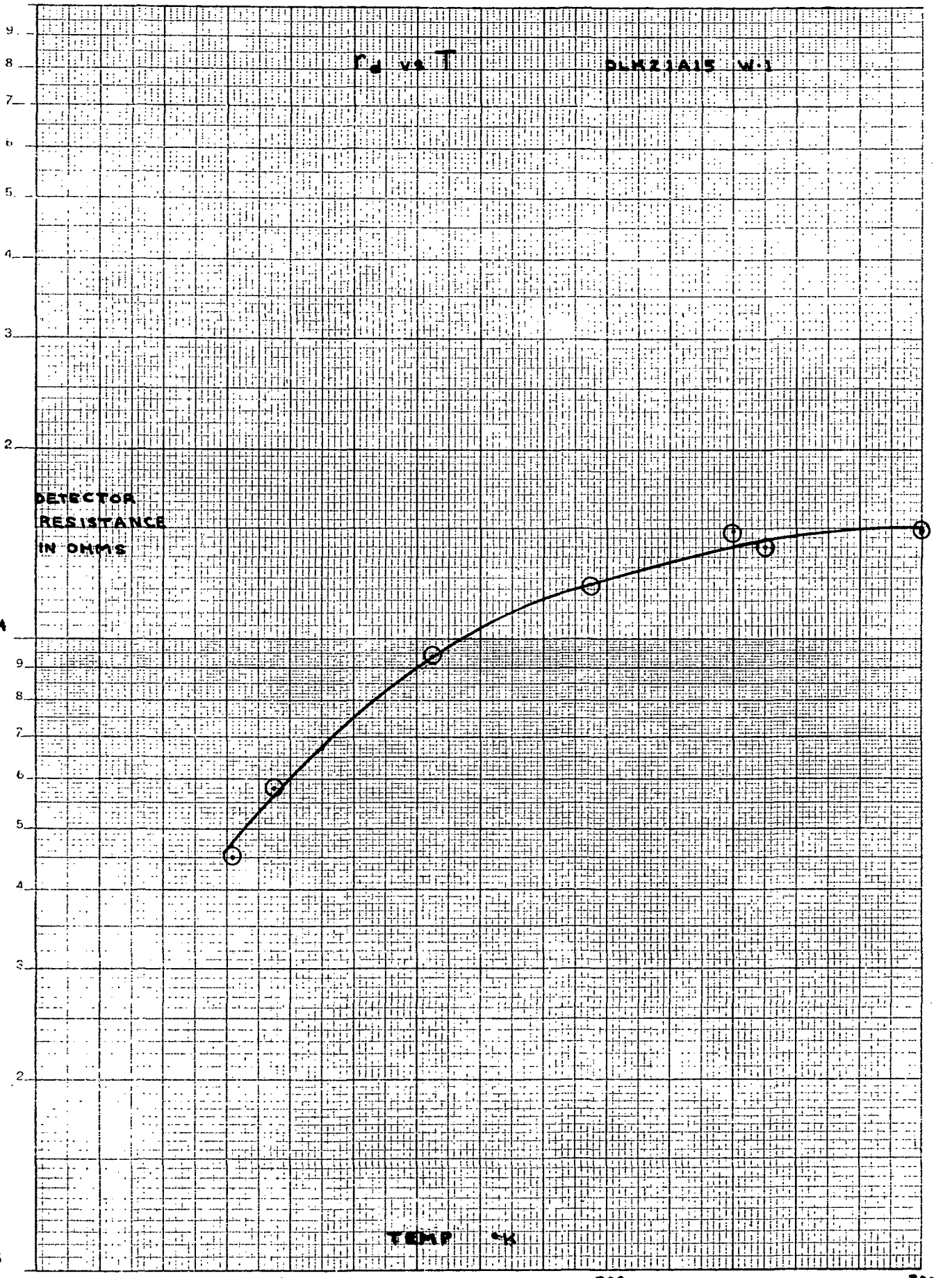




10<sup>5</sup>

10<sup>4</sup>

10<sup>3</sup>



$R_d$  vs  $T$

6BK21A15 W-1

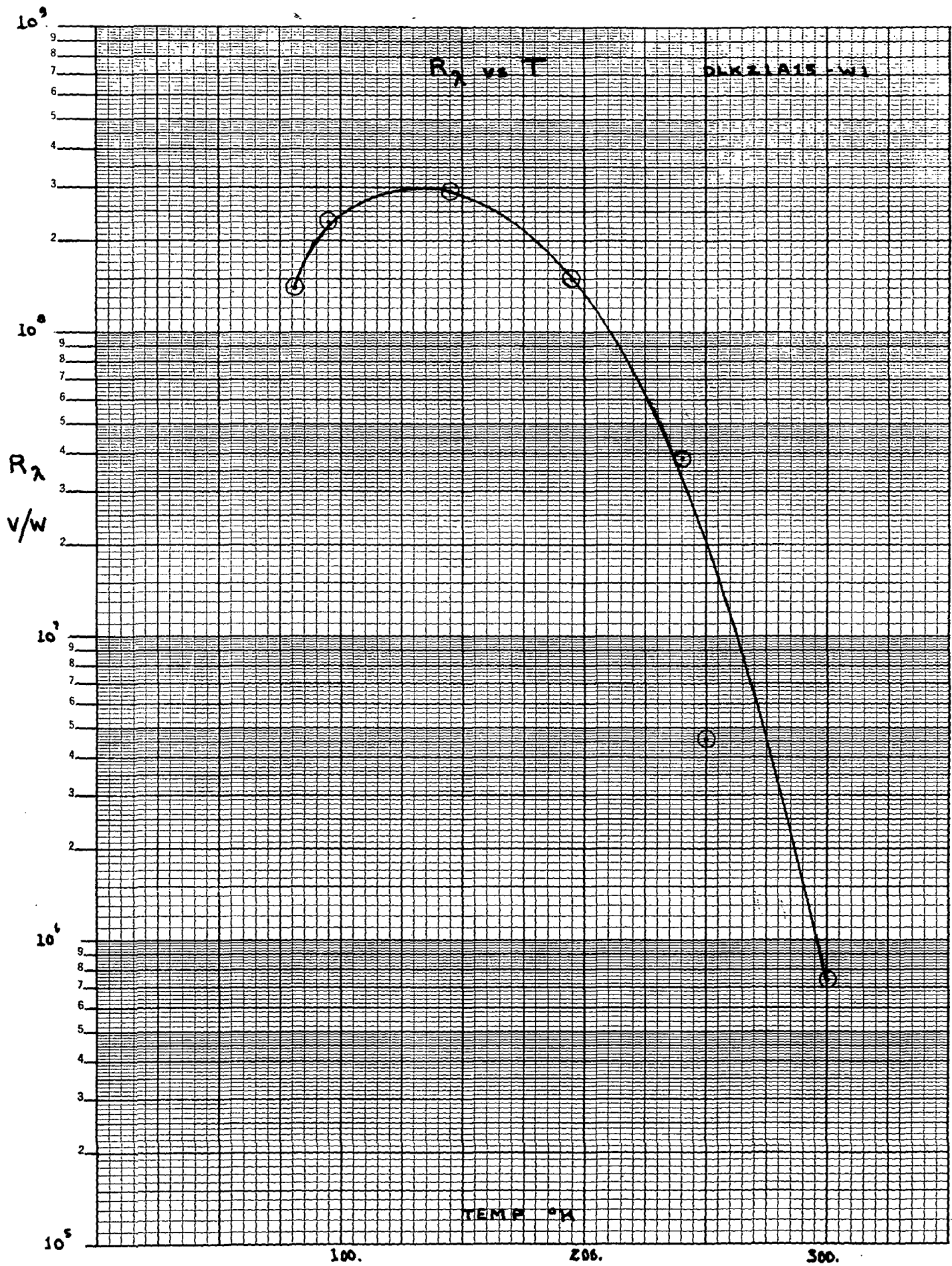
DETECTOR  
RESISTANCE  
IN OHMS

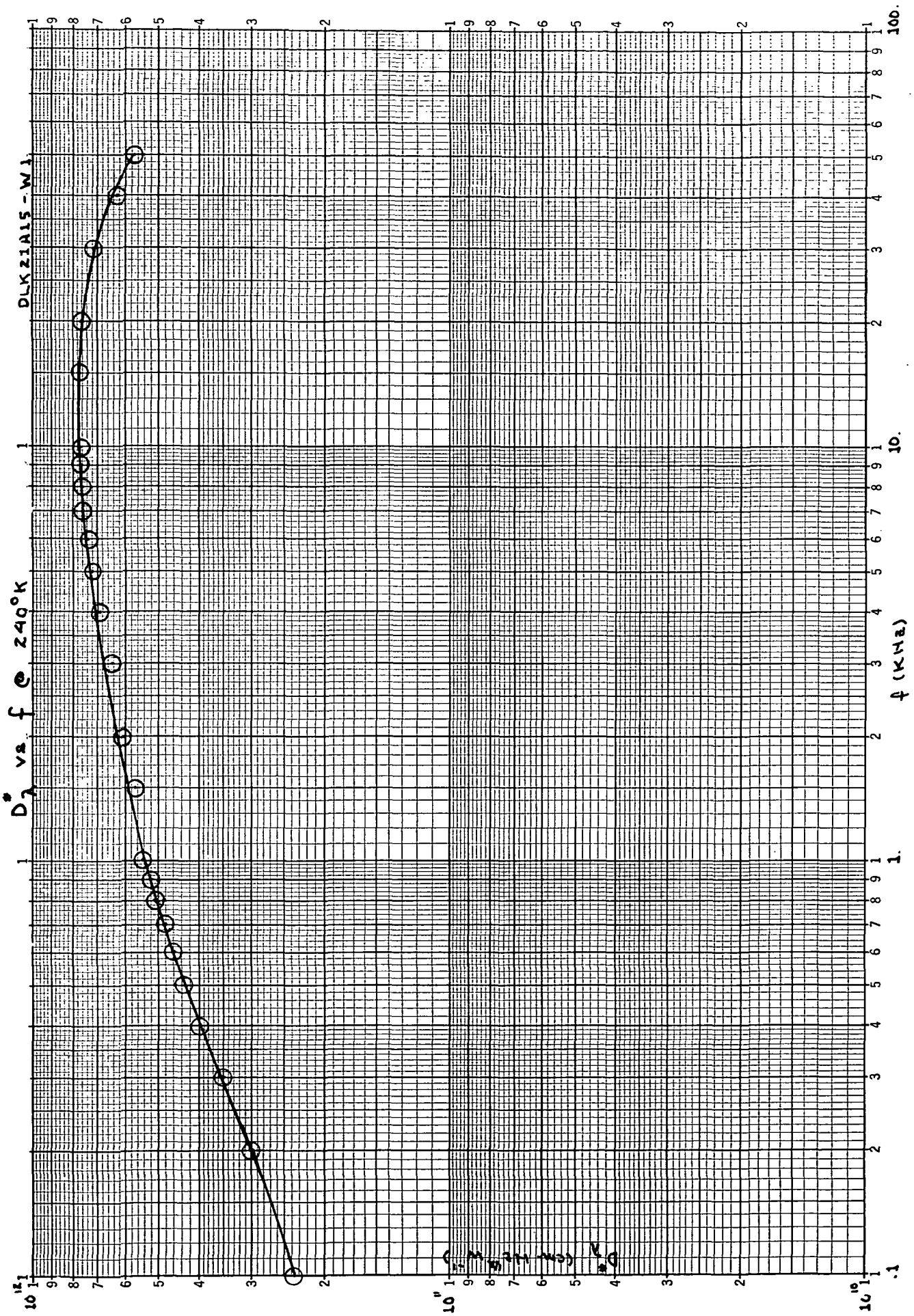
TEMP °C

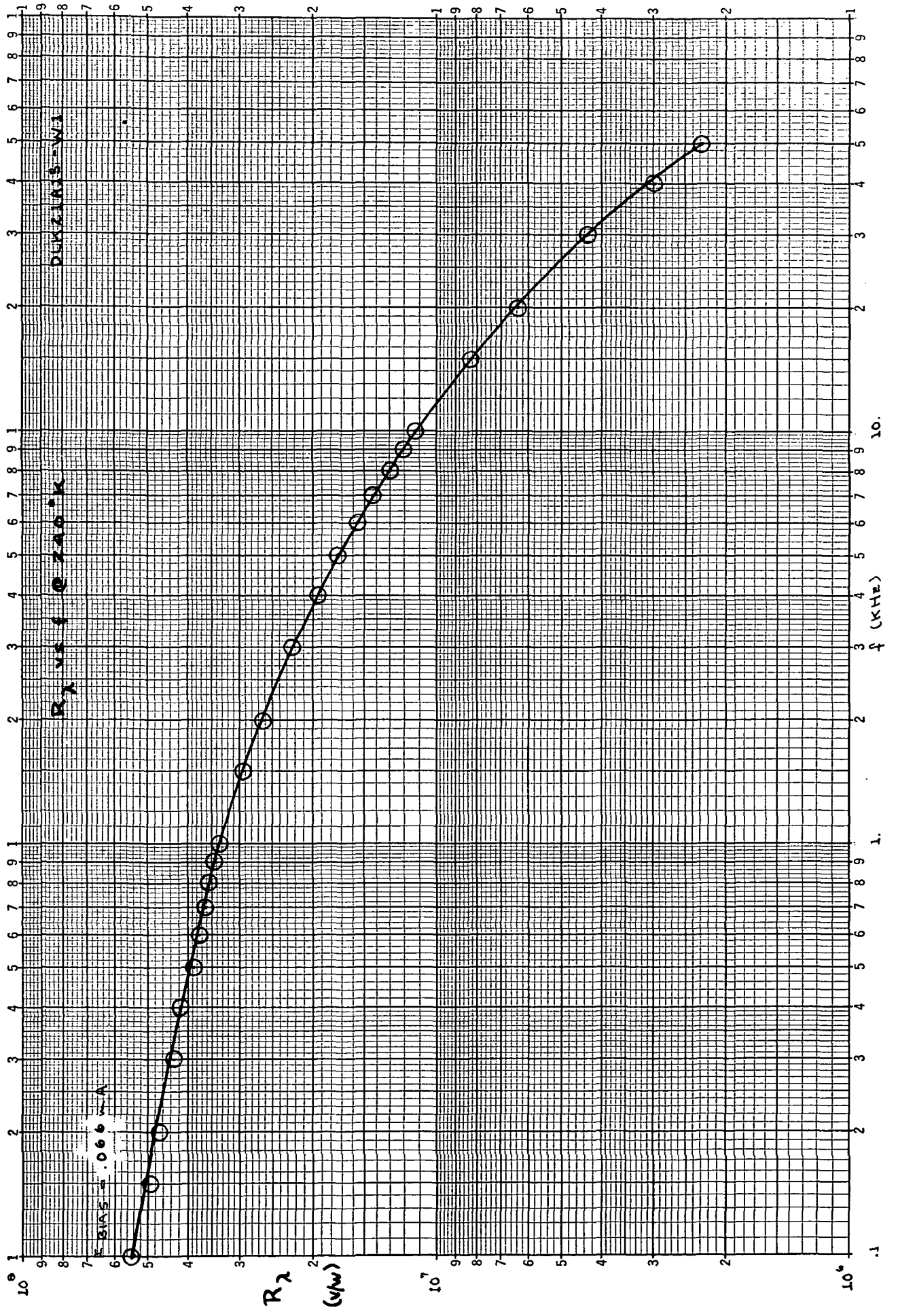
100.

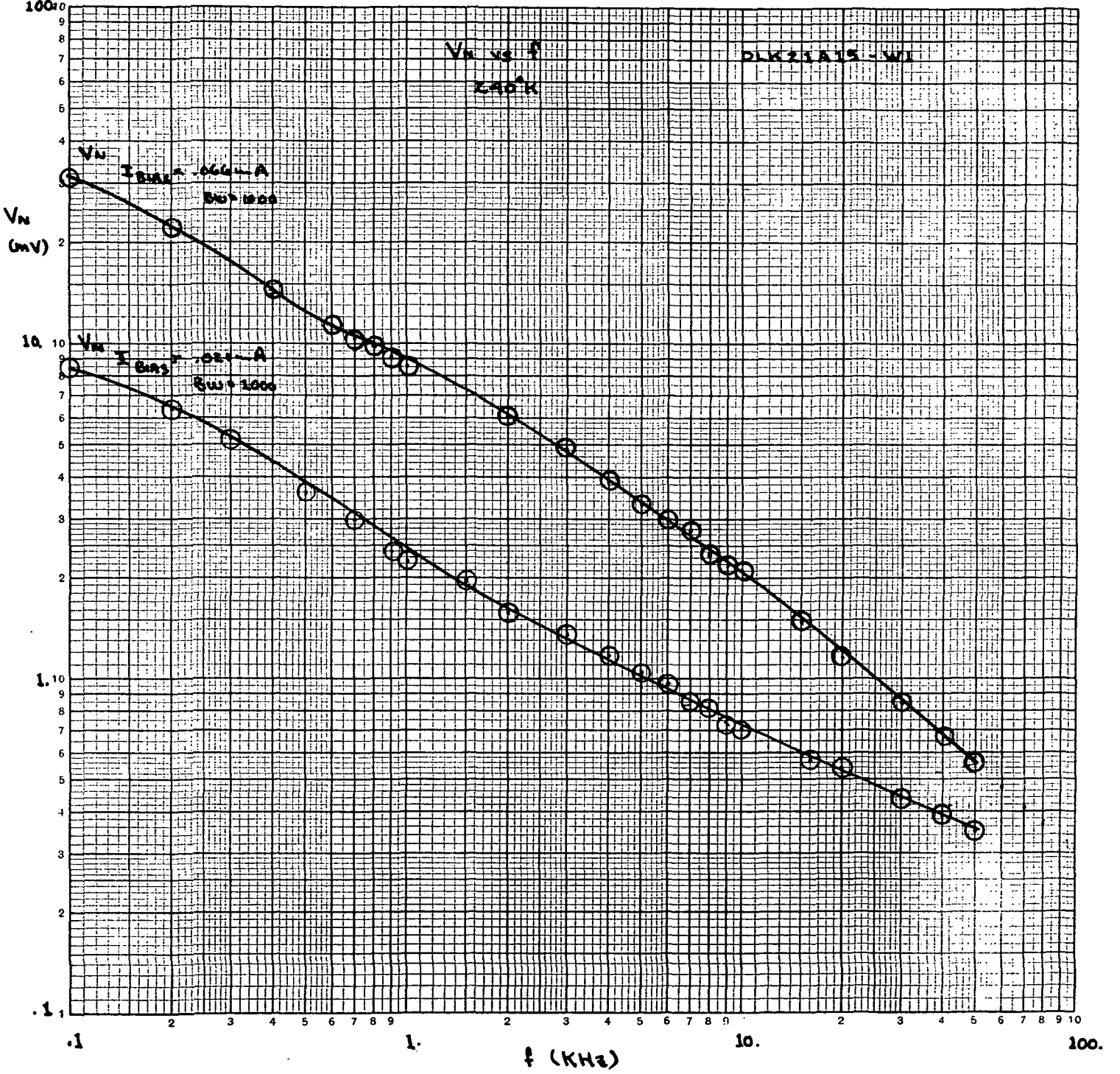
200.

300.









$10^{12}$

$D_{\lambda}^* \text{ vs } \lambda @ 240^{\circ}\text{K}$

DLK 21A15 - W1

$10^{11}$

$D_{\lambda}^*$   
 $\text{cm}^{-2}\text{Hz}^{-1}\text{W}^{-1}$

$10^{10}$

$\lambda \text{ (}\mu\text{m)}$

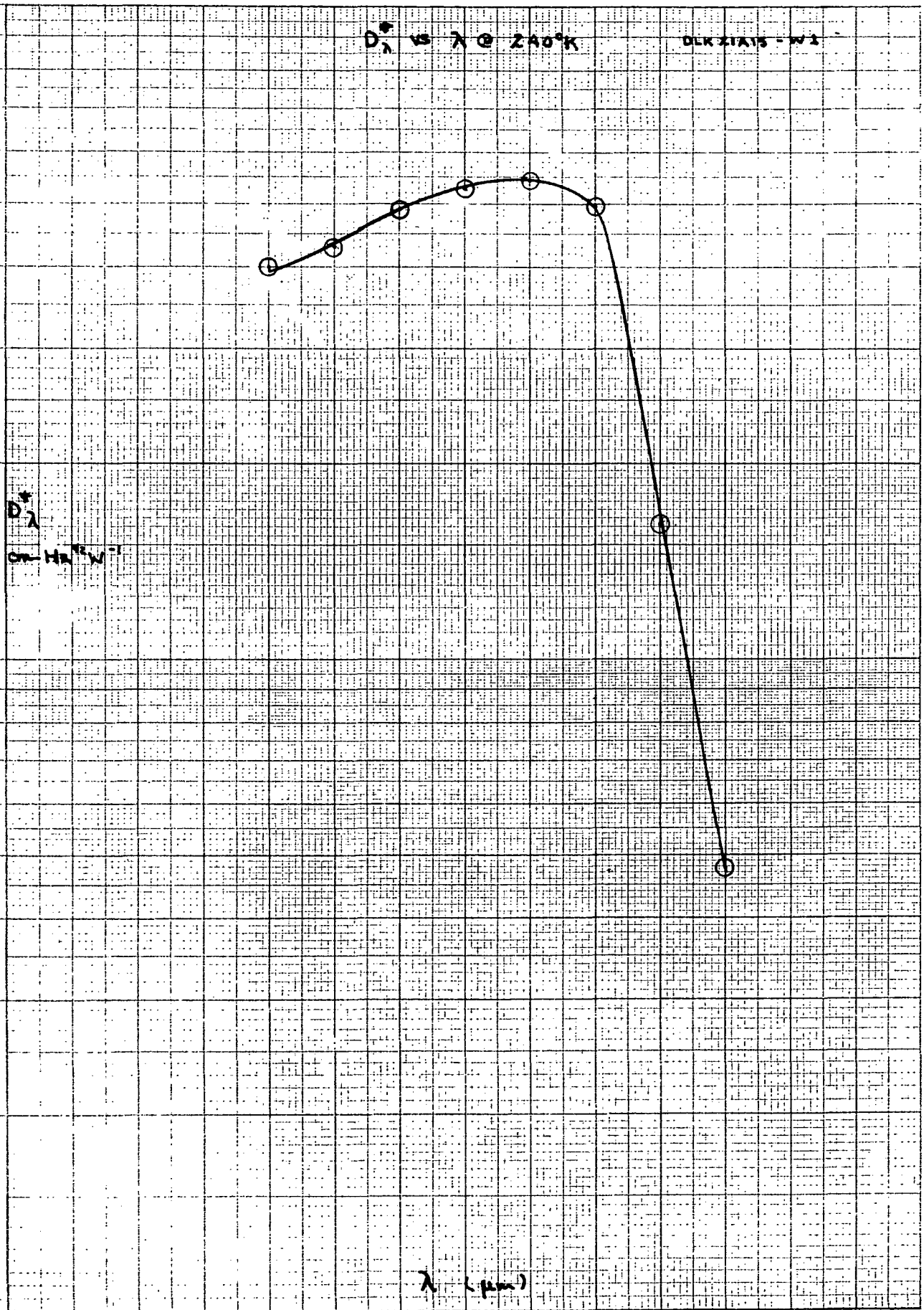
1.2

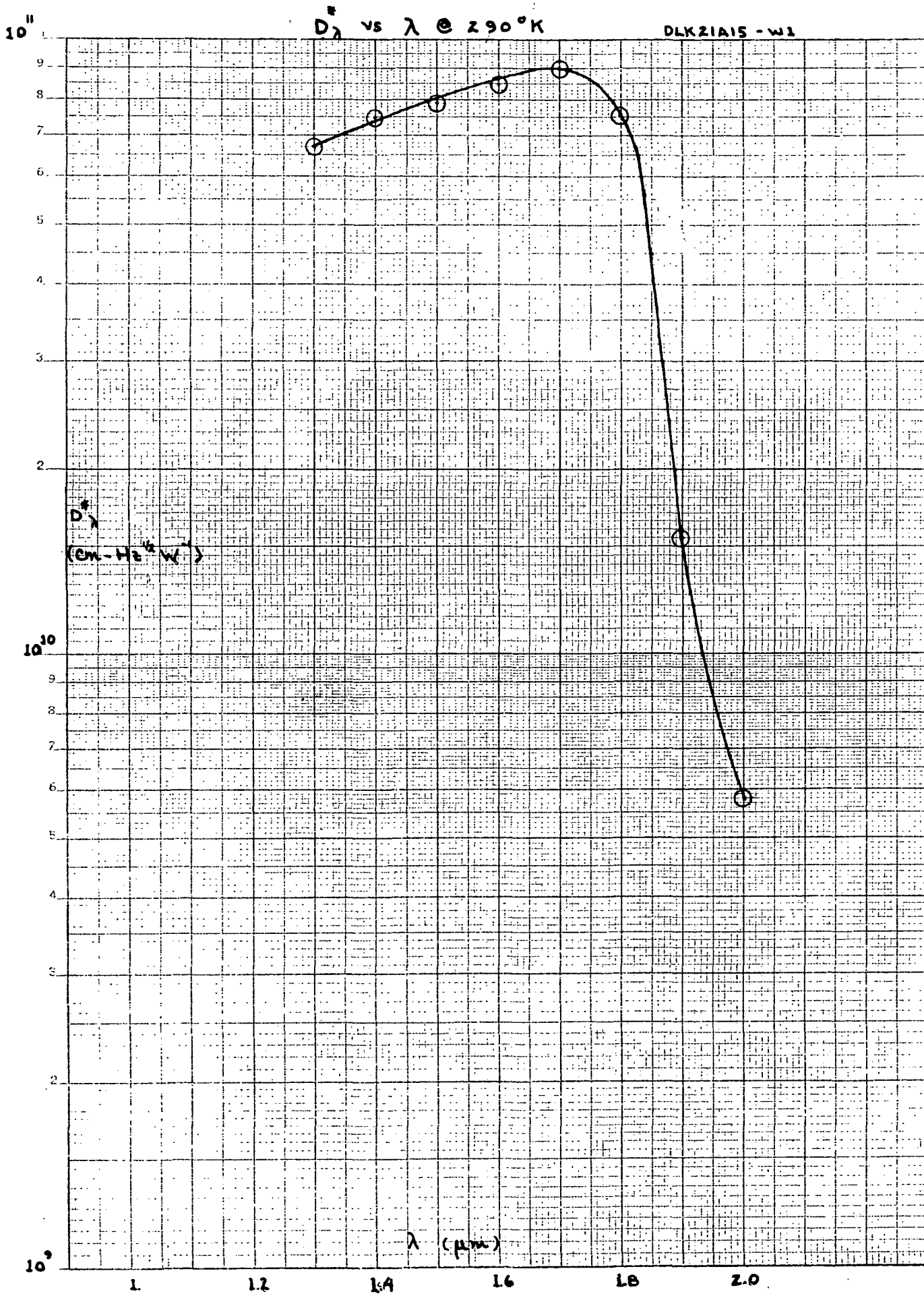
1.4

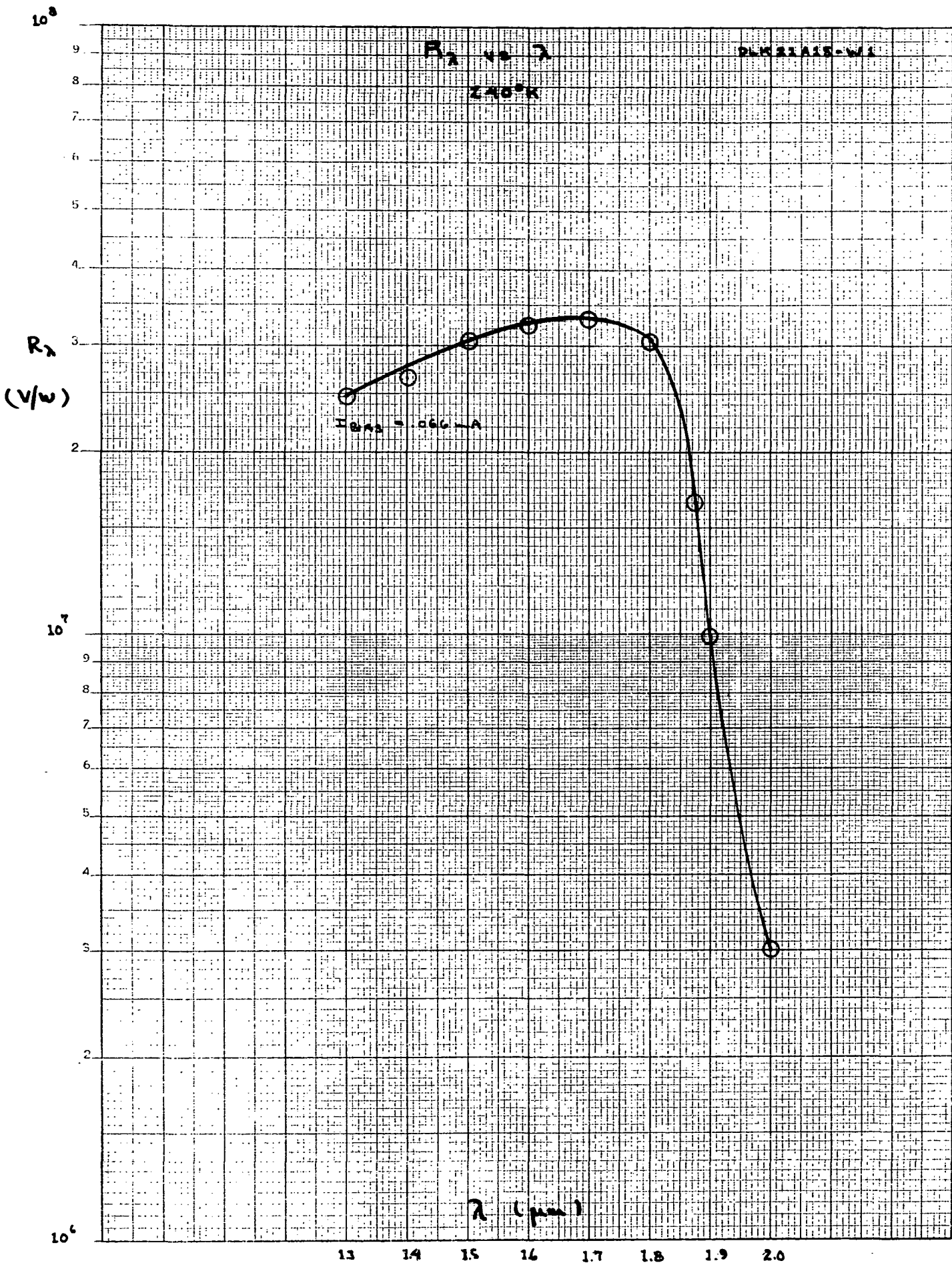
1.6

1.8

2.0

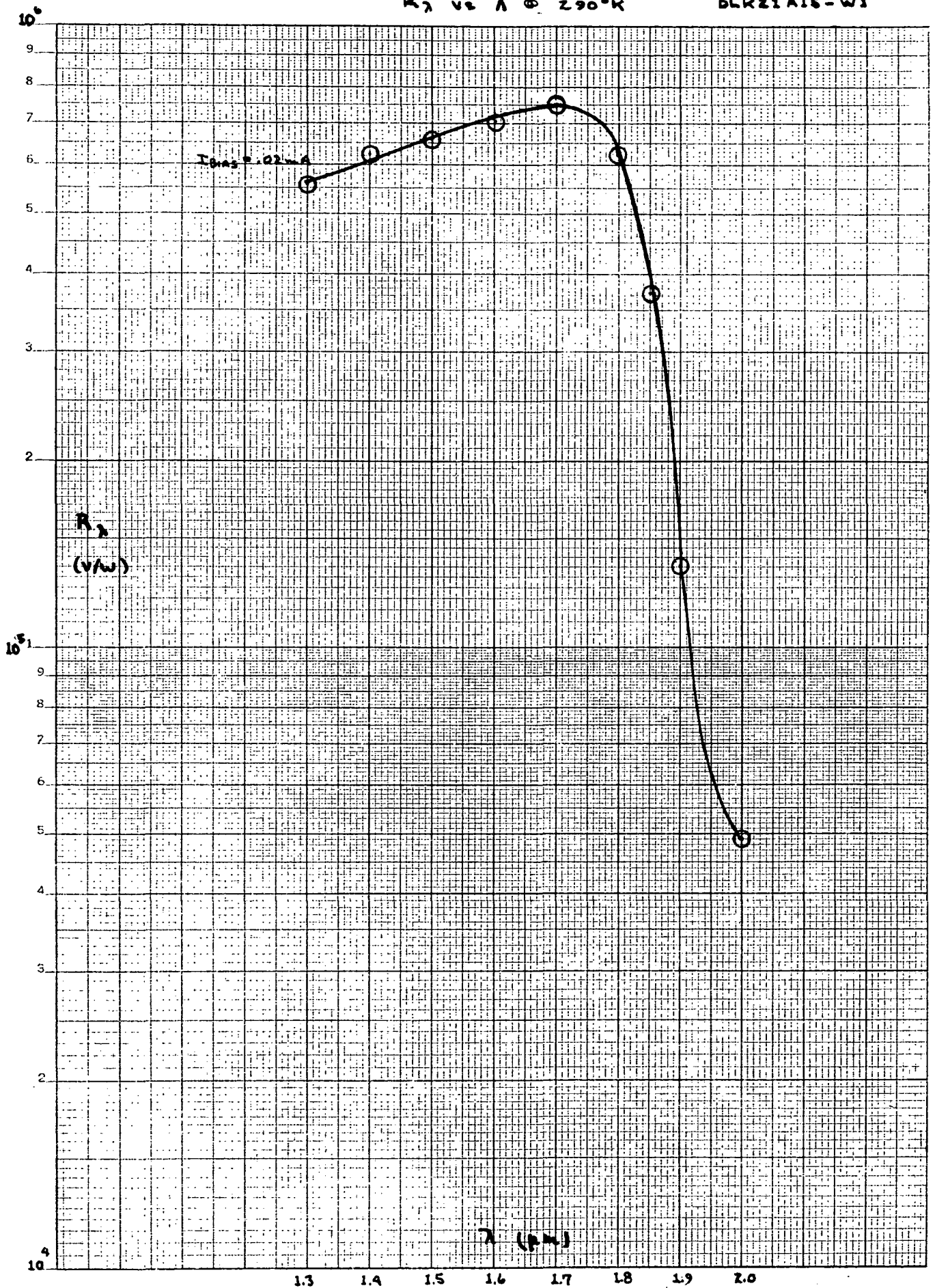






$R_2$  vs  $\lambda$  @ 290°K

DLK21A15-W1

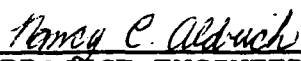


TEST REPORT 23971-2  
FOR  
DLK21A15 S/N W2 INFRARED DETECTOR  
FOR  
NASA/GODDARD

CONTRACT NO.

NAS 5-21646

  
PRODUCT ASSURANCE  
ENGINEER

  
PROJECT ENGINEER

  
PROGRAM MANAGER

Honeywell Inc.  
Radiation Center  
2 Forbes Road  
Lexington, Massachusetts 02173

ELEVATED OPERATING TEMPERATURE NEAR INFRARED PHOTODETECTOR

TEST REPORT

Manufacturer  
 HONEYWELL RADIATION CENTER  
 2 Forbes Road  
 Lexington, Massachusetts 02173

Detector Number - DLK21A15-W3

Date of Measurements - JAN 1973

DETECTOR DESCRIPTION

CONDITIONS OF MEASUREMENT

Type	HgCdTe Photo-conductive
Dimensions	$1.0 \times 10^{-2}$ cm. X $1.16 \times 10^{-2}$ cm
Sensitive Area, A	$1.2 \times 10^{-4}$ cm <sup>2</sup>
Window Material	Sapphire
Field of View	71° 06' Degrees
Resistance	2210 ohms @ 240°K
Operating Bias Current	0.23 ma

Detector Temperature	240 °K
Chopping Frequency	1000 Hz
Noise Bandwidth Δf	6.2 Hz
Blackbody Temperature T <sub>BB</sub>	1000 °K
Amplifier Gain	10 <sup>5</sup> nominal
Distance - Source to Det. d	16.35 cm
Blackbody Aperature Shape & Size	Circular 0.0125 in Dia.
Spectral Wavelength Intervals	0.1 μm

TEST RESULTS @ OPT. BIAS

Signal, S	31.0 mv
Noise, N	0.115 ms
D* <sub>BB</sub>	$9.5 \times 10^9$ cm Hz <sup>1/2</sup> /watt
R <sub>BB</sub>	$2.3 \times 10^4$ volts/watt
P <sub>n</sub> [NEP]	$1.2 \times 10^{-10}$ watts/Hz <sup>1/2</sup>
λ <sub>peak</sub>	2.2 μm
D* <sub>λpk</sub>	$7.9 \times 10^{10}$ cm Hz <sup>1/2</sup> /watt
R <sub>λpk</sub>	$2.0 \times 10^5$ volts/watt
τ <sub>response</sub>	16 μs
τ <sub>detective</sub>	.76 μs @ 0.23 ma

T<sub>c</sub> = chopper blade temp. = 300°K  
 ε<sub>c</sub> = chopper blade emissivity ≈ 1.0  
 ε<sub>BB</sub> = blackbody emissivity ≈ 1.0  
 A<sub>BB</sub> = area of blackbody aperature (cm<sup>2</sup>)

Radiant Signal Wave Shape and Amplitude

$$N(t) = \frac{\pi R^2}{2} I_0 \left\{ 1 - \frac{4R}{r} \sum_{K=1}^{\infty} \left( \frac{2r}{K\pi R} \right)^2 J_K \right.$$

$$\left. \bullet \left( \frac{K\pi R}{2r} \right) \sin \frac{K\pi}{2} \cos K\omega t \right\}$$

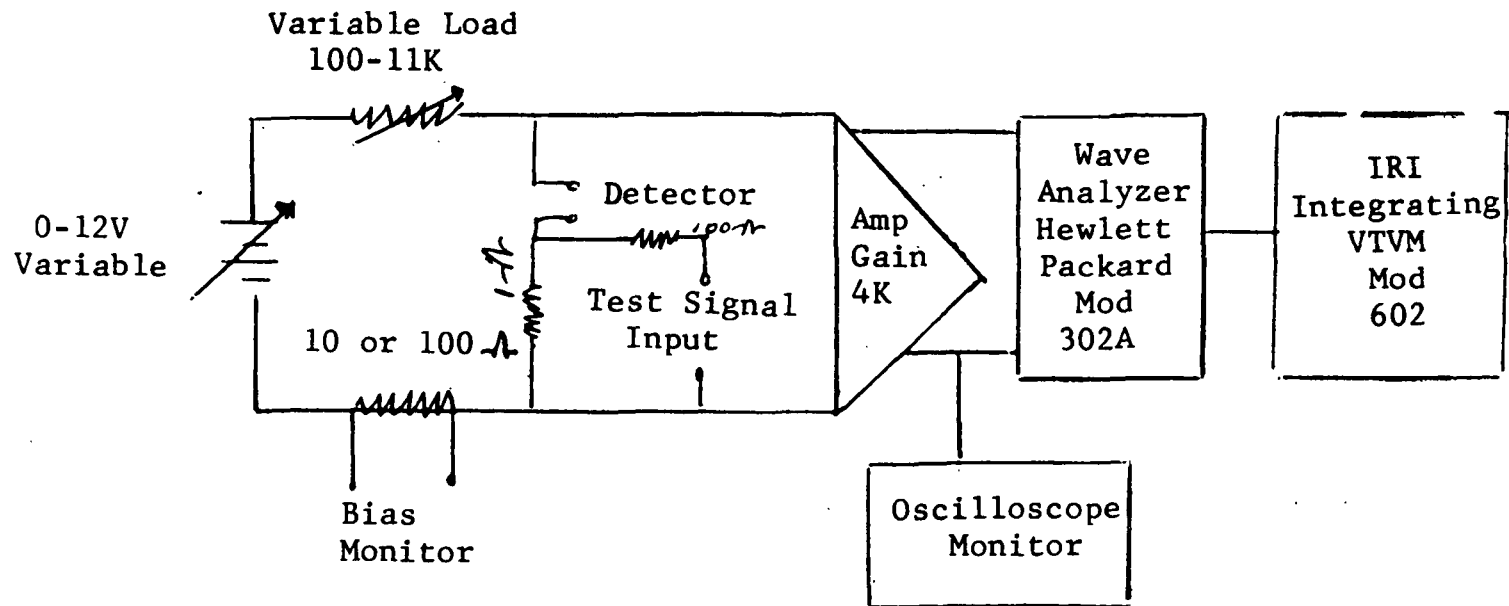
where: I<sub>0</sub> = radiant emittance from source (watts-cm<sup>-2</sup>)  
 2R = source aperature dia.  
 2r = chopper tooth width (inches) = 0.1987  
 J<sub>1</sub> = 1st order Bessel function

ref: R.B. McQuistan, Journal of the Optical Society of America, 48, 1, 63, Jan. '58

$$D^*_{BB} = \frac{1.10 \times 10^{12} (\Delta f)^{1/2} d^2 S/N}{(\epsilon_{BB} T_{BB}^4 - \epsilon_c T_c^4) A^{1/2} A_{BB}}$$

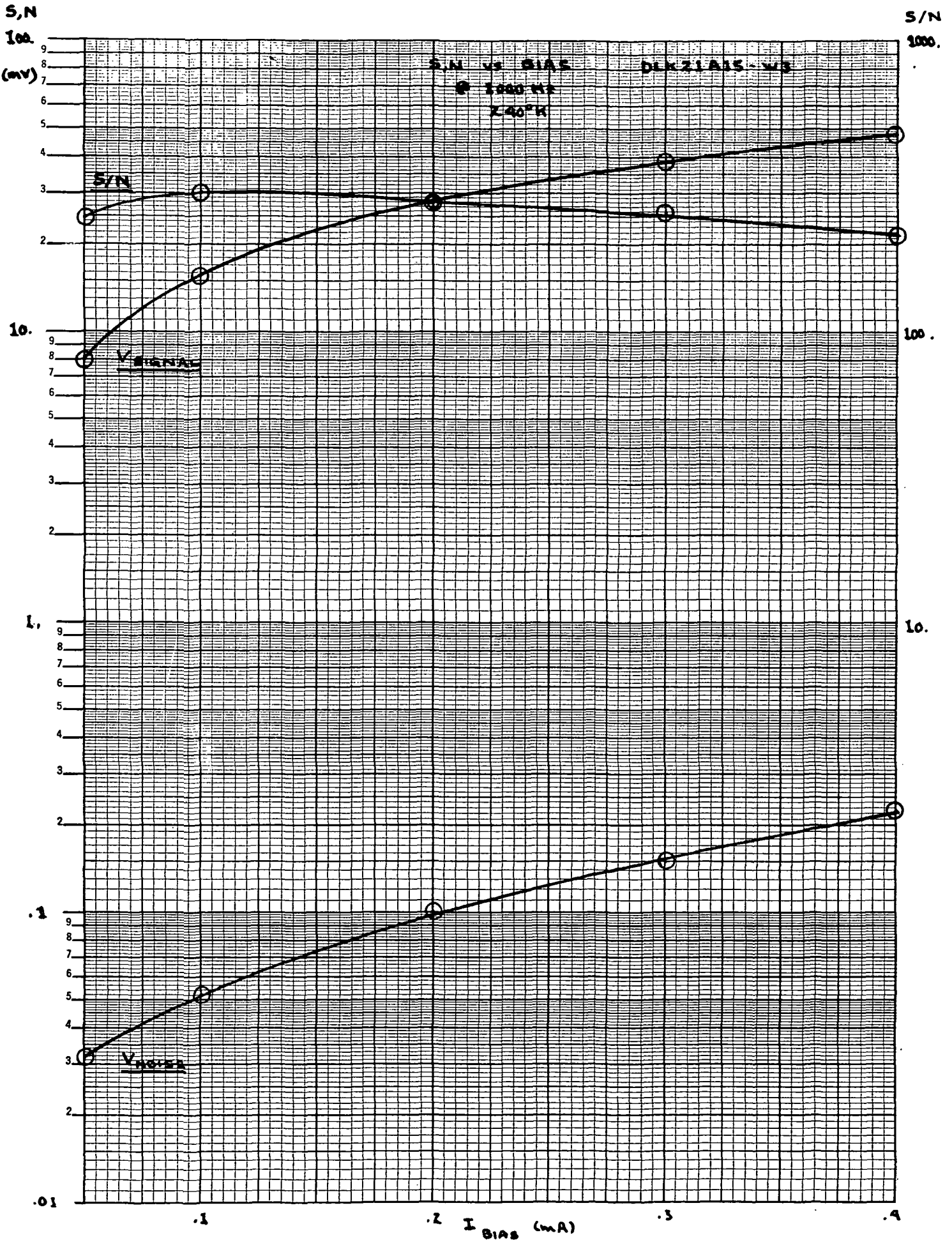
(see attached derivation)

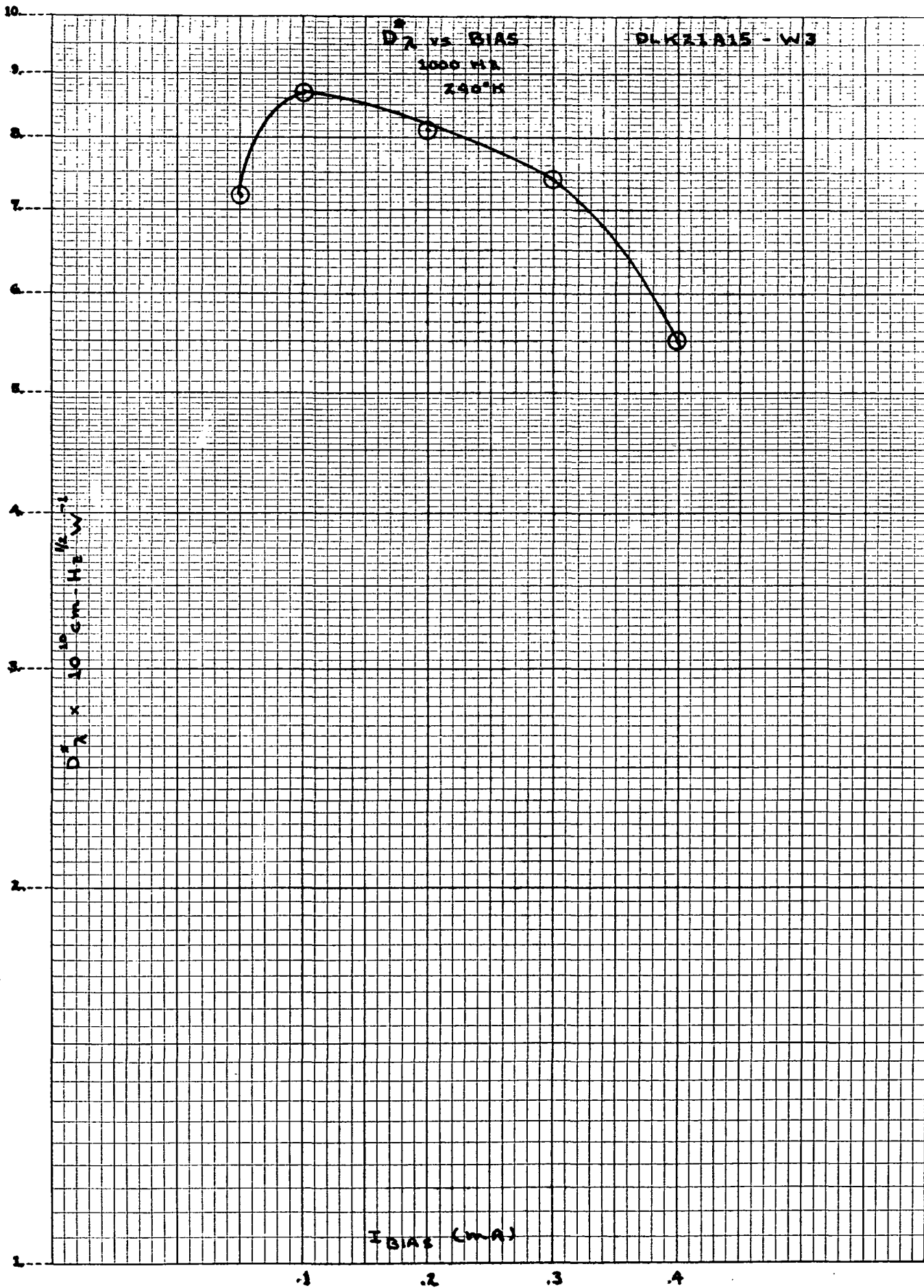
## Detector Readout Circuitry

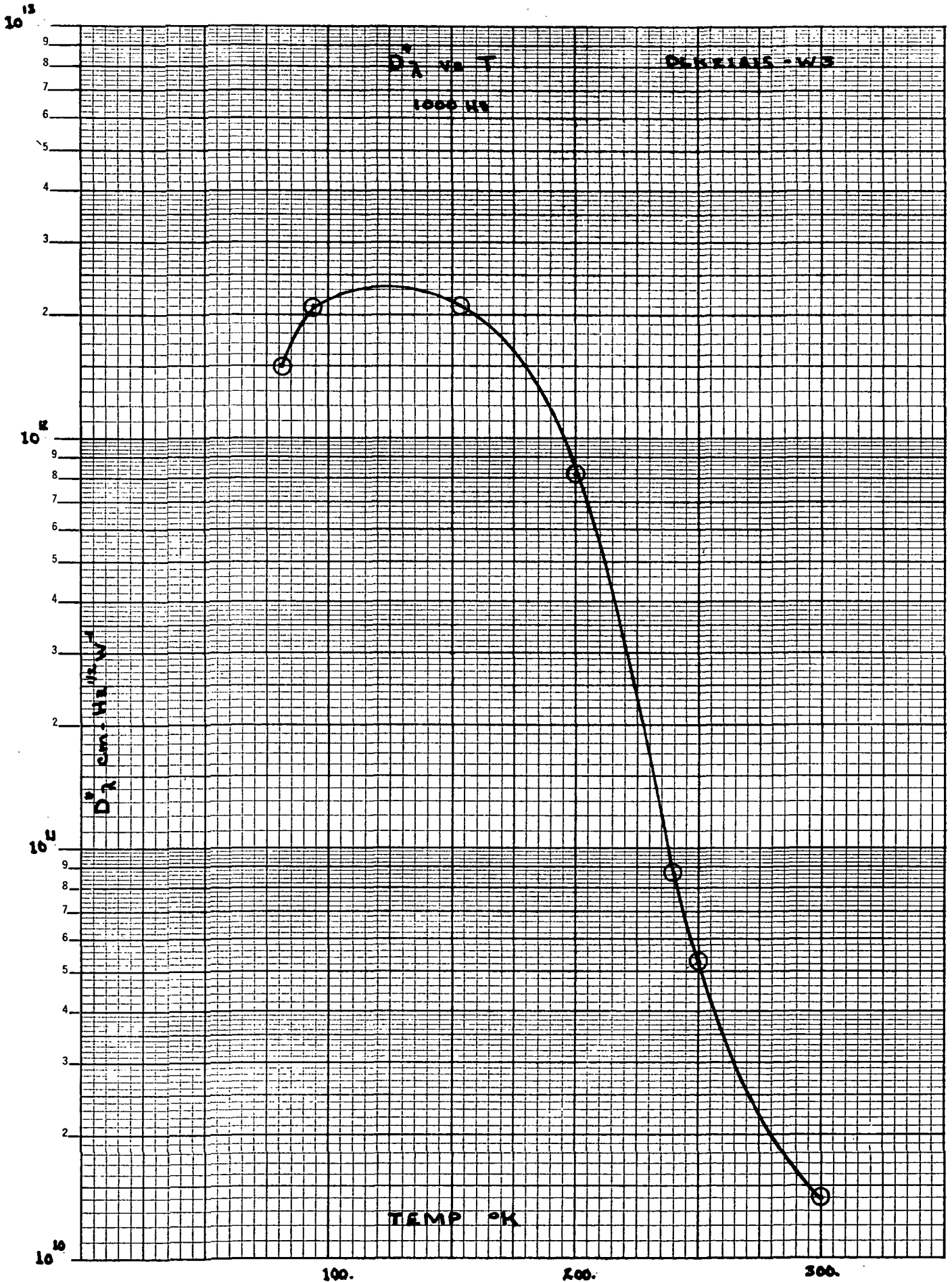


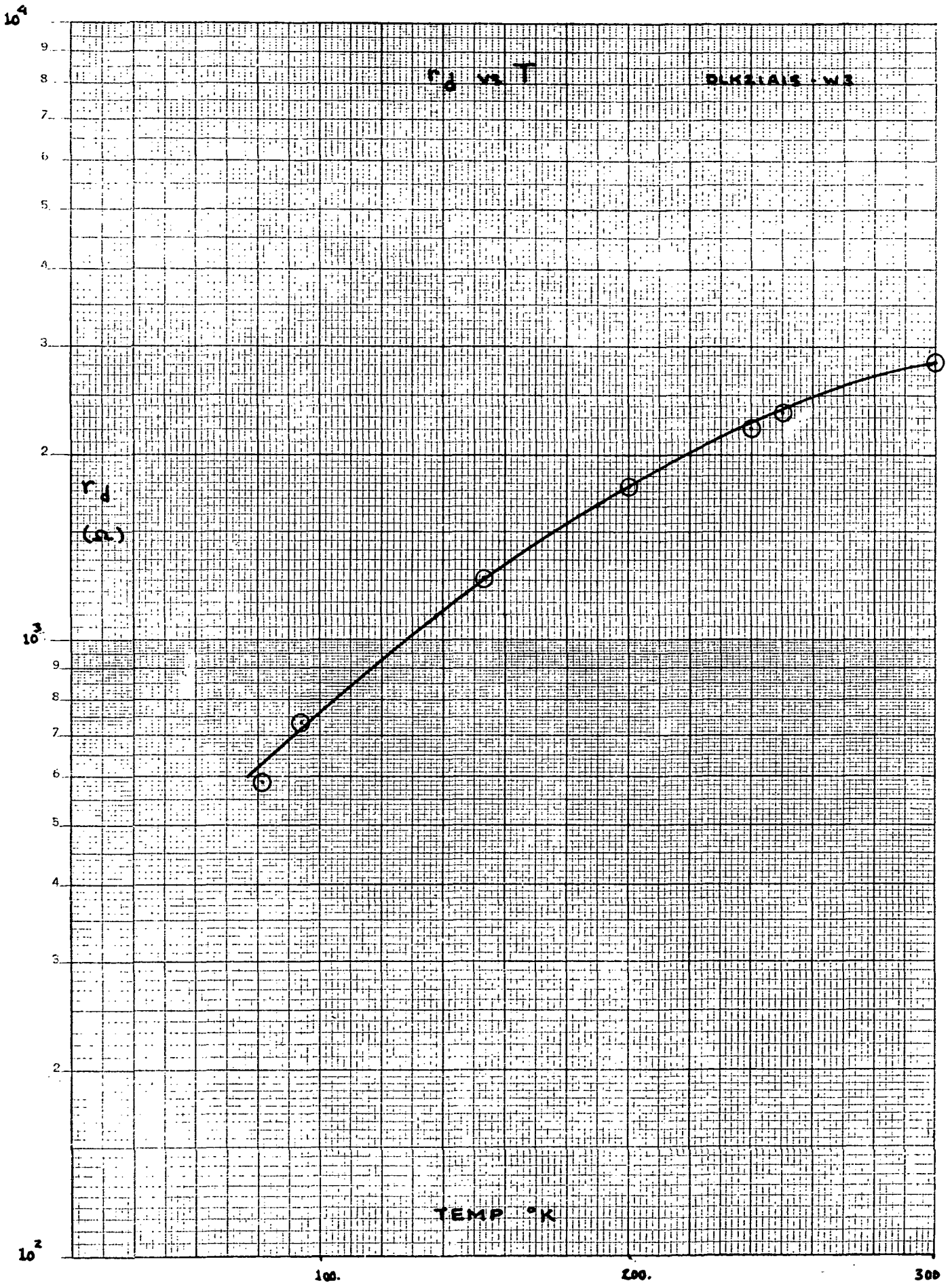
### 3.0 Graphs

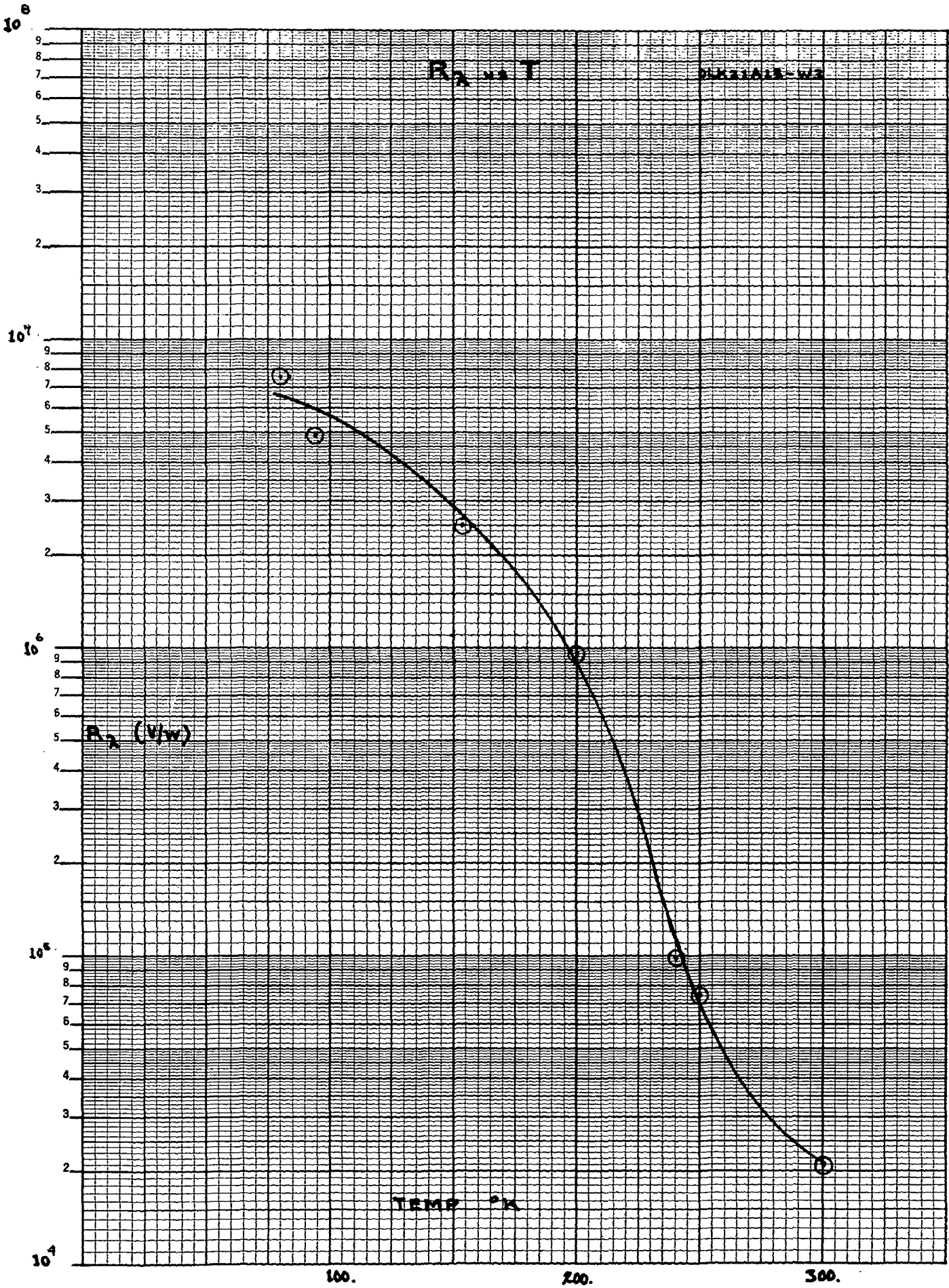
S,N vs Bias @ 1000 Hz, 240°K  
D<sub>λ</sub>\* vs Bias @ 1000 Hz, 240°K  
D<sub>λ</sub>\* vs T @ 1000 Hz, optimum bias  
r<sub>d</sub> vs T  
D<sub>λ</sub>\* vs f @ 240°K, operating bias  
R<sub>λ</sub> vs T @ 1000 Hz, operating bias  
R<sub>λ</sub> vs f @ 240°K, operating bias  
V<sub>n</sub> vs f @ 240°K, operating bias  
D<sub>λ</sub>\* vs λ @ 240°K, operating bias  
D<sub>λ</sub>\* vs λ @ 290°K, optimum bias  
R<sub>λ</sub> vs λ @ 240°K, operating bias  
R<sub>λ</sub> vs λ @ 290°K, optimum bias

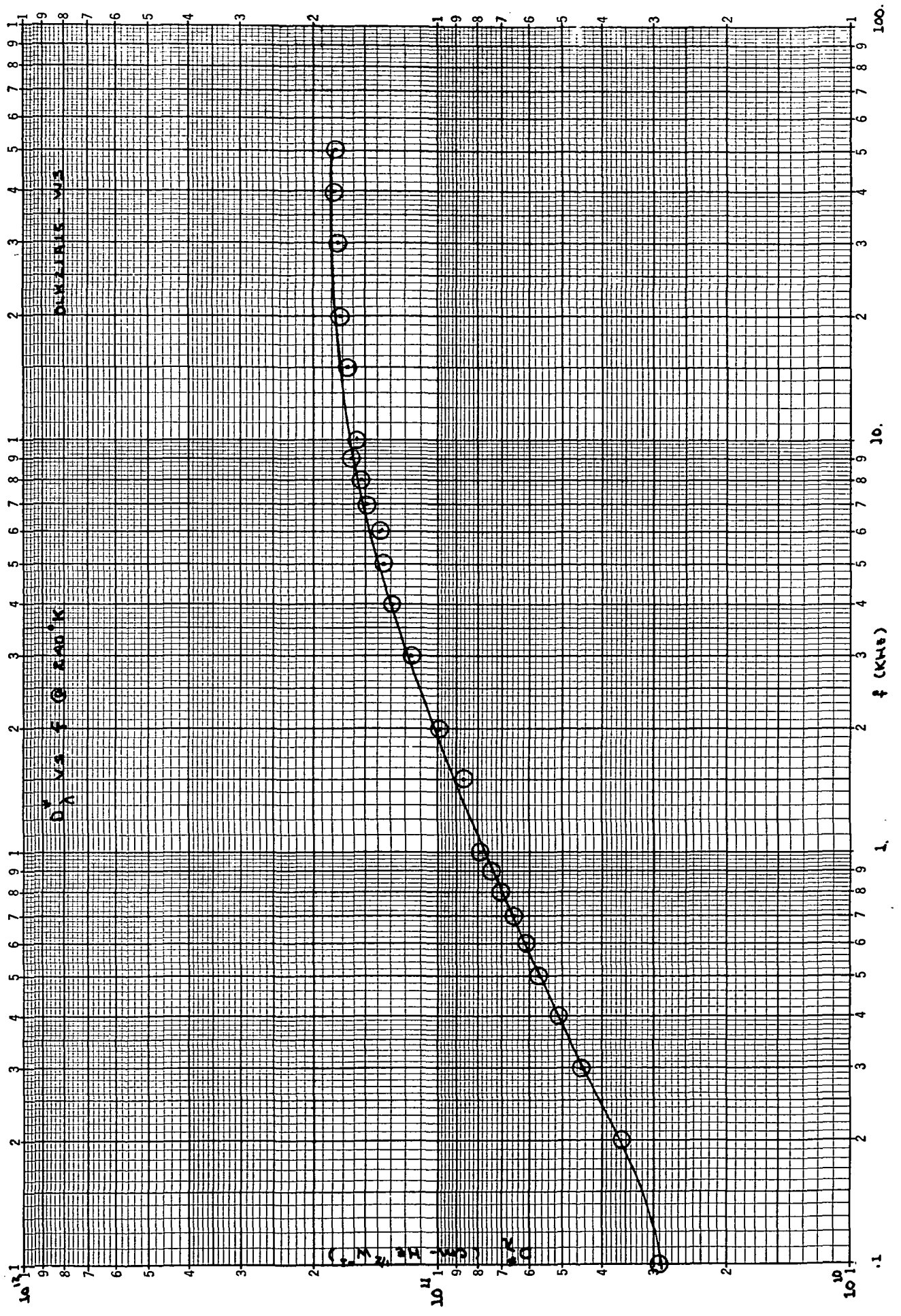


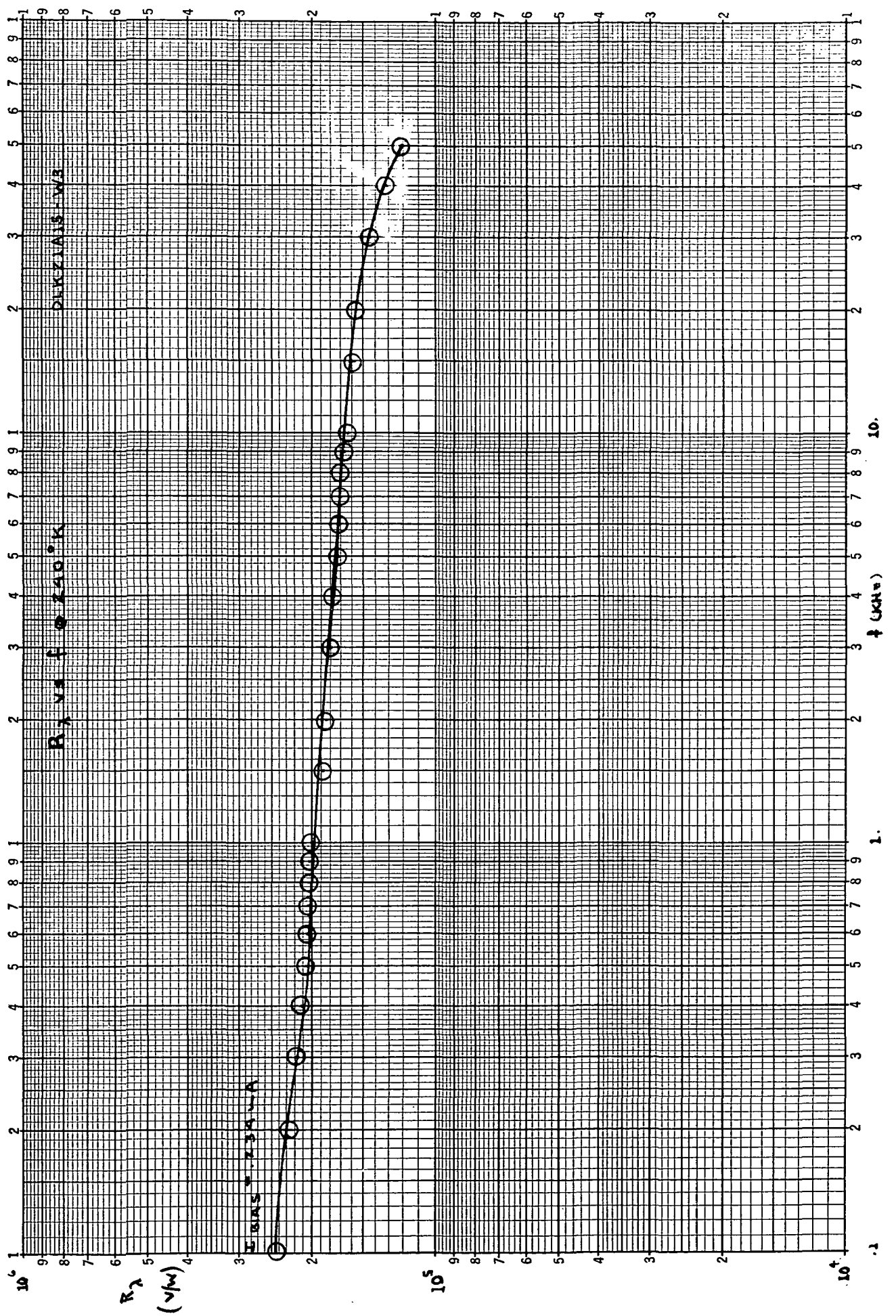


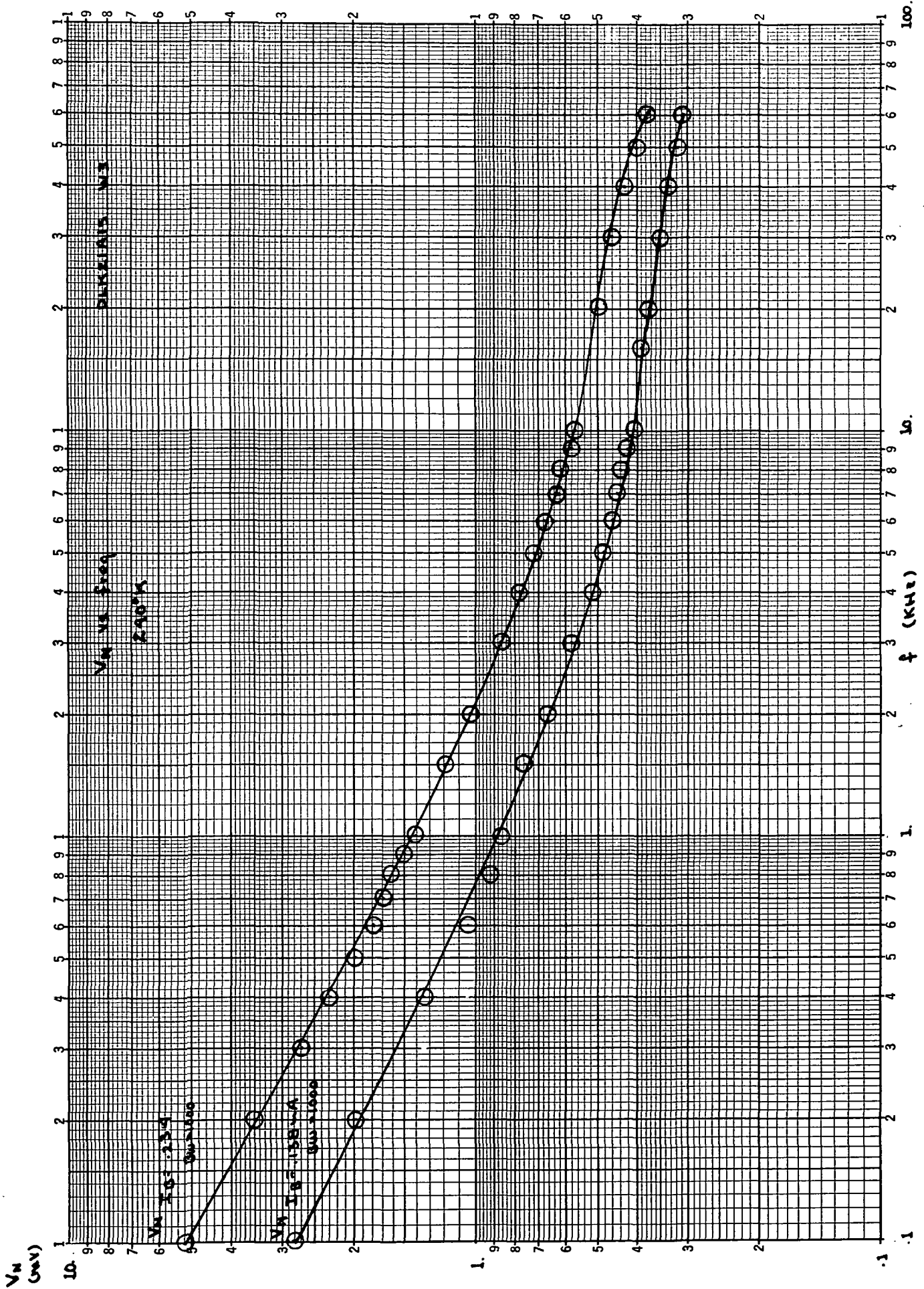


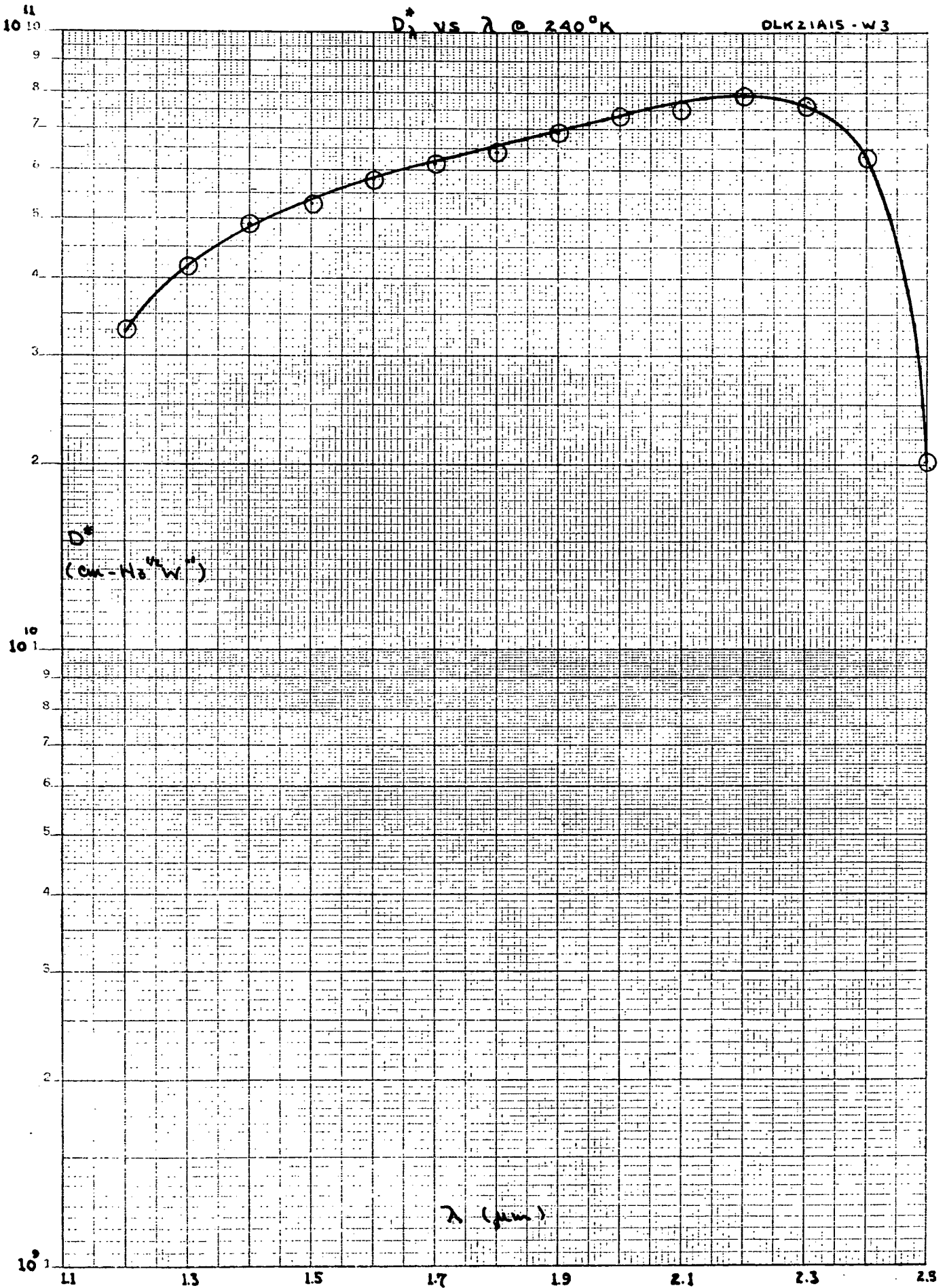


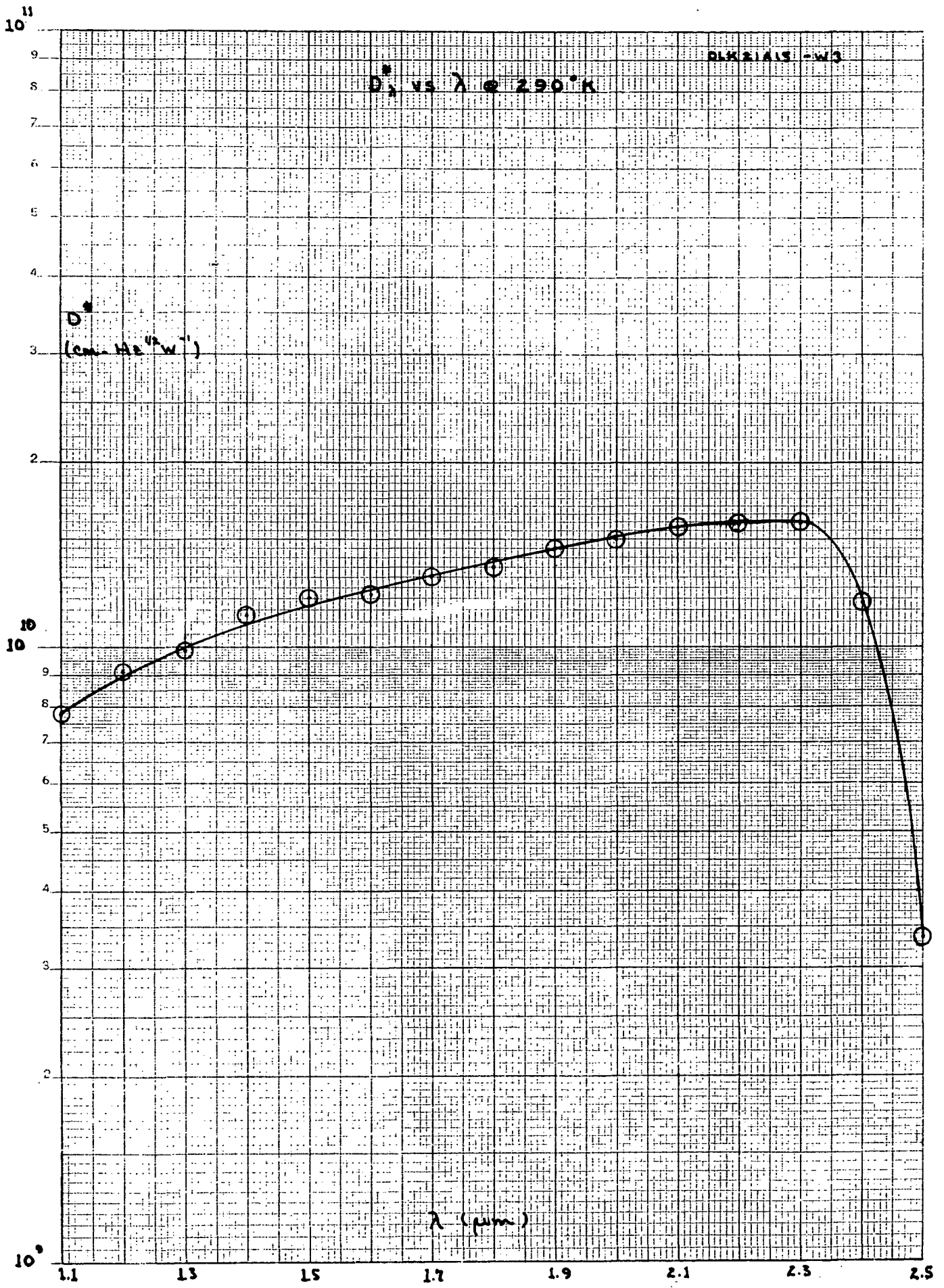


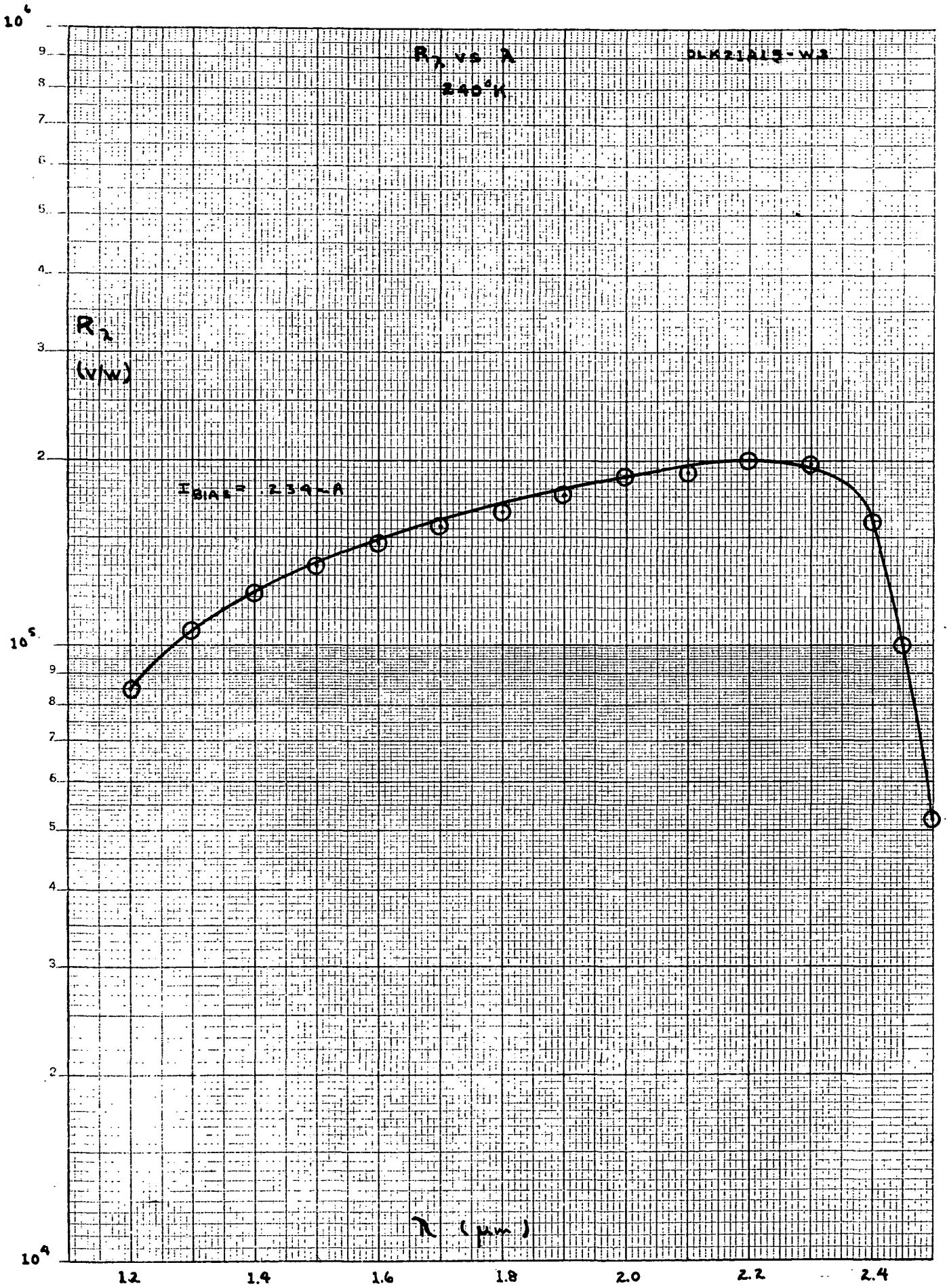


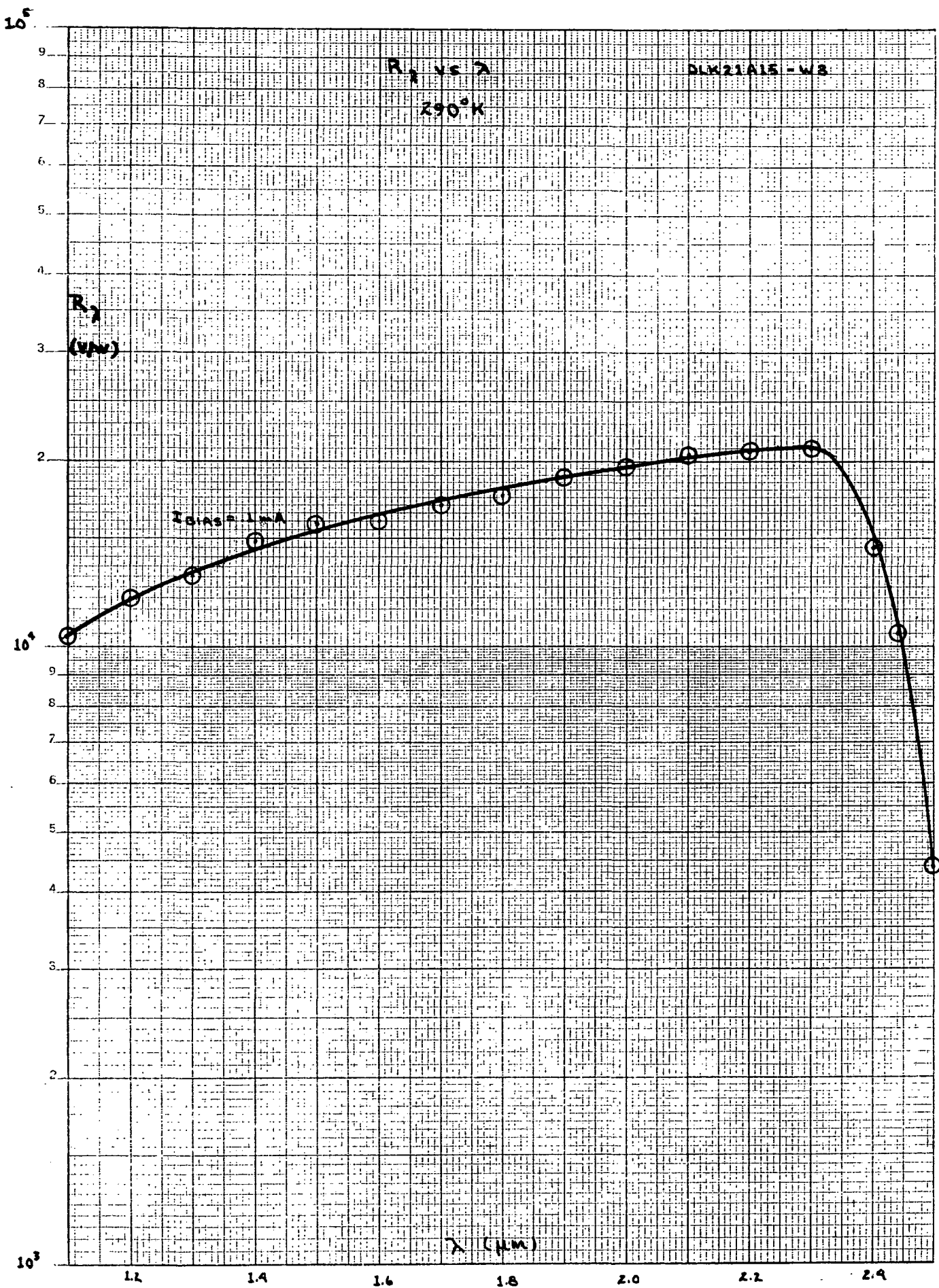








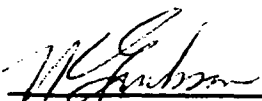




TEST REPORT 23971-3  
FOR  
DLK21A15 S/N W3 INFRARED DETECTOR  
FOR  
NASA/GODDARD

CONTRACT NO.

NAS 5-21646

  
PRODUCT ASSURANCE  
ENGINEER

  
PROJECT ENGINEER

  
PROGRAM MANAGER

Honeywell Inc.  
Radiation Center  
2 Forbes Road  
Lexington, Massachusetts 02173

## TABLE OF CONTENTS

### SECTION

- 1.0 Test Report Summary
- 2.0  $D^*_{BB}$  Derivation
- 3.0 Graphs
- 4.0 Handling and Use Precautions

NOTE: PLEASE READ "HANDLING AND PRECAUTIONS"  
BEFORE USING THIS DETECTOR

ELEVATED OPERATING TEMPERATURE NEAR INFRARED PHOTODETECTOR

TEST REPORT

Manufacturer  
 HONEYWELL RADIATION CENTER  
 2 Forbes Road  
 Lexington, Massachusetts 02173

Detector Number - DLK21A15-W2

Date of Measurements - JAN '73

DETECTOR DESCRIPTION

Type	HgCdTe Photo-conductive
Dimensions	$9.14 \times 10^{-3}$ cm. X $9.14 \times 10^{-3}$ cm
Sensitive Area, A	$8.6 \times 10^{-5}$ cm <sup>2</sup>
Window Material	Sapphire
Field of View	70° 20' Degrees
Resistance	ohms @ 240°K. 13,330
Optimum Bias Current	0.09 ma

CONDITIONS OF MEASUREMENT

Detector Temperature	240 °K
Chopping Frequency	1000 Hz
Noise Bandwidth $\Delta f$	6.2 Hz
Blackbody Temperature $T_{BB}$	1000 °K
Amplifier Gain	10 <sup>3</sup> nominally
Distance - Source to Det. $d$	24 cm
Blackbody Aperture Shape & Size	Circular 0.0125 in Dia.
Spectral Wavelength Intervals	0.10 $\mu$ m

TEST RESULTS @ OPT. BIAS

Signal, S	130 mv
Noise, N	0.63 ms
$D^*_{BB}$	$2.7 \times 10^{10}$ cm Hz <sup>1/2</sup> /watt
$R_{BB}$	$1.1 \times 10^6$ volts/watt
$P_n$ [NEP]	$3.4 \times 10^{-13}$ watts/Hz <sup>1/2</sup>
$\lambda_{peak}$	1.87 $\mu$ m
$D^*_{\lambda pk}$	$6.5 \times 10^{11}$ cm Hz <sup>1/2</sup> /watt
$R_{\lambda pk}$	$2.7 \times 10^7$ volts/watt
$\tau_{response}$	212. $\mu$ s
$\tau_{detective}$	4.9 $\mu$ s @ 0.097 ma

$T_c$  = chopper blade temp. = 300°K  
 $\epsilon_c$  = chopper blade emissivity  $\approx$  1.0  
 $\epsilon_{BB}$  = blackbody emissivity  $\approx$  1.0  
 $A_{BB}$  = area of blackbody aperture (cm<sup>2</sup>)

Radiant Signal Wave Shape and Amplitude

$$N(t) = \frac{\pi R^2}{2} I_0 \left\{ 1 - \frac{4R}{r} \sum_{K=1}^{\infty} \left( \frac{2r}{K\pi R} \right)^2 J_1 \right.$$

$$\left. \cdot \left( \frac{K\pi R}{2r} \right) \sin \frac{K\pi}{2} \cos K\omega t \right\}$$

where:  $I_0$  = radiant emittance from source (watts-cm<sup>-2</sup>)

$2R$  = source aperture dia.

$2r$  = chopper tooth width (inches) = 0.1987

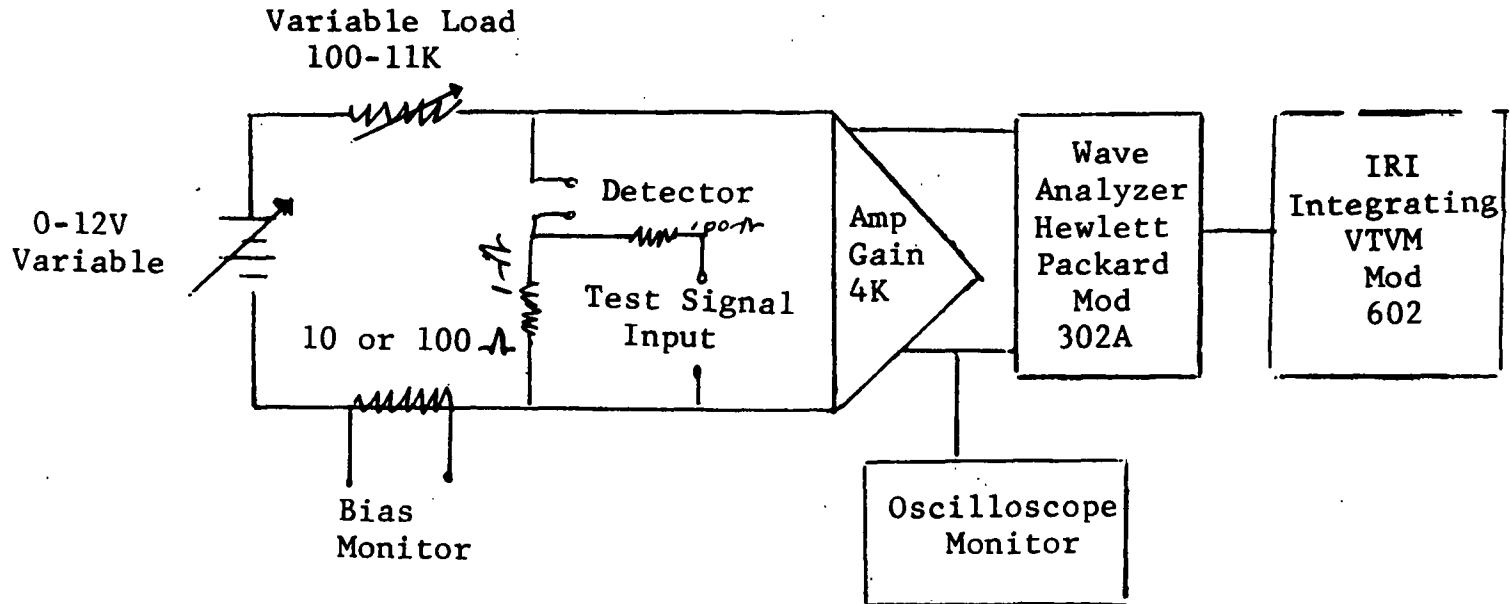
$J_1$  = 1st order Bessel function

ref: R.B. McQuistan, Journal of the Optical Society of America, 48, 1, 63, Jan. '58

$$D^*_{BB} = \frac{1.10 \times 10^{12} (\Delta f)^{1/2} d^2 S/N}{(\epsilon_{BB} T_{BB}^4 - \epsilon_c T_c^4) A^{1/2} A_{BB}}$$

(see attached derivation)

## Detector Readout Circuitry



## 2.0 $D_{BB}^*$ Derivation

The detectivity can be defined as:

$$D^* = \frac{A^{\frac{1}{2}} \Delta f^{\frac{1}{2}} S/N}{P}$$

Where:  $A$  = Sensitive area of the detector, in square centimeters.

$\Delta f$  = Frequency bandwidth of the noise measuring circuit  
in Hertz

$S/N$  = Signal to noise ratio of the detector

$P$  = Input signal power

The input power is:

$$f = \frac{\emptyset A_{BB} A}{d^2}$$

Where:  $A_{BB}$  = Area of blackbody aperture in square centimeters

$\emptyset$  = Flux density of the emitted irradiance in volts per  
square centimeter of blackbody aperture area

$d$  = Distance between blackbody & incident plans of  
detector

Calculation of flux density,  $\emptyset$ , is as follows:

$$\emptyset = \frac{\sigma (\epsilon_{BB} T_{BB}^4 - \epsilon_c T_c^4)}{(\pi c_1)}$$

Where:  $\sigma$  = Stefan Boltzman constant =  $5.6686 \times 10^{-12}$  Watts  
 $\text{cm}^{-2} \text{K}^{-4}$

$\epsilon_{\text{BB}}$  = Blackbody emissivity

$T_{\text{BB}}$  = Blackbody temperature

$\epsilon_{\text{c}}$  = Chopper blade emissivity

$T_{\text{c}}$  = Chopper blade temperature

$c_1$  = rms factor for chopper and blackbody aperture

$\pi$  = 3.1416

The input power is:

$$P_{\text{BB}} = \frac{\sigma (\epsilon_{\text{BB}} T_{\text{BB}}^4 - \epsilon_{\text{c}} T_{\text{c}}^4) A_{\text{BB}} A}{d^2 (\pi c_1)}$$

$D_{\text{BB}}^*$  is:

$$D_{\text{BB}}^* = \frac{(\Delta f)^{\frac{1}{2}} d^2 (\pi c_1) S / (kN)}{\sigma (\epsilon_{\text{BB}} T_{\text{BB}}^4 - \epsilon_{\text{c}} T_{\text{c}}^4) A_{\text{c}}^{\frac{1}{2}} A_{\text{BB}}}$$

Where:  $k$  = Experimentally determined correction factor for  
Hewlet Packard wave analyzer noise readings = 1.12

The rms chopping factor for an 80 blade chopper and .0125 inch diameter operation is 2.24. Thus combining constants and neglecting the  $(\epsilon_{\text{c}} T_{\text{c}}^4)$  terms.

$$D_{\text{BB}}^* = \frac{1.10 \times 10^{12} (\Delta f)^{\frac{1}{2}} S / N d^2}{\epsilon_{\text{BB}} T_{\text{BB}}^4 A_{\text{c}}^{\frac{1}{2}} A_{\text{BB}}}$$

### 3.0 Graphs

$S, N$  vs Bias @ 1000 Hz, 240°K

$D_{\lambda}^*$  vs Bias @ 1000 Hz, 240°K

$D_{\lambda}^*$  vs T @ 1000 Hz, optimum bias

$r_d$  vs T

$D_{\lambda}^*$  vs f @ 240°K, operating bias

$R_{\lambda}$  vs T @ 1000 Hz, operating bias

$R_{\lambda}$  vs f @ 240°K, operating bias

$V_n$  vs f @ 240°K, operating bias

$D_{\lambda}^*$  vs  $\lambda$  @ 240°K, operating bias

$D_{\lambda}^*$  vs  $\lambda$  @ 290°K, optimum bias

$R_{\lambda}$  vs  $\lambda$  @ 240°K, operating bias

$R_{\lambda}$  vs  $\lambda$  @ 290°K, optimum bias

S.N

1000.10

(mV)

S.N vs BIAS

DLK21A15-W2

@ 1000 Hz  
240°K

S/N

V<sub>BIAS</sub>

V<sub>BIAS</sub>

I<sub>BIAS</sub> (mA)

100.1

10.1

1

.1

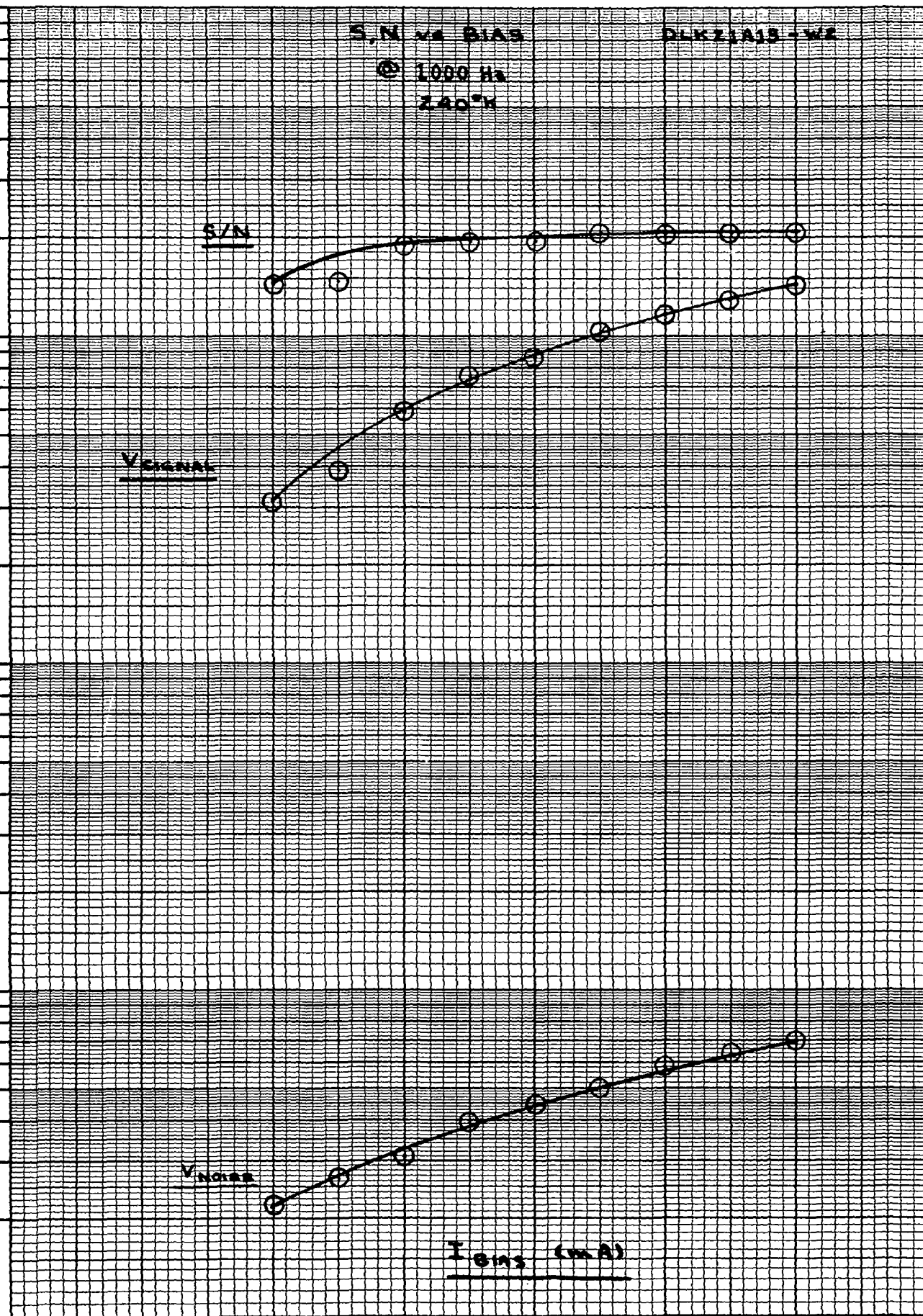
.02

.04

.06

.08

.1



$D^* \lambda$  vs BIAS

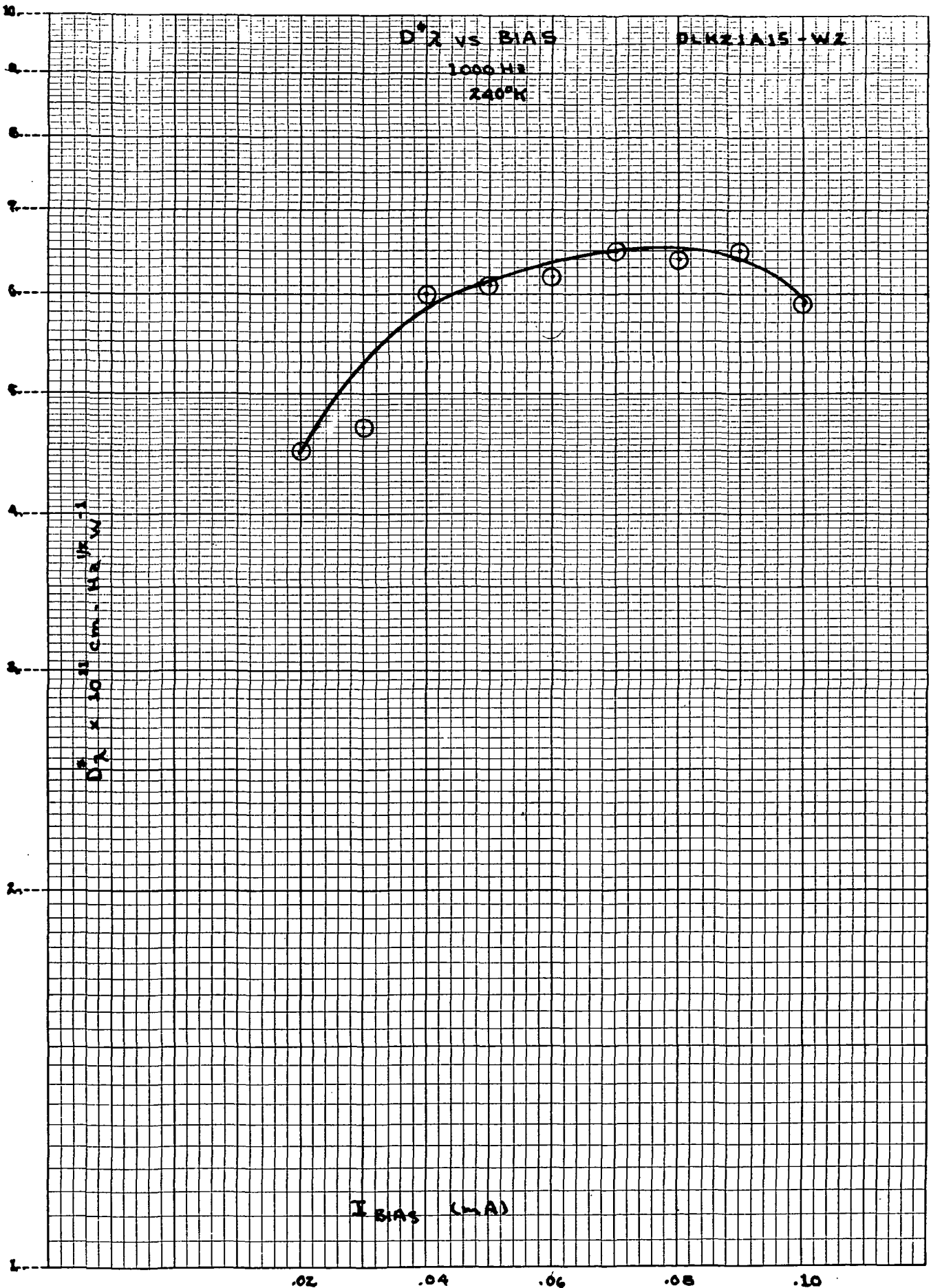
DLKZ-1A15 - WZ

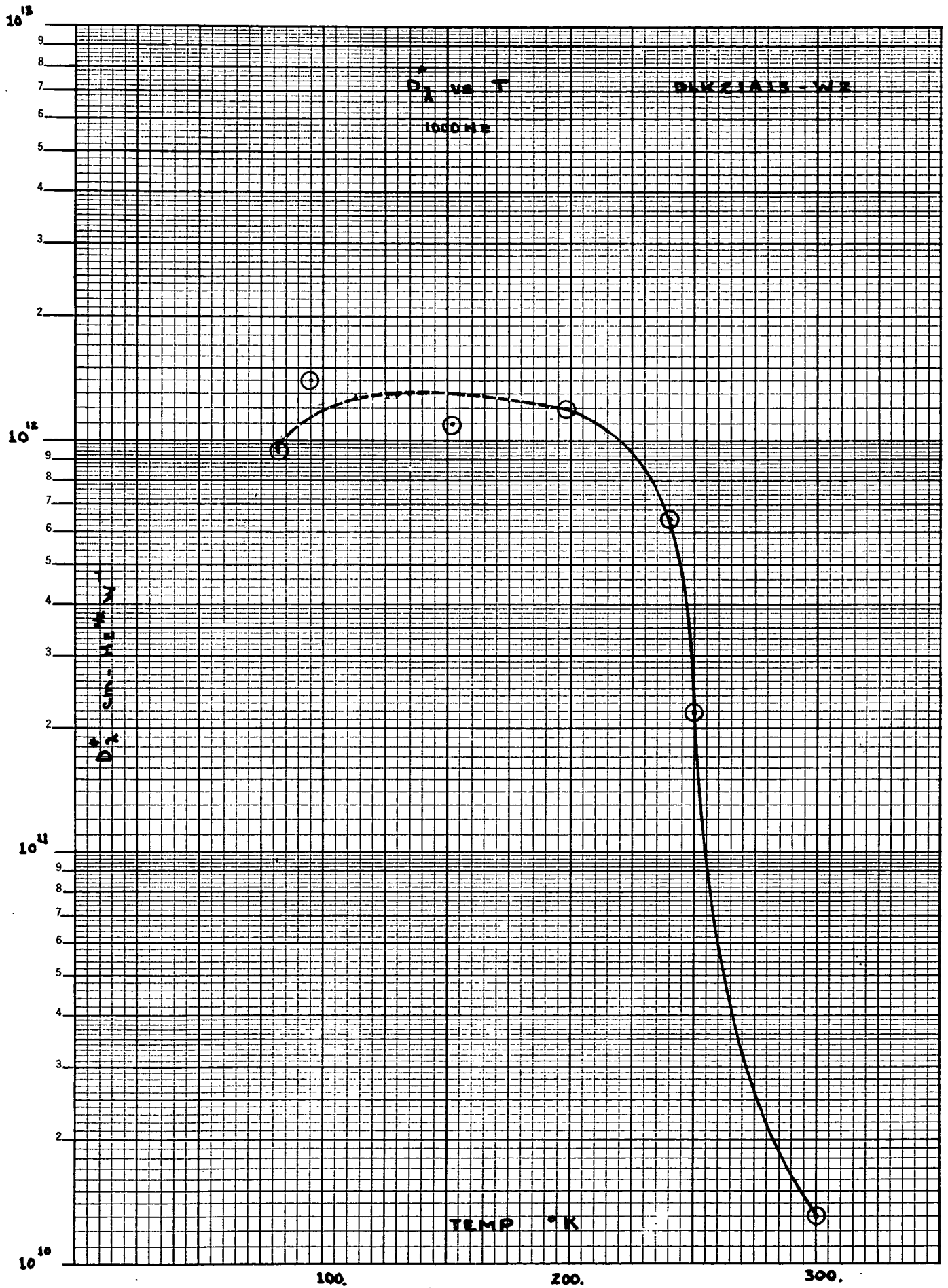
1000 Hz

240°K

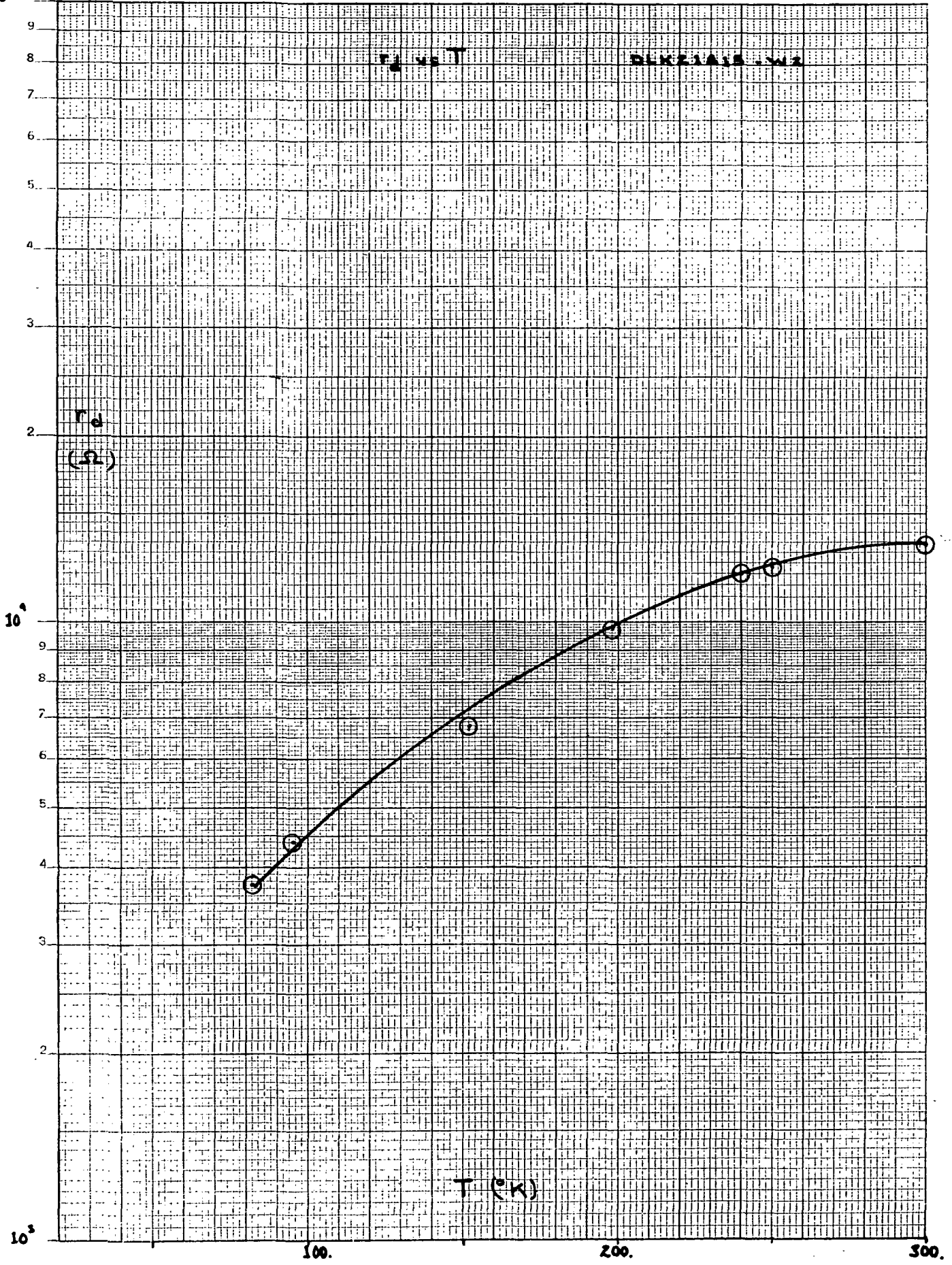
$D^* \lambda \times 10^{11} \text{ cm}^2 \text{ Hz}^{-1/2} \text{ W}^{-1/2}$

I BIAS (mA)





$10^5$



$R_d$   
( $\Omega$ )

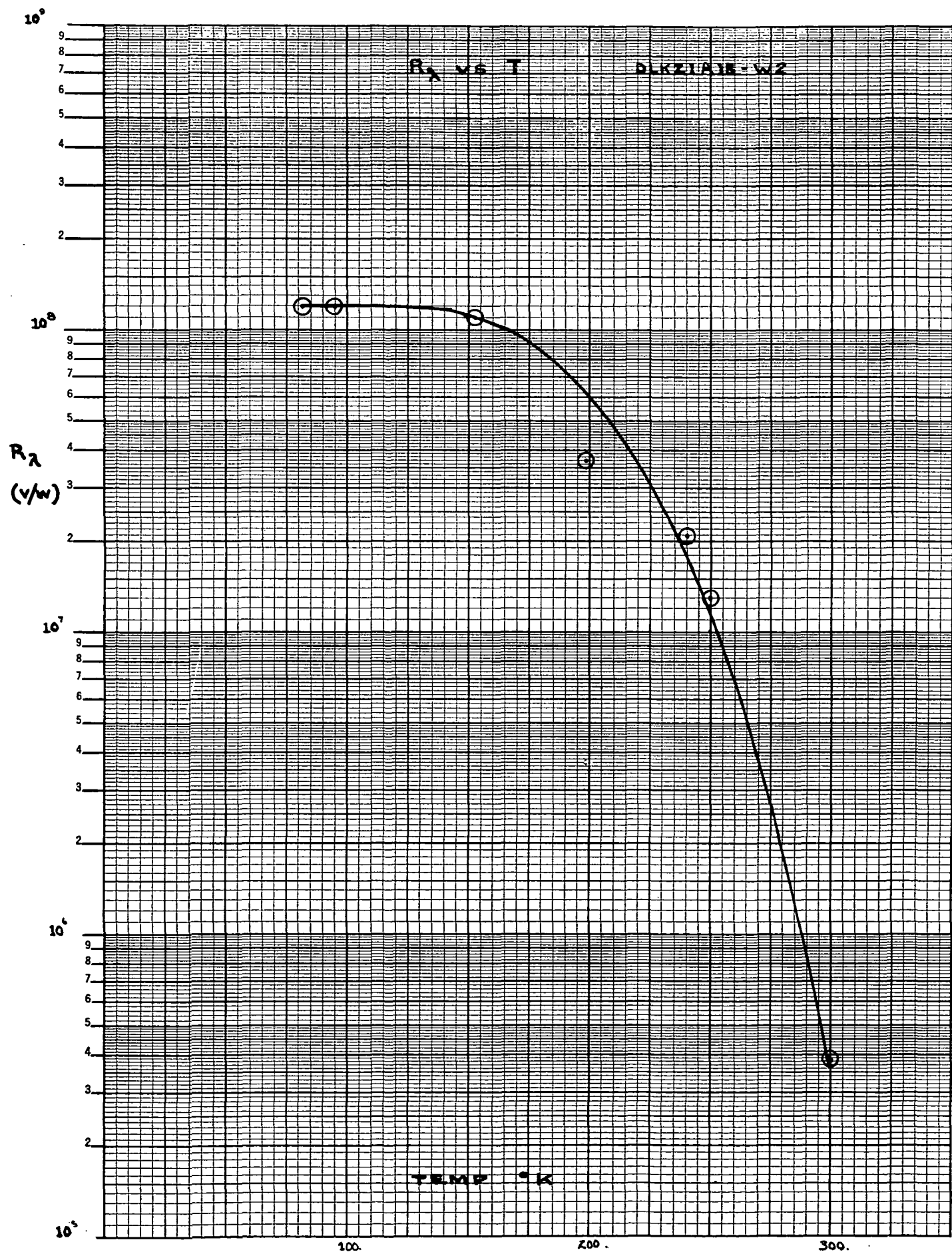
$T$  ( $^{\circ}K$ )

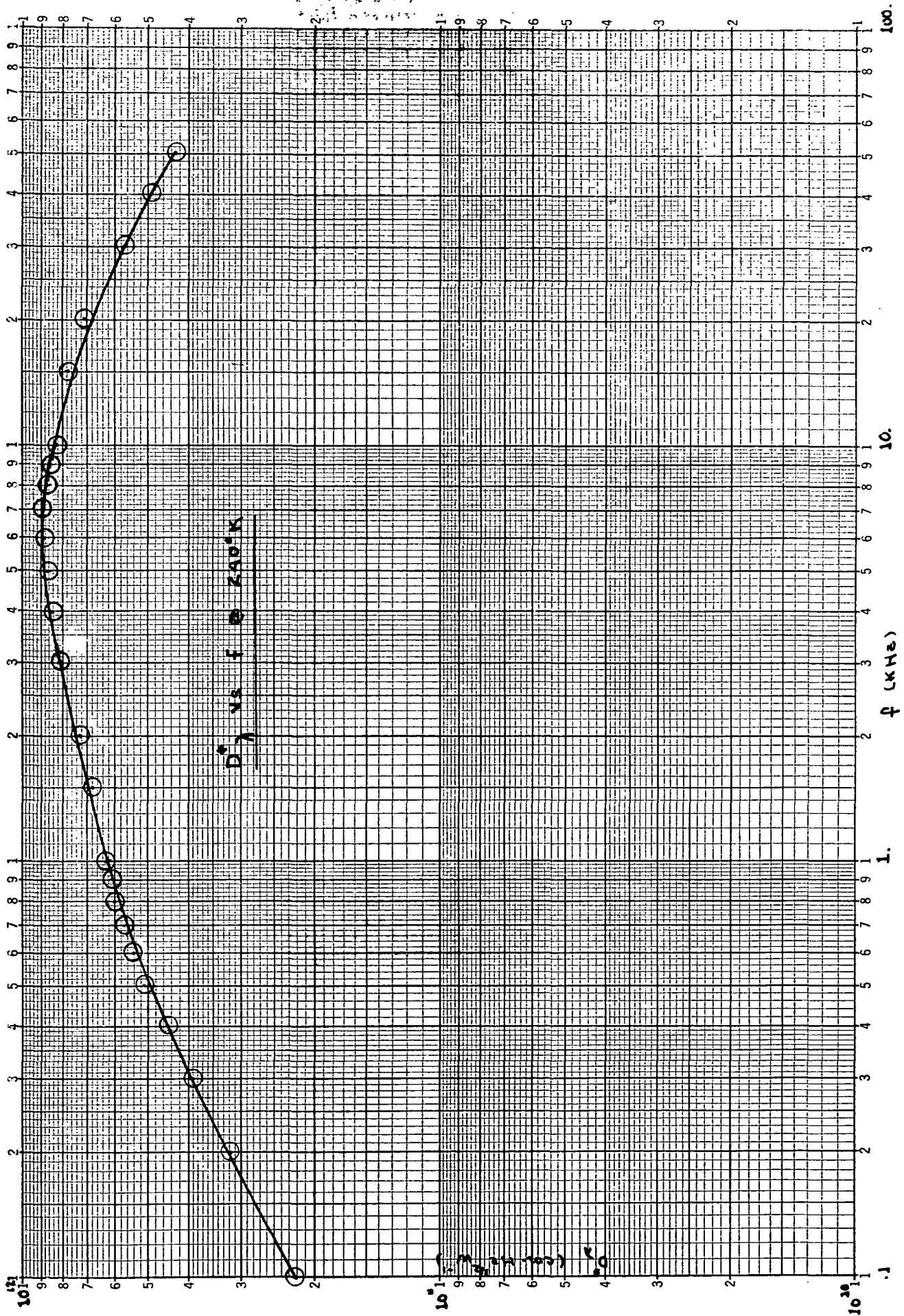
$10^3$

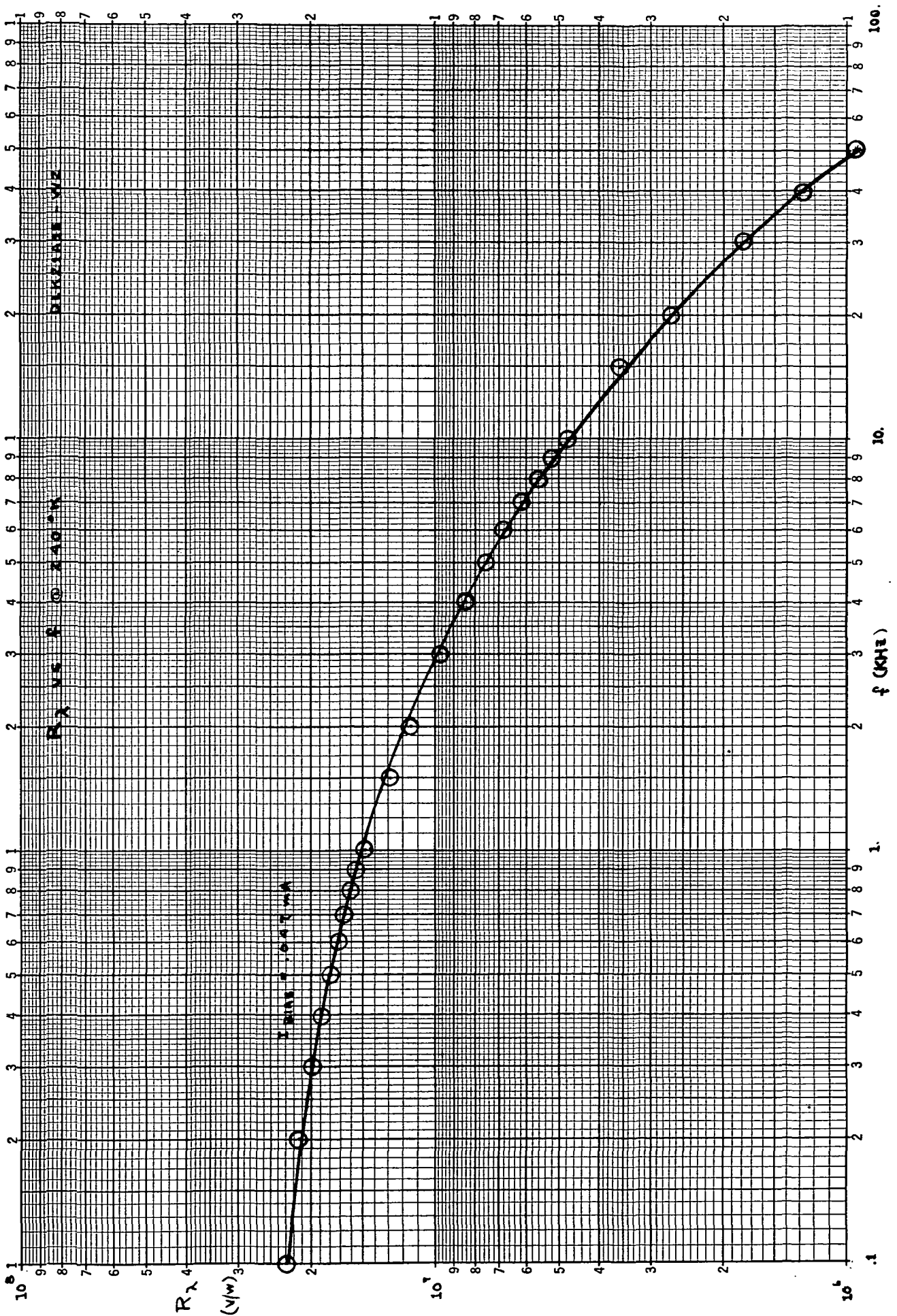
100.

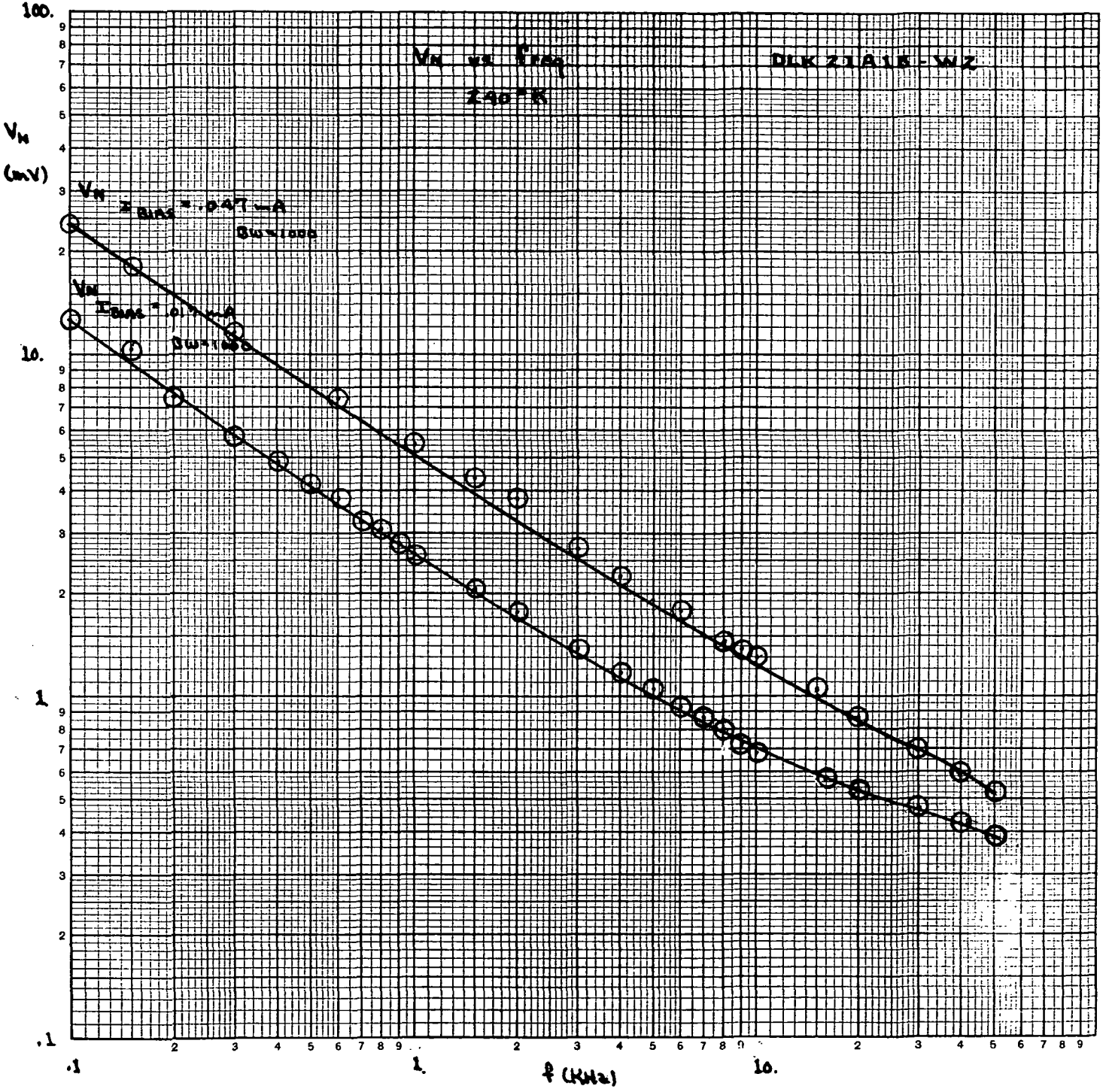
200.

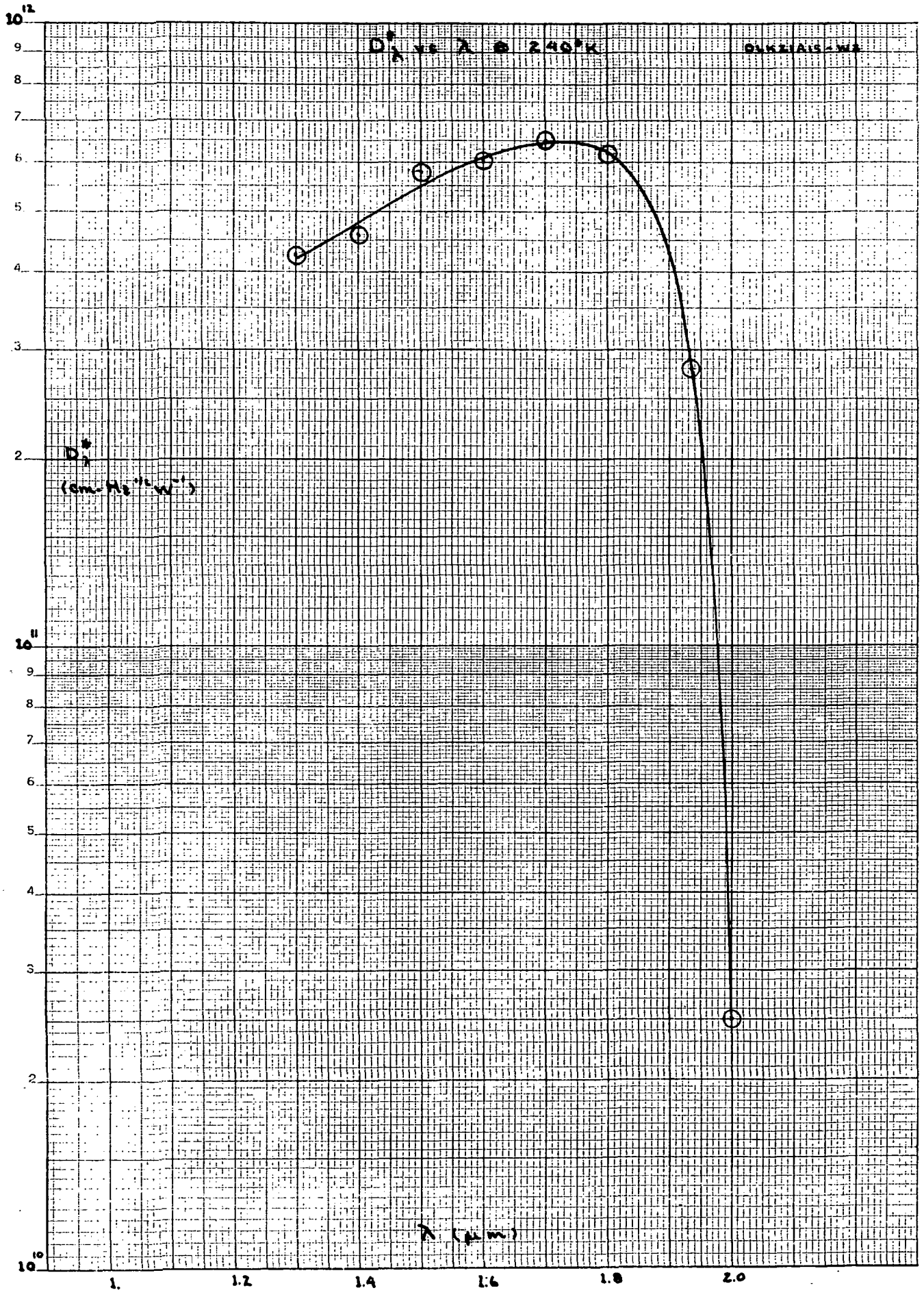
300.

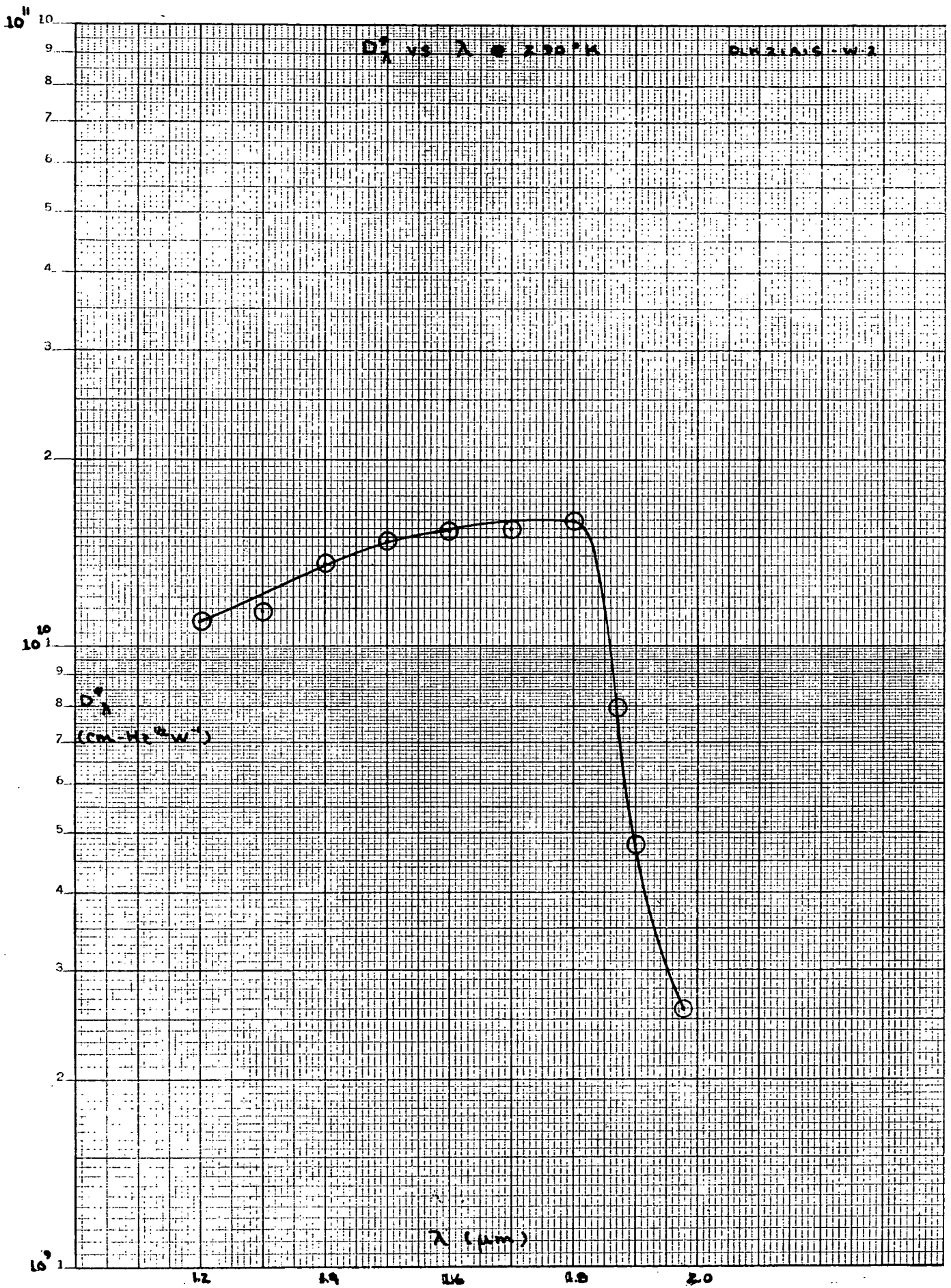




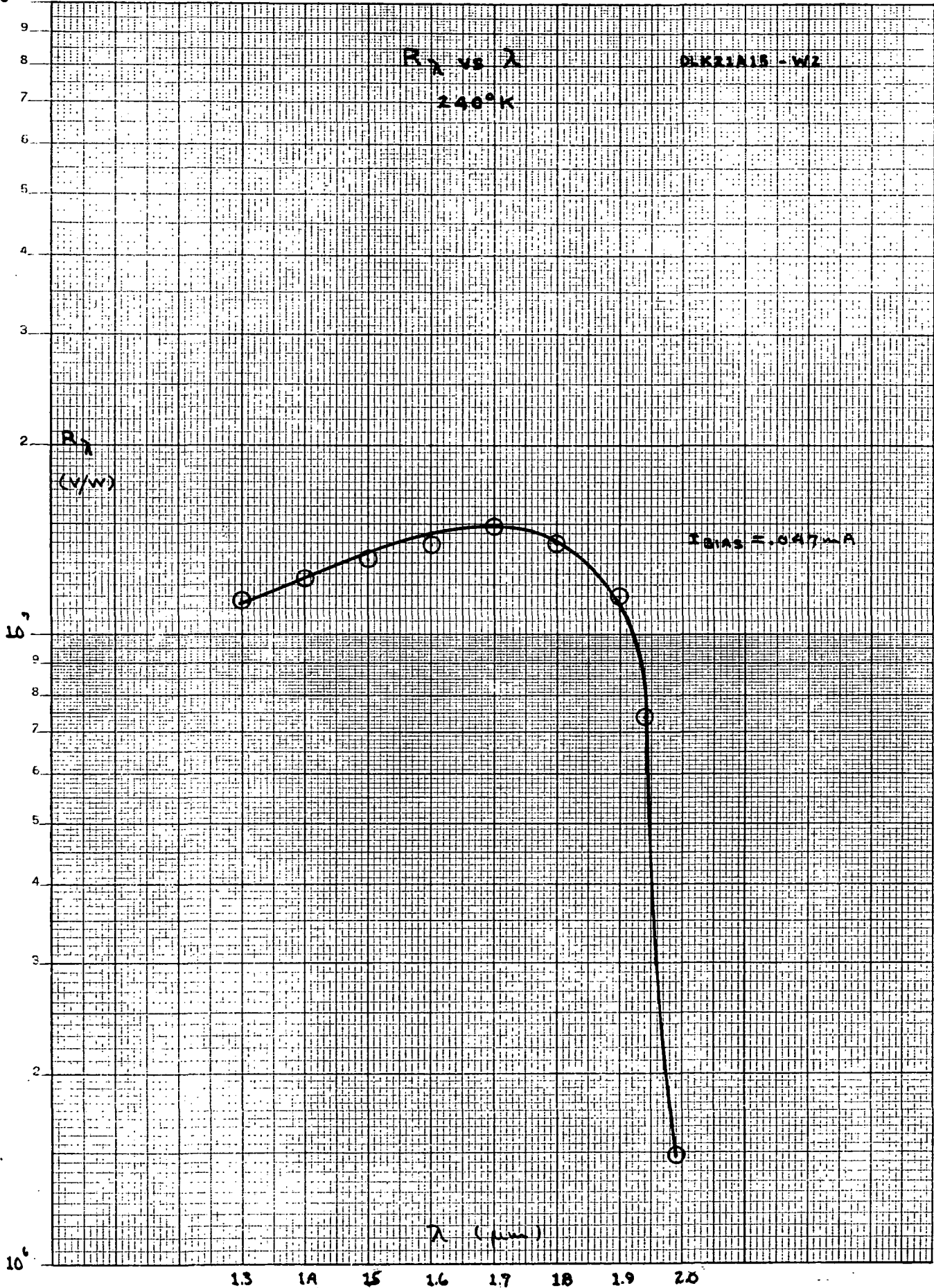




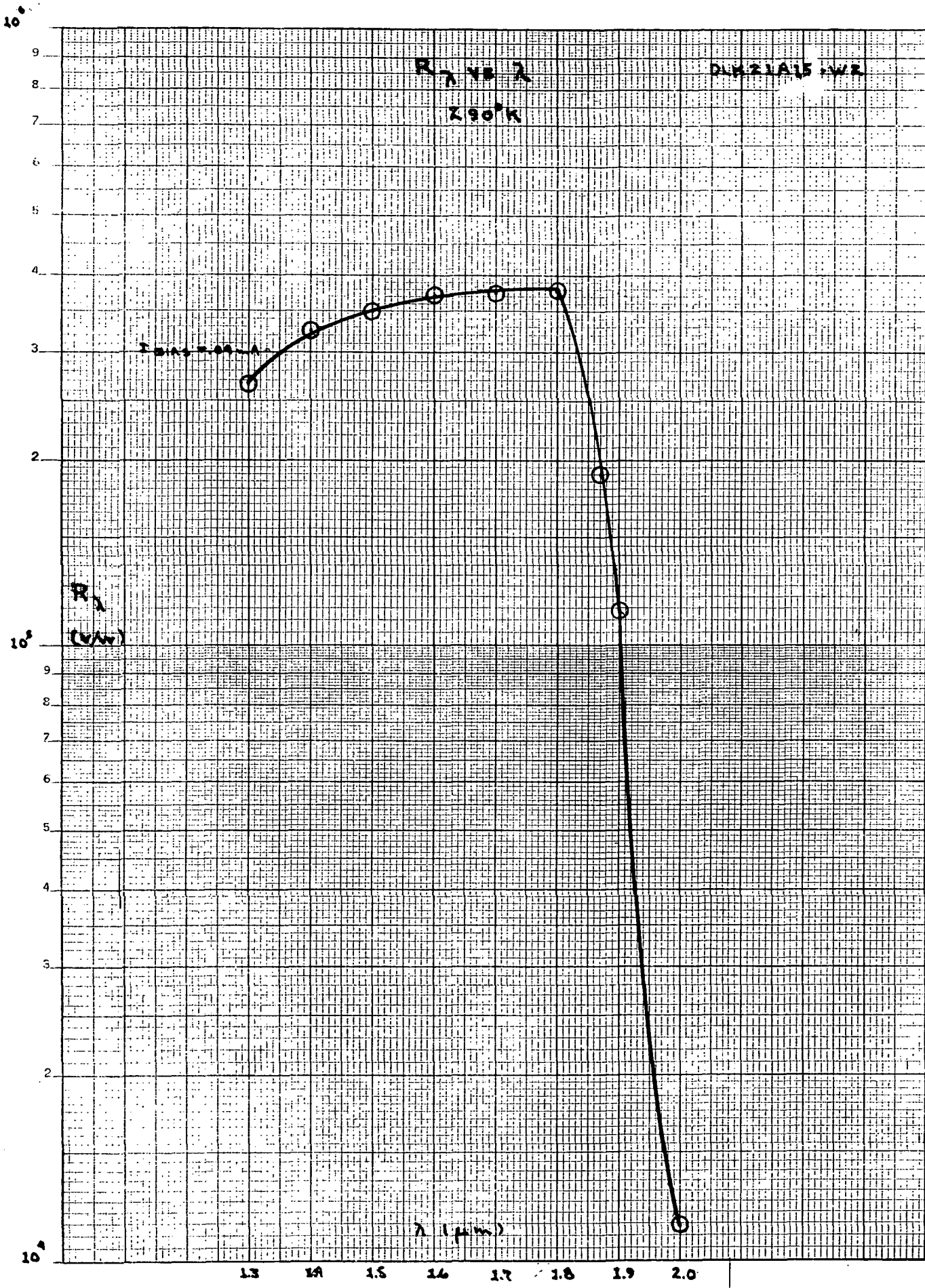




$10^8$



$10^6$



#### 4.0 HANDLING AND PRECAUTIONS FOR HRC PRECISION I.R. DETECTORS

This precision infrared detector was built in the laboratories of the Honeywell Radiation Center under the utmost care. This device was produced using some of the most modern technology in existence. However, as with any precision piece of equipment, there are tolerance limitations to which it can be subjected physically, thermally, and electrically.

##### 4.1 Operating Temperature

The device is designed to operate at the approximate temperatures noted in Section 1.0 of this report.

##### 4.2 Storage

This unit is designed to be stored at temperatures up to 185°F (85°C) for short periods of time. Do not exceed this limit. Prolonged exposure to high temperatures may produce a degradation of device performance.

##### 4.3 Window and Housing

Parts may crack or break if subjected to high impact. Always transport device in the container in which it was shipped.

##### 4.4 Detector Element Burnout

The detector element is capable of dissipating only milliwatts of power. Do not over bias.

A. Caution: If lead from detector device should break contact with the test circuit:

1. Turn off bias and amplifier power source.
2. Discharge coupling capacitor by shorting test leads.
3. Re-connect detector element to bias supply.
4. Turn bias power on again.

B. When the detector is connected to any power source, there must be no voltage differential between the contacts until after circuit is complete.

C. Do not use any amplifier circuitry that will produce current into detector or generate current surges.

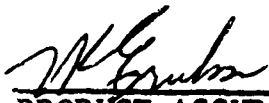
- D. If the detector is operated in the cooled condition with a cooling unit that may malfunction without operator's knowledge, the manufacturer suggests that a current/voltage limiter be installed in the bias circuit to prevent a runaway condition when the detector element warms.

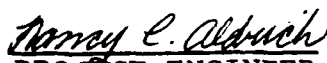
4.5 Normally, the meters used to measure resistance utilize a 1.5 volt battery. The current generated by the battery is sufficient to cause detector burnout. Therefore, if it is necessary to measure resistance, observe the following:

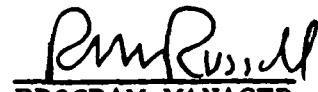
- A. Use wheatstone bridge with an external battery to produce a current/voltage level compatible with the manufacturer's test results.
- B. When the device is in an operating circuit or system, use a VTVM with selector switch set to voltage. Read voltage drop across detector and compute resistance by OHM's Law. Be cautious of power ground loops between VTVM and detector circuitry. Connect common ground first, then connect VTVM to high side of detector. If VTVM is of a high impedance, it is advisable to use a series limiting resistance in VTVM lead. Resistance values up to 1% of VTVM input impedance will cause no voltage reading errors.

TEST REPORT 23971-4  
FOR  
DLK21A15-W4 INFRARED DETECTOR  
FOR  
NASA/GODDARD

CONTRACT NO.  
NAS 5-21646

  
PRODUCT ASSURANCE  
ENGINEER

  
PROJECT ENGINEER

  
PROGRAM MANAGER

Honeywell Inc.  
Radiation Center  
2 Forbes Road  
Lexington, Massachusetts 02173

## TABLE OF CONTENTS

### SECTION

- 1.0 Test Report Summary
- 2.0  $D^*_{BB}$  Derivation
- 3.0 Graphs
- 4.0 Handling and Use Precautions

NOTE: PLEASE READ "HANDLING AND PRECAUTIONS"  
BEFORE USING THIS DETECTOR

# ELEVATED OPERATING TEMPERATURE NEAR INFRARED PHOTODETECTOR

## TEST REPORT

Manufacturer  
**HONEYWELL RADIATION CENTER**  
 2 Forbes Road  
 Lexington, Massachusetts 02173

Detector Number - DLK21A15-W/4

Date of Measurements -

### DETECTOR DESCRIPTION

Type	HgCdTe Photo-conductive
Dimensions	$9.63 \times 10^{-3}$ cm. X $1.06 \times 10^{-2}$ cm
Sensitive Area, A	$9.8 \times 10^{-5}$ cm <sup>2</sup>
Window Material	Sapphire
Field of View	$69^{\circ} 34'$ Degrees
Resistance	ohms @ 240°K 499
Optimum Bias Current	/ ma

### CONDITIONS OF MEASUREMENT

Detector Temperature	240 °K
Chopping Frequency	5000 Hz
Noise Bandwidth $\Delta f$	6.2 Hz
Blackbody Temperature $T_{BB}$	1000 °K
Amplifier Gain	$10^3$ nominal
Distance - Source to Det. $d$	33 cm
Blackbody Aperture Shape & Size	Circular 0.0125 in Dia.
Spectral Wavelength Intervals	.1 $\mu$ m

### TEST RESULTS @ OPT. BIAS

Signal, S	1.1 mv
Noise, N	.052 mV
$D^*_{BB}$	$8.0 \times 10^9$ cm Hz <sup>1/2</sup> /watt
$R_{BB}$	$1.3 \times 10^4$ volts/watt
$P_n$ [NEP]	$2.34 \times 10^{-11}$ watts/Hz <sup>1/2</sup>
$\lambda_{peak}$	2.3 $\mu$ m
$D^*_{\lambda pk}$	$6.9 \times 10^{10}$ cm Hz <sup>1/2</sup> /watt
$R_{\lambda pk}$	$1.12 \times 10^5$ volts/watt
$\tau_{response}$	6.15 $\mu$ s
$\tau_{detective}$	2.05 $\mu$ s @ 1.25 ma

$$D^*_{BB} = \frac{1.10 \times 10^{12} (\Delta f)^{1/2} d^2 S/N}{(\epsilon_{BB} T_{BB}^4 - \epsilon_c T_c^4) A^{1/2} A_{BB}}$$

(see attached derivation)

$T_c$  = chopper blade temp. = 300°K  
 $\epsilon_c$  = chopper blade emissivity  $\approx$  1.0  
 $\epsilon_{BB}$  = blackbody emissivity  $\approx$  1.0  
 $A_{BB}$  = area of blackbody aperture (cm<sup>2</sup>)

### Radiant Signal Wave Shape and Amplitude

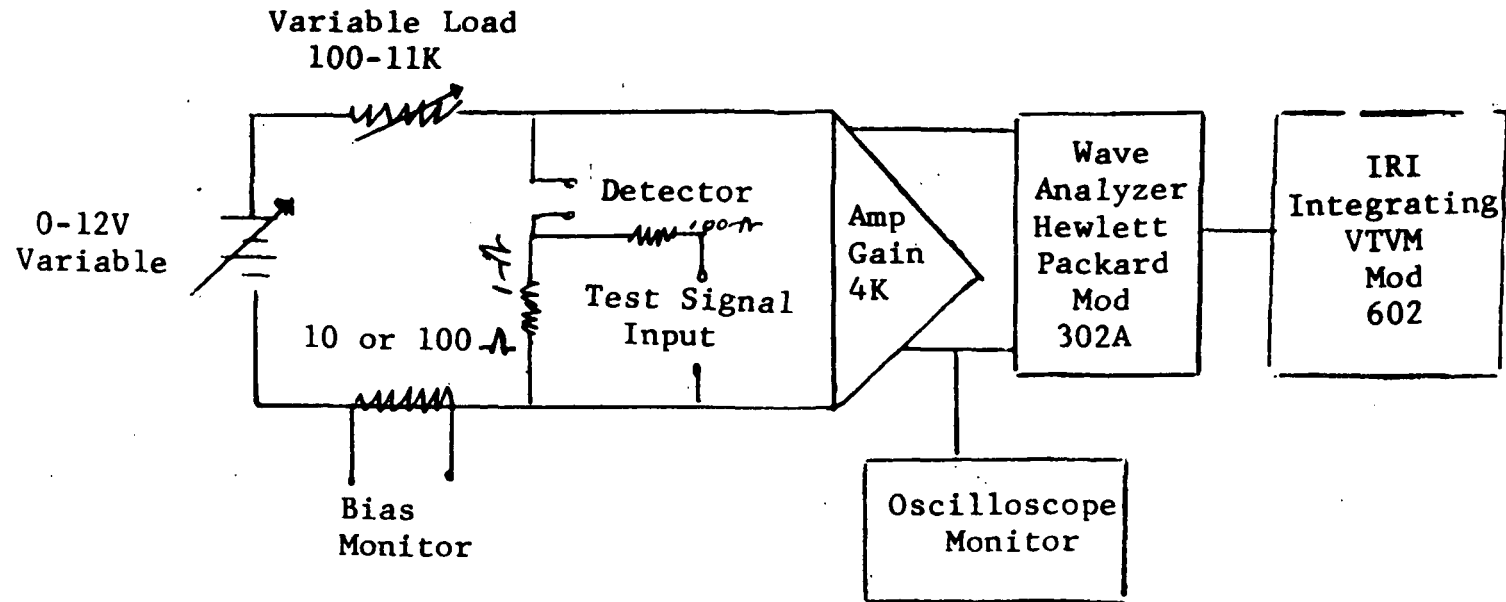
$$N(t) = \frac{\pi R^2}{2} I_0 \left\{ 1 - \frac{4R}{r} \sum_{K=1}^{\infty} \left( \frac{2r}{K\pi R} \right)^2 J_K \right.$$

$$\left. \cdot \left( \frac{K\pi R}{2r} \right) \sin \frac{K\pi}{2} \cos K\omega t \right\}$$

where:  $I_0$  = radiant emittance from source (watts-cm<sup>-2</sup>)  
 $2R$  = source aperture dia.  
 $2r$  = chopper tooth width (inches) = 0.1987  
 $J_K$  = 1st order Bessel function

ref: R.B. McQuistan, Journal of the Optical Society of America, 48, 1, 63, Jan. '58

Detector Readout Circuitry



## 2.0 $D_{BB}^*$ Derivation

The detectivity can be defined as:

$$D^* = \frac{A^{1/2} \Delta f^{1/2} S/N}{P}$$

Where:  $A$  = Sensitive area of the detector, in square centimeters.  
 $\Delta f$  = Frequency bandwidth of the noise measuring circuit in Hertz  
 $S/N$  = Signal to noise ratio of the detector  
 $P$  = Input signal power

The input power is:

$$f = \frac{\phi A_{BB} A}{d^2}$$

Where:  $A_{BB}$  = Area of blackbody aperture in square centimeters  
 $\phi$  = Flux density of the emitted irradiance in volts per square centimeter of blackbody aperture area  
 $d$  = Distance between blackbody & incident plans of detector

Calculation of flux density,  $\phi$ , is as follows:

$$\phi = \frac{\sigma (\epsilon_{BB} T_{BB}^4 - \epsilon_c T_c^4)}{(\pi c_1)}$$

Where:  $\sigma$  = Stefan Boltzman constant =  $5.6686 \times 10^{-12}$  Watts  
 $\text{cm}^{-2} \text{ } ^\circ\text{K}^{-4}$

$\epsilon_{\text{BB}}$  = Blackbody emissivity

$T_{\text{BB}}$  = Blackbody temperature

$\epsilon_{\text{c}}$  = Chopper blade emissivity

$T_{\text{c}}$  = Chopper blade temperature

$c_1$  = rms factor for chopper and blackbody aperture

$\pi$  = 3.1416

The input power is:

$$P_{\text{BB}} = \frac{\sigma (\epsilon_{\text{BB}} T_{\text{BB}}^4 - \epsilon_{\text{c}} T_{\text{c}}^4) A_{\text{BB}} A}{d^2 (\pi c_1)}$$

$D^*_{\text{BB}}$  is:

$$D^*_{\text{BB}} = \frac{(\Delta f)^{\frac{1}{2}} d^2 (\pi c_1) S / (kN)}{\sigma (\epsilon_{\text{BB}} T_{\text{BB}}^4 - \epsilon_{\text{c}} T_{\text{c}}^4) A_{\text{BB}}^{\frac{1}{2}}}$$

Where:  $k$  = Experimentally determined correction factor for  
Hewlet Packard wave analyzer noise readings = 1.12

The rms chopping factor for an 80 blade chopper and .0125 inch diameter operation is 2.24. Thus combining constants and neglecting the  $(\epsilon_{\text{c}} T_{\text{c}}^4)$  terms.

$$D^*_{\text{BB}} = \frac{1.10 \times 10^{12} (\Delta f)^{\frac{1}{2}} S / N d^2}{\epsilon_{\text{BB}} T_{\text{BB}}^4 A_{\text{BB}}^{\frac{1}{2}}}$$

### 3.0 Graphs

S,N vs Bias @ 1000 Hz, 240 °K

S,N vs Bias @ 5000 Hz, 240 °K

$D^*\lambda$  vs Bias @ 1000 Hz, 240 °K

$D^*\lambda$  vs Bias @ 5000 Hz, 240 °K

$r_d$  vs T

$D^*\lambda$  vs f @ 240 °K

$R_\lambda$  vs f @ 240 °K

$V_n$  vs f @ 240 °K

$D^*\lambda$  vs 1/T @ 5000 Hz

$R_\lambda$  vs 1/T @ 5000 Hz

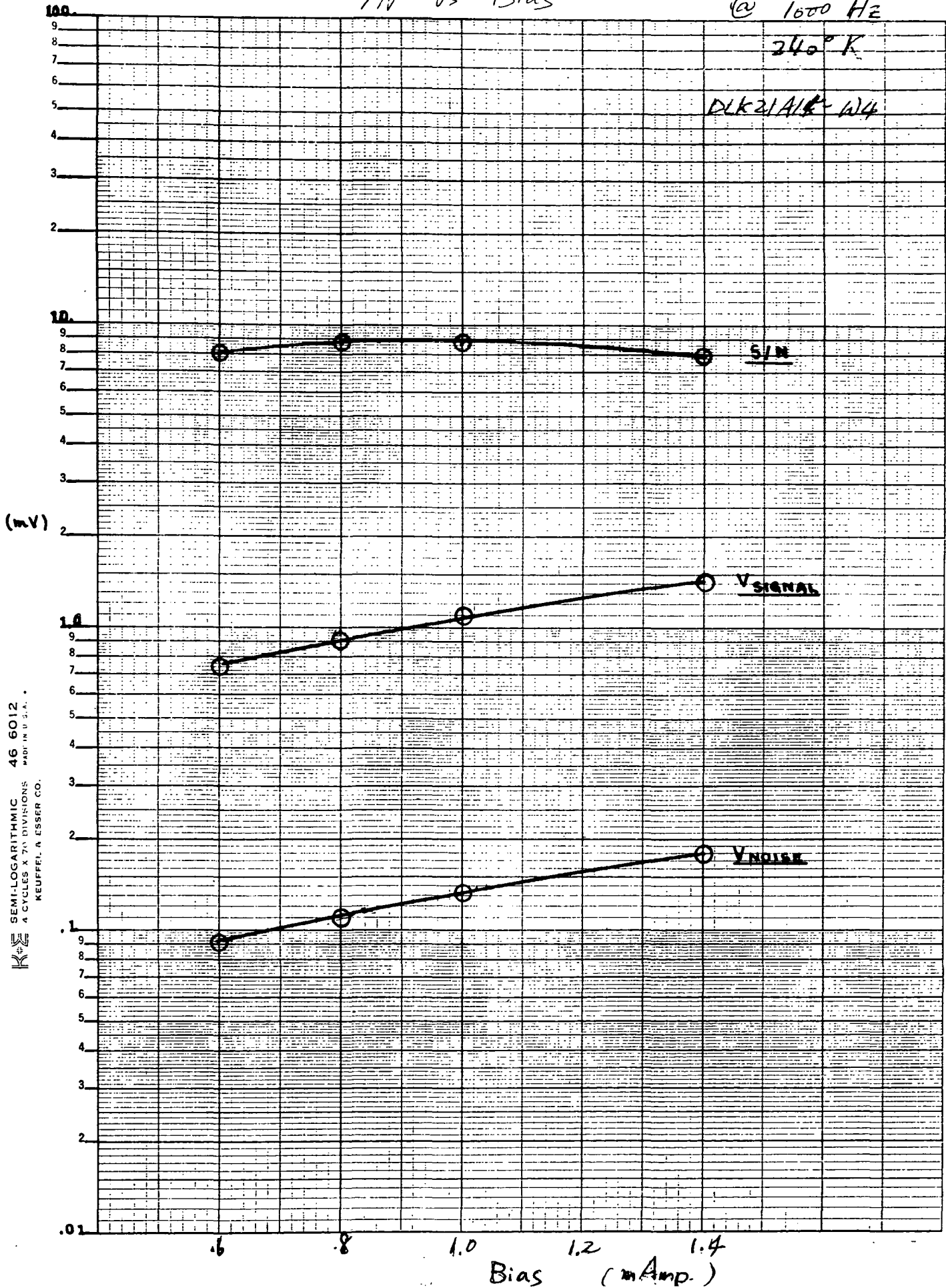
$R_\lambda$  vs  $\lambda$  @ 240 °K

S/N vs Bias

@ 1000 Hz

240° K

DLK21A1K-W4

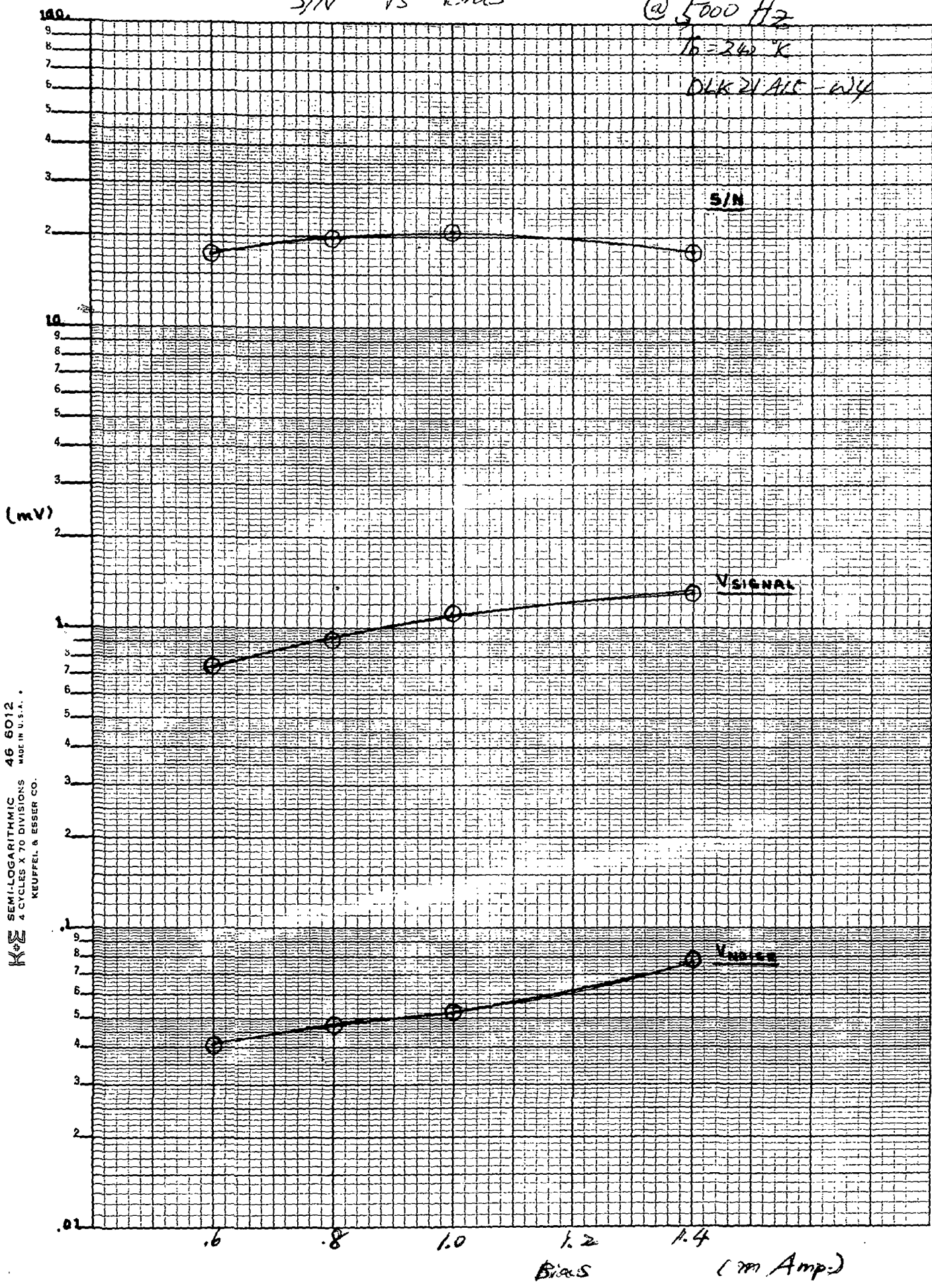


S/N VS BIAS

@ 5000 Hz

$T_0 = 240^\circ K$

DLK 21 ALC - WY



KE SEMI-LOGARITHMIC 46 6012  
4 CYCLES X 70 DIVISIONS  
MADE IN U.S.A.  
KEUFFEL & ESSER CO.

$D_{\lambda}^*$  vs Bias

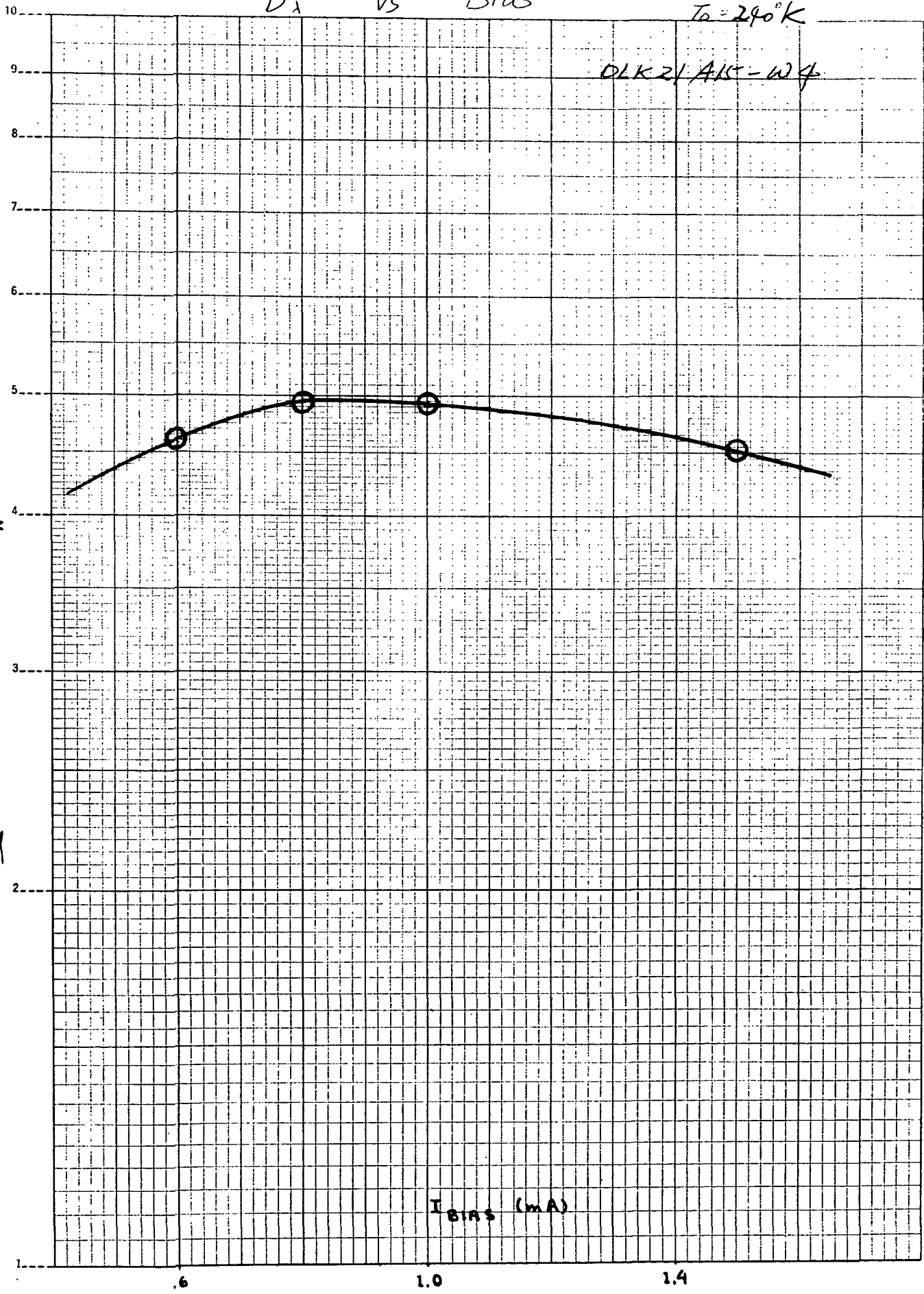
@ 1000 Hz  
 $T_0 = 290^{\circ}K$

DLK 21 A15 - W4

$D_{\lambda}^* \times 10^{10} \text{ cm Hz}^{1/2} \text{ W}^{-1}$

$I_{\text{BIAS}} \text{ (mA)}$

KEE SEMI-LOGARITHMIC 46 4652  
1 CYCLE X 70 DIVISIONS MADE IN U.S.A.  
KEUFFEL & ESSER CO.

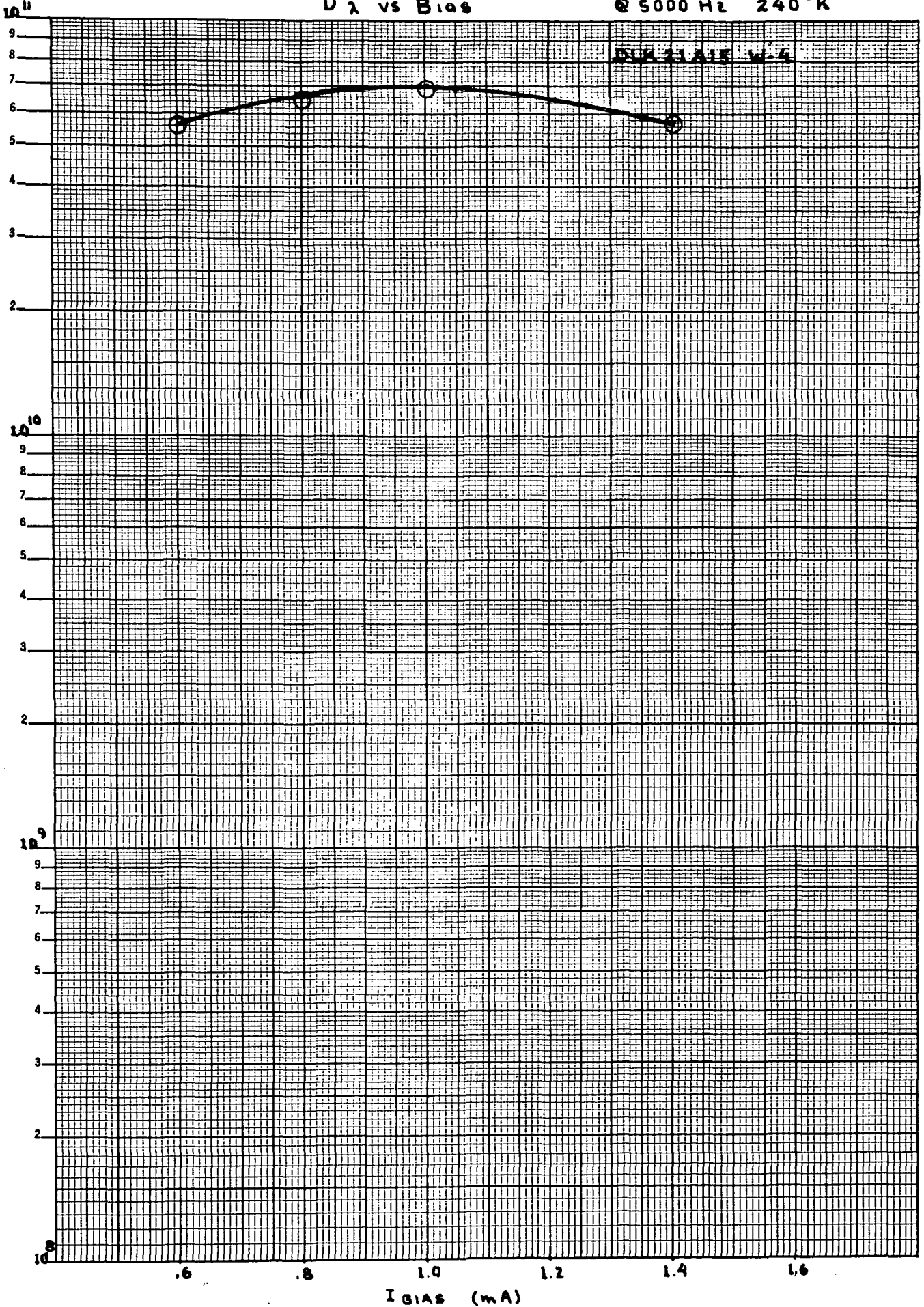


$D_{\lambda}^2 \times 10^{10} \text{ cm Hz}^{-1/2} \text{ W}^{-1}$

$D_{\lambda}^2$  vs Bias

@ 5000 Hz 240°K

DUK 21A15 W 4

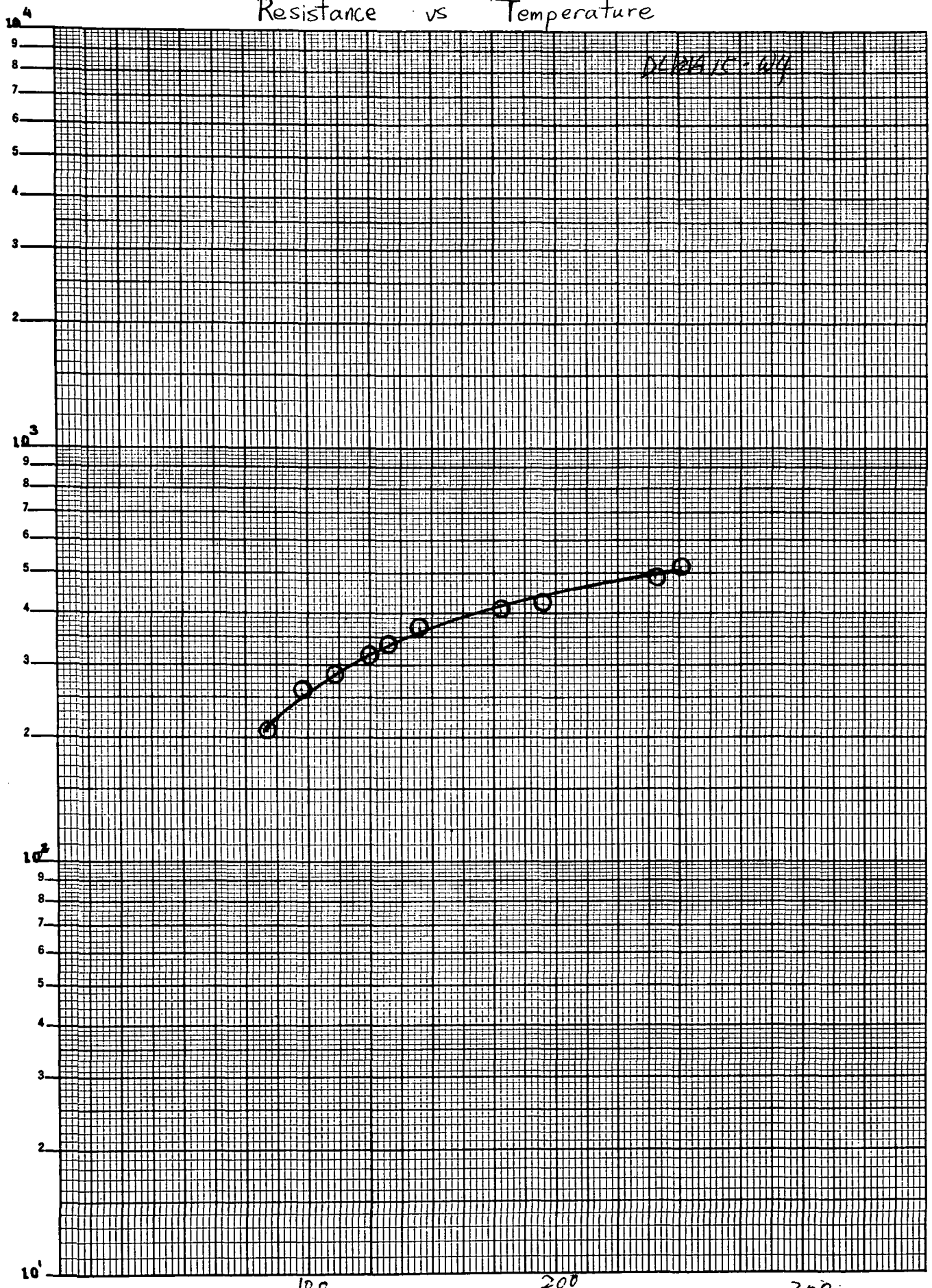


# Resistance vs Temperature

DELTA 15-104

$R_d$  ( $\Omega$ )

K&E SEMI-LOGARITHMIC  
3 CYCLES X 140 DIVISIONS  
MADE IN U.S.A.  
KEUFFEL & ESSER CO.



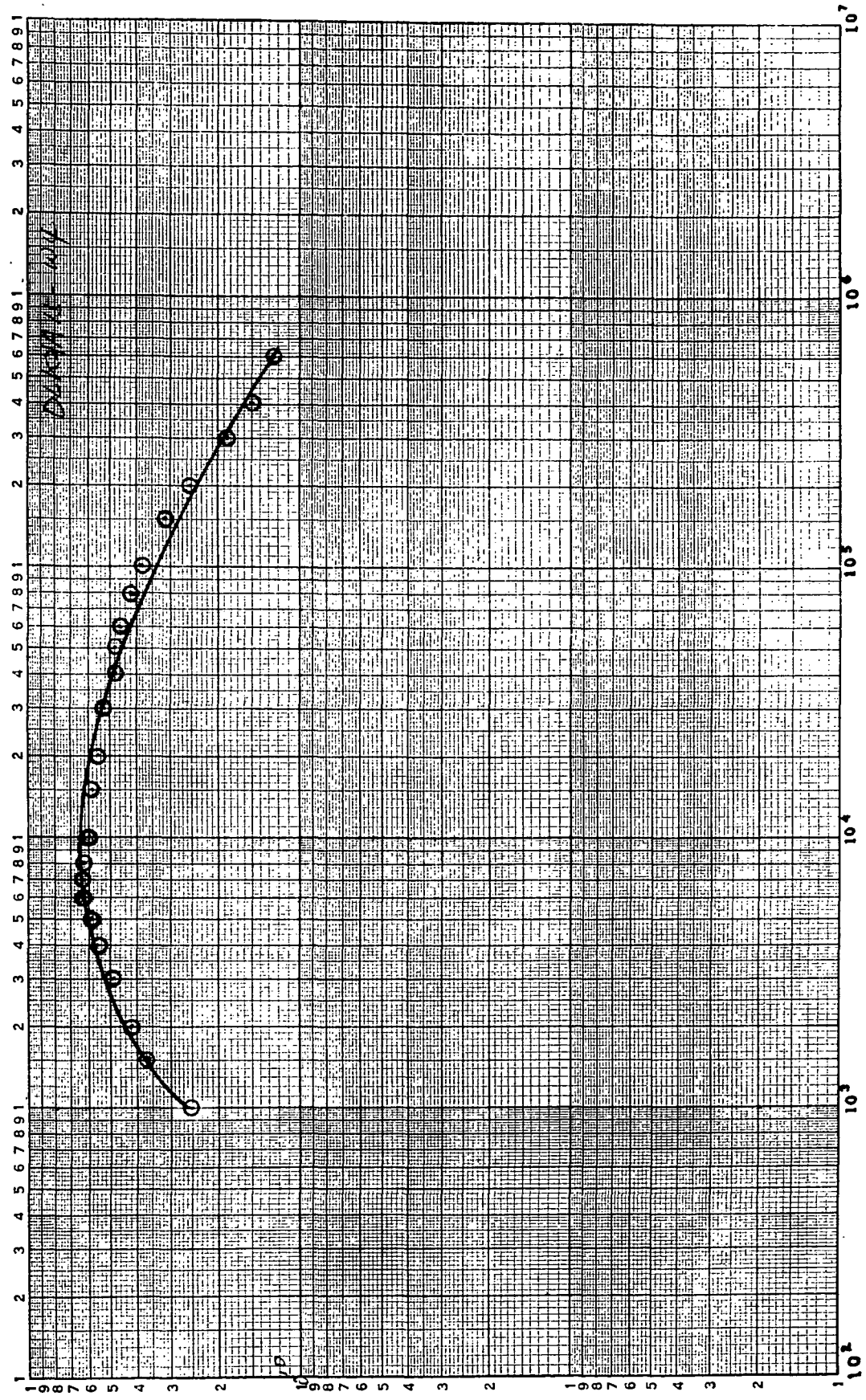
TEMP (°K)

300

$T_D = 240^\circ K$   
 $I_b = 1.25 \text{ mA}$

$D_\lambda^*$  vs frequency

@



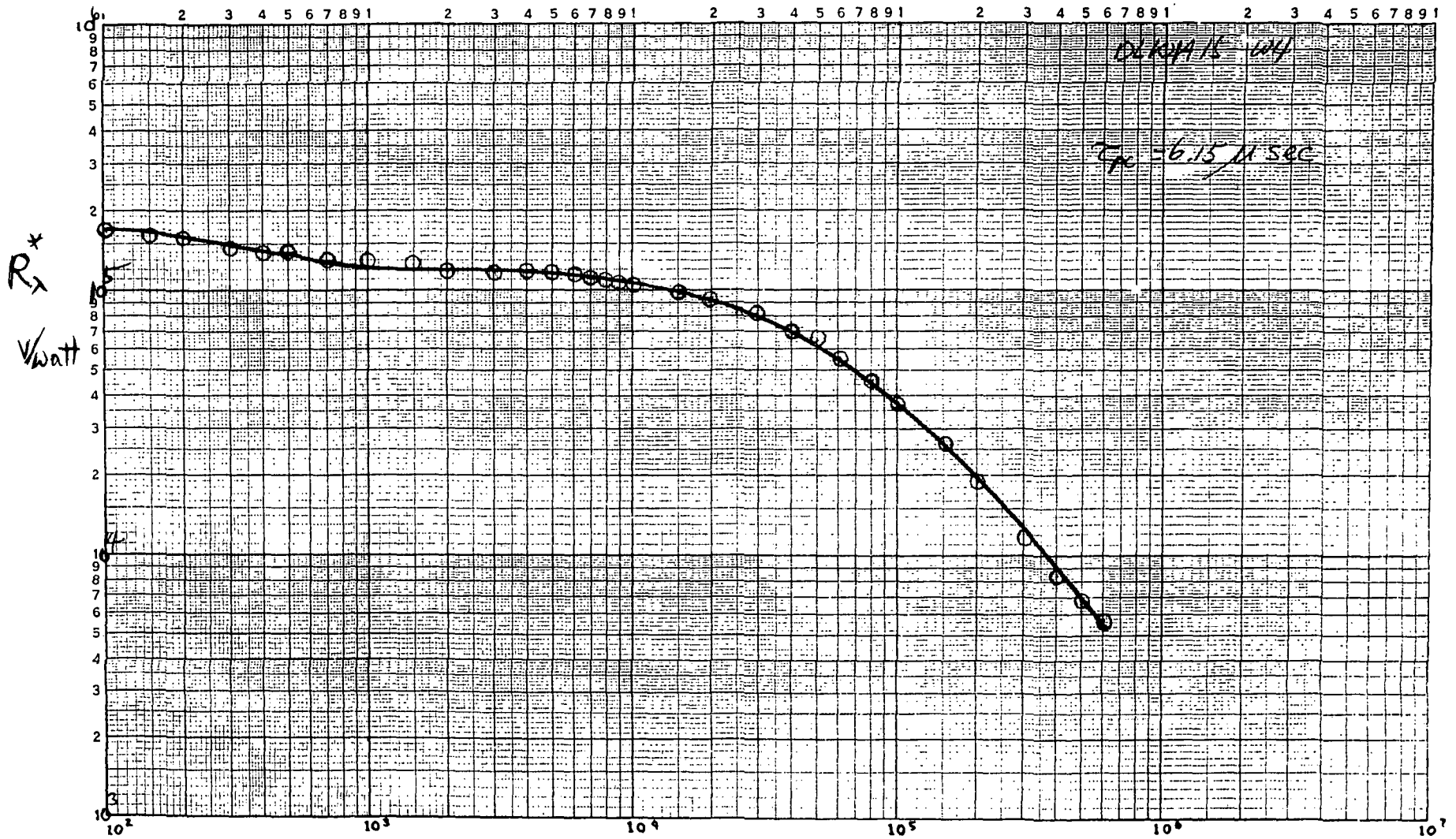
frequency (Hz)

$D_T^*$

$\text{cm}^{1/2} / \text{watt}$

# Responsivity vs Frequency

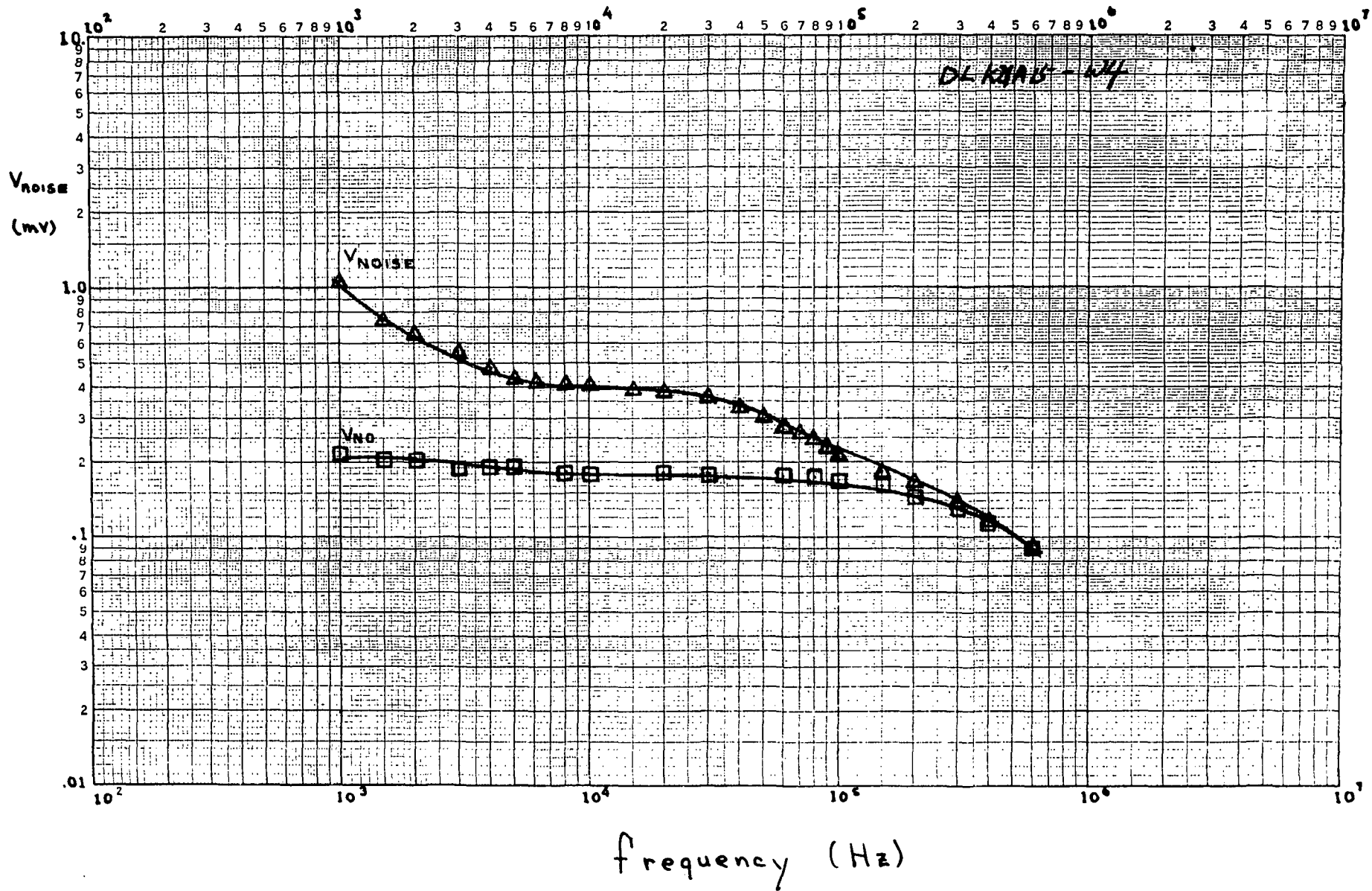
@  $T_D = 240^{\circ}K$   
 $I_b = 1.25mA$



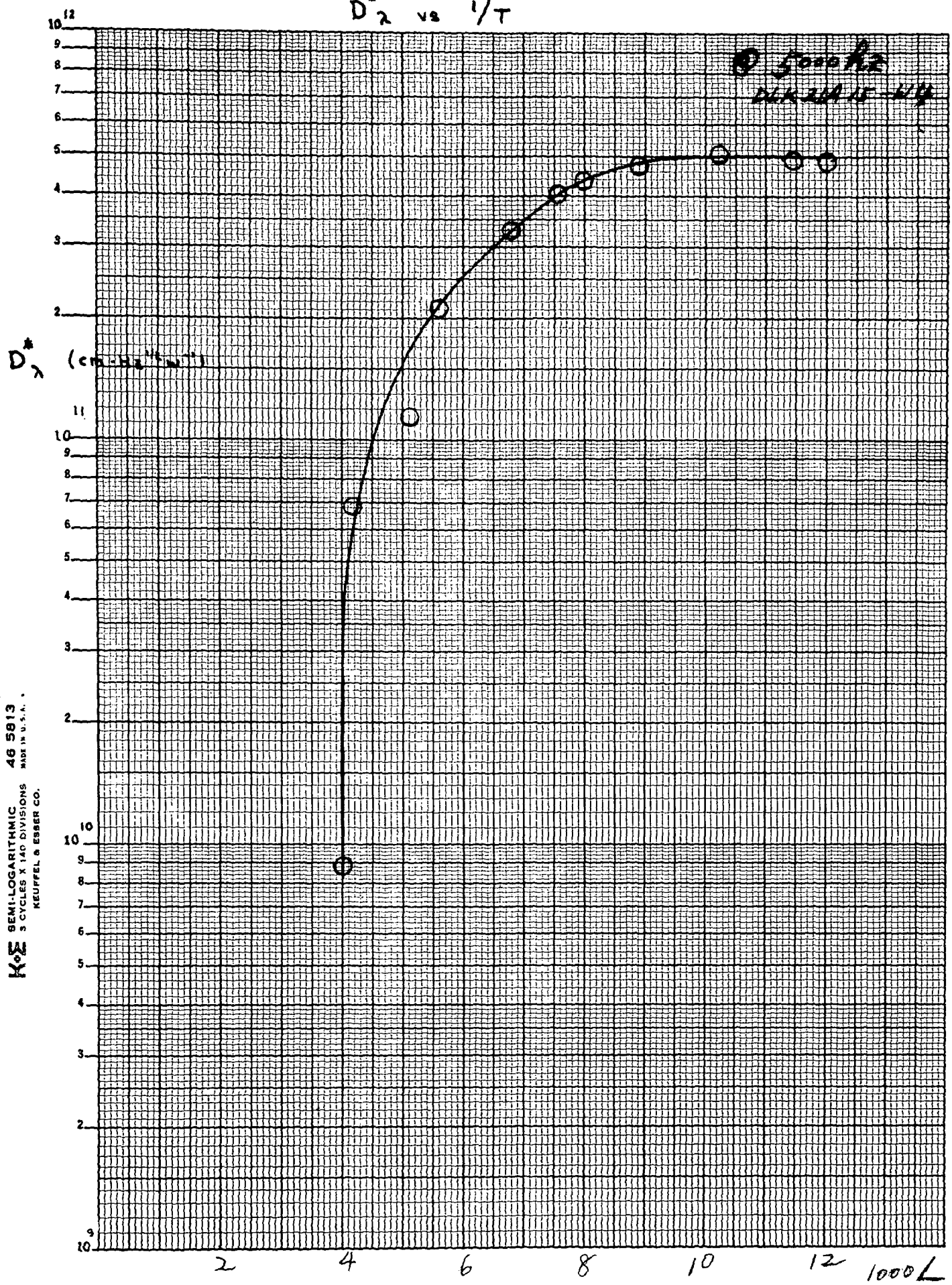
Frequency (Hz)

# Noise vs Frequency

@  $T_D = 240^\circ K$   
 $I_B = 1.25 mA$   
 $\Delta f = 100 Hz$



$D_2^*$  vs  $1/T$



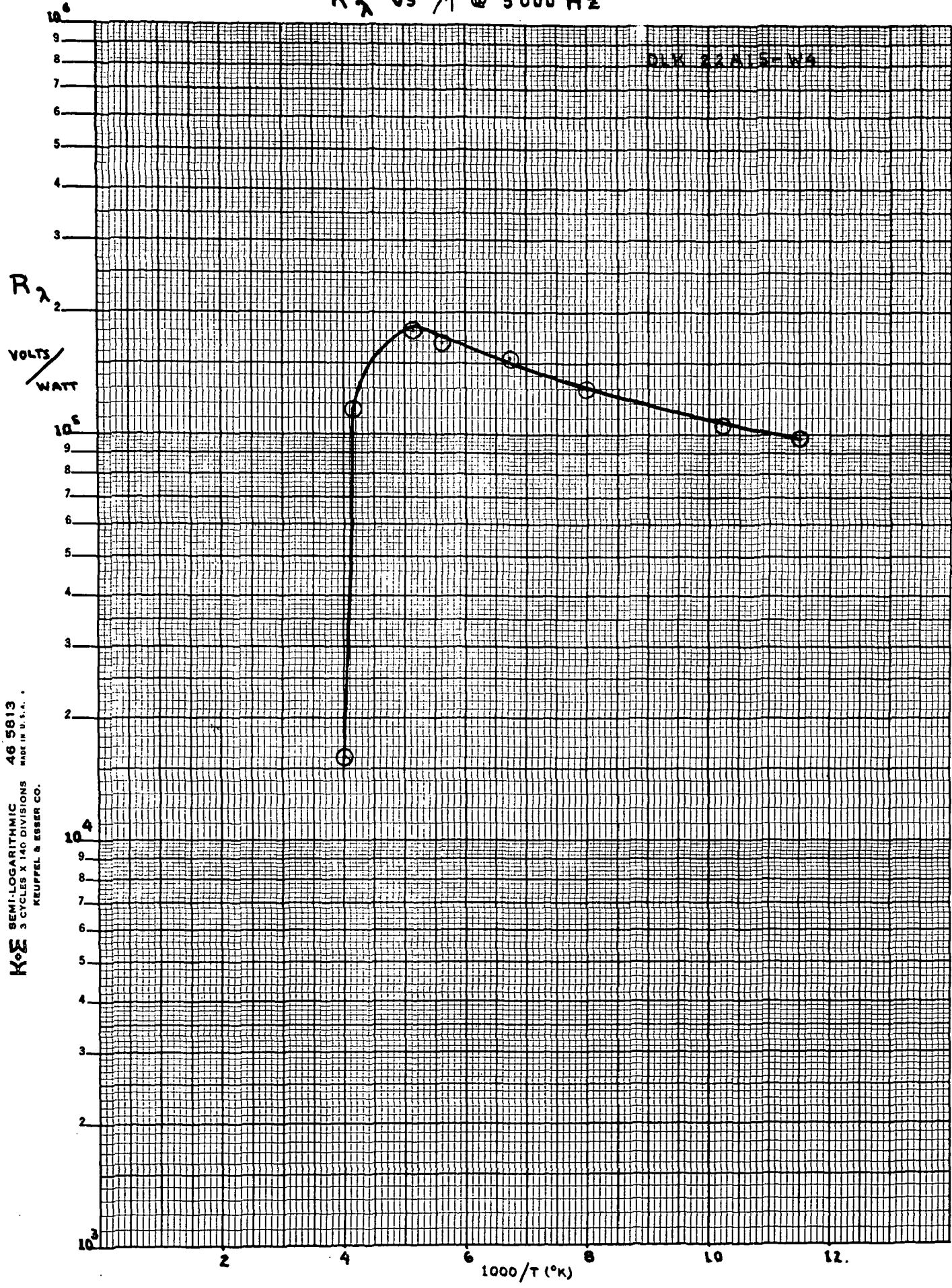
K&E SEMI-LOGARITHMIC 46 5813  
3 CYCLES X 140 DIVISIONS MADE IN U.S.A.  
KEUFFEL & ESSER CO.

$R_{\lambda}$  vs  $1/T$  @ 5000 Hz

DLK 22A15-W4

$R_{\lambda}$

VOLTS  
/  
WATT

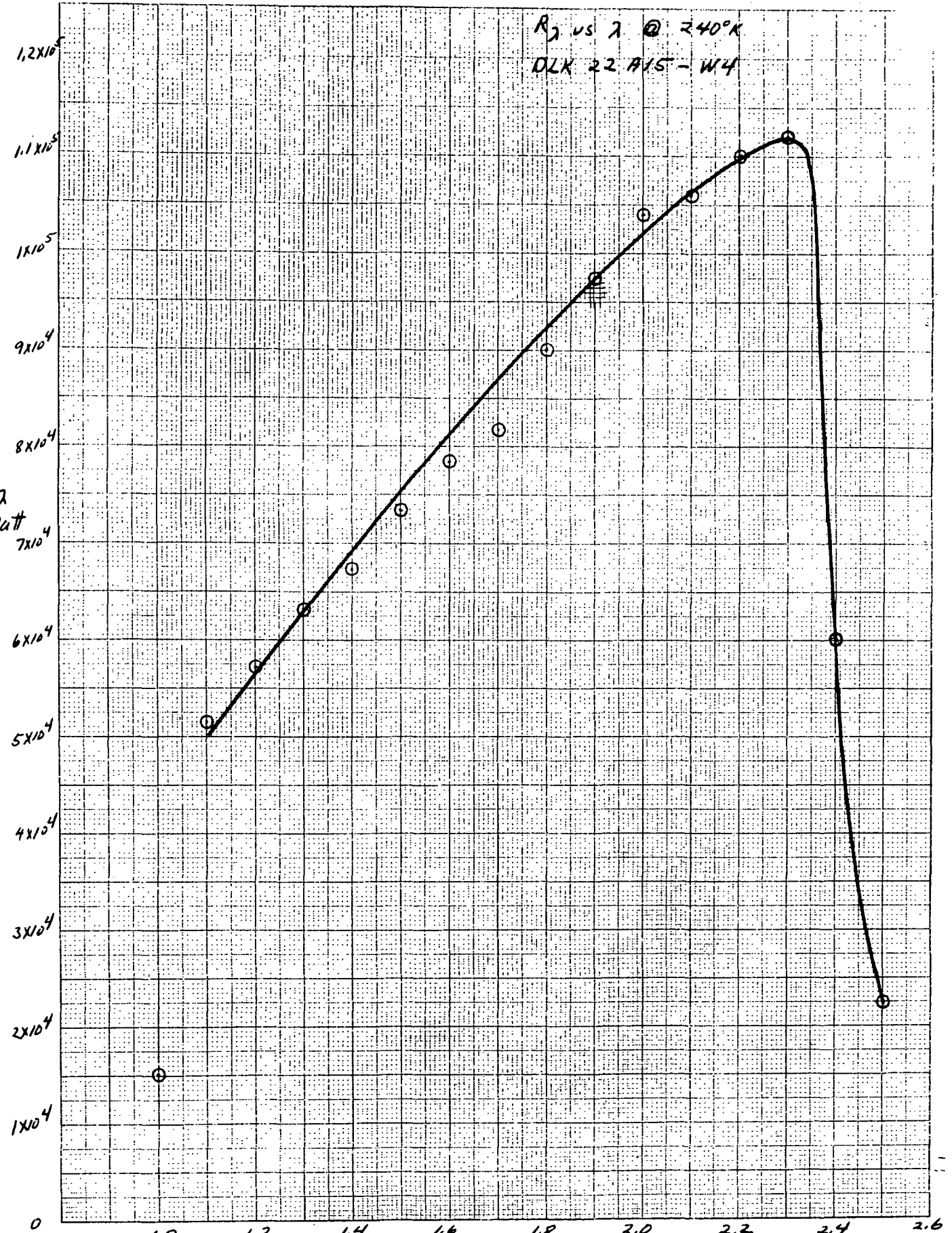


K&E SEMI-LOGARITHMIC  
46 5613  
MADE IN U.S.A.  
3 CYCLES X 140 DIVISIONS  
KRUPP & ESSER CO.

$R_\lambda$  vs  $\lambda$  @ 240°K  
DLK 22 715-W4

$R_\lambda$   
V/watt

19 X 10 TO THE 10TH PERCENTIMETER 46 1510  
REPRODUCED BY THE NATIONAL BUREAU OF STANDARDS



Wavelength ( $\mu\text{m}$ )

#### 4.0 HANDLING AND PRECAUTIONS FOR HRC PRECISION I.R. DETECTORS

This precision infrared detector was built in the laboratories of the Honeywell Radiation Center under the utmost care. This device was produced using some of the most modern technology in existence. However, as with any precision piece of equipment, there are tolerance limitations to which it can be subjected physically, thermally, and electrically.

##### 4.1 Operating Temperature

The device is designed to operate at the approximate temperatures noted in Section 1.0 of this report.

##### 4.2 Storage

This unit is designed to be stored at temperatures up to 185°F (85°C) for short periods to time. Do not exceed this limit. Prolonged exposure to high temperatures may produce a degradation of device performance.

##### 4.3 Window and Housing

Parts may crack or break if subjected to high impact. Always transport device in the container in which it was shipped.

##### 4.4 Detector Element Burnout

The detector element is capable of dissipating only milliwatts of power. Do not over bias.

A. Caution: If lead from detector device should break contact with the test circuit:

1. Turn off bias and amplifier power source.
2. Discharge coupling capacitor by shorting test leads.
3. Re-connect detector element to bias supply.
4. Turn bias power on again.

B. When the detector is connected to any power source, there must be no voltage differential between the contacts until after circuit is complete.

C. Do not use any amplifier circuitry that will produce current into detector or generate current surges.

- D. If the detector is operated in the cooled condition with a cooling unit that may malfunction without operator's knowledge, the manufacturer suggests that a current/voltage limiter be installed in the bias circuit to prevent a runaway condition when the detector element warms.

4.5 Normally, the meters used to measure resistance utilize a 1.5 volt battery. The current generated by the battery is sufficient to cause detector burnout. Therefore, if it is necessary to measure resistance, observe the following:

- A. Use wheatstone bridge with an external battery to produce a current/voltage level compatible with the manufacturer's test results.
- B. When the device is in an operating circuit or system, use a VTVM with selector switch set to voltage. Read voltage drop across detector and compute resistance by OHM's Law. Be cautious of power ground loops between VTVM and detector circuitry. Connect common ground first, then connect VTVM to high side of detector. If VTVM is of a high impedance, it is advisable to use a series limiting resistance in VTVM lead. Resistance values up to 1% of VTVM input impedance will cause no voltage reading errors.

APPENDIX B  
NEAR INFRARED (Hg,Cd)Te PHOTODETECTORS

[N. C. Aldrich and T. Koehler]

Honeywell Radiation Center  
Lexington, Massachusetts

Prepared for marketing purposes only -  
not to be used for publication.

Presented at the  
IRIS Detector Specialty Group Meeting Held in  
Washington, D.C., 13-15 March 1973

\*This work has been sponsored by NASA-GSFC and University of  
Michigan

NEAR INFRARED (Hg,Cd)Te PHOTODETECTORS

[N. C. Aldrich and T. Koehler]

Honeywell Radiation Center  
Lexington, Massachusetts

Presented at the  
IRIS Detector Specialty Group Meeting Held in  
Washington, D.C., 13-15 March 1973

\*This work has been sponsored by NASA-GSFC and University of Michigan

## Near Infrared (Hg,Cd)Te Photodetectors

by

N. C. Aldrich and T. Koehler

The status of near infrared photoconductive and photovoltaic (Hg,Cd)Te detectors is reviewed. Previously we have reported on the successful use of (Hg,Cd)Te in: 1 to 3-micrometer room temperature photodiodes for laser receivers<sup>1</sup>, n-color detectors<sup>2</sup> and near infrared detectors operating at 90 °K for the Skylab S-192 experiment.<sup>3</sup> Expanding these areas, this paper will discuss near infrared photoconductors operating at near room temperatures and a two color near infrared photovoltaic detector. This data adds to our family of (Hg,Cd)Te detectors in the near infrared for both photoconductive (Figure 3) and photovoltaic element (Figure 4).

Earth resources applications require information in the 1.55 to 1.75-micrometer region and the 2.05 to 2.35-micrometer region. Figure 5 shows typical data for near infrared photoconductors as a function to the high performance observed in near infrared photoconductors. The model for this trapping is discussed in detail in Broudy and Beck's paper<sup>4</sup>.

The performance of a 2.6-micrometer detector as a function of temperature is shown in Figure 6. While the detectivity at low temperatures (80° - 150 °K) is above  $10^{12}$  the detectivity at 200 °K is  $2 - 3 \times 10^{11}$  and at 240 °K it is  $2 - 3 \times 10^{10}$  cm Hz<sup>1/2</sup>/W. In order to increase the performance of these detectors at 200 - 240 °K, the wavelength must be as short as possible to decrease internally generated noise indicated by the  $D^*\lambda$  limit shown in Figure 7. The detectivity as a function of temperature for a 2.35-micrometer detector is shown in Figure 8 and as expected the detectivity between 200 °K and 240 °K is almost an order of magnitude greater than the 2.6-micrometer detector while the detectivity for low temperature is in the low  $10^{12}$  region as was the case with the 2.6-micrometer detectors.

Figure 9 shows the signal, noise and zero bias noise for a 2.35-micrometer detector. As expected<sup>6</sup> when the bias current is raised the noise increases the Johnson noise dominates beyond 80 kHz while with the lower bias the Johnson noise dominates above 20 kHz. The detective time constant is less than 10 microseconds for 0.16 mA bias and less than 2 microseconds for 0.55 mA bias without degradation in detectivity.

The 1.55 to 1.75-micrometer data is summarized in Figure 10 which shows the detectivity in the mid  $10^{11}$  cm Hz<sup>1/2</sup>/W region at 243 °K as a function of electrical bias and the detective time constant as a function of electrical bias.

A two-color near infrared photovoltaic (Hg,Cd)Te detector has been fabricated for the University of Michigan. The unit consists of two single elements which were stacked in pyramid configuration and a silicon substrate and printed circuit as shown in Figure 11. The single elements were fabricated from two slabs of zone leveled (Hg,Cd)Te with X values of 0.43 and 0.58 which are equivalent to 1.8 and 2.5-micrometer cutoff wavelengths at 300 °K. The junctions were formed by proton bombardment through a thin passivation layer of ZnS. The active area of the junction was defined by a proton mask as  $5.07 \times 10^{-4}$  cm<sup>2</sup>. Indium contacts were evaporated through 0.002-inch diameter holes in the ZnS. The elements were diced and assembled with a transparent epoxy interface layer. A typical bottom element is shown in Figure 12.

The electrical properties of the junctions were determined from capacitance-voltage (C-V) and current-voltage (I-V) characteristics. The capacitance showed a V<sup>-1/2</sup> dependence, indicating an abrupt junction. The zero bias capacitance at 77 °K was 1.55 pF for the top elements and 16.2 pF for the bottom elements. The differential capacitance indicated the substrate background concentration is  $2 \times 10^{16}$  cm<sup>-3</sup>, p-type. The I-V at 77 °K indicates a series resistance of 12 Kohm for the top element and 1 K for the bottom element. A typical I-V for a bottom element is shown in Figure 13. The shunt resistance at 77 °K is  $10^7$  ohm for the top element and  $4 \times 10^6$  ohm for the bottom element. A plot of the saturation current and RA product as a function of temperature (Figure 14) indicates that the resistance and hence thermal noise of the device is limited by the shunt resistance of the diode at 77 °K.

The frequency response of these devices is limited to 10 MHz by the series resistance and junction capacitance at zero bias, or 50 MHz with 6 volts reverse bias.

The optical properties of the two-color detector are shown in Figure 15, where the top element peaks at 1.8 micrometers and acts as a cold blocking filter for the bottom element which responds from 1.9 to 2.5 micrometers.

The detectivity ( $D^*_\lambda$ ) is limited by the shot noise of the saturation current or the thermal noise of the shunt resistance. This  $D^*_\lambda$  can be expressed in terms of the resistance area product (RA ohm-cm<sup>2</sup>). At zero bias  $D^*_\lambda$  can be expressed as

$$D^*_\lambda = \frac{\lambda \eta \sqrt{RA}}{hc \sqrt{4kT}}$$

where  $RA = \frac{kT}{qJ_0 A}$

$J_0$  = saturation current density  
 $A$  = detector area

or RA is determined by the shunt resistance. Cooling the detector reduces  $J_0$  and increases RA until the shunt limit is reached. Experimental data confirms this temperature dependence of detectivity except for changes in quantum efficiency due to minority carrier property changes. Figure 16 shows this temperature dependence of detectivity.

The current status of 2-color PV (Hg,Cd)Te is summarized in Figure 17. The 77 °K performance can be improved considerably above the current  $D^*_\lambda = 6 \times 10^{11}$  cm Hz<sup>1/2</sup>/W by increasing the shunt resistance by improving surface passivation.

## REFERENCES

1. Soderman, D.A., and Pinkston, W.H., "(Hg,Cd)Te Photodiode Laser Receivers for the 1 to 3 micrometer Spectral Region," *Applied Optics*, 11, 2162, Oct. 1972
2. Halpert, H. and Musicant, B.L., "N-Color (Hg,Cd)Te Photodetectors," *Applied Optics*, 11, 2157, Oct. 1972
3. Aldrich, N.C. and Beck, J.D., "Performance of S-192 (Hg,Cd)Te Arrays," *Applied Optics*, 11, 2153, Oct. 1972
4. Broudy, R.M. and Beck, J.D. "Trapping Photoconductivity in (Hg,Cd)Te Detectors," IRIS Detector Specialty Meeting, March 13-15, 1973, Washington, D.C.

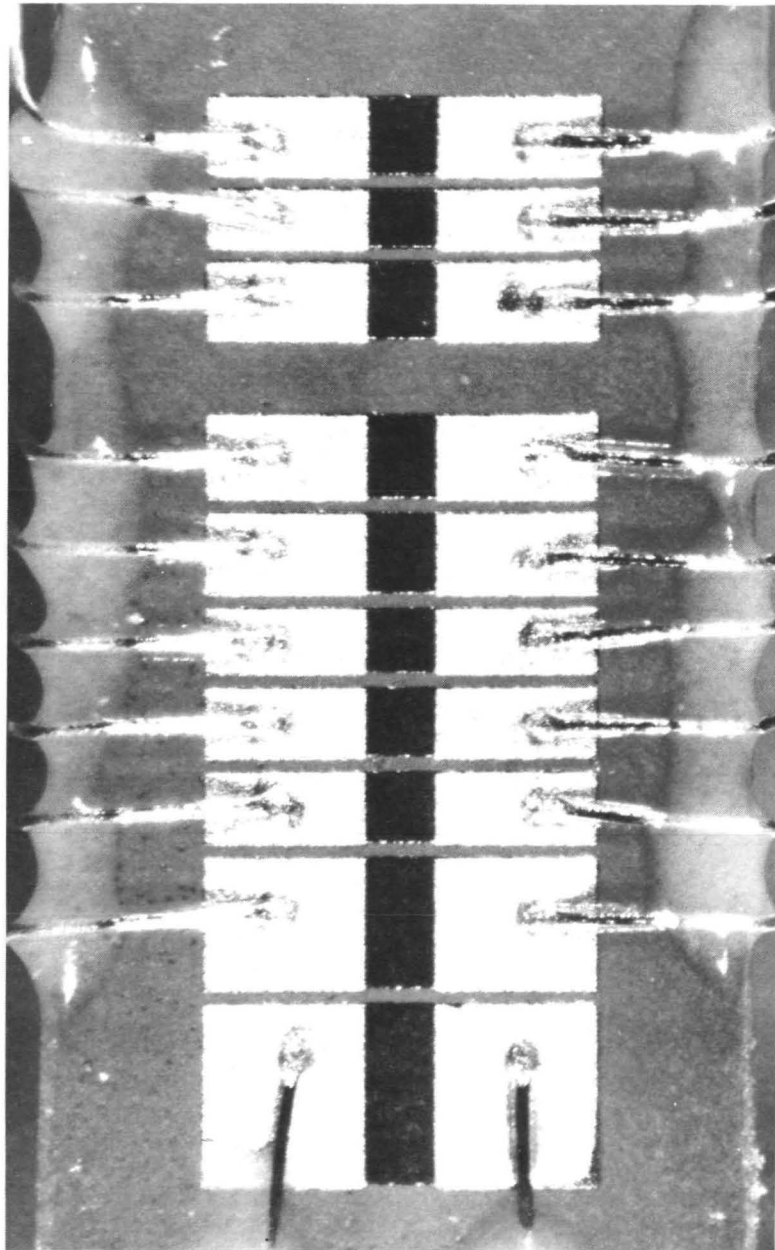


Figure 1 S-192 (Hg,Cd)Te ARRAY



Figure 2 DLK-95A HIGH SPEED (Hg,Cd)Te PHOTODIODE  
DETECTOR PREAMPLIFIER MODULE

CLASS OF NEAR-INFRARED (Hg,Cd)Te PHOTOCONDUCTORS

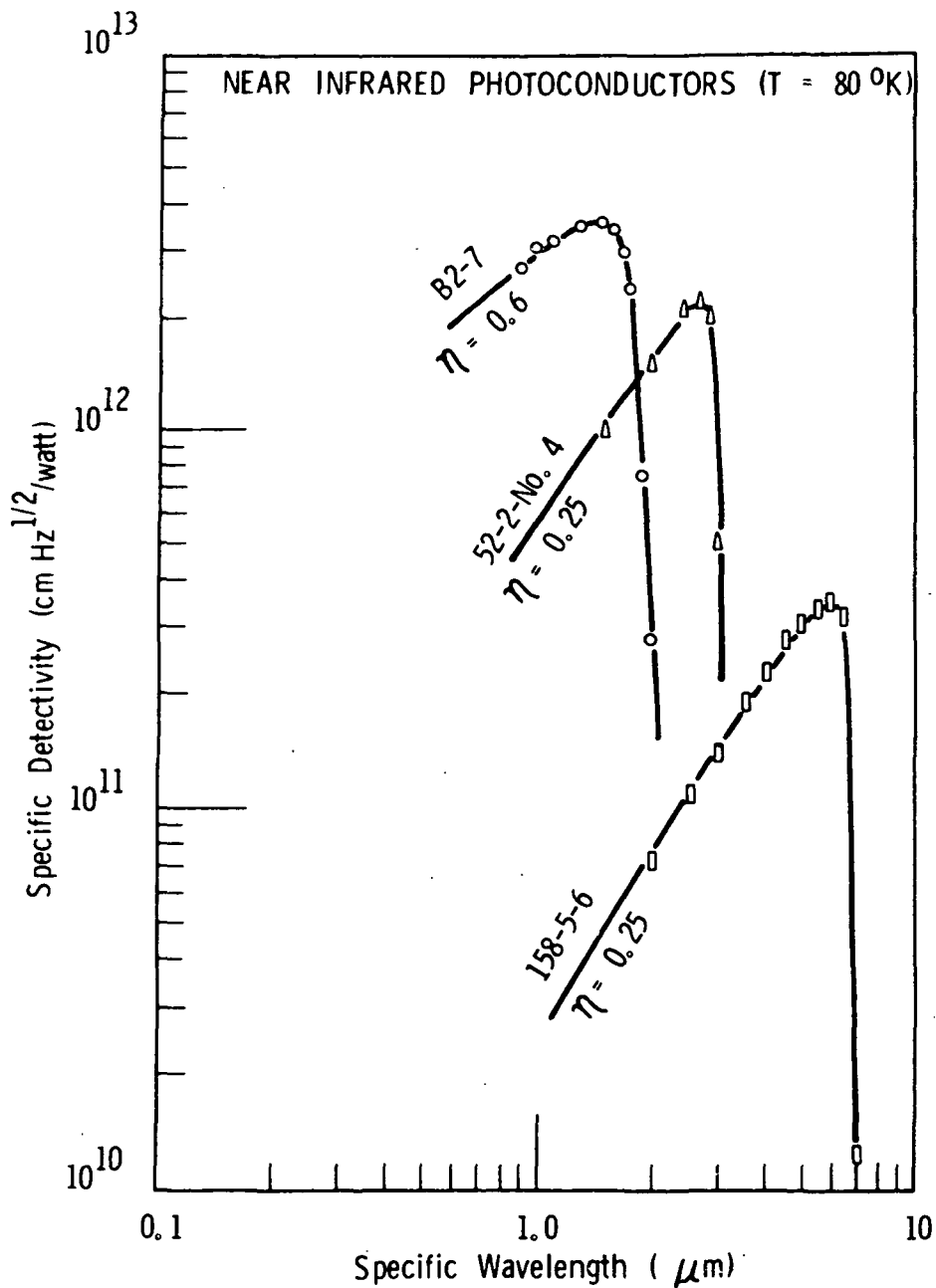


Figure 3 CLASS OF NEAR INFRARED (Hg,Cd)Te PHOTOCONDUCTORS

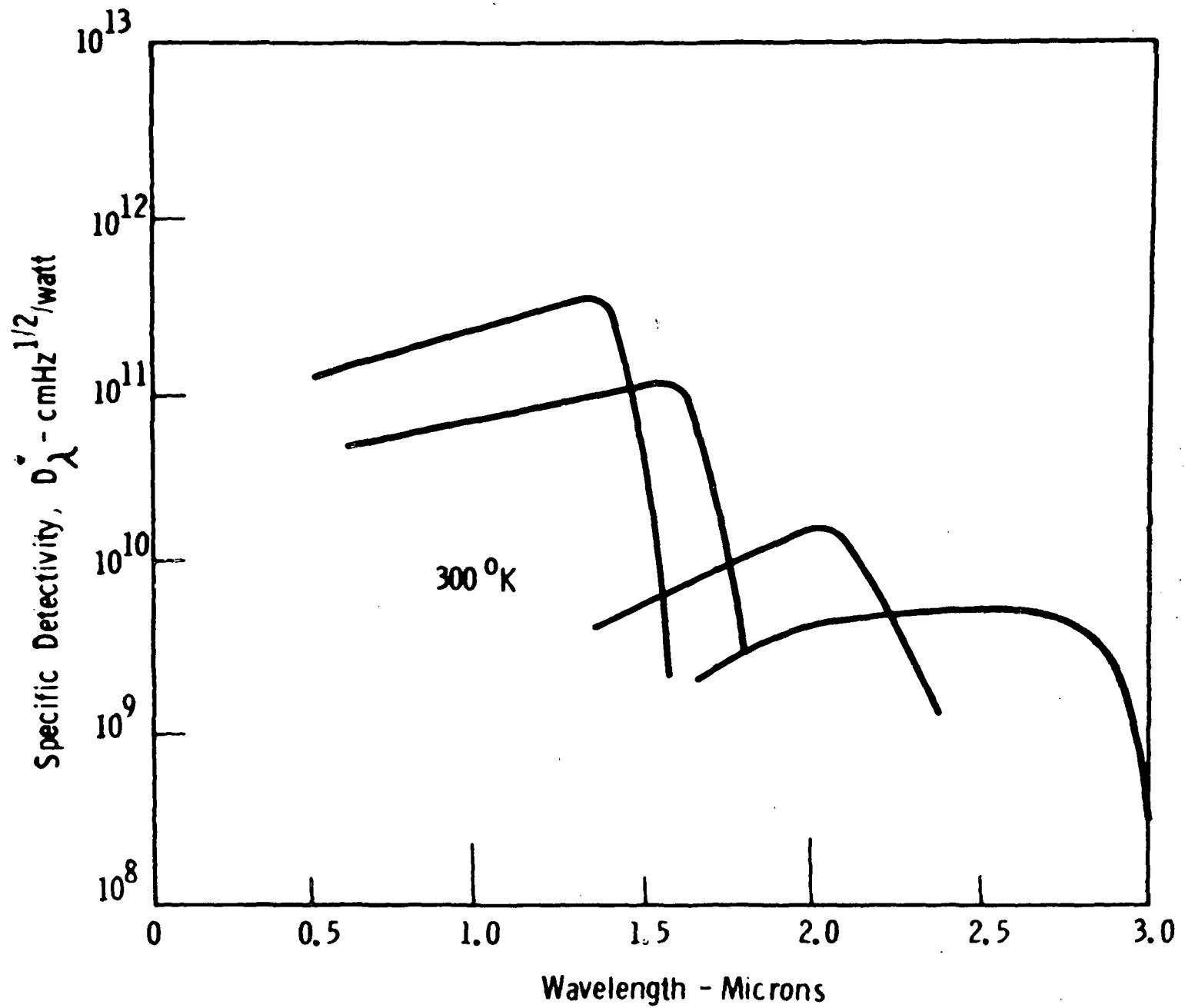
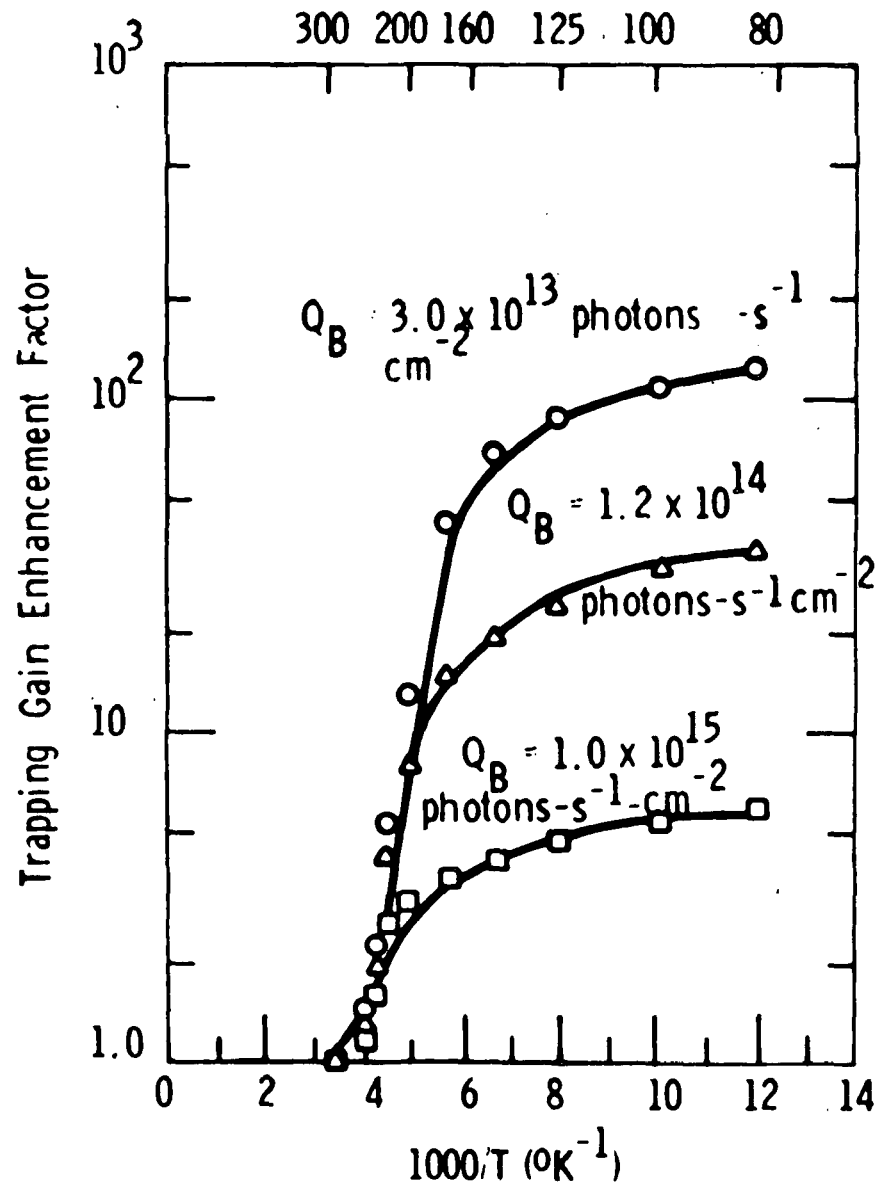


Figure 4 NEAR INFRARED DETECTORS - PHOTOVOLTAIC



MODEL: EXPONENTIAL DENSITY OF TRAPS

WHERE:  $E_m = E_g/2 + 4kT$  eV  
 $N_0 = 2.9 \times 10^{15}$  eV<sup>-1</sup>  $\cdot$  cm<sup>-3</sup>  
 $N_t = 2.5 \times 10^{14}$  cm<sup>-3</sup>  
 $E_x = 0.09$  eV  
 $E_g = 0.438$  eV  
 $\eta = 0.5$   
 $\tau = 3 \times 10^{-6}$   
 $d = 1.0 \times 10^{-3}$  cm

— Calculated  
 ○ Experiment  
 △ Experiment  
 □ Experiment

DETECTOR: K13-18 B-3-1

MEASUREMENT CONDITIONS:

$E = 27$  V/cm      FOV = 180°

Figure 5 TRAPPING GAIN AS A FUNCTION OF TEMPERATURE

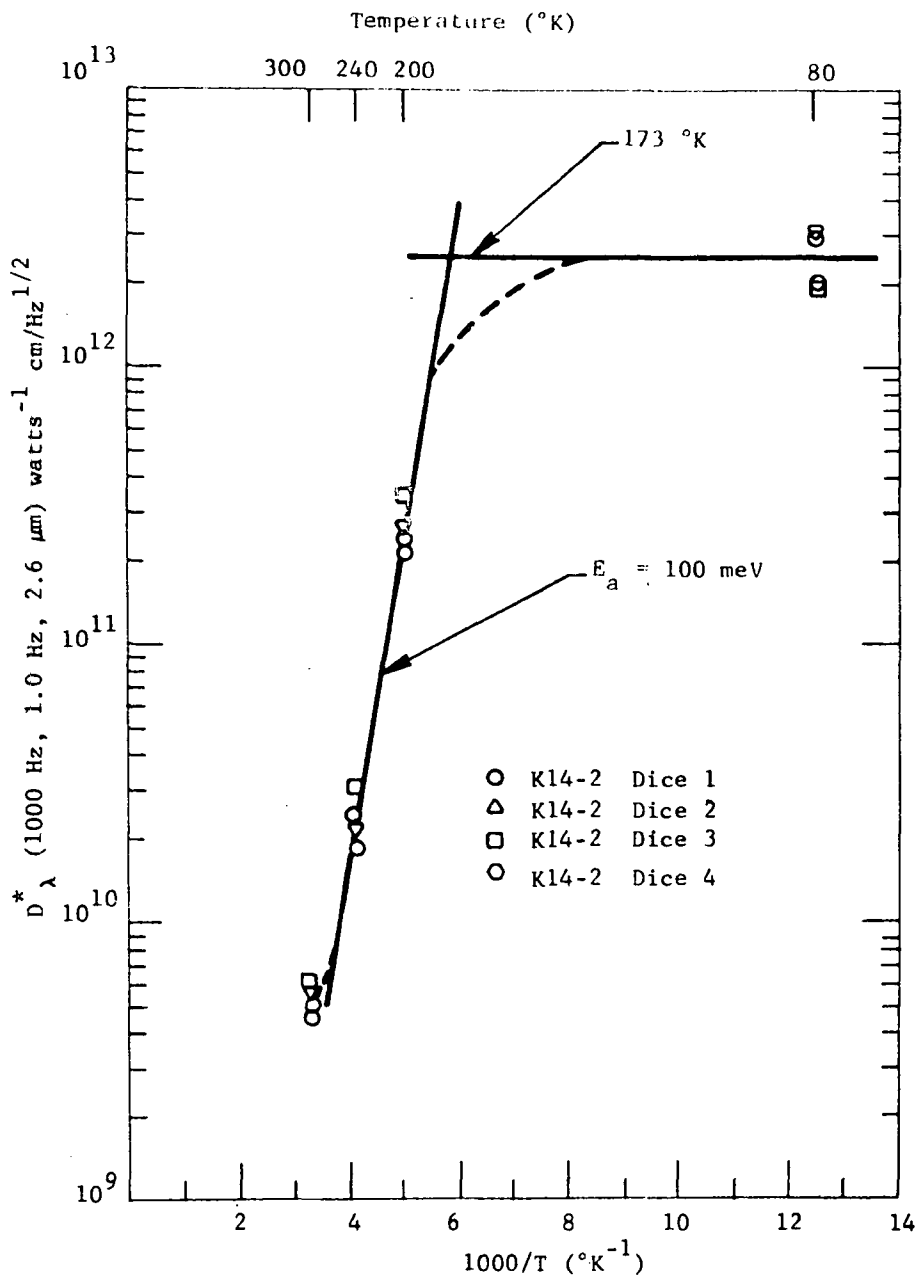


Figure 6. DETECTIVITY AS A FUNCTION OF TEMPERATURE FOR 2.6 MICRON DETECTORS

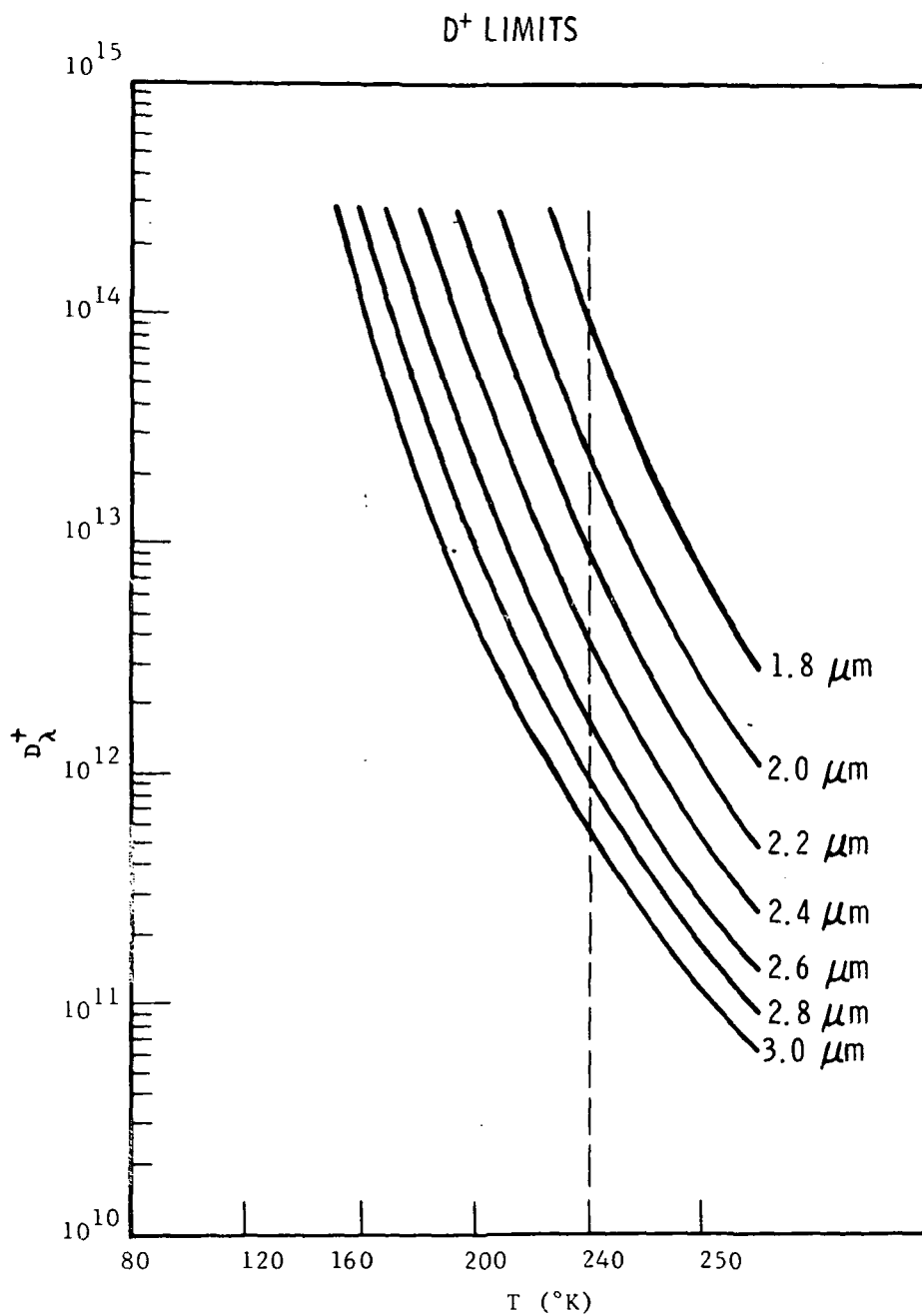


Figure 7  $D^+$  LIMITS

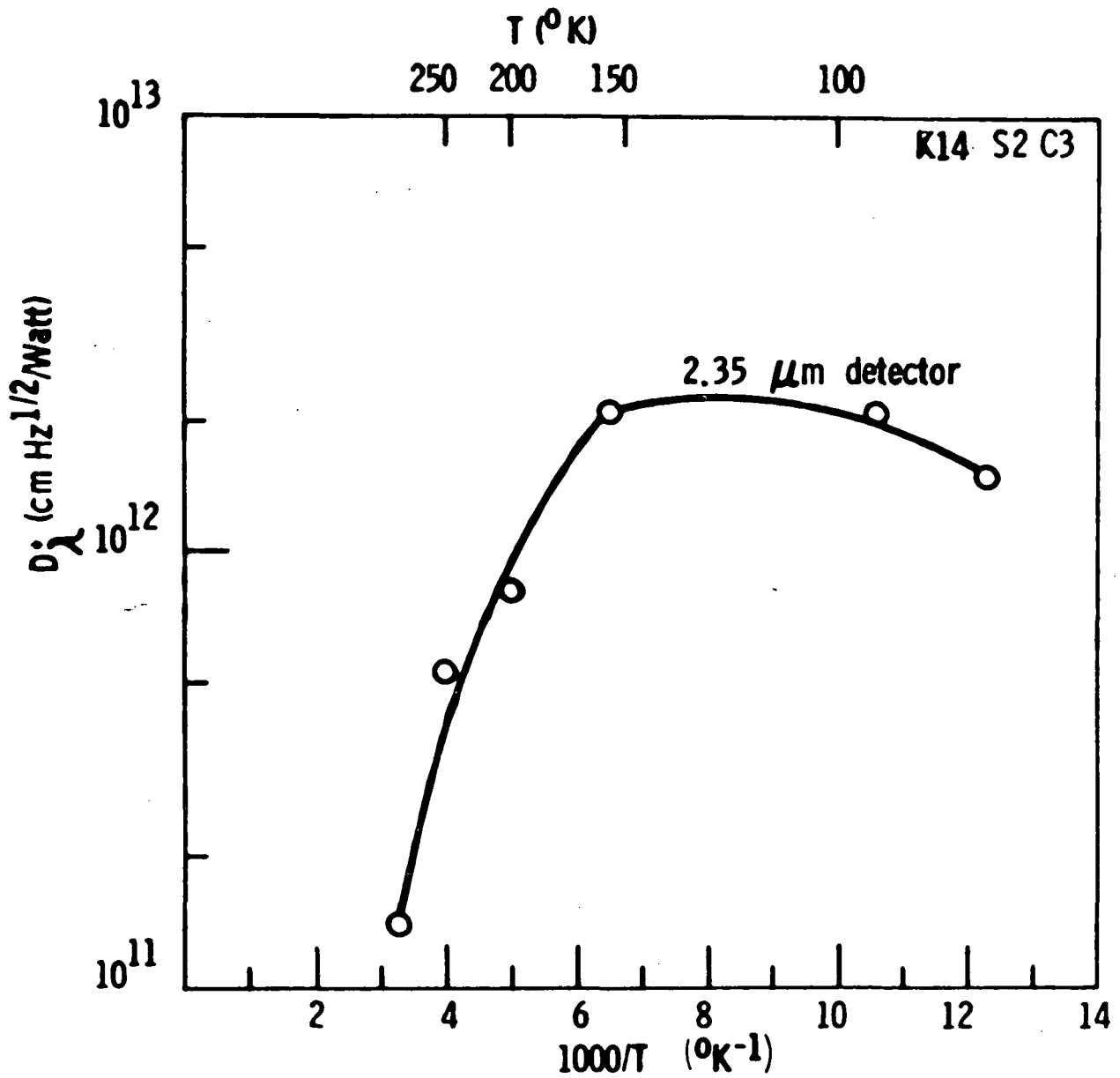


Figure 8 DETECTIVITY AS A FUNCTION OF TEMPERATURE FOR A 2.35 MICRON DETECTOR

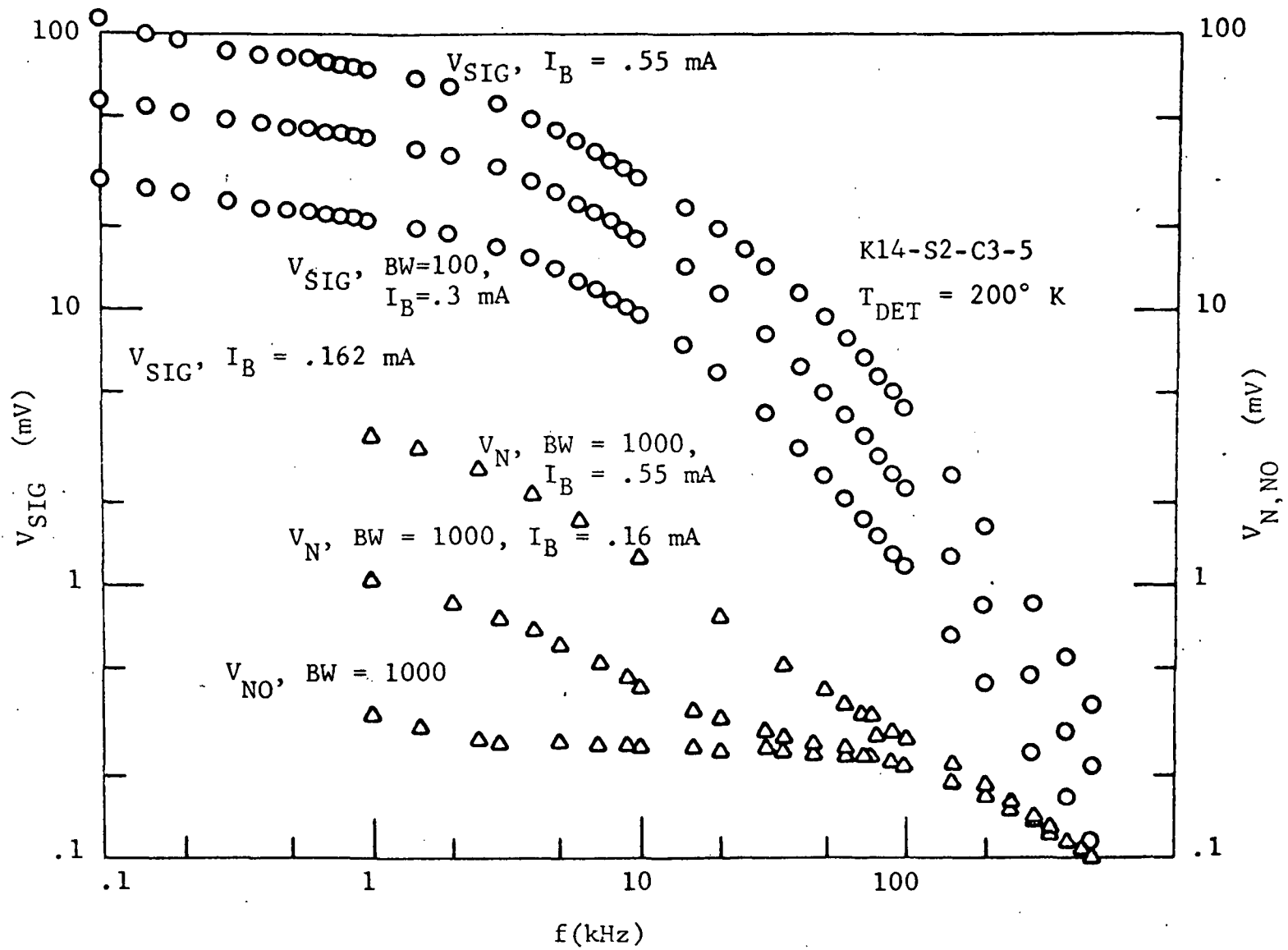


Figure 9 SIGNAL AND NOISE AS A FUNCTION OF FREQUENCY FOR A 2.35 MICRON DETECTOR

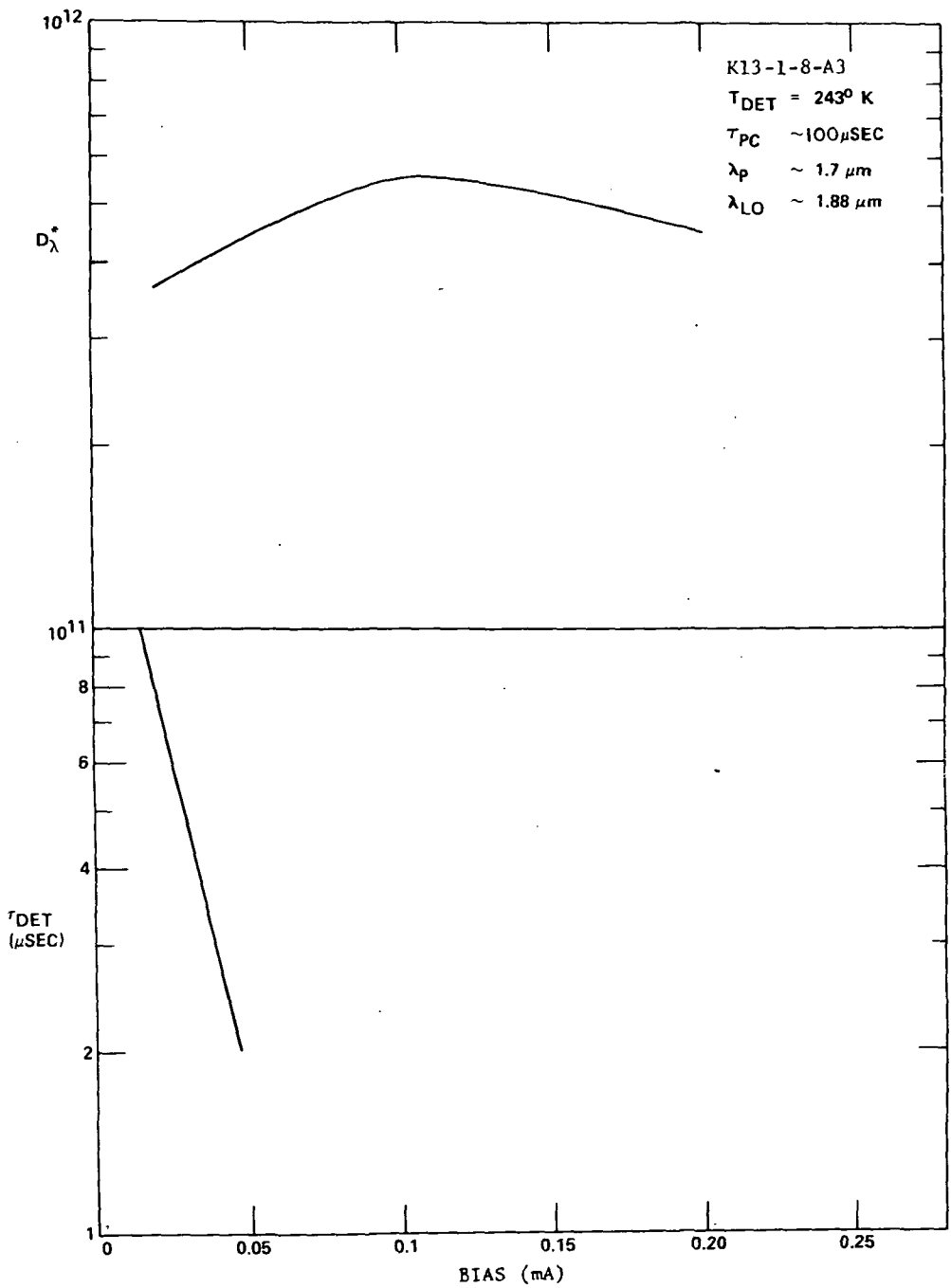


Figure 10 DETECTIVITY AND DETECTIVE TIME CONSTANT AS A FUNCTION OF ELECTRICAL BIAS FOR A 1.9 MICRON DETECTOR

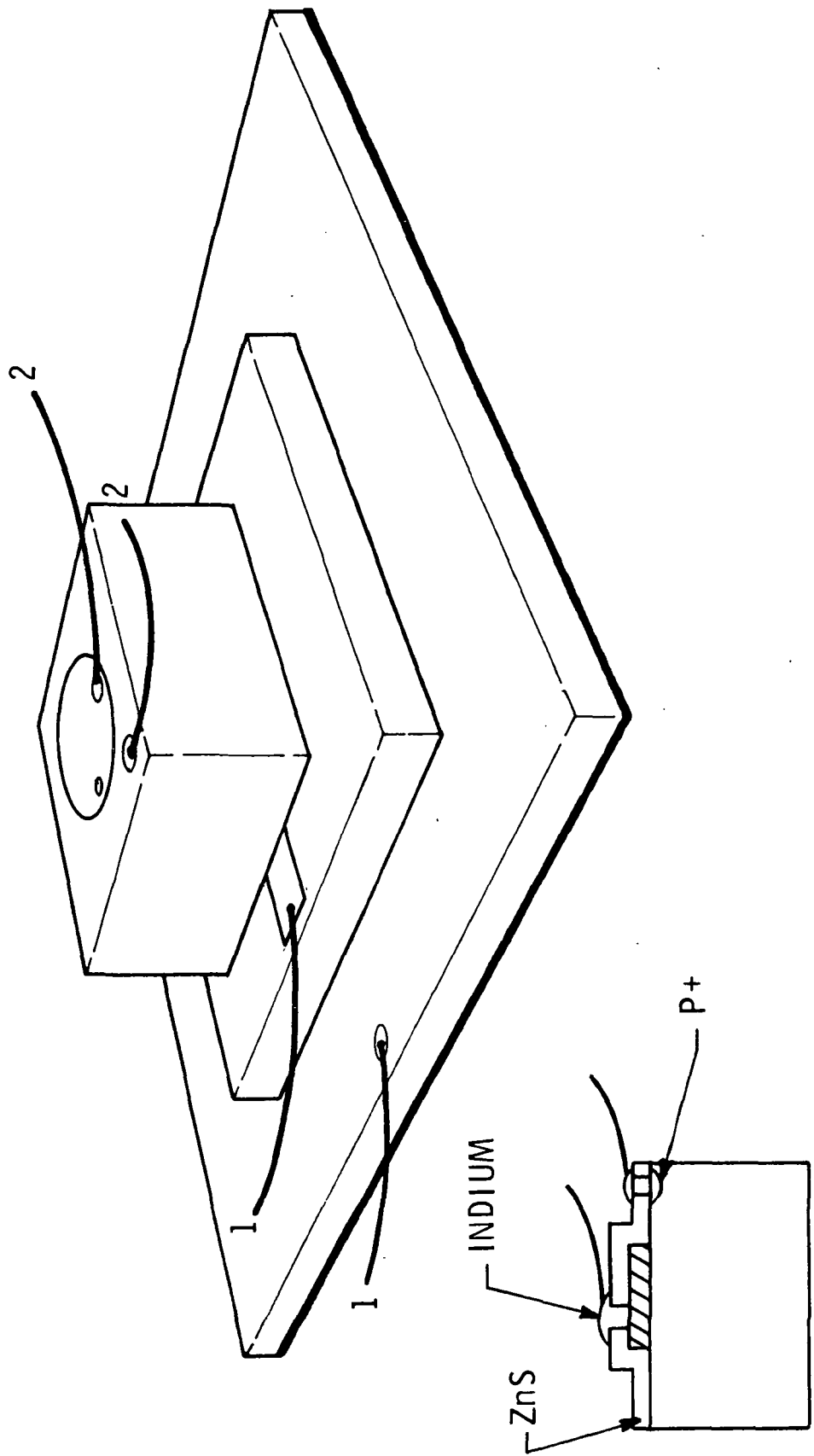


Figure 11 2 COLOR PV

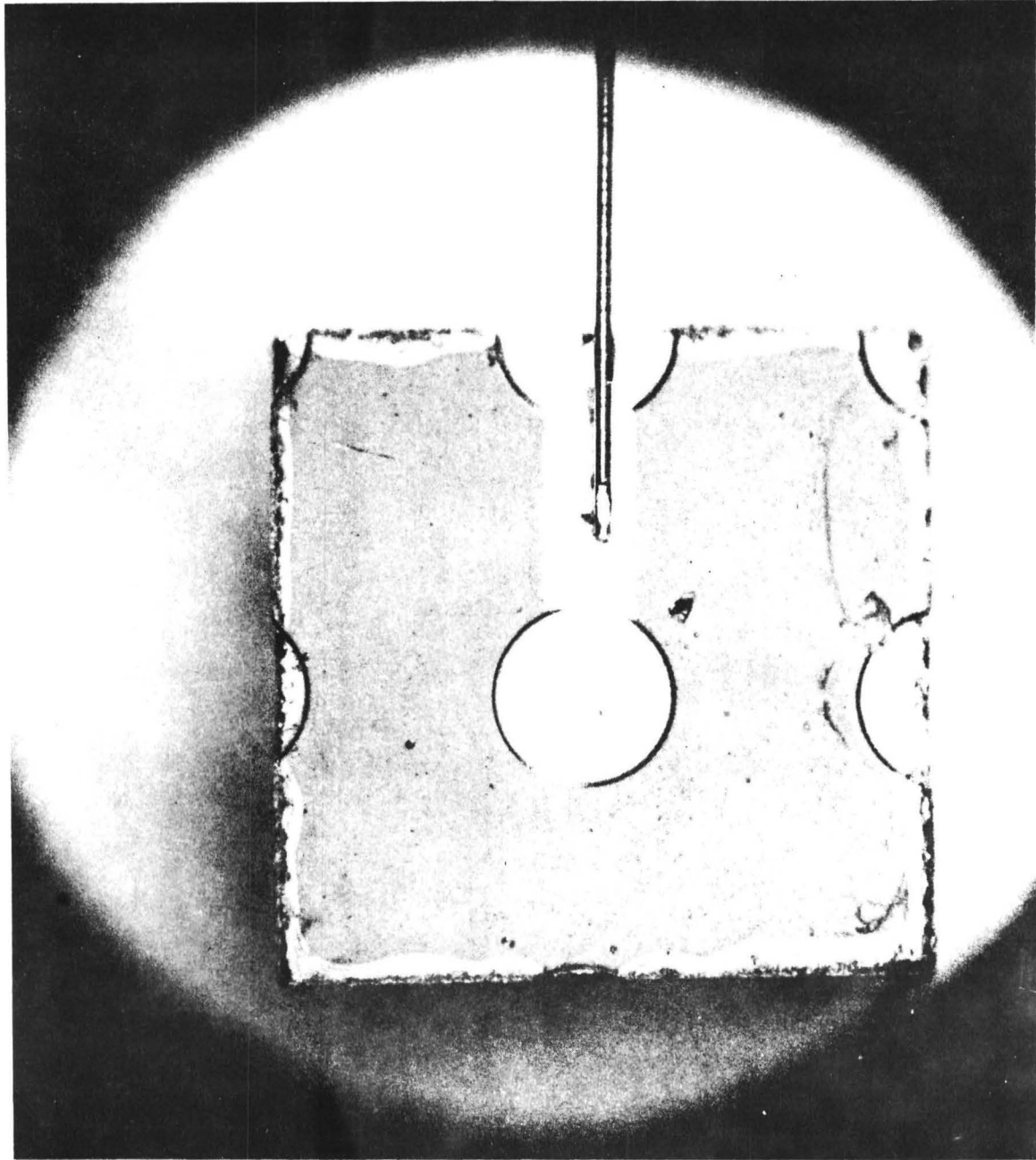


Figure 12 BOTTOM ELEMENT OF 2-COLOR DETECTOR. DIAMETER  $.0254 \text{ cm}^2$

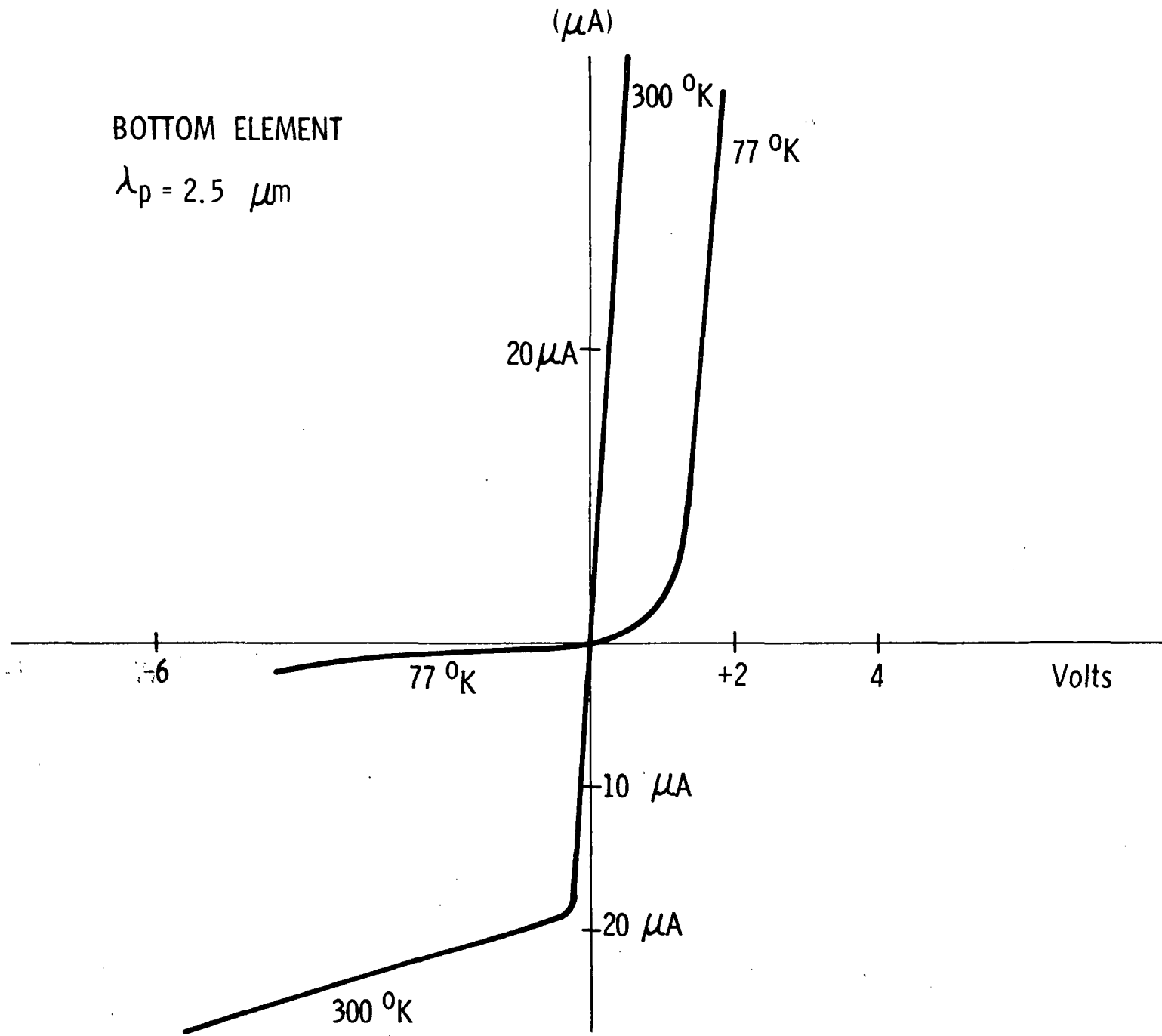


Figure 13 CURRENT-VOLTAGE CHARACTERISTIC OF TYPICAL BOTTON ELEMENT OF 2-COLOR

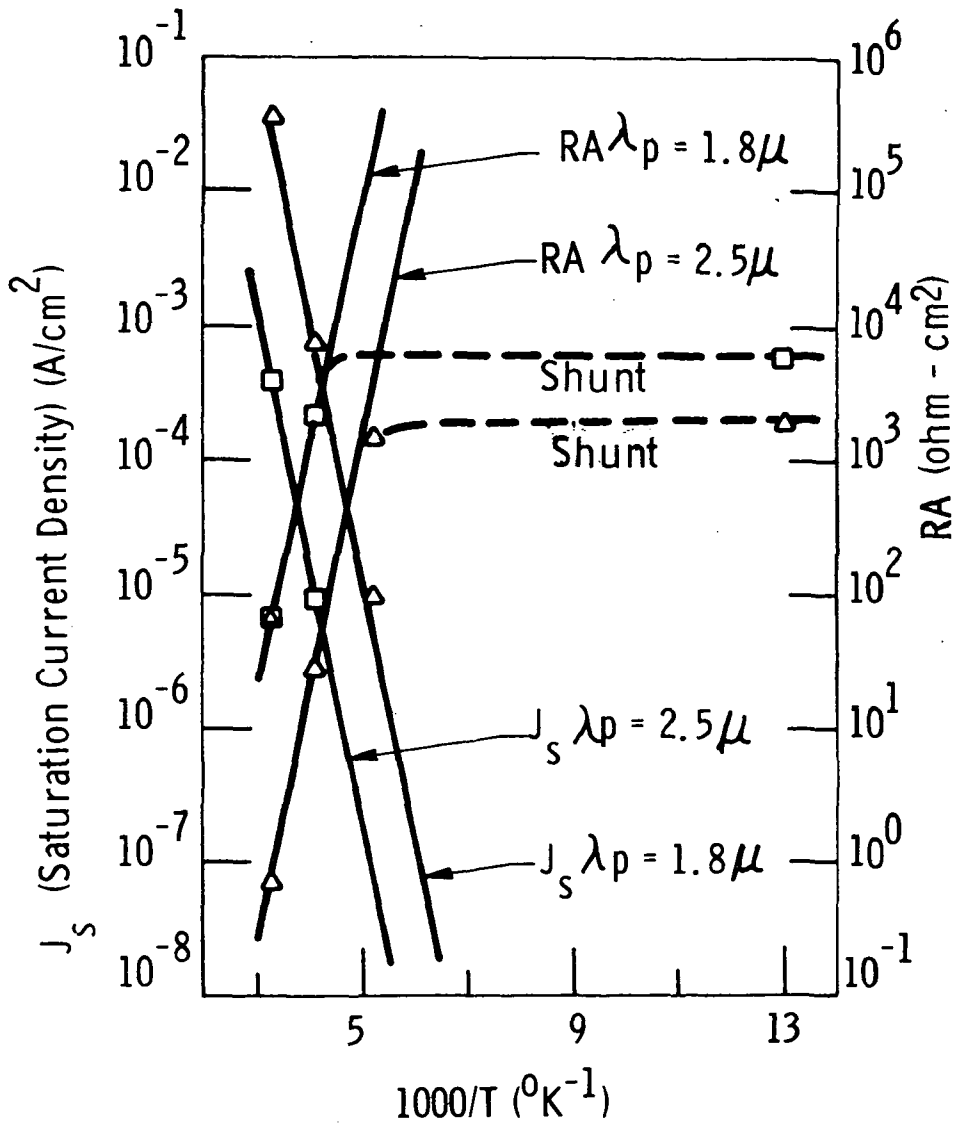


Figure 14 SATURATION CURRENT AND RA AS A FUNCTION OF TEMPERATURE

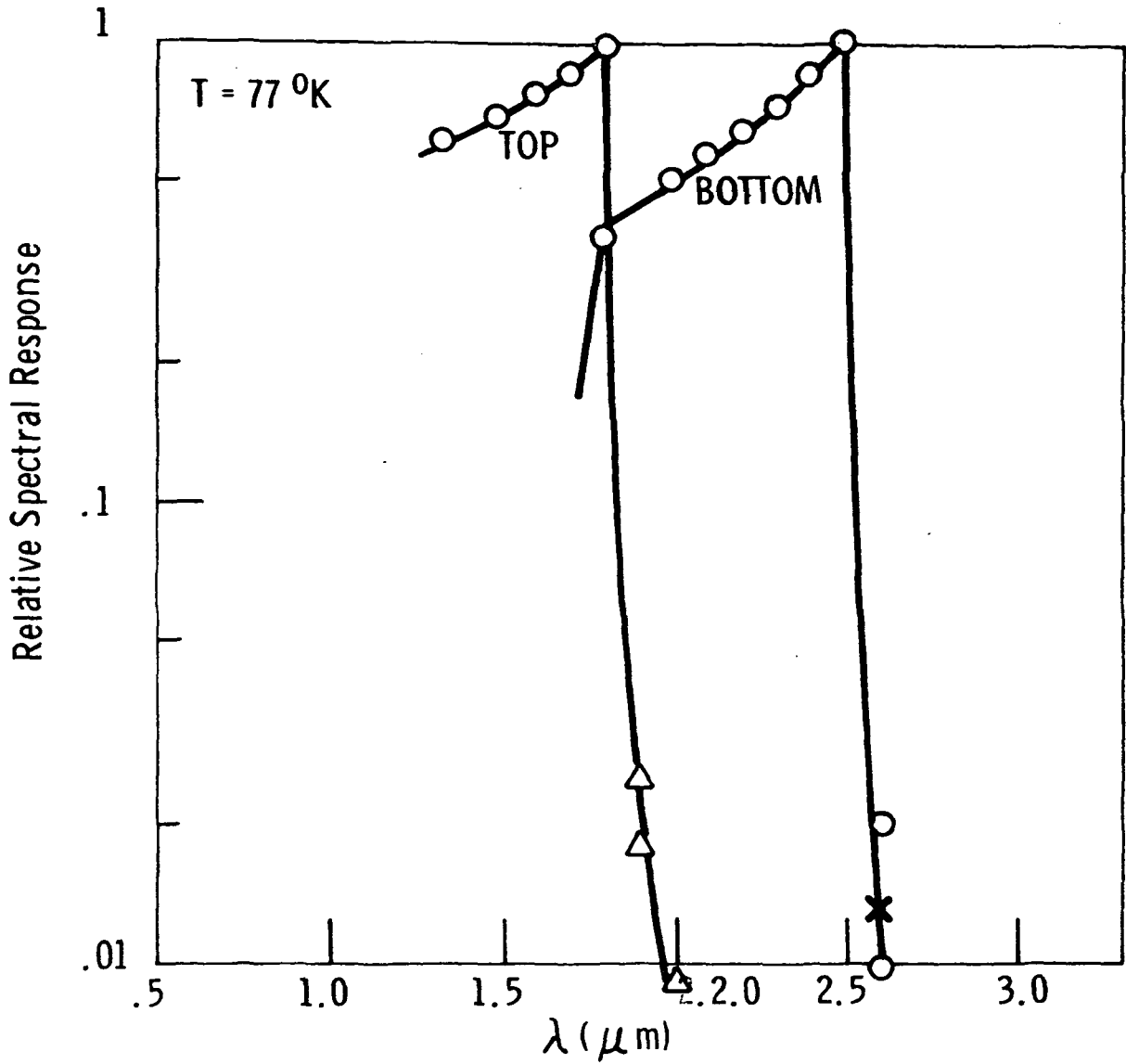


Figure 15 SPECTRAL RESPONSE OF 2-COLOR DETECTOR

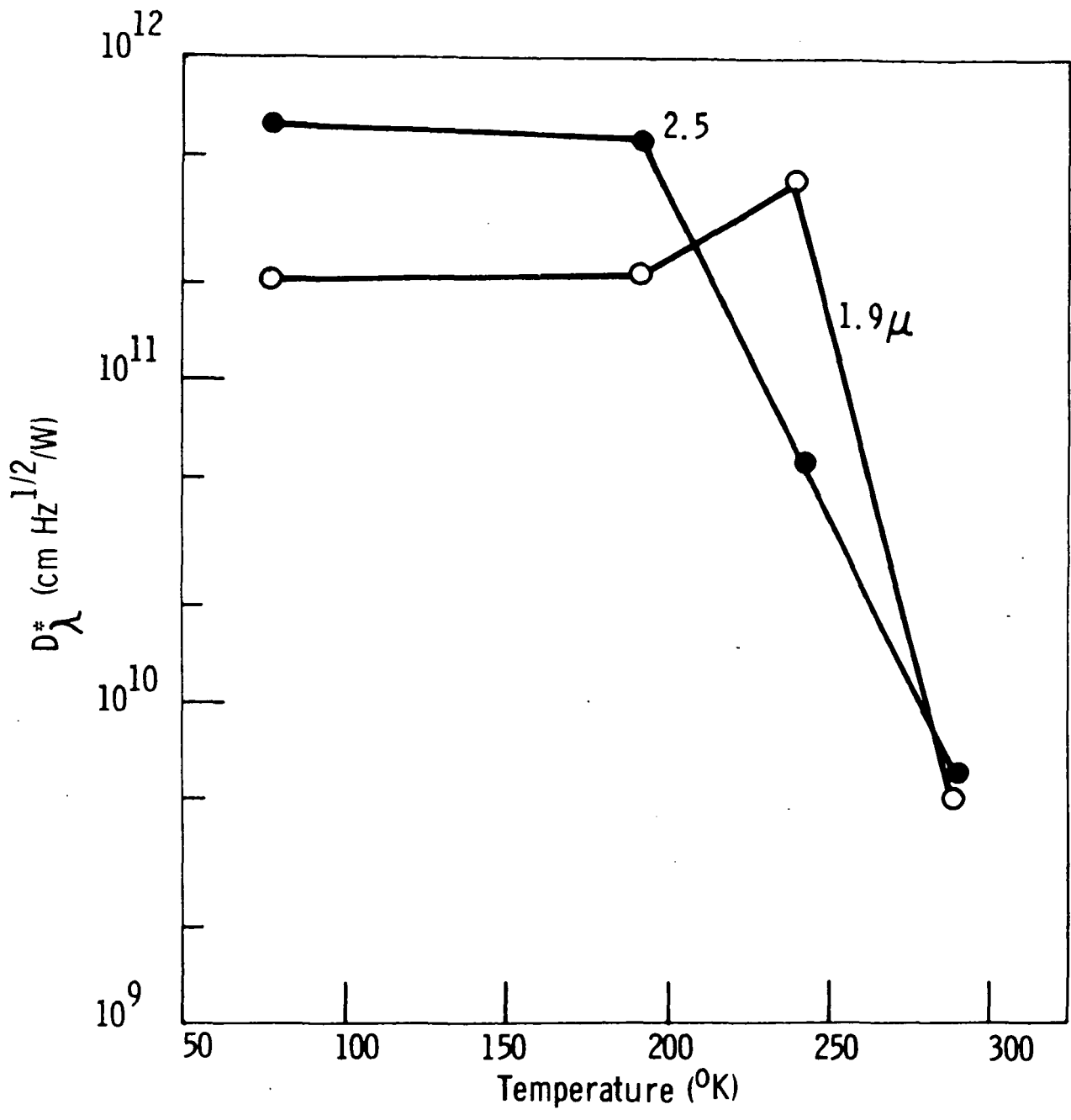


Figure 16  $D^*_\lambda$  AS A FUNCTION OF TEMPERATURE FOR 2-COLOR PV DETECTOR

	TOP		BOTTOM	
	300 <sup>o</sup> K	77 <sup>o</sup> K	300 <sup>o</sup> K	77 <sup>o</sup> K
$\lambda_p$ ( $\mu$ m)	1.8		2.5	
$D^*_\lambda$ cm Hz <sup>1/2</sup> /W	$5 \times 10^9$	$1.6 \times 10^{11}$	$6 \times 10^9$	$6. \times 10^{11}$
$\eta$ (%)	5	40	32	48
$A_D$ (cm)	$5.07 \times 10^{-4}$		$5.07 \times 10^{-4}$	
$R_{sh}$ (ohm)	73 m $\Omega$	$10^7$	$8. \times 10^5$	$4 \times 10^6$
R series (K ohm)	8	12	.4	1
C (V = 0) (pfd)	1.85	1.55	28	16.2
$V_{Breakdown}$	---	~50 Volts	---	~50 Volts

Figure 17 SUMMARY - 2 COLOR PV DETECTORS

APPENDIX C  
LIST OF SYMBOLS

LIST OF SYMBOLS  
for Section 2.2.1

SYMBOL	MEANING
$\alpha$	Absorption coefficient
$V_a$	Amplifier noise
$V_o$	Applied dc bias
$E$	Applied electric field across detector
$\omega$	Angular frequency = $2\pi f$
$A_{det}$	Area of detector
$Q_B$	Background photon flux
$k$	Boltzmann's constant
$n_o$	Dark electron concentration
$p_o$	Dark hole concentration
$l$	Detector length
$d$	Detector Thickness
$\tau_{det}$	Detective Time Constant
$w$	Detector width
$P_{diss}$	Dissipated power
$Q_l$	Effective generation term
$E_{gap}$	Energy gap
$G_r$	Generation rate
$V_{gr}$	Generation - recombination noise
$p$	Hole concentration
$V_j$	Johnson noise = $4kT_{rd}\Delta f$
$N_{gr_o}$	Low frequency generation recombination noise
$R_o$	Low frequency responsivity
$\Delta f$	Noise measurement bandwidth
$V_{1/f}$	1/f noise
$h$	Plank's constant

SYMBOL	MEANING
$\Delta n$	Photogenerated electron concentration
$\Delta p$	Photogenerated hole concentration
$\eta$	Quantum efficiency
$r_z$	Refractive index
$r_d$	Resistance
$\tau_{pc}$	Response Time
$c$	Speed of light
$T$	Temperature
$\lambda$	Wavelength

III LIST OF SYMBOLS FOR SECTIONS 2.2.3 AND 2.2.4

SYMBOL	MEANING	UNITS
$A_s$	Sample area	$\text{cm}^2$
$c$	Speed of light in a vacuum	$\text{cm}/\text{sec}$
$d$	Sample thickness	$\text{cm}$
$e$	Electron charge	coulombs
$E$	energy	eV
$E$	Electric field	$\text{V}/\text{cm}$
$E_g$	Energy of the gap	eV
$E_s$	Trap saturation energy	eV
$E_a$	Trap activation energy	eV
$E_x$	Energy at which $N(E) = N(0)/e$	eV
$E_c \equiv E_g$	Conduction band energy	eV
$E_v \equiv 0$	Valence band energy	eV
$E_m$	Maximum energy of operant traps (approx)	$E_v$
$f_t(E)$	Trapped hole occupation probability	---
$G_t$	Trapping gain	---
$G$	Generation rate of excess carriers	$\text{cm}^{-3}\text{-sec}^{-1}$
$h$	Planck's constant	erg-sec
$H$	Spectral irradiance	$\text{watts}/\text{cm}^2$
$I$	Current	Amperes
$k$	Boltzmann's constant	$\text{eV}/^\circ\text{K}$
$l$	Sample length	$\text{cm}$
$m_h^*$	Effective hole mass (normalized)	---
$m_e^*$	Effective electron mass (normalized)	---
$N(E)$	Density of trap states at energy $E$	$\text{cm}^{-3}\text{-eV}^{-1}$
$N_t$	Total density of traps	$\text{cm}^{-3}$
$N_0, N(0)$	Density of traps at $E = 0$	$\text{cm}^{-3}\text{-eV}^{-1}$
$n$	Total concentration of electrons in the conduction band	$\text{cm}^{-3}$

LIST OF SYMBOLS (CONT)

SYMBOL	MEANING	UNITS
$n_i$	Intrinsic carrier concentration	$\text{cm}^{-3}$
$n_o$	Equilibrium electron concentration	$\text{cm}^{-3}$
$\Delta n$	Excess electron concentration	$\text{cm}^{-3}$
$n_t$	Total number of trapped electrons	$\text{cm}^{-3}$
$n_{to}$	Equilibrium trapped electron concentration	$\text{cm}^{-3}$
$\Delta n_t$	Excess trapped electron concentration	$\text{cm}^{-3}$
$n_l$	$N_c \exp [(E_a - E_c)/kT]$	$\text{cm}^{-3}$
$N_v$	Effective density of states at the valence band edge	$\text{cm}^{-3}$
$N_c$	Effective density of states at the conduction band edge	$\text{cm}^{-3}$
$N_A$	Acceptor impurity concentration	$\text{cm}^{-3}$
$N_D$	Donor impurity concentration	$\text{cm}^{-3}$
$p$	Total concentration of holes in the valence band	$\text{cm}^{-3}$
$p_o$	Equilibrium hole concentration	$\text{cm}^{-3}$
$\Delta p$	Excess hole concentration	$\text{cm}^{-3}$
$p_t$	Total number of trapped holes	$\text{cm}^{-3}$
$p_{to}$	Equilibrium trapped hole concentration	$\text{cm}^{-3}$
$\Delta p_t$	Excess trapped hole concentration	$\text{cm}^{-3}$
$p_l$	$= N_v \exp [(E_v - E_a)/kT]$	$\text{cm}^{-3}$
$\Delta p_t(E)$	Trapped hole occupation probability	---
ph	photon	
$Q$	Total photon flux	$\text{ph/s-cm}^2$
$Q_B$	Background photon flux	$\text{ph/s-cm}^2$
$Q_s$	Signal photon flux	$\text{ph/s-cm}^2$
$r_s$	Sample resistance	ohms
$Q_{Bo}$	Room background photon/flux	$\text{ph/s-cm}^2$

LIST OF SYMBOLS (CONT)

SYMBOL	MEANING	UNITS
$R_{\lambda}$	Responsivity at wavelength $\lambda$	V/watt
$R_{vt}$	Excitation rate of electrons from valence band to trap	$\text{cm}^{-3} \text{s}^{-1}$
$R_{ct}$	Excitation rate of electrons from conduction band to trap	$\text{cm}^{-3} \text{s}^{-1}$
$R_{tc}$	Excitation rate of electrons from trap to conduction band	$\text{cm}^{-3} \text{s}^{-1}$
$R_{tv}$	Excitation rate of electrons from trap to valence band	$\text{cm}^{-3} \text{s}^{-1}$
$r_v$	Hole capture probability per unit time	$\text{cm}^3/\text{s}$
$r_c$	Electron capture probability per unit time	$\text{cm}^3/\text{s}$
T	Temperature	$^{\circ}\text{K}$
t	Time	s
$V_{\text{sig}}$	Signal voltage	volts
w	Sample width	cm
$\eta$	Effective quantum efficiency	---
$\tau$	Lifetime	s
$\tau_{\text{SR}}$	Shockley-Read lifetime	s
$\tau_{\text{inst}}$	Instantaneous lifetime	s
$\lambda$	Wavelength	$\mu\text{m}$
$\sigma$	Conductivity	mho/cm
$\mu_e$	Electron mobility	$\text{cm}^2/\text{V-s}$
$\mu_h$	Hole mobility	$\text{cm}^2/\text{V-s}$